Grain Growth, Phase Transition and Optical Properties of Modified TiO_2

Ph. D. Thesis

By

NASIMA KHATUN

DISCIPLINE OF PHYSICS

INDIAN INSTITUTE OF TECHNOLOGY INDORE

NOVEMBER 2018

Grain Growth, Phase transition and Optical Properties of Modified TiO_2

A THESIS

Submitted in partial fulfillment of the
requirements for the award of the degree
of
DOCTOR OF PHILOSOPHY

by
NASIMA KHATUN

DISCIPLINE OF PHYSICS
INDIAN INSTITUTE OF TECHNOLOGY INDORE
NOVEMBER 2018

INDIAN INSTITUTE OF TECHNOLOGY INDORE

CANDIDATE’S DECLARATION

I hereby certify that the work which is being presented in the thesis entitled “**GRAIN GROWTH, PHASE TRANSITION AND OPTICAL PROPERTIES OF MODIFIED TiO_2”** in the partial fulfillment of the requirements for the award of the degree of **DOCTOR OF PHILOSOPHY** and submitted in the **DISCIPLINE OF PHYSICS, Indian Institute of Technology Indore**, is an authentic record of my own work carried out during the time period from July 2014 to November 2018 under the supervision of Dr. Somadity Sen, Associate Professor, Discipline of Physics, IIT Indore

The matter presented in this thesis has not been submitted by me for the award of any other degree of this or any other institute.

Signature of the student with date
(NASIMA KHATUN)

This is to certify that the above statement made by the candidate is correct to the best of my/our knowledge.

Signature of Thesis Supervisor #1 with date
(Dr. SOMADITYA SEN)

NASIMA KHATUN has successfully given his/her Ph.D. Oral Examination held on **19th June 2019**.

Signature of Chairperson (OEB) Date:	Signature of External Examiner Date:	Signature(s) of Thesis Supervisor(s) Date:
Signature of PSPC Member #1 Date:	Signature of PSPC Member #2 Date:	Signature of Convener, DPGC Date:

Signature of Head of Discipline
Date:

ACKNOWLEDGEMENTS

This thesis is the last step toward the end of my journey for the completion of Ph. D. degree. This journey was not possible without the constant support, motivation and encouragement of some people.

First and foremost, I would like to express my deep and sincere gratitude to my supervisor Dr. Somaditya Sen, for giving me the opportunity to do research and providing me with profound comments, guidance and constant encouragement, and support throughout my Ph. D. years. His dynamism and enthusiasm towards work have deeply encouraged me to work more energetically and passionately.

I would like to thank my PSPC members Dr. Parasharam M. Shirage and Dr. Sanjay Kumar Singh for evaluating and giving their valuable comments for improving my research work. I also thank Dr. Sunil Kumar for his constructive discussion. Thanks to Dr. Ashok Kumar Mocherla for correcting language of two thesis chapters.

During my Ph. D., I was fortunate enough to get financial support from IIT Indore and MHRD, Govt. of India for providing me the fellowship as a teaching assistant. I gratefully acknowledge science and engineering research board (SERB) for providing me financial support to attend international conference. I also owe my sincere thanks to Discipline of Physics, IITI for providing the generous funding, laboratory facilities and rich environment to explore new ideas. I am also grateful to all the academic and administrative staff of IITI for providing practical support with friendly enthusiasm and grace. I thank Mr. Kinney Pandey, Nitin Upadhyay, Debasis for helping me in the technical works at SIC Indore. I also thank Mr. P. K. Parthiban of Glassblowing section IIT Indore. I am very thankful to Dr. Pankaj Sagdeo for providing optical measurement facilities.

I gratefully acknowledge the collaborators outside my institute: Dr. P. Rajput, Dr. S. N. Jha, Dr. D. Bhattacharyya of RRCAT Indore and BARC Mumbai for permitting me to use the facilities at their institute. I would like to acknowledge Dr. R. J. Choudhary from UGC-DAE, Indore, Dr. C. P. Vinod from CSIR-National Chemical Laboratory,

Pune, for characterizations facilities. I am also grateful to Dr. Sajal Biring, Ming Chi University of Technology, Taiwan for his immense support and providing characterizations facilities.

Writing PhD thesis without the help of colleagues is not possible. I sincerely thank my lab mates Arun, Tulika, Nasir, Anita, Gaurav, Saurabh, Ruhul, Prashant and Saniya for providing friendly and fulfilled environment in lab. My special appreciation goes to Anita, Ruhul and Sourabh for their love, care and support that they showered on me. In particular, I want to thank, Tulika and Anita with whom I shared my residence and I admire their care and support. I also thank Dr. E.G. Rini and Dr. Swasti Saxena for their advices and motivation. I am very thankful to Gargee for her moral support during my good as well as awful times. Moreover, I want to thank intern students especially Jayanti, kiran, Aditya, Gyanendra, Eshika for helping me in experiments. I would also like to thank Soma mam for her motherly care and love.

I heartily thank to my school and college friends and teachers who show faith on me and motivate me to do research.

Most importantly, I would like to express my sincere gratitude to my family; parents, siblings, their extended family and my lovely niece and nephew. Smiling and innocent faces of my cute niece (Fija and Nira) and nephew (Habib, Najim and Boomboom) always kept me stressed out. My sibling’s (Mustak, Nargis and Najia) constant support throughout my academic life, made my path smooth up to this level. My family has been a continuous source of love, concern, care and strength during these years.

On a very special and personal note I extend regards from the core of my heart to my parents (Ma: Mamtaj Begum and Abbea: Sk. Nowsed Ali) for their encouragement and inspiration. It is their love and trust that served as a beacon through the long nights at IITI. I dedicate you everything!

Nasima Khatun

Dedicated to my family

LIST OF PUBLICATIONS

(A) From Thesis Work: Journal Publications

1. **Nasima Khatun**, E.G. Rini, Parasharam Shirage, Parasmani Rajput, S. N. Jha and Somaditya Sen, "Effect of lattice distortion on bandgap decrement due to Vanadium substitution in TiO_2 nanoparticles" Mat. Sci. Semicon. Proc. 50 (2016) 7–13.
2. **Nasima Khatun**, Parasmani Rajput, Dibyendu Bhattacharya, S.N. Jha, Sajal Biring and Somaditya Sen, "Anatase to rutile phase transition promoted by vanadium substitution in TiO_2: a structural, vibrational and optoelectronic study" Ceram. Int. 43 (16) (2017) 14128-14134.
3. **Nasima Khatun**, Saurabh Tiwari, C. P. Vinod, Chuan-Ming Tseng, Shun Wei Liu, Sajal Biring and Somaditya Sen, "Role of oxygen vacancies and interstitials on structural phase transition, grain growth and optical properties of Ga doped TiO_2". J. Appl. Phys. 123 (24) (2018) 245702.
4. **Nasima Khatun**, Anita, Ruhul Amin and Somaditya Sen, "Bandgap tuning by lattice distortion in V and Ga doped TiO_2" J. Integr. Ferroelectr. (Taylor & Francis) 94(1) (2018) 91-95.
5. **Nasima Khatun**, Saurabh Tiwari, Jayanti Lal, Chuan-Ming Tseng, Shun Wei Liu, Sajal Biring and Somaditya Sen, "Stabilization of anatase phase by uncompensated Ga-V co-doping in TiO_2: A structural phase transition, grain growth and optical property study" Ceram. Int. Ceram. Int. 44 (18) (2018) 22445-22455.
6. **Nasima Khatun**, Saurabh Tiwari, Chuan-Ming Tseng, Shun Wei Liu, Sajal Biring and Somaditya Sen, "Effect of substitution, interstitial and oxygen vacancies on grain growth process, phase transition, and optical properties in charge compensated Ga-V co-doped TiO_2" (C**ommunicated**).

(B) From Other Work: Journal Publications

1. Anita, Arun Kumar Yadav, **Nasima Khatun**, Sunil Kumar, Chuan-Ming Tseng, Sajal Biring, and Somaditya Sen, "Size and strain dependent anatase to rutile phase transition in TiO_2 due to Si incorporation" J Mater Sci: Mater Electron. 28 (24) (2017) 19017–19024.
2. Saurabh Tiwari, **Nasima Khatun**, Parasmani Rajput, Dibyendu Bhattacharya, S. N. Jha, Chuan-Ming Tseng, Shun-Wei Liu, Sajal Biring and Somaditya Sen, "Effect of defect states and oxygen vacancies on optical transitions due to Co^{2+} substitution in CeO_2" Appl. Phys. A 124 (9) (2018) 609.
3. A. Verma, A. K. Yadav, **Nasima Khatun**, Sunil Kumar, Ravindra Jangir, Velaga Srihari, V. Raghavendra Reddy, Shun Wei Liu, Sajal Biring, Somaditya Sen, "Structural, dielectric and ferroelectric studies of thermally stable and efficient energy storage ceramic material: $(Na_{0.50-x}K_xBi_{0.50-x}La_x)TiO_3$" Ceram. Int. 44(16) (2018) 20178-20186.
4. Saurabh Tiwari, **Nasima Khatun**, Tulika Shrivastava, Sunil Kumar, S.-W. Liu, Sajal Biring and Somaditya Sen, "Structural, optical and mechanical properties of sol-gel synthesized Mn-doped CeO_2", Superlattices Microstruct., 122 (2018) 316-323.
5. Saurabh Tiwari, **Nasima Khatun**, Nirmalendu Patra, Ashok k Yadav, Dibyendu Bhattacharya, S. N. Jha, Chuan M Tseng, Shun W Liu, Sajal Biring and Somaditya Sen, "Role of oxygen vacancies in Co/Ni Substituted CeO_2: A comparative study" Ceram. Int. 44(3) (2018) 3823-3832.

(C) Conference Papers:

1. **Nasima Khatun** and Somaditya Sen, "Magnetic and Dielectric properties of V doped TiO_2 nano-particles" Proc. Of the Intl. Conf. on Nanotechnology for better living. 3 (2016) 170.

2. **Nasima Khatun**, Ruhul Amin, Anita, and Somaditya Sen, Effect of V-Nd co-doping on phase transformation and grain growth process of TiO_2, AIP Conf. Proc., 1953 (2018) 040028.
3. **Nasima Khatun**, Saurabh Tiwari, Ruhul Amin, Sajal Biring and Somaditya Sen, "Structural and optical properties of aliovalent Vanadium substituted TiO_2" AIP Conf. Proc. (2018) (A**ccepted)**.
4. Ruhul Amin, Prashant Mishra, **Nasima Khatun**, Saniya Ayaz, Tulika Srivastava, Somaditya Sen, "Effect of titanium on the structural and optical property of NiO nanopowders" AIP Conf. Proc. 1953 (2018) 040028.
5. Anita Verma, Arun Kumar Yadav, **Nasima Khatun**, Sunil Kumar and Somaditya Sen, "A Study of Low Frequency Dielectric Dispersion and Impedance Spectroscopy of Lead-Free $0.94(Na_{0.50}Bi_{0.50})Ti_{0.95}V_{0.05}O_3$-$0.06BaTiO_3$ Ceramics" AIP Conf. Proc. (2018) (A**ccepted)**.
6. Saurabh Tiwari, **Nasima Khatun**, Somaditya Sen, "Effect of Co and Ni doping on structural, optical and vibrational properties of CeO2" AIP Conf. Proc. (2018) **(Accepted)**.

(D) <u>Workshop/School/Conference/Training Courses participated:</u>

1. "Researcher Connect Program" organized by Wiley in collaboration with Indian Institute of Technology Indore, on October 26, 2015. IIT Indore, Indore, India.
2. **Nasima Khatun** and Somaditya Sen. "Structural and electrical properties of V-doped TiO_2 nanoparticles" Presented **POSTER** at International Conference on Recent Trends in Engineering and Material Sciences (ICRTEMS-2016), Jaipur National University, Jaipur, India
3. **Nasima Khatun** and Somaditya Sen. "Precursors, synthesis method, sintering parameters and grain size effect on dielectric and ferroelectric properties of $BaTiO_3$". Presented **POSTER** at

International Conference on Material Science and Technology (ICMST-2016) St. Thomas College, Kerala, India.

4. **Nasima Khatun,** Anita Verma, Ruhul Amin and Somaditya Sen**,** " Temperature dependent dielectric properties of V doped TiO_2" Presented **ORAL** at International Symposium on Integrated Functionalities (ISIF-2017), New Delhi, India.
5. **Nasima Khatun,** Sourabh Tiwari, Ruhul Amin, Prashant Mishra and Somaditya Sen. "Effect of co-doping on Phase Transformation, Grain Growth and optical properties of TiO_2" Presented **POSTER** at Industry academic conclave (IAC-2017) at IIT Indore, Indore, India.
6. **Nasima Khatun**, Anita, Sourhabh Tiwary, Ruhul Amin and Somaditya Sen. "Effect Co-doping on Phase Transformation, Grain Growth and optical properties of TiO_2" Presented **POSTER** at International Workshop on Advanced Nanoscience and Engineering (IWANE-2017), IIT Indore, Indore, India.
7. Anita Verma, Arun Kumar Yadav, **Nasima Khatun**, Sunil Kumar, A.K. Sinha, Somaditya Sen, "Structural, dielectric and ferroelectric properties of lead-free piezoelectric $0.90(Na_{0.50}Bi_{0.50}Ti)O_3$-$0.10AgNbO_3$ ceramic" Presented **POSTER at** International symposium on Integrated Functionalities (ISIF-2017), New Delhi, India.
8. Anita Verma, Arun Kumar Yadav, **Nasima Khatun**, Sunil Kumar, Somaditya Sen, "Study of structural, dielectric and ferroelectric properties of lead-free piezoelectric $(Na_{0.50-x}K_xBi_{0.50-x}La_xTi)O_3$ ceramics" Presented **POSTER** at International Workshop on Advanced Nanoscience and Engineering (IWANE-2017), IIT Indore, Indore, India.
9. **Nasima Khatun** and Somaditya Sen. "Effect of Ga-V co-doping on dielectric properties of TiO_2" Presented **ORAL** at International Conference on Electronic and Advanced Materials (EAM -2018), Florida, USA.

TABLE OF CONTENTS

Acknowledgements i-ii

List of Publications v-viii

List of Figures xiii-xxiii

List of Tables xxiv

Nomenclature xxv-xxvi

Chapter 1: Introduction

1.1 Crystal Structure 1-2

- 1.1.1 Rutile 2-3
- 1.1.2 Anatase 3-4
- 1.1.3 Brookite 4

1.2 Properties of TiO_2 5

- 1.2.1 Physical properties 5
- 1.2.2 Optical properties 5
- 1.2.3 Optoelectronic properties 6
- 1.2.4 Electrical properties 6
- 1.2.5 Magnetic properties 7

1.3. Applications of TiO_2 7

- 1.3.1 As a pigment 7-8
- 1.3.2 As a photocatalyst 8-10
- 1.3.3 As a UV absorber 10

1.4 Phase transition 10-11

- 1.4.1. Synthesis Methods 11
  - 1.4.1.1 Solid-state reaction method 11-12
  - 1.4.1.2 Hydrothermal method 12-14
  - 1.4.1.3 Sol-gel synthesis method 14-15
- 1.4.1.2 Temperature and Time 16

1.4.1.3 Environment of calcination 16-17
1.4.1.4 Pressure 17-18
1.4.1.5 pH 18
1.4.1.6 Strain 18-19
1.4.1.7 Crystallites size 19
1.4.1.8 Agglomeration or interfaces 20
1.4.1.9 Impurities 20-21
1.4.1.9.1 Additives/external impurities 21-23
1.4.1.9.2 Internal impurities/dopants 23-26
1.5 Motivation of the present work 26-27
1.6 Chapter details 27-29

Chapter 2: Experimental details

2.1 Synthesis process 31-32
2.2.1 Sol-gel synthesis 32-33
2.2.2 Doped sample preparation 33-38
2.2 Characterization techniques 38
2.2.1 Thermal gravimetric analysis (TGA) 38-39
2.2.2 N_2 adsorption-desorption study 39-41
2.2.3 X-ray diffraction (XRD) 42-44
2.2.4 X-ray photoelectron spectroscopy (XPS) 44-45
2.2.5 X-ray absorption spectroscopy (XAS) 45-48
2.2.6 Raman spectroscopy 49-51
2.2.7 Electron Microscopy 51
2.2.7.1 Transmission electron microscope (TEM) 51-52
2.2.7.2 Scanning electron microscope (SEM) 52-55
2.2.8 UV-Vis absorption spectroscopy and diffuse reflectance Spectroscopy 55-56

Chapter 3: Effect of Ga doping on grain growth, structural phase transition and optical properties of TiO_2

3.1 Overview 57

3.2 Experimental 58

3.3 Results and discussions 58

  3.3.1 Thermal gravimetric analysis 58-59

  3.3.2 Structural analysis 59-67

  3.3.3 Raman spectroscopic studies 67-70

  3.3.4 XPS analysis 71-74

  3.3.5 Grain growth and morphological analysis 74-78

  3.3.6 Optical properties 78-82

3.4 Summary 82-83

Chapter 4: Effect of V doping on grain growth, structural phase transition and optical properties of TiO$_2$

3.1 Overview 85

3.2 Experimental 85

3.3 Results and discussions 86

  3.3.1 Structural analysis 86-91

  3.3.2 Raman spectroscopic studies 91-98

  3.3.3 XANES/EXAFS analysis 98-101

  3.3.4 Grain growth, microstructure and morphological analysis 101-105

  3.3.5 Optical properties 105-108

3.4 Summary 108-109

Chapter 5: Effect of charge compensated Ga-V (1:1) co-doping on grain growth, structural phase transition and optical properties of TiO$_2$

3.1 Overview 111

3.2 Experimental 112

3.3 Results and discussions 112

  3.3.1 Structural analysis 112-117

  3.3.2 XPS analysis 117-120

  3.3.3 Grain growth and morphological analysis 120-123

  3.3.4 Surface area and pore size studies 123-124

  3.3.5 Optical properties 125-127

3.4 Summary 127-128

Chapter 6: Effect of charge uncompensated Ga-V (4:1) co-doping on grain growth, structural phase transition and optical properties of TiO_2

3.1 Overview 129
3.2 Experimental 130
3.3 Results and discussions 130
    3.3.1 Structural analysis 130-138
    3.3.2 Grain growth, microstructure and morphological analysis 138-144
    3.3.3 Surface area and pores size studies 144-145
    3.3.4 Optical properties 145-147
3.4 Summary 147-148

Chapter 7: Conclusions and future scope

6.1 Major findings and achievements 149
    6.1.1 Synthesis and solubility 149
    6.1.2 Phase transition and activation energy 149-152
    6.1.3 Structural properties 152-153
    6.1.4 Grain growth, particles size, and lattice strain 153-154
    6.1.5 Bandgap and Urbach energy 154-157
6.2 Future Scope 157

References 159-184

LIST OF FIGURES

Chapter 1:

Figure 1.1: (a) and (b) Packing of TiO_6 octahedra in rutile phase, shared two edges and six corners to the nearest neighbor octahedra. Shared edges of TiO_6 octahedra are shown using navy blue solid lines. (c) Arrangements of equatorial and apical O atoms in TiO_6 octahedra. 2

Figure 1.2: (a) and (b) Packing of TiO_6 octahedra in anatase phase are showing four edges sharing of the same TiO_6 octahedra from two different directions. Shared edges of TiO_6 octahedra are shown using navy blue solid lines. (c) Arrangements of equatorial and apical O atoms in TiO_6 octahedra. 3

Figure 1.3: (a) and (b) Packing of TiO_6 octahedra in brookite phase are showing three edges sharing of the same TiO_6 octahedra from two different directions. Shared edges of TiO_6 octahedra are shown using navy blue solid lines. (c) Arrangements of equatorial and apical O atoms in TiO_6 octahedra. 4

Figure 1.4: Use of TiO_2 as a white pigment in different fields. 8

Figure 1.5: Schematic of photocatalytic activity of TiO_2 in presence of UV light. 9

Figure 1.6: Different morphology of TiO_2: (a) needle shape [79], (b-c) nanoflower and nanorod [85], (d-e) hollow cube [86], (f) polyhedron shape [87] (g) platelet rectangle [88], (h) belt like [89], and (i) cube shape [90]. 13

Figure 1.7: Phase transition dependent on initial crystallite size (figure reprinted with permission from [91]. Copyright © 2013 American Chemical Society). 19

Figure 1.8: Interface nucleation of anatase particle to form 20

rutile phase. (figure reprinted with permission from [122]. Copyright © 2015 American Chemical Society).

Chapter 2:

Figure 2.1: Schematic diagram of a sol-gel synthesis route used in our work 33

Figure 2.2: Step by step experimental pictures for V-doped TiO_2 sample. 36

Figure 2.3: Images of charge compensated Ga-V (1:1) co-doped TiO_2 samples prepared at 450 °C (Top panel) and 800 °C (Bottom panel) for 6 h shows color changes with doping composition. 38

Figure 2.4: TGA/DSC system used in this work. 39

Figure 2.5: N_2 adsorption-desorption setup using an automated gas sorption analyzer Quantchrome autosorb iQ2. (a) Complete setup used in our experiment, (b) computer attached with the setup, (c) heating unit for degassing and (d) N_2 cylinder. 40

Figure 2.6: Four different types of hysteresis loops according to IUPAC report [5]. 41

Figure 2.7: Diffraction of X-rays through lattice/atomic planes of a crystal (indicating Bragg's law). 42

Figure 2.8: Bruker D2 phaser diffractometer (tabletop powder XRD machine) for XRD measurement. 43

Figure 2.9: Schematic diagram showing working mechanism of X-ray photoelectron spectroscopy. 45

Figure 2.10: The photoelectric effect; an X-ray is absorbed and a core level electron is promoted out of the atom. Inset shows schematically for X-ray absorption measurements: An incident beam of monochromatic X-rays of intensity I_0 passes through a sample of thickness t, and the transmitted beam has intensity I. 47

Figure 2.11: Decay of the excited state: (a) fluorescence 48

process and (b) Auger process. In both cases, the probability of emission (X-ray or electron) is directly proportional to the absorption probability.

Figure 2.12: Vibrational energy level diagram of Rayleigh, Stokes and anti-stokes line of Raman spectroscopy. 49

Figure 2.13: (a) Raman spectroscopy connected with PC. (b) Laser power supply unit and (c) sample mounting stage. 50

Figure 2.14: Schematic diagram of transmission electron microscopy (TEM). 52

Figure 2.15: Schematic diagram of scanning electron microscopy (SEM). 54

Figure 2.16: (a) Image of Supra55 Zeiss-FESEM used in our work, (b) Inca software attached within the computer for EDX and elementary mapping and (c) Gold coating set up. 55

Figure 2.17: Experimental set up for diffuse reflectance measurement: (a) Carry 60 UV-Vis spectrometer and (b) schematic of diffuse reflectance. 56

Chapter 3:

Figure 3.1: Thermogravimetric analysis of pure TiO_2 (T0) in temperature range of 27 °C to 800 °C showing loss of adsorbed water, nitrates and carbonates. 59

Figure 3.2: XRD pattern of all Ga doped TiO_2 samples heated at eight different temperatures ((a) 450 °C, (b) 500 °C, (c) 550 °C, (d) 600 °C, (e) 650 °C, (f) 700 °C, (g) 750 °C, and (h) 800 °C). 61

Figure 3.3: XRD pattern of all Ga doped TiO_2 samples at eight different temperatures (~450-800 °C) in the range of $2\theta = 24.5$-$28°$ showing a gradual shift in $A\rightarrow R$ phase transition to a higher temperature due to Ga doping in TiO_2. 62

Figure 3.4: (a) Fraction of rutile phase with temperature for all Ga-doped samples showing delayed phase transition due to Ga 63

doping. (b), (c), (d), (e), and (f) show ln(f_R) vs 1/T fits for T0, TG2, TG5, TG7, and TG10 samples, (g) shows variation of activation energy with Ga concentration.

Figure 3.5: Rietveld refinement of anatase Ga doped TiO_2 samples prepared at 450 °C. 64

Figure 3.6: Rietveld refinement of rutile Ga doped TiO_2 samples prepared at 800 °C. 64

Figure 3.7: (a) Variation of lattice constants with Ga content in TiO_2 sample prepared at 450 ^{0}C (anatase) and (b) 800 ^{0}C (rutile). Insets of the corresponding figures show unit cell volume changes with Ga content for both the phases. 65

Figure 3.8: (a) Raman spectrums of Ga doped TiO_2 samples prepared at 450 °C. (a) Inset shows the blue shifting of the first E_g mode of corresponding spectrums. (b) Change in Raman shift and FWHM of the first E_g mode with Ga concentration. 68

Figure 3.9: RT Raman spectrums of Ga doped TiO_2 samples prepared at 800 °C. Inset shows the blue shifting of E_g mode of corresponding spectrums. 69

Figure 3.10: Raman spectra in the range ~100-800 cm^{-1} of all the samples at temperature range 450-800 °C showing A→R phase transition ((a) T0, (b) TG2, (c) TG5, (d) TG7 and (e) TG10). (f) Delayed rutile phase transition in Ga-doped samples is confirmed from rutile phase fraction with temperature. 70

Figure 3.11: Change in activation energy with Ga concentration from the Raman spectrum. 70

Figure 3.12: XPS spectra of anatase phase (450 °C) samples: (a-b) T0, (c-e) TG5 and (f-h) TG10. 71

Figure 3.13: TEM images of T0 (a) and TG5 (b) nanoparticles in pure anatase phase (450 ^{0}C). (c) and (d) shows the HRTEM images of corresponding samples. (e) and (f) show SAED pattern of T0 and TG5 samples. (g) Variation of crystallite size calculated from Scherrer equation with Ga doping. 75

Figure 3.14: Twin boundary {112} of anatase phase where 76

nucleation of rutile phase first starts (Left). Schematic diagram of the grain growth process of pure and Ga doped samples with temperature (Right). Grain growth process of pure TiO_2 (Top) and restrain grain growth process due to Ga doping (Bottom).

Figure 3.15: FESEM images (a-e) of the samples prepared at 800 °C and (f) variation of particles size with doping concentration. 77

Figure 3.16: Elemental analysis of TG5 sample prepared at 800 °C; where (a) SEM image, (b) elemental composition in weight and atomic ratio from EDX spectrum, and elemental mapping of Ti K (c), O K (d) and Ga K (e) showing a uniform distribution of elements. 78

Figure 3.17: (a) DRS spectrum of samples prepared at 450 °C, (b) variation of bandgap and Urbach energy with Ga concentration. (c, d, e, f, and g) shows linear fits of lnF(R) vs *hv* plot (blue circles are original data points and pink lines are linear fits to data points). 79

Figure 3.18: (a) DRS spectrum of all samples prepared at 800 °C, (b) variation of bandgap and Urbach energy with Ga concentration. (c, d, e, f, and g) shows linear fits of lnF(R*)* vs *hv* plot (blue circles are original data points and pink lines are linear fits to data points). 80

Chapter 4:

Figure 4.1: XRD patterns of V doped TiO_2 samples heated at seven different temperatures (450-750 °C). 86

Figure 4.2: ((a-d)) Close view of XRD patterns of all samples in 2θ range from 24° to 28.5°. It shows that phase transition is promoted by V incorporation. 87

Figure 4.3: (a) Fraction of rutile phase with temperature for all V-doped samples showing promotion of phase transition due to V doping. (b) Shows variation of activation energy with V 88

concentration.

Figure 4.4: (a) Rietveld refinement of V-doped TiO_2 samples heated at 450 °C. (b) Variation of lattice constants and (c) unit cell volume with V concentration. 89

Figure 4.5: (a) Rietveld refinement of V-doped samples heated at 750 ^{o}C. (b) Variation of lattice constants with V concentration. 90

Figure 4.6: (a) Raman spectrums of samples prepared at 450 °C and (b) change in Raman shift and FWHM of first E_g mode with V concentration (dotted lines are to guide the eye). 92

Figure 4.7: Raman spectra of samples heated at 600 °C. 93

Figure 4.8: (a) and (b) Lorentzian fitting of Raman vibrational modes of samples T0 and TV6 prepared at 600 °C. 94

Figure 4.9: Raman spectra of samples heated at 750 °C. 95

Figure 4.10: (b) and (c) Lorentzian fitting of Raman vibrational modes of T0 and TV6 samples prepared at 750 °C. 95

Figure 4.11: Vibration corresponding to Raman modes of rutile TiO_2 (B_{1g}, E_g and A_{1g}). The red and Navy blue balls denote Oxygen (O) and Titanium (Ti) atoms respectively and magenta arrows show the direction of vibrations. 96

Figure 4.12: (a) Blue shift of multiphonon mode (M) and (b) redshift of E_g mode with increasing V concentration. (c) Variation of FWHM of all Raman modes with V concentration. 97

Figure 4.13: XANES spectra of T0, TV3 and TV9 samples prepared at 450 °C: (a) Ti K-edge and (b) V K-edge. 98

Figure 4.14: XANES spectra of T0, TV3 and TV6 samples prepared at 750 °C: (a) Ti K-edge and (b) V K-edge. 100

Figure 4.15: EXAFS fitting of T0 (a, b) and TV3 (c, d) samples prepared at 750 °C: R-dependent Mod$|\chi(R)|$ and 101

$\mathrm{Re}|\chi(R)|$.

Figure 4.16: FESEM images of pure TiO_2 nanoparticle in anatase phase (450 °C) at different magnification. 101

Figure 4.17: HRTEM images of T0 (a-b) and TV9 (d-e) nanoparticles prepared at 450 °C. SAED pattern of corresponding samples: (c) T0 and (f) TV9. 102

Figure 4.18: (a) Variation of crystallites size and (b) strain of V doped TiO_2 samples prepared at 450 °C with V concentration. 103

Figure 4.19: (a) SEM image of TV6 sample (750 °C) and (b) EDX spectrum of the same sample. Chemical compositions of the elements are shown in the inset of (b). Elemental mapping of O, Ti, and V elements are shown in (c-d). 103

Figure 4.20: FESEM images of pure T0 (a), TV1 (b), TV3 (c) and TV6 (d)) samples prepared at 750 °C. 104

Figure 4.21: TEM images of samples prepared at 750 °C ((a) T0, (b) TV1, (c) TV3 and TV6 (d)). 105

Figure 4.22: (a) DRS spectrum of samples heated at 450 °C, (b) variation of bandgap and Urbach energy with V concentration. (c, d, e, f, and g) shows linear fits of lnF(R) vs hυ plot (blue circles are original data points and red lines are linear fits to data points). 106

Figure 4.23: (a) DRS spectrum of samples heated at 750 °C, (b) schematic diagram of bandgap tailoring. (c, d, e, f, and g) Shows linear fits of lnF(R) vs hυ plot (blue circles are original data points and red lines are linear fits to data points). (b) Variation of bandgap and Urbach energy with V concentration. 107

Chapter 5:

Figure 5.1: XRD patterns of all the Ga-V (1:1) co-doped samples at six different temperatures (450-700 °C) in the range of 2θ = 20-80°. 113

Figure 5.2: Zoomed view of XRD patterns of all the samples at six different temperatures (450-700 °C) in the range of 2θ = 24-28.5°. 114

Figure 5.3: (a) Change in f_R with temperature for all the samples and (b) change in activation energy with concentration. 115

Figure 5.4: (a) Rietveld refinement of Ga-V (1:1) co-doped samples prepared at 450 °C and (b-c) change in lattice constants and unit cell volume with doping concentration. 116

Figure 5.5: (a) Rietveld refinement of Ga-V co-doped samples prepared at 700 °C and (b-c) change in lattice constants and unit cell volume with doping concentration. 117

Figure 5.6: Fitting of XPS spectra of Ti 2p, Ga 3d and O 1s of TGV5 and TGV10 samples prepared at 450 °C. 119

Figure 5.7: (a) Variation of crystallites size and (b) strain with doping concentration of samples prepared at 450 °C. 120

Figure 5.8: HRTEM images of T0 ((a) and (c)) and TGV5 ((b) and (d)) samples. Inset shows the SEAD pattern of the corresponding sample. 121

Figure 5.9: FESEM images of the samples prepared at 700 °C: (a) T0, (b) TGV2, (c) TGV5, (d) TGV7, and (e) TGV10. 122

Figure 5.10: EDX and elemental mapping of TGV10 sample prepared at 700 °C. 123

Figure 5.11: (a-e) Nitrogen adsorption/desorption isotherms of the samples prepared at 450 °C and (f-j) pore size distribution 124

curve on desorption isotherm (using BJH method) of the samples.

Figure 5.12: (a) DRS spectrum of all the samples prepared at 450 °C, (b) variation of bandgap and Urbach energy with Ga-V doping concentration. (c, d, e, f, and g) shows linear fits of lnF(R) vs hυ plot (violet circles are original data points and pink lines are linear fits to data points). 125

Figure 5.13: (a) DRS spectrum of all the samples prepared at 700 °C, (b) variation of bandgap and Urbach energy with Ga-V doping concentration. (c, d, e, f, and g) shows linear fits of lnF(R) vs hυ plot (violet circles are original data points and pink lines are linear fits to data points). 126

Chapter 6:

Figure 6.1: XRD patterns of all the samples prepared at eight different temperatures (450-800 °C) in the range of 2θ = 20-80°. 131

Figure 6.2: XRD pattern of samples heated at 800 °C in the range 2θ = 26-40°. 132

Figure 6.3: XRD patterns of all the samples prepared at eight different temperatures (~450-800 °C) in the range of 2θ = 24.5-28°. (e) Fraction of rutile phase (f_R) at a different temperature. 133

Figure 6.4: Fits of ln(f_R) vs 1/T ((a): T0; (b): TGV1; (c): TGV3 and (d): TGV4). (e) Variation of activation energy with doping concentration (solid line is just a guide to the eye). 134

Figure 6.5: (a) Rietveld refinement of Ga-V (4:1) co-doped samples prepared at 450 °C. (b) Change of lattice constants, and (c) unit cell volume with Ga-V doping concentration. 135

Figure 6.6: Rietveld refinement of Ga-V (4:1) co-doped samples prepared at 800 °C. 137

Figure 6.7: (a) Change of lattice constants and (b) unit cell 138

volume with Ga-V (4:1) doping concentration.

Figure 6.8: (a) TEM images of T0 and (c) TGV3 samples prepared at 450 °C. Inset shows the histogram of particles size distribution of corresponding samples. (b and d) HRTEM images of T0 and TGV3 and insets show SAED pattern of corresponding samples. 139

Figure 6.9: Linear fits of βcos(θ) vs 4sin(θ) of Ga-V (4:1) co-doped samples prepared at 450 °C. (e) Change of strain and crystallites size with doping concentration. 140

Figure 6.10: XRD patterns of samples prepared at 450 °C in the range 2θ = 22-28°. 141

Figure 6.11: FESEM images of the samples prepared at 800 °C: (a) T0, (b) TGV1, (c) TGV3, and (d) TGV4. 142

Figure 6.12: (a) and (c) Show TEM images of TGV1 sample prepared at 800 °C and inset show the corresponding SAED patterns. HRTEM images (b) and (d) show lattice fringes of the particles. 143

Figure 6.13: (a-d) Nitrogen adsorption/desorption isotherms of the samples prepared at 450 °C and (e-h) Barrett-Joyner Halenda (BJH) pore size distribution curve of the samples. 145

Figure 6.14: Room temperature DRS data of Ga-V (4:1) co-doped samples prepared at 450 °C (a) and 800 °C (b). (c) and (d) shows the change of bandgap and Urbach energy with doping concentration. 146

Chapter 7:

Figure 7.1: Rutile phase fraction (f_R) at different temperature (450-800 °C) and change in activation energy of Ga (a-b), V (c-d), Ga-V (1:1) (e-f) and Ga-V (4:1) (g-h) doped samples. 150

Figure 7.2: Variation of lattice constants of anatase and rutile 152

phase of TiO_2 by Ga (a-b), V (c-d), Ga-V (1:1) (e-f) and Ga-V (4:1) (g-h) doping into TiO_2.

Figure 7.3: Change in crystallites size and strain of Ga (a-b), V (c-d), Ga-V (1:1) (e-f) and Ga-V (4:1) (g-h) doped samples prepared at 450 °C. 154

Figure 7.4: Variation of bandgap and Urbach energy by incorporation of Ga (a-b), V (c-d), Ga-V (1:1) (e-f) and Ga-V (4:1) (g-h). 155

LIST OF TABLES

Chapter 1:

Table 1.1: Effects of different complex agents of sol-gel method on phase formation/transition temperature, crystallites size and surface area. 15

Table 1.2: Effects of temperature and time on anatase to rutile weight ratio. 16

Table 1.3: List of additives influences phase transition and grain growth process of TiO_2. 22

Chapter 3:

Table. 3.1: XPS fitting results of T0, TG5, and TG10 samples. 72

Table 3.2: List of reports available on Ga doped TiO_2. 81

Chapter 4:

Table 4.1: Refinements structural parameters obtained from EXAFS fitting of Ti K-edge; N is the coordination number, R is the bond distance and σ^2 is the Debye-Waller factor. The numbers in parentheses indicate the uncertainty in best estimates. 100

Chapter 5:

Table 5.1: Particles size of the samples prepared at 700 °C. 122

Chapter 6:

Table 6.1: BET surface area, pore diameter, pore volume of Ga-V (4:1) co-doped TiO_2 samples prepared at 450 °C. 145

Chapter 7:

Table 7.1: Effect of Ga, V, Ga-V (1:1) and Ga-V (4:1) doping on different parameters of TiO_2 156

NOMENCLATURE

Abbreviations

XRD	X-Ray Diffraction
EDX	Energy-Dispersive X-Ray Analysis Spectroscopy
FESEM	Field Emission Scanning Electron Microscope
XAS	X-Ray Absorption Spectroscopy
EXAFS	Extended X-Ray Absorption Fine Structure Spectroscopy
XANES	X-Ray Absorption Near Edge Spectroscopy
XPS	X-Ray Photoelectron spectroscopy
RT	Room Temperature
CIF	Crystallographic Information File
FWHM	Full Width Half Maximum
UV	Ultra Violate
Vis	Visible
DRS	Diffuse reflectance spectroscopy
PL	Photoluminescence
PCA	Photocatalytic activity
FESEM	Field Emission Scanning Electron Microscopy
BET	Brunauer–Emmett–Teller
BJH	Barrett-Joyner-Halenda
HRTEM	High-Resolution Transmission Electron Microscope
XPS	X-ray photoelectron spectroscopy
COD	Crystallography Open Database

Symbols

α	Alpha
β	Beta
γ	Gamma
θ	Theta
hkl	Miller indices
K	Kelvin
KJ	Kilo Joules
cm	Centimeter
nm	Nanometer
µm	Micrometer
h	Planck's constant
a.u	Arbitrary unit
eV	Electron volt
$a\ b\ c$	Lattice Constant
E_A	Activation Energy
E_B	Binding Energy
E_U	Urbach Energy
E_G	Bandgap
°	Degree
Å	Angstrom

Chapter 1

Introduction

Titanium dioxide (TiO_2) also known as titania, is studied since the beginning of material research. It is important due to its multifunctional properties such as tunable bandgap (anatase ~ 3.2 eV and rutile ~ 3.0 eV) [1] and high photo-corrosion stability. Different crystal structures and corresponding electronic band structure facilitates its applications in different fields, such as, optoelectronic devices [2, 3], self-cleaning glass coating materials [4, 5], photocatalyst [6, 7], fuel cell [8], dye-sensitized solar cell [9, 10], sensor [11, 12], opacifier and white pigment [13, 14], etc.. It facilitates environmentally beneficial reactions through photocatalytic activity by splitting of water to produce hydrogen, curing polluted air/water. Low cost, nontoxicity, and high chemical stability add a special importance for its application in different fields.

1.1 Crystal Structure

Ilmenite ($FeTiO_3$) ore is the main source of titanium dioxide. TiO_2 has been mostly synthesized using “sulfate” or “chloride” method [15]. In these methods, iron is extracted from this ore yielding pure TiO_2. TiO_2 mainly has three naturally occurring polymorphs [16]. In order of abundance, these are rutile (tetragonal, space group-$P4_2/mnm$), anatase (tetragonal, space group-$I4_1/amd$), and brookite (orthorhombic, space group-*Pbca*) [16, 17]. A fourth naturally occurring polymorph of TiO_2 is “TiO_2(B)” (monoclinic, bronze-type, space group-$C2/m$) [18]. It was also observed experimentally, that there are some other high-pressure polymorphs of TiO_2: “TiO_2(II)” (orthorhombic, columbite type (α-PbO_2), space group-*Pbcn*) [19-22], “TiO_2(OI)” (orthorhombic, space group-*Pbca*) [23], “TiO_2(H)” (tetragonal, hollandite type, space group-$I4/m$) [24], “TiO_2(MI)” (monoclinic, baddeleyite type, space group-$P2_1/c$) [20, 21, 25], “TiO_2(OII)” (orthorhombic, cotunnite type, space group-*Pnma*) [23] and "c-TiO_2" (cubic, fluorite type, space group-*Fm*3*m*) [16, 26]. Depending on crystal structure, different physical and chemical properties such as density, bandgap, refractive index, hardness, dielectric permittivity etc. of TiO_2 are different [27-29]. These govern their applications and usage in the multifunctional field. Details of the three main crystal structures are discussed below.

1.1.1 Rutile

There are huge numbers of industrial and research applications of TiO_2 in rutile form like paint, paper, ink, food, medicine, varnishes etc.. It's a stable phase of TiO_2. The unit cell of rutile TiO_2 consists of two formula units (TiO_2) with six atoms per primitive unit cell. It has a tetragonal structure with lattice constant a = b = 4.587 Å and c = 2.954 Å [26]. Each Ti^{4+} ion is octahedrally coordinated with six O^{2-} ions. TiO_6 octahedra in rutile phase have two different type of Ti-O bond length, with equatorial bond length 2.01 Å being slightly shorter than apical bond length 1.96 Å [30].

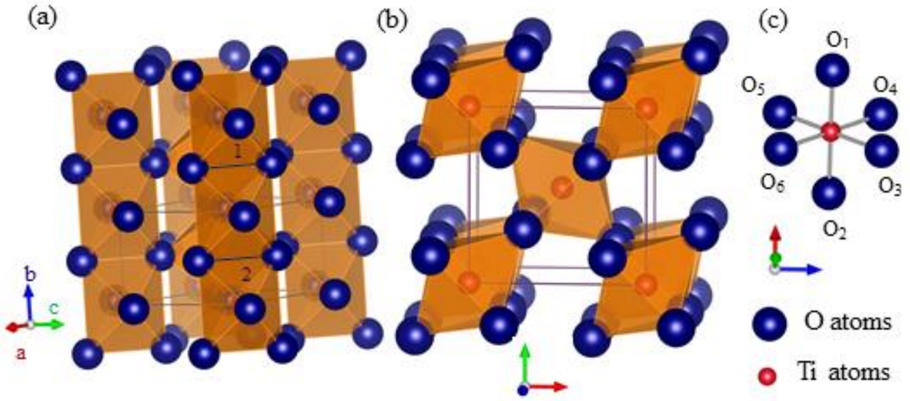

Figure 1.1: (a) and (b) Packing of TiO_6 octahedra in rutile phase, shared two edges and six corners to the nearest neighbor octahedra. Shared edges of TiO_6 octahedra are shown using navy blue solid lines. (c) Arrangements of equatorial and apical O atoms in TiO_6 octahedra.

The equatorial four O^{2-} ions are coplanar and occupy a rectangular arrangement [26]. However, the packing of TiO_6 octahedra is regular. The octahedra share six corners in *a*-*b* planes and two edges in the *c* direction with nearest neighbor octahedra [31]. The two opposite edges of an octahedron are shared with similar edges of the neighboring ones. It has less empty space outside the TiO_6 octahedra. Hence, it shows the highest density (~ 4.13 g/cm^3) [30] among the three common polymorphs of TiO_2.

1.1.2Anatase

Among the three polymorphs of TiO_2, anatase is the most active form for photocatalytic applications [28, 32]. Most of the semiconducting nanoparticle applications of TiO_2 are in the anatase phase. This phase is generally formed at a very lower temperature (300-450 °C) in ambient condition. The unit cell of anatase TiO_2 consists of six formula units (TiO_2) with six atoms per primitive unit cell.

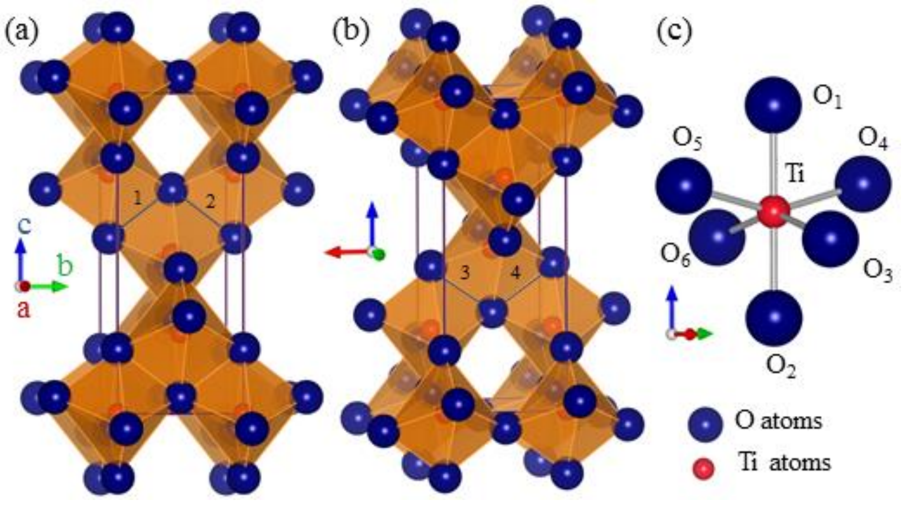

Figure 1.2: (a) and (b) Packing of TiO_6 octahedra in anatase phase are showing four edges sharing of the same TiO_6 octahedra from two different directions. Shared edges of TiO_6 octahedra are shown using navy blue solid lines. (c) Arrangements of equatorial and apical O atoms in TiO_6 octahedra.

It has tetragonal crystal structure with lattice constants a = b = 3.782 Å and c = 9.502 Å [26]. Each Ti^{4+} ion is octahedrally coordinated with six O^{2-} ions. The TiO_6 octahedron is distorted. The apical Ti-O bond length is ~2.00 Å, slightly longer than the equatorial Ti-O bond length ~1.95 Å [30]. There are crossed rows of zigzag chains of octahedra that run along *a* and *b* directions. Consequently, the anatase phase can be considered as a layered structure with more empty space outside the TiO_6 octahedra. The layers are linked with each other by soft apical Ti–O bonds [30]. Hence, anatase has a lesser density (3.76 g/cm^3) [30] than rutile.

1.1.3 Brookite

Commercial synthesis of brookite TiO_2 is very difficult due to its complicated structure. It is only available as natural single crystals [33]. Very few studies have been reported on its properties due to its complicated crystal structure. It consists of eight formula units per unit cell with six atoms per primitive unit cell [26]. It has an orthorhombic structure with lattice constant a = 9.191 Å, b = 5.463 Å and c = 5.157 Å [34]. It also has the same TiO_6 building block but with different Ti-O bond lengths. Like anatase, it also has distorted TiO_6 octahedra. All four equatorial and two apical Ti-O bond length are different in this phase. It shares 3 edges and 5 corners with nearest neighbor octahedra [31]. It has less empty space than anatase but more than rutile. Hence, it has a moderate density (~4.098 g/cm^3).

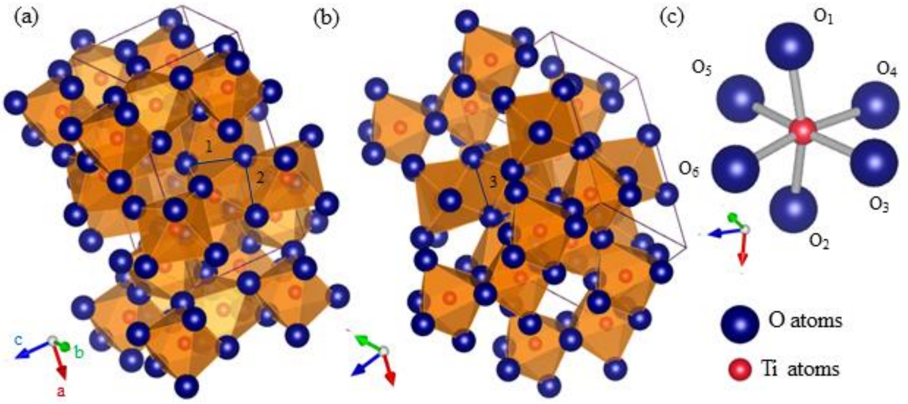

Figure 1.3: (a) and (b) Packing of TiO_6 octahedra in brookite phase are showing three edges sharing of the same TiO_6 octahedra from two different directions. Shared edges of TiO_6 octahedra are shown using navy blue solid lines. (c) Arrangements of equatorial and apical O atoms in TiO_6 octahedra.

1.2 Properties of TiO_2

Depending on different crystal structure and corresponding electronic band structure, TiO_2 shows different physical and chemical properties. Commercial synthesis of brookite is very difficult and it is not used for any application. Hence, below is a discussion on the properties of anatase and rutile.

1.2.1 Physical properties

Pure TiO_2 in anatase phase is brownish or light honey color. With heating (~600-700°C in an air atmosphere) anatase is converted into the rutile phase. Rutile is white in color. Both anatase and rutile phases are odorless with a molecular weight of 79.866 g/mol. TiO_2 in both phases is insoluble in water. The density of rutile ($\rho_R = 4.13$ g/cm^3) is higher than anatase ($\rho_A = 3.76$ g/cm^3) [30]. The refractive index of anatase and rutile are 2.488 and 2.609. Melting and boiling point of rutile TiO_2 is 1843 °C and 2972 °C. Depending on pressure and environment, melting and boiling point shifts.

1.2.2 Optical properties

TiO_2 is a n-type wide bandgap semiconductor (anatase ~3.2 eV and rutile ~ 3.0 eV) [1]. From density functional theory (DFT) [35], it was observed that anatase has an indirect bandgap while rutile has a direct bandgap. Due to the indirect bandgap of anatase, photo-generated electrons and holes exhibit a longer lifetime than direct bandgap rutile. These electrons and holes have a higher migration rate (goes from interior to surface). A low charge carriers recombination rate results due to a light average effective mass of electron and hole of anatase compared to rutile. Hence, anatase TiO_2 nanoparticles are used as a promising candidate for photocatalytic applications. Due to high refractive index, higher opacity and wide bandgap of rutile TiO_2, it is used as a white pigment in different applications.

1.2.3 Optoelectronic properties

TiO_2 belongs to a class of solids with superior functionalities for conversion of light into other forms of energy. Processes of optical absorption and emission are highly dependent on defects related to dopants, different synthesis methods (involving calcination environment, pressure, time and temperature) [36-39] or form of sample (thin film, nanoparticle, bulk, and single crystal) [40, 41]. Depending on its optoelectronic properties, TiO_2 is used in various applications like in dye-sensitized solar cell, fuel cell, photodetectors, gas sensing etc. From different reports, it was observed that no bandgap related photoluminescence (PL) is observed for anatase TiO_2, as it is an indirect bandgap semiconductor. When irradiated with ultra-violate light, it shows a broad visible light PL for anatase and visible/infrared PL for rutile [42, 43]. PL arises from free carriers and oppositely charged trapped carriers. PL intensity increases and decreases for anatase when it is synthesized in a vacuum and oxygen-rich condition. In rutile, a reverse trend is observed [44]. But despite a wide effort dedicated to improving its optoelectronic performances, the microscopic nature of the fundamental electronic and optical excitons is still not clearly understood.

1.2.4 Electrical properties

TiO_2 has a wide bandgap of 3 eV (rutile) and 3.2 eV (anatase) at room temperature. Due to its wide band gap, TiO_2 has many advantages such as higher breakdown voltage, lower electronic noise, sustainability of large electrical fields, high-power and high-temperature operation. Among unitary metal oxides, it has a highest dielectric permittivity ~100 for rutile [45, 46] and ~6 for anatase [47]. Nowadays, it is observed that by selective co-doping, it shows colossal permittivity (10^3 to 10^4) which is stable in a wide frequency (40 Hz to 10^6 Hz) [48] and temperature range (80 K to 450 K) [49]. It also shows very low dielectric loss ($\leq$ 0.05) [49]. These properties make the material suitable for various electrical applications.

1.2.5 Magnetic properties

Dilute magnetic semiconductors (DMS) are considered as a promising candidate for spintronic applications, due to their coexisting semiconducting and ferromagnetic behavior. Various reports show that room temperature ferromagnetism (RTF) can be achieved by doping different magnetic elements like Fe, Ni, Co etc. [38, 50]. However, even for non-magnetic elements, like Ga, V, Cu etc. RTF has been reported [51-53]. Also, it has been observed that defects in TiO_2 lattice can generate magnetism [54, 55]. In some cases, RTF is explained in terms of unpaired electrons in orbital or oxygen vacancies [54], cation vacancies [55] and bound magnetic polarons (BMP) [56]. In BMP, an electron locally bound by an oxygen vacancy (O_V) and through orbital overlapping, it shows ferromagnetism.

1.3. Applications of TiO_2

1.3.1 As a pigment

The worldwide production of titanium dioxide (TiO_2) only as a pigment is several million tons per year (~7.4 million tons in 2016 according to “Mineral commodity summaries 2017” published by U.S. Geological Survey). Because of its very high refractive index (2.6 for rutile) and brightness, it is used as a white pigment [13, 14]. Very few materials are better candidates than TiO_2. Rutile form of TiO_2 is mostly used as a pigment. TiO_2 is tentatively used in two thirds amongst all pigments. Thin films of TiO_2 serve as an excellent reflective optical coating for dielectric mirrors due to its refractive index and color. TiO_2 provides whiteness and opacity in powder form, to products such as paints, coatings, plastics, papers, inks, foods, medicines (i.e. pills and tablets) as well as most toothpaste[13]. The definitions of "the perfect white", "the whitest white", or other similar terms are assigned to TiO_2 when it comes to issues related to paints. The particle size of the TiO_2 particles is optimized to improve opacity. When used as a pigment, it is called titanium white, Pigment White 6 (PW6), or CI 77891.

Figure 1.4: Use of TiO_2 as a white pigment in different fields.

1.3.2 As a photocatalyst

In 1967, Akira Fujishima first discovered the photocatalytic activity (PCA) for TiO_2. Fujishima and Honda in 1972, discovered splitting of water on TiO_2 electrodes through photocatalytic reactions [57]. After this discovery, a new era of photocatalysis has begun. Photocatalysis is basically a reaction which uses light to activate a catalyst (photocatalyst) and thus change the speed of a chemical reaction by lowering the activation energy for the primary reaction to occur. Because of nontoxicity, chemical stability, inertness, cheap cost, and easily tunable bandgap, TiO_2 is wildly used as an important photocatalyst among all photocatalyst. Electron-hole pairs are created when pure or doped TiO_2 is exposed to light. For pure TiO_2, UV irradiation which is higher than its bandgap is required. Visible or infrared (IR) light is sufficient for doped TiO_2. These electron-hole pairs react with surface adsorbed air or water molecules and facilitate photo-catalytic activities.

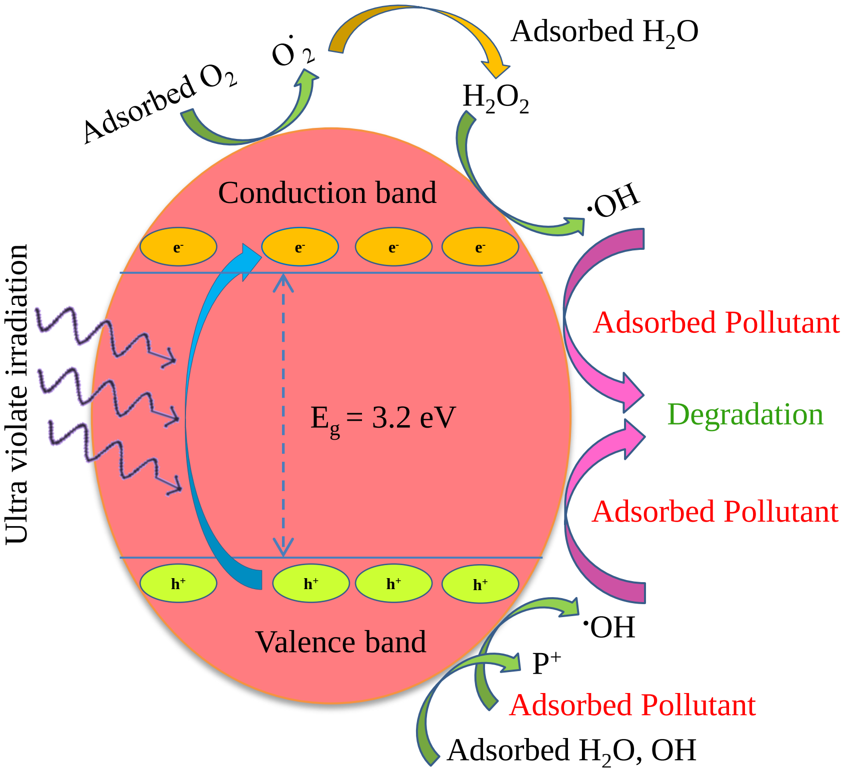

Figure 1.5: Schematic of photocatalytic activity of TiO_2 in presence of UV light.

At present time, there are two main concerns of the world: environment pollution and energy crisis. TiO_2 has a great potential to solve both the problems through PCA. It reacts to environmental waste and produces hydrogen and water. This hydrogen is collected and used as fuel cell [8]. Polluted air and water can also be cleaned by this process. PCA on object-surface has attracted tremendous attention for practical applications. Some of these examples are self-cleaning glass coating materials, tiles, and windows, where the super-hydrophilic properties are used. It is also used as an antibacterial agent [58, 59] due to its strong oxidation activity. Many organic substances can break down on TiO_2 surface because of its very high oxidation potential.

Anatase phase of TiO_2 is most active for PCA than rutile and brookite. From several reports, it was observed that (001) plane of anatase is most pronounced for PCA than thermodynamically stable (101) plane [60, 61]. It is also observed that at interface PCA is most effective. A mixture of anatase and rutile gives the best PCA for TiO_2. Degussa

P25 is considered as ideal photocatalyst of TiO_2, where anatase in 75% and rutile is 25% [62, 63].

1.3.3 As a UV absorber

Titanium dioxide has a high refractive index. It is also a strong UV-absorbent and prevents discoloration under UV illumination. These factors are instrumental in protecting human skins from UV exposure [64]. Visible light is less scattered by TiO_2 nanoparticles than pigments, without affecting UV protection. Skin irritation is lesser in TiO_2 than other UV absorbents. Hence, it is used widely in sunscreens. Sunscreens designed for infants or people with sensitive skin are often based on titanium dioxide [65].

1.4 Phase transition

Crystal structure strongly controls the physical and chemical properties of a material. Hence, the applicability of any material is strongly dependent on such properties which are actually controlled by the crystal structure.

Among the three polymorphs, anatase and brookite are metastable phases while rutile is the most thermodynamically stable phase [66]. In all the three phases, the arrangement of the basic TiO_6 octahedra building blocks gives rise to different properties [16]. Difference between the three phases originates from the Ti-O bond length in TiO_6 octahedra and number of corners and edges shared by the octahedra as discussed above. In general, the anatase crystalline phase of TiO_2 is easily formed at lower temperatures. This is because surface free energy of anatase is lower compared to rutile despite rutile has lower Gibbs free energy than anatase [27, 67]. Brookite is rarely available [68, 69]. Commercial synthesis of brookite TiO_2 is very difficult. It is only available as natural single crystals [33]. Both anatase and brookite phases are metastable. With the increase of temperature a first order phase transition [33] takes place when both the metastable phases are irreversibly and exothermally [27] converted into rutile phase. However, it is unclear from reports that whether this transition is in the order, anatase→brookite→rutile or brookite→anatase→rutile. A brookite→anatase→rutile route has been suggested by Ye *et al.* [70]. On the other hand, a anatase→brookite→rutile has been suggested by Mitsuhashi and Kleppa *et al.* [31]from calorimetric studies on phase transition enthalpies. They suggested that thermodynamic phase stability is like anatase<brookite<rutile. This allows the anatase phase to either transform directly to rutile phase or take an intermediate brookite phase transition to a final rutile phase. Anatase→rutile (A→R) phase conversion is not a simple distortive/displacive phase transformation. A total structural reconstruction takes place by breaking and reforming of bonds [27]. During A→R phase transformation, *a* and *b* lattice constant expand while *c* contracts resulting in shrinkage (~8%) of unit cell volume [27, 33, 71]. Most of the applications of TiO_2 are in anatase and rutile phase. Hence, it is very important to know the factors responsible for grain growth process and delay/promotion of A→R phase transformation.

There are several factors which control grain growth process and delay/promotion of A→R phase transformation. Synthesis methods, environment, pressure, calcination temperature/time, strain, initial crystallite size, presence of dopants, pH, defects and impurities etc. controls the grain growth and thereby transformation.

Each factor are discussed in detail below

1.4.1. Synthesis Methods

Synthesis methods are critically important in this case. Phase formation, particle size, growth rate, transition temperatures etc. are highly dependent on synthesis methods. Few commonly used methods are discussed below:

1.4.1.1 Solid-state reaction method

Most common and ancient method to prepare any material is the solid-state reaction method. In this method mainly oxides are used as precursors of elements. Stoichiometric ratio of each precursor are mixed together and thereafter ground for several hours for uniform mixing. Then the mixture is heated at a very high temperature (≥ 600 °C). After cooling, the samples are ground and X-ray diffraction measurements were performed to check the formation of the right phase. If the desired crystal structure is not formed, then further grinding and heating at a temperature higher or equal to the previous temperature. This cycle of grinding and heating is repeated until the desired material with the right phase is formed.

Anatase phase is formed at a lower temperature and is stable up to ~450-500 °C at normal ambient conditions. Thereafter the anatase phase transforms into the rutile phase. Hence, the anatase phase is difficult to be achieved by solid-state reaction process. Purely rutile or mixed phases of anatase and rutile can be easily prepared by this method. Umadevi *et al.* [72] reported that it is possible to prepare anatase TiO_2 nanoparticle by this method when heated at 500 ^{o}C for 5h. Particle formed in this method have flake-like shape and of size ~50-60 nm. Recently it was observed that using 'green' solid-state synthesis anatase phase is stable up to a higher temperature ~800 ^{o}C [73]. There are very few reports on anatase TiO_2 preparation by this method. From literature, it was observed that TiO_2 rutile nanoparticles and ceramics were mostly synthesized by this method [49, 74-76]. Particles formed in this method have distorted spherical to irregular rod like shape. Grain sizes of TiO_2 ceramics prepared by conventional solid-state sintering method have bigger size compared to the grain size prepared by microwave sintering and spark plasma sintering process [75-77].

1.4.1.2 Hydrothermal method

The shape and size can be controlled by this method as pressure and temperature, both can be controlled. Basic medium is mainly used to prepare TiO_2 by this method [78-81]. However, there are a few reports where acidic medium was used [67]. Kasuga *et al.* [79] prepared needle-shaped TiO_2 (anatase) nanotube of diameter ~6 nm and length

~100 nm by this method using NaOH aqueous solution and heated it at 110 °C for 20 h. Tang *et al.* [81] reported TiO_2 nanotube by the same method with diameter ~5 nm and length ~80-500 nm. It was observed that mostly nanotubes of TiO_2 are formed by hydrothermal method [1, 38, 78-81]. However, there are a few reports where nano-ribbon[82], nanoflakes [83], nano-flower[84] etc. were prepared by this method. It was also observed by many authors that by varying temperature, time, pressure and acid or base concentration, phase formation (anatase, brookite or rutile) and phase transition (A→R) temperature can be changed.

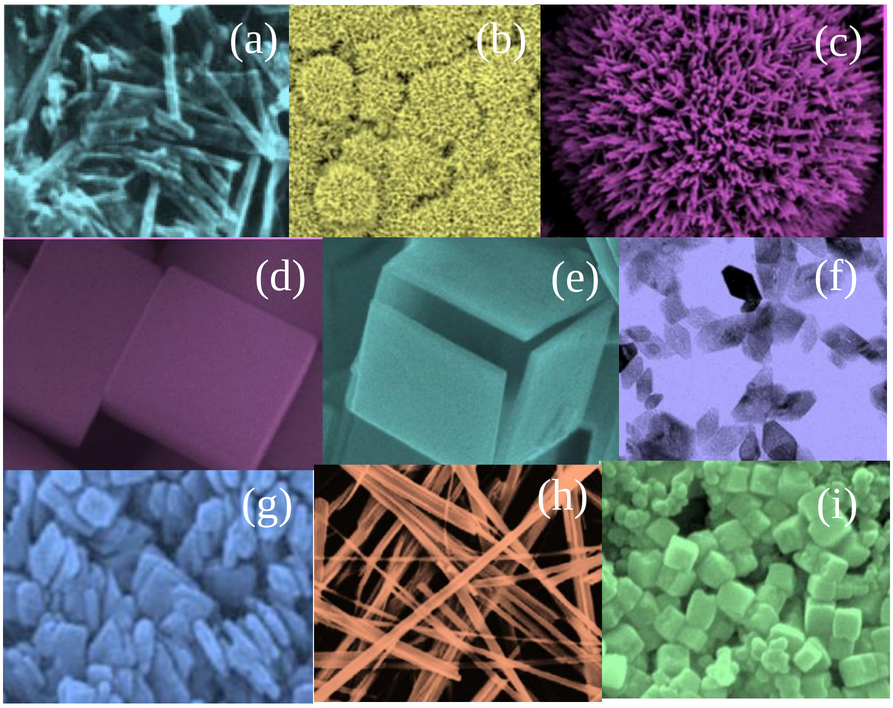

Figure 1.6: Different morphology of TiO_2: (a) needle shape [79], (b-c) nanoflower and nanorod [85], (d-e) hollow cube [86], (f) polyhedron shape [87] (g) platelet rectangle [88], (h) belt like [89], and (i) cube shape [90].

Sabyrov and Penn co-workers [91] had shown that anatase nanoparticles of size ~3.1-12.7 nm (with an aging rate of 0 to 48h) are formed at 200 °C. Rutile phase was formed at 250 °C. Ding and Liu co-workers [67] reported that 95% anatase and 5% rutile phase was formed when sample was prepared at 100 °C. On the other hand at 150

°C the ratio of rutile phase increases (anatase: 58% and rutile: 42%). Hydrothermal method generally lowers the phase formation temperature of anatase or the rutile phases and also reduces the A→R phase transition temperature to very low values as compared to solid-state reaction method and sol-gel method, as pressure plays an important role in this method.

1.4.1.3 Sol-gel synthesis method

This process is commonly used to prepare nanomaterials. In this method, precursors which are soluble in water, acids, bases or applying heat are used. Stoichiometric ratio of each soluble precursor are mixed together and stirred for some time to make a homogeneous solution. The resultant solution is heated to obtain a gel. The gel is thereafter heated on an oven and finally burnt at a higher temperature. In most cases, the powders obtained are in amorphous form. To get the desired material, the powders are denitrified or decarburized at a higher temperature (~250-500 °C) [92]. The materials obtained by this method are of nanoscale dimensions. One of the most important advantages of this method is the homogeneity of the material composition.

The low-temperature attribute of this method makes this a suitable process to prepare both anatase and rutile phase TiO_2. Anatase phase nanoparticle is mostly prepared by using this method. Heating at higher temperature leads to a phase transition from anatase to rutile phases. Beyond a certain temperature, the anatase phase irreversibly converts into the rutile phase.

Gelling/chelating agents, pH, and calcination environment determine a lot of properties of the resultant powders. Morphology, particle size, grain growth rate, crystallization and phase transition temperature etc. are affected by the above parameters. Wang *et al.* [93] reported that ethylene glycol with different amount of H_2O controls particle size and morphology. Addition of citric acid enhanced the crystallization process at lower temperatures (~300° C) [94]. Addition of higher amount of citric acid results in larger particle size of anatase TiO_2 [95]. A comparative study on phase formation and transition temperature, crystallite size, surface area, and grain growth process using different complex agents by Azizi *et al.* [96] are shown below in Table 1.

Table 1.1: Effects of different complex agents of sol-gel method on phase formation/transition temperatures, crystallites size and surface area.

Complex agents	Crystallite size (nm)	Crystalline phase and (A/R)	Surface area (m^2/g^{-1})
$T_{Calcinating}$ =400 ^{o}C			
Acetylacetone	10	A	86
Ethylene glycol	13	A	76
Citric acid	8	A	75
Urea	10	A	60
$T_{Calcinating}$ =500 ^{o}C			
Acetylacetone	21	A	51
	28	R (2.33)	
Ethylene glycol	17	A	37
	29	R (4.26)	
Citric acid	14	A	51
	22	R (1.17)	
Urea	14	A	24
	--	R (6.7)	
$T_{Calcinating}$ =700 ^{o}C			
Acetylacetone			
Ethylene glycol	31	R	--
Citric acid	30	R	--
Urea	27	R	--
	31	R	--

1.4.1.2 Temperature and Time

Temperature and time are important parameters in phase formation, crystal growth and phase transition of TiO_2. Heat treatment of amorphous titania at elevated temperature converts it to a crystalline anatase phase below 600 °C in an air atmosphere, with further heating at higher temperatures convert it to rutile structure in between ~400-1100 °C [15, 27]. Buchholcz *et al.* [1] reported that below 600 °C, sample is in anatase phase and when the temperature was further increased (from ~600 to ~900 °C) appearance of rutile phase was observed.

Using hydrothermal method, Ding *et al.* [67] reported changes in the A/R ratio of anatase and rutile phases varied with temperature and time when solution concentration is constant.

Table 1.2: Effects of temperature and time on anatase to rutile weight ratio.

Temperature (°C)	Time	A (%)	R (%)	Temperature (°C)	Time	A (%)	R (%)
100	3 h	95	5	150	1 h	85	15
100	12 h	87	13	150	3 h	58	42
100	2 d	31	69	150	12 h	10	90
100	30 d	0	100	150	2 d	0	100

1.4.1.3 Environment of calcination

Apart from the process, temperature and time, the atmosphere of calcination is an important factor which controls relative phase stability of TiO_2 nanoparticles. Ahonen *et al.* [97] reported that A→R transition starts at a higher temperature in a nitrogen atmosphere (~580 °C) than in an air atmosphere (~500 °C). Again in a reducing environment A→R transition was promoted while retarded in the oxidizing environment [98].

Wang *et al.* [99] reported that rutile phase was stronger when anatase powders were heated at 1000 °C in presence of pure oxygen atmosphere than when heated in vacuum. Hence, oxygen-rich environment promotes A→R. In both cases, ratio of rutile phases is below 10%. It was observed that A→R is faster in the air than pure O_2 or vacuum [33] due to lower convective heat transfer than air.

Iida *et al.* [100] reported that grain size of TiO_2 particle calcined in H_2 atmosphere exceeds that in O_2, Ar, air, and vacuum. The rate of A→R transition decreases with an increase of partial pressure of O_2 of the atmosphere.

There are different reports on the onset temperature of A→R. However, most observations, for TiO_2 grown in an air atmosphere, the onset temperature is in the range ~600-700 °C [27, 101].

1.4.1.4 Pressure

Pressure too has significant effects on phase formation, grain growth and phase transition on TiO_2 synthesis and decarburization and denitrification. Anatase phase transforms to rutile phase with an increase of temperature but transforms to some other crystal structure with increased pressure. The new structure is also pressure dependent. At 2-5 GPa pressure, anatase phase transforms into an orthorhombic (α-PbO_2) structure. With further pressure increase (>10 GPa) it transforms into monoclinic baddeleyite ($P2_1/c$) structure [21]. On the other hand, the rutile structure transforms into monoclinic baddeleyite type structure at a pressure of ~12 GPa [102]. Cubic fluorite type TiO_2 structure was prepared by heating anatase to 1627-1827 °C at 48 GPa and reported it as possibly ultrahard material [103]. At a temperature >727 °C and pressure >60 GPa, Cotunnite type ($PbC1_2$) crystal structure was formed. This is the hardest and least compressible oxide [29].

Using *in-situ* synchrotron radiation x-ray diffraction, the effect of pressure on transformation from amorphous→anatase→rutile phase was discussed by Albetran *et al.* [104]. Sealed and heated in quartz capillary, anatase phase starts appearing at 200 °C. Under normal atmospheric condition, anatase phase starts to appear at a much higher temperature ~400 °C. This was reported to be because of increased oxygen partial pressure in the capillary. At 600 °C, in normal atmospheric condition, anatase phase starts to transform into the rutile phase. But sample heated at gas pressure ~0.36 MPa up to 800 °C shows only anatase phase. It was also observed that particles size of capillary sealed samples is smaller (~85±31 nm) than normal atmospheric condition grew samples (~118±44 nm). Hence, pressure plays a significant role in phase formation temperature, crystal growth and phase transition temperature of TiO_2.

1.4.1.5 pH

The acidity/basicity (pH) of the solution is also an important factor to control the phase transition and rate of grain growth [91, 105-107]. When pH of sol-gel increases from 4.5 to 6.5, the phase transition temperature decreases [108]. A completely A→R conversion happens at 800 °C for pH ~4.5, whereas, it happens at 650 °C for pH ~6.5. It was confirmed from X-ray Photoelectron Spectroscopy (XPS) studies that increased oxygen vacancies are responsible for such changes irrespective of the particle size. Tsega *et al.* [109] reported that nanoparticles prepared at different pH value (3.2-6.8) by a sol-gel method, calcined at 500 °C for 2h. In the pH range, 4.4-6.8 only anatase phase is observed, while anatase, brookite co-exist with majority rutile phase for pH ~3.2. Strain increased and crystallites size decreased with increased pH value from ~3.2 to 6.8. From literature[110], it was observed that the decrease of pH accelerates the A→R transition.

1.4.1.6 Strain

Strain also a very important parameter for phase transition and grain growth of TiO_2 [111, 112]. Choudhury *et al.* [113] in their report observed a positive strain (~0.0345), when particles are in anatase phase and a negative strain (~0.0006) when particles are in rutile phase. A similar type of result was observed by Moghaddam *et al.* [114].

1.4.1.7 Crystallites size

Crystallite size is one of the most important parameters for stabilization of anatase phase and brookite phase. It also controls the A→R phase transformation [115, 116]. From most experimental reports, it was observed that the anatase phase is stable below particles size ~10-15 nm [117], whereas brookite phase is stable in between ~11-35 nm. Rutile phase becomes stable at all particles size above ~35 nm. Large brookite particles directly transform to rutile phase. For very small anatase nanoparticles an A→R phase transition may happen directly or via an intermittent brookite phase. Phase stability crossover diameter of anatase TiO_2 particle was calculated to be ~2.5 nm at 27 °C in vacuum [118].

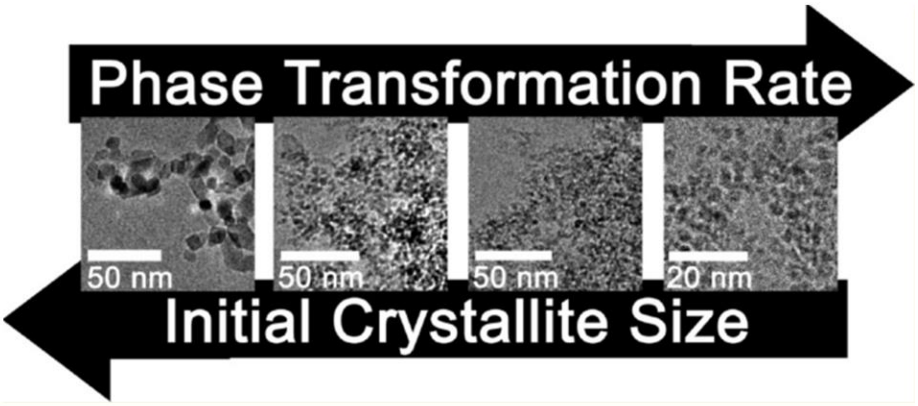

Figure 1.7: Phase transition dependent on initial crystallite size (figure reprinted with permission from [91]. Copyright © 2013 American Chemical Society).

Many authors had reported [91, 119] that phase transition from anatase to rutile and grain growth rate also depends on initial particles size of anatase TiO_2. Sabyrov *et al.* [91] had shown that ~3.1-3.7 nm sized crystallites, transforms to 100% rutile of size ~6-12.7 nm after 12h aging and heating at 250 °C. Hence, the rate of phase transition increased if initial crystallite size decreased.

1.4.1.8 Agglomeration or interfaces

Phase transition and grain growth rate critically depend on agglomeration and surface interface of particles [119, 120].

Aggregation of anatase nanocrystals can be avoided by silica. In such a treatment, anatase phase can even be stable above ~900 °C in an air atmosphere [121].

Faster phase transition and higher grain growth rate has been reported for densely agglomerated particles compared to loosely agglomerated particles by Sabyrov *et al.* [91].

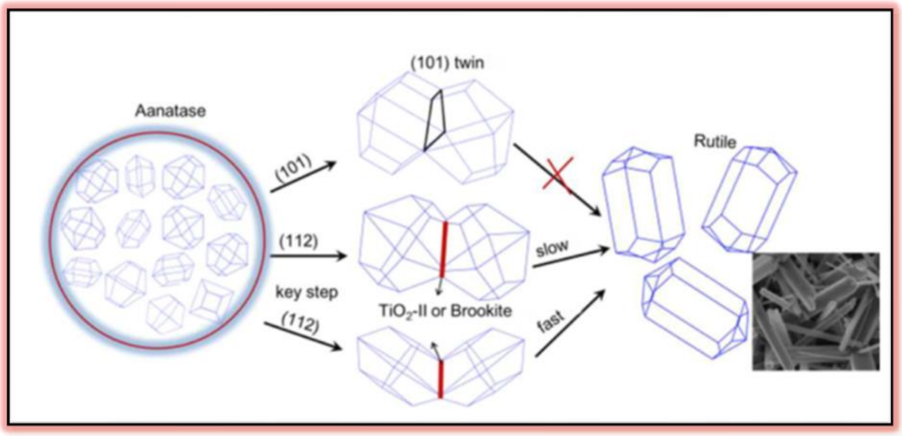

Figure 1.8: Interface nucleation of anatase particle to form rutile phase. (figure reprinted with permission from [122]. Copyright © 2015 American Chemical Society).

Also, the rate of A→R is enhanced by the presence of rutile nuclei [15]. Nucleation happens at the surface as well as in the bulk, and also at the interface of two anatase nanoparticles, during the A→R. One of these processes takes a leading role in the phase transformation. The predominant process may change from interface nucleation at low temperature to surface nucleation at intermediate temperatures and to bulk nucleation at very high temperatures. The phase fraction, i.e. the ratio of A/R, depends on the particle packing and the calcination time.

1.4.1.9 Impurities

Crystal growth and phase transition are largely affected by the addition of external and internal impurities. Thus doping and substitution are the easiest ways to control crystal growth and morphology, phase formation and phase transition temperature, thereby, tune the physical and chemical properties of the modified materials.

1.4.1.9.1 Additives/external impurities

External impurity sitting in the samples as an additional phase, also affects crystallization of TiO_2, phase transition (A→R) and grain growth process [99, 123]. Addition of SiO_2 into TiO_2 xerogels shifted the crystallization temperature of anatase TiO_2 to higher temperature [123]. At 10% SiO_2 addition, activation energy (E_A) for nucleation growth of anatase TiO_2 becomes almost double (E_A: 181 kJ/mol (0% SiO_2) and E_A: 368 kJ/mol (10% SiO_2)). Phase transition temperature also shifted to a higher temperature (~680 °C for 0% SiO_2 and ~1000 °C for $\geq$ 5% SiO_2). Amorphous SiO_2 layer forms on the surface of the anatase TiO_2 nanoparticles, suppresses diffusion of molecules between anatase particles during sintering at high temperature, thereby, limiting the growth process and surface nucleation for rutile phase.

WO_3 addition also modifies A→R. Different reports are available on it [99, 124, 125]. Zhu *et al.* [124] reported that phase transition is accelerated and A→R onset temperature is reduced. On the other hand, Yu *et al.* [125] reported that it inhibits the phase transition. But Wang *et al.* [99] showed that addition of WO_3 in pure anatase accelerates the phase transition whereas, in case of P25 (25% A + 75% R), it inhibits the phase transition. Yu *et al.* [125] have shown that monolayer of WO_3 strongly retards A→R onset temperature, but multilayer of WO_3 has little effect. Other additives like aluminum, potassium, phosphorus, sulfur, lanthanum, cerium, zirconium etc. control grain growth process, surface morphology, crystallization temperature, and phase transition temperature, and thereby, tune the properties of TiO_2. Depending on the type of additive, different types of morphology of TiO_2 can be synthesized [126]. Details of a few examples are tabulated below [15]:

Table 1.3: List of additives influences phase transition and grain growth process of TiO_2.

Authors	Elements	Inhibit	Promote	Grain growth
Hishita *et al.* [127]	Rare earth elements (Y_2O_3, La_2O_3, CeO_2, Nd_2O_3, Sm_2O_3, Gd_2O_3, Ho_2O_3, Dy_2O_3, Er_2O_3, Tm_2O_3, Yb_2O_3.)	√	×	Promoted
Iida *et al.* [100]	NiO, CoO, MnO_2,	×	√	Strongly promoted
	FeO_2, CuO, MoO_3	×	√	Strongly promoted
	Na_2O, WO_3,	√		Have no effect
	Cr_2O_3.		√	Slightly promoted
Francisco *et al.* [128]	CeO_2,	√	×	Inhibit
	CuO	×	√	Promoted
Zhang and Banfield [129]	Al_2O_3	√		Inhibit
Shannon and Pask [33]	CuO		√	Promoted
Criado and Real [130]	PO_4^{3-}	√		Inhibit
Zhenfeng *et al.* [124]			√	Promoted

However, conclusions on a few additives are sometimes contradictory. The distribution, nature, stability, and amount of additives used provides a huge matrix of unknown unexplored quest on the A→R transformation.

1.4.1.9.2 Internal impurities/dopants

In contrast to processing parameter phase transition, grain growth, surface morphology etc. can be easily controlled by internal impurities or defects created due to doping. It is also useful to tune the optical, electrical, optoelectronic and dielectric properties of TiO_2.

The A→R transformation is affected by the presence of intentionally incorporated dopants. A solid solution of a dopant in the anatase lattice, where the dopant ion substitutes a Ti ion, may induce different levels of oxygen vacancies (O_V). Such variations in O_V, are instrumental in the mechanism of delaying or accelerating the phase transition (A→R). It is recognized widely that the most important factor affecting the phase transformation is the presence and amount of defects on the oxygen sublattice (TiO_{2-x}) [126, 131, 132]. Easy arrangement and transformation are promoted by increased amount of O_V in the oxygen sublattice [33].

Solid solutions with interstitial dopant ions may lead to spurious results. The lattice may be stabilized or destabilized, depending on the properties of the dopant ion, like ionic radius, oxidation state, and amount of doping.

Beyond the solubility limit, precipitation of impurity phases occurs. These precipitated phases may generate heterogeneous nucleation which in turn facilitates the phase transition. There are two types of dopants: cationic and anionic. Both influence the crystallization temperature, A→R transition, grain growth, surface morphology, and modifies the properties of TiO_2. These are discussed below.

(a) Anionic

Interesting modifications in the photocatalytic performance of TiO_2 are observed due to anion doping. Only a few reports on anion doping are reported discussing the phase transition. This may be due to the lack of confirmation of the doping. It is generally assumed that dopant anions fill up O_V sites.

If the anionic radius is within 15% of host ion, appreciable solubility is observed. However, most anions are not comparable to the ionic radius of O^{2-}(III) (1.22 Å). Oxygen is only ~6% smaller than nitrogen, N^{3-} (~1.3 Å). Thereby, a possibility of nitrogen replacing oxygen exists. Stabilization of the lattice may take place due to such a replacement on account of the larger size of the dopant ion. Hence, nitrogen doping inhibits phase transition. But the charge of N^{3-} is different from O^{2-}. Hence, for charge balance, N^{3-} removes O^{2-}. Thereby, O_V increases and lattice becomes destabilized [132, 133], promoting the phase transition. Fluorine, F^-(III), (~1.16 Å) is ~5% smaller compared to O^{2-}. Hence, it is expected that F^- can substitute oxygen in TiO_2. From charge balance point of view, replace of each O^{2-} anion requires inclusion of two F^- ions which are extremely unlikely from ionic size consideration. On the other hand, inclusion of one F^- ion in an oxygen vacancy site results in a reduction of Ti^{4+} into Ti^{3+} which would decrease the level of O_V. Upon reduction of Ti^{4+} to Ti^{3+}, ionic radius of titanium increases. Both the mechanism of F^- inclusion expands the lattice, which would expect to inhibit phase transition and has been reported [72]. Fluorine doping not only inhibits phase transition but also retards grain growth of TiO_2.

Depending on ionic size and charge of anion, other anions responsible for promotion and inhibition of phase transition can be listed as follows: $Cl^{1-} > N^{3-} > O^{2-} > F^{1-}$.

(b) Cationic

Cation dopants dominating the A→R transition, are widely reported. Cations of small radius and low valence promote the A→R transition.

This is due to increased O_V resulting out of substitution of lesser charged cations in place of Ti^{4+} ions [33, 131, 134]. For such doping either O_V will be formed in the case of proper substitution, or the dopant will occupy an interstitial site to maintain charge neutrality [123, 135]. On the other hand, when a larger cation of higher valence state substitutes Ti^{4+}, the anatase TiO_2 lattice gathers extra positive charge and reduction in O_V is observed. Hence, interstitials are created. These processes strongly determine the structural stability and capacity to reorganize the chemical bonds to form rutile. Hence, in case of substitutional cationic solid solubility, a small cation of low valence (<4) should accelerate the A→R transition and large cation of high valence (>4) should delay it.

Sometimes it has been argued that the incorporated foreign ions do not substitute but rather goes to interstitial sites. Introduction of cations of smaller ionic radius results in lattice contraction mainly along *c* direction. This contraction along the *c* axis promotes A→R [136]. With the incorporation of interstitial dopants having larger ionic radius than the Ti^{4+}, the anatase structure becomes more stable which inhibits A→R [137-139]. From a structural stability point of view, there are few reports on interstitial destabilization of lattice resulting in promotion of A→R.

Phase transition not only depends on charge and ionic radius but also on the concentration of doping. Dopants may occupy substitutional/interstitial sites or segregate on the surface depending on concentration [140]. Formation energy mostly determines the type of substitutional/interstitial doping or segregation on the surface at different concentrations. One example was provided by Arroyo *et al.* [140]. They reported that interstitials are predominant for lower doping of Mn (< 1.5 mol %). Phase transition is inhibited due to decrease of O_V. For higher Mn doping (> 2 mol %), the dopant ions segregate on the surface of TiO_2 and promote rutile transformation.

$$Mn^{4+} + Ti^{4+} + 2\,O^{2-} \rightarrow (Mn^{2+} + O^{2-} + O_V) + Ti_i^{4+} + \frac{1}{2}\,O_2$$

Another important issue is that certain cations may exist in more than one valence states. Their associated potentials are responsible for different type of reactions which result in inhibition or promotion of phase transition. Two factors influence the phase transition: oxygen vacancies and Ti^{3+} interstitials. As a reference, one can see that different valence state of $Fe^{3+/2+}$ can influence in both ways. Iron creates oxygen vacancies through the reaction below

$$2\,Fe^{3+} + O^{2-} \rightarrow 2\,Fe^{2+} + O_V + \frac{1}{2}\,O_2$$

This O_V promotes phase transition.

Also it may create interstitials as per the reaction,

$$Fe^{3+} + Ti^{4+} + 2\,O_{2-} \rightarrow (Fe^{2+} + O_V + O^{2-}) + Ti_i^{3+} + \frac{1}{2}\,O_2$$

Here, the Ti^{3+} interstitials are responsible for inhibition of phase transition.

In case of Al-doped TiO_2 sample [141], Al^{3+} (VI-0.675 Å) has a slightly smaller ionic radius and lesser charge than Ti^{4+}. Al^{3+} should be creating more oxygen vacancies due to its lesser charge. But however, Al^{3+} substitution generates Ti^{3+} interstitials to maintain charge balance and thereby reduce oxygen vacancies which result in inhibition of phase transition.

$$Al^{3+} + Ti^{4+} + 2O^{2-} \rightarrow (Al^{3+} + \frac{3}{2}O^{2-} + \frac{1}{2}O_V) + Ti_i^{3+} + \frac{1}{4}O_2$$

1.5 Motivation of the present work

As discussed above there are several parameters which control crystallization temperature, onset/phase transition (A→R) temperature, grain growth process and optical properties of TiO_2. Among them, doping is the easiest way. It has been discussed that charge and ionic radius are extremely important in influencing these factors. Keeping in mind these points, we have synthesized four series of samples:

- Gallium doped system (Ga^{3+} having less charge and bigger ionic radius (VI-0.76 Å))

- Vanadium doped system (V^{5+} having higher charge and smaller ionic radius (VI-0.68 Å))
- Charge compensated Ga-V co-doped system (Ga: V = 1:1)
- Charge uncompensated Ga-V co-doped system (Ga: V = 4:1)

Due to ionic radius mismatch and charge imbalance, dopants occupy substitutional/interstitial sites or creates oxygen vacancies which will modify crystal structure of TiO_2. These structural modifications are the key factors for controlling crystallization temperature, onset/phase transition (A→R) temperature, grain growth process and optical properties of TiO_2.

1.6 Chapter details

Systematic flow of the research work is provided below:

i. Synthesis and solubility test of doped/co-doped samples
ii. Effect of doping/co-doping on anatase crystal structure (lattice constant, unit cell volume, strain)
iii. Effect of structural modification of anatase phase on onset temperature, A→R temperature, and activation energy.
iv. Surface morphology, size and grain growth process of anatase and rutile phase affected due to doping/co-doping.
v. Modification of optical properties of anatase and rutile phase of TiO_2 due to structural distortion.

The remaining chapters of this thesis are summarized as follows:

Chapter 2: Experimental details and characterization techniques

Synthesis processes, solubility limit of doping and different characterization technique are discussed in this chapter.

Chapter 3: Effect of Ga doping on grain growth, structural phase transition and optical properties of TiO_2

Effect of smaller size and lesser charged Ga^{3+} doping on the onset and A→R temperature, grain growth process of anatase and rutile phase of TiO_2 have been detailed in this chapter. Valence states of elements (Ga, Ti), substitutional/interstitial occupancy of Ga^{3+} ion and or creation of oxygen vacancies are confirmed by X-ray photoelectron spectroscopy (XPS). Effects of interplay of substitutional, interstitials and oxygen vacancies on the optical property of TiO_2 are also discussed here.

Chapter 4: Effect of V doping on structural phase transition, grain growth and optical properties of TiO_2

Effect of smaller size and higher charged V^{5+} doping on the onset and phase transition temperature, grain growth process of anatase and rutile phase of TiO_2 have been detailed in this chapter. Local environment and valence states of elements (V, Ti) are investigated by X-ray absorption near edge structure (XANES) and extended X-Ray absorption fine structure (EXAFS) measurements. Effects different valence states of V ion on optical properties of TiO_2 are also discussed here.

Chapter 5: Effect of charge compensated Ga-V (1:1) co-doping on structural phase transition, grain growth and optical properties of TiO_2

Effect of Ga-V co-doping in 1: 1 ratio on the onset and phase transition temperature, grain growth process of TiO_2 have been detailed in this chapter. Valence states of elements (Ga, V, Ti), substitutional/interstitial occupancy of Ga and V ion and or creation of oxygen vacancies are investigated by XPS measurement. Effects of interplay of substitutional, interstitial of Ga and V and oxygen vacancy on the optical property of TiO_2 are also investigated.

Chapter 6: Effect of charge uncompensated Ga-V (4:1) co-doping on grain growth, structural phase transition and optical properties of TiO_2

Effect of Ga-V co-doping in 4: 1 ratio on the onset and phase transition temperature, grain growth process of TiO_2 have been detailed in this chapter. Surface morphology and facets are confirmed by HRTEM analysis. Optical properties of TiO_2 influenced by modified crystal structure are also shown here.

Chapter 7: Conclusions and Future Scope

This chapter summarizes the results of present research work with concluding remarks. The possible future scope of present study has also been discussed here

Chapter 2

Experimental Details

This chapter provides basic information about the synthesis (sample preparation) and characterization techniques used in present research work. All presently studied samples have been prepared using sol-gel synthesis routes. As far as characterization techniques are concerned, we have performed (i) Thermogravimetric analysis (TGA) to confirm the phase formation temperature, (ii) N_2 adsorption-desorption study using an automated gas sorption analyzer to study surface area and pore size distribution (iii) X-ray diffraction (XRD) to confirm the formation of right phase and structural phase transition behavior of materials, (iv) X-ray photoelectron spectroscopy (XPS) to identify elements valence states, oxygen vacancies and interstitials in the samples, (v) XANES and EXAFS to investigate the local environment and valence states of elements, (vi) Raman spectroscopy to study the changes in vibrational modes, (vii) High resolution transmission electron microscope, (viii) Field emission scanning electron microscope (FESEM) to study morphology and size of the material, (ix) Energy dispersive X-Ray spectroscopy (EDX) to confirm chemical composition of the material, (x) UV-Vis spectroscopy to study the band gap change due to doping. Fullprof –Suite (for Rietveld refinement of XRD data), XPS peak analyzer 4.1 software for XPS data analysis, Athena and Artemis for data processing and analysis of XANES/EXAFS data, Image J for analysis of HRTEM and FESEM images, etc. has been used for analysis of structural and physical properties. Specific details about the synthesis of samples and characterization techniques are discussed in this chapter.

2.1 Synthesis process

Semiconducting nanoparticles are useful in the field of material science with direct and indirect applications in daily life. Synthesis of new nanoparticles broadens the field of applications.

Nanoparticles may be prepared with the help of several methods: solid-state reaction, hydrothermal, co-precipitation, vapor-phase synthesis, sol-gel etc.. Sol-gel is a widely used method well-known due to its simplicity and inexpensive requirements. No special/expensive equipment is needed. It consumes less energy. The most important aspect is the molecular level mixing of precursors which provides excellent homogeneous and single phase samples of high purity. Extremely fine particles are processed at comparatively low temperatures.

2.1.1 Sol-gel synthesis

Pure and doped TiO_2 samples were synthesized by modified sol-gel method. Dihydoxy-bis titanium (TALH: $C_6H_{18}N_2O_8Ti$; 50% aqueous solution (alfa Aesar)) was taken as Ti precursor. Required amount of Ti precursor was mixed with deionized (DI) water in a beaker, at room temperature, while stirring. In another beaker required amount of doping precursor (M) was mixed with appropriate solvents like nitric acid (HNO_3) and ammonium hydroxide (NH_4OH). The dopant precursor solution was then added dropwise into the Ti solution. After one hour of mixing, some gelling agents were added to the solution. This mixture was stirred for another 1 h for homogeneous mixing. Thereafter it was slowly heated. Temperature of this solution was maintained at 80 °C for 4-5 h to get a thick gel. By this time the Ti ions and doping elements ions have got attached homogenously to the polymeric chains. The gel containing the homogeneously distributed ions of all the different elements was burnt on a hot plate at 100 °C in normal ambient condition. The atmospheric oxygen reacts with the ions and results in a black dry powder, containing partial oxides of the elements with a lot of carbon and nitrogen trapped in the matrix. To get rid of the extra elements (mainly carbon and nitrogen), the powders were denitrified and decarburized at 450 °C in an air atmosphere for 6 h to get desired nanoparticles.

For pure TiO_2

$$C_6H_{18}N_2O_8Ti + C_6H_8O_7 + (CH_2OH)_2 \rightarrow$$

$$— (C_2H_5\text{-}O\text{-}Ti\text{-}O\text{-}C_2H_5)_n —$$

$$\rightarrow TiO_2 + H_2O\uparrow + N_2\uparrow + CO_2\uparrow$$

For doped TiO_2

$$C_6H_{18}N_2O_8Ti + M + C_6H_8O_7 + (CH_2OH)_2 \rightarrow$$

$$— (C_2H_5\text{-}O\text{-}Ti\text{-}O\text{-}C_2H_5\text{-}O\text{-}M\text{-}O\text{-}C_2H_5)_n —$$

$$\rightarrow Ti_{(1-x)}M_xO_2 + H_2O\uparrow + N_2\uparrow + CO_2\uparrow$$

Further calcination followed at higher temperatures to analyze the grain growth and phase transition (A→R) behavior. Schematic diagram of the sol-gel process is shown in figure 2.1.

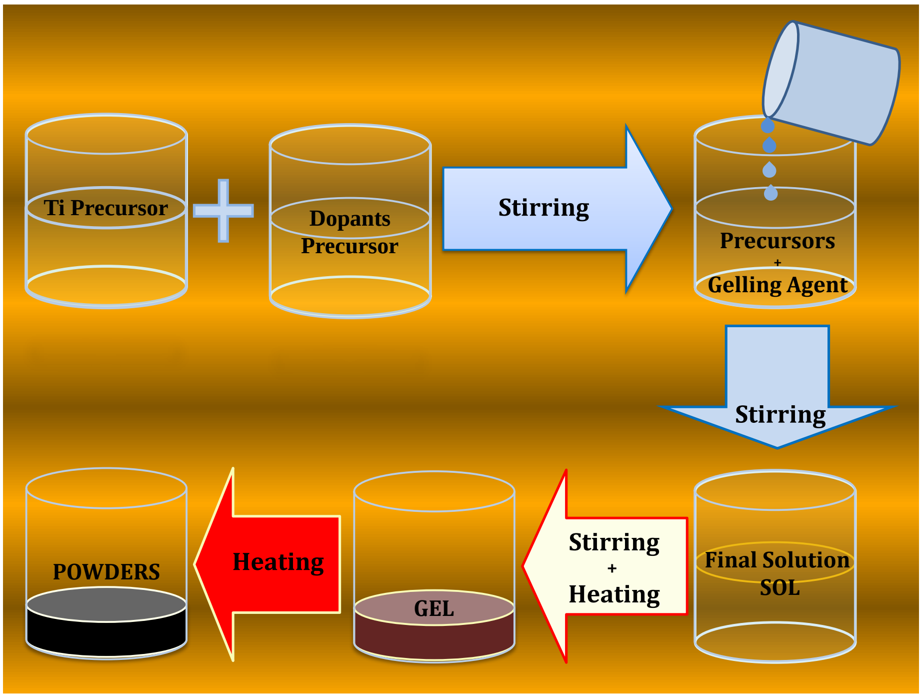

Figure 2.1: Schematic diagram of a sol-gel synthesis route used in our work.

2.1.2 Doped Sample Preparation:

For all doped samples, the procedure is the same as discussed in **section 2.1.1.** Required amount of precursors were measured for all doped samples and mixed in a similar fashion as discussed above. For all doped samples the gels were burnt, decarbonized and denitrified similar to the process discussed in Section 2.1.1. The processes of obtaining these solutions are discussed in detail in the following sections.

a) Ga doped TiO_2 synthesis

$Ti_{(1-x)}Ga_xO_2$ samples were synthesized for $x = 0$, 0.025, 0.050, 0.075, and 0.100 and named T0, TG2, TG5, TG7, and TG10 respectively. Gallium nitrate: $Ga(NO_3)_3$ (Alfa Aesar, purity-99.99%) and Dihydroxy-bis titanium (TALH: $C_6H_{18}N_2O_8Ti$ (Alfa Aesar, 50% w/w aqueous solution)) were used as Ga and Ti precursors. An appropriate amount of $Ga(NO_3)_3$ was dissolved in DI water. The Ga-solution was added dropwise to the Ti solution (as detailed in Section 2.1.1) at room temperature while stirring. A solution of citric acid and ethylene glycol (1:1) were mixed to the precursor solution. The resultant solution was further stirred for another 1 h to obtain a uniformly distributed homogeneous solution which was further heated at a constant temperature of ~80 °C, while stirring. Evaporation of water from the solution results in gel formation around ~3-4 hrs.

$$C_6H_{18}N_2O_8Ti + Ga(NO_3)_3 + C_6H_8O_7 + (CH_2OH)_2 \rightarrow$$

$$— (C_2H_5\text{-}O\text{-}Ti\text{-}O\text{-}C_2H_5\text{-}O\text{-}Ga\text{-}O\text{-}C_2H_5)_n —$$

$$\rightarrow Ti_{(1-x)}Ga_xO_2 + H_2O\uparrow + N_2\uparrow + CO_2\uparrow$$

Gels were burnt on a hot plate at 100 °C in ambient condition resulting in black powders. These powders transformed into light honey color TG nanoparticles after decarburization and denitrification at 450 °C for 6 h in an air atmosphere. These are the starting materials for our analysis.

TG nanoparticles were subsequently heated at eight different temperatures (450 °C, 500 °C, 550 °C, 600 °C, 650 °C, 700 °C, 750 °C and 800 °C) in 50 °C steps. Different samples transit from anatase to rutile phase (A→R) at different annealing temperature. Hence to provide enough time to maximize the phase transition possible at a specific temperature, the furnace was maintained at that specific temperature for 6 h. Processing parameters (like heating/cooling rates, calcination time, environment, etc.) were kept constant for all samples at all temperature. Solubility limit of Ga is around ~10% for both the phases, beyond that rutile phase was formed.

b) V doped TiO_2 synthesis

$Ti_{(1-x)}V_xO_2$ were synthesized for $x = 0, 0.01, 0.03, 0.06$ and 0.09 and named T0, TV1, TV3, TV6, and TV9 respectively. A vanadium precursor solution was prepared by dissolving Vanadium Pentoxide (V_2O_5; Alfa Aesar (99.9%)) in ammonium hydroxide (NH_4OH). The V-solution was added dropwise to the Ti solution (prepared similarly as Section 2.1.1) at room temperature while stirring. The gelling solution of citric acid and glycerol (1:1) were added to the precursor solution. Resultant mixture was further stirred for another 1 h followed by heating at a constant temperature of ~80 °C. Evaporation of water from the solution results in gel formation around ~3-4 hrs.

$$C_6H_{18}N_2O_8Ti + V_2O_5 + C_6H_8O_7 + C_3H_8O_3 \rightarrow$$
$$— (C_2H_5\text{-}O\text{-}Ti\text{-}O\text{-}C_2H_5\text{-}O\text{-}V\text{-}O\text{-}C_2H_5)_n —$$
$$\rightarrow Ti_{(1-x)}V_xO_2 + H_2O\uparrow + N_2\uparrow + CO_2\uparrow$$

Gels were burnt on a hot plate at 100 °C in ambient condition resulting in black powders. These powders transformed into light wine to dark wine color with increasing doping concentration after decarburization and denitrification at 450 °C for 6h in an air atmosphere.

The nanoparticles were further heated at eight different temperatures (from 450 °C to 750 °C) in 50 °C steps for 4 h each to observe the phase transition (A→R) behavior. Processing parameters were kept constant for all samples at all temperature as discussed in section 2.2(a). Solubility limit of V was ~9% in anatase phase while in rutile phase ~6%.

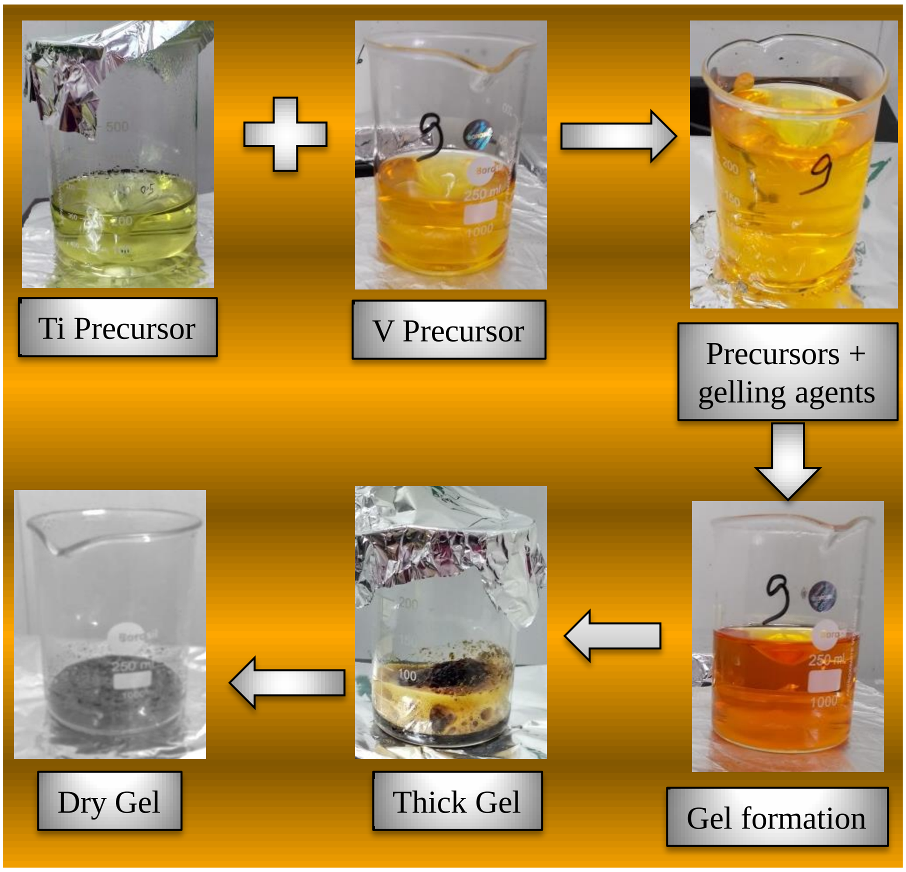

Figure 2.2: Step by step experimental pictures for V-doped TiO_2 sample.

c) Charge compensated Ga-V (1:1) co-doped TiO_2 synthesis

$Ti_{(1-x)}(Ga_{0.5}V_{0.5})_xO_2$ samples were synthesized for $x = 0, 0.025, 0.050, 0.075$, and 0.100 and named T0, TGV2, TGV5, TGV7, and TGV10 respectively. The same Ti, Ga and V precursors were used to make soluble solution as discussed in section 2.2.(a) and 2.2.(b). Ratio of Ga^{3+}: V^{5+} were maintained as 1:1 for all samples. Citric acid and ethylene glycol (1:1) were added to the precursor solution. The rest of the process is same as discussed above.

$$C_6H_{18}N_2O_8Ti + Ga(NO_3)_3 + V_2O_5 + C_6H_8O_7 + (CH_2OH)_2 \rightarrow$$

$$—(C_2H_5\text{-}O\text{-}Ti\text{-}O\text{-}C_2H_5\text{-}O\text{-}G\text{-}O\text{-}C_2H_5\text{-}O\text{-}Ti\text{-}O\text{-}C_2H_5\text{-}O\text{-}V\text{-}O\text{-}C_2H_5)_n—$$

$$\rightarrow Ti_{(1-x)}(Ga_{0.5}V_{0.5})_xO_2 + H_2O\uparrow + N_2\uparrow + CO_2\uparrow$$

After decarburization and denitrification at 450 °C for 6h in an air atmosphere, the black powders changes color from white to yellow to dark yellow, with increasing dopant concentration.

The nanoparticles are further heated at six different temperatures in 50 °C steps from 450 °C to 700 °C. The temperature was kept steady at each step for 6 h at each temperature to ensure the complete phase transition. Processing parameters were kept constant for all samples at all temperature as discussed in section 2.2(a). Solubility limit of Ga-V (1:1) is ~10% for both the phases.

d) Uncompensated Ga-V co-doped TiO_2 synthesis

$Ti_{(1-x)}(Ga_{0.8}V_{0.2})_xO_2$ samples were synthesized for $x = 0$, 0.015, 0.031 and 0.046 and named T0, TGV1, TGV3, and TGV4 respectively. The same Ti, Ga and V precursors were used to make soluble solution as discussed in section 2.2.(a) and 2.2.(b). Ratio of Ga^{3+}: $V^{4+/5+}$ were maintained as 4:1 for all samples. Citric acid and ethylene glycol (1:1) were mixed to the precursor solution. The rest of the process is same as discussed above.

$$C_6H_{18}N_2O_8Ti + Ga(NO_3)_3 + V_2O_5 + C_6H_8O_7 + (CH_2OH)_2 \rightarrow$$
$$—(C_2H_5\text{-}O\text{-}Ti\text{-}O\text{-}C_2H_5\text{-}O\text{-}G\text{-}O\text{-}C_2H_5\text{-}O\text{-}Ti\text{-}O\text{-}C_2H_5\text{-}O\text{-}V\text{-}O\text{-}C_2H_5)_n —$$
$$\rightarrow Ti_{(1-x)}(Ga_{0.8}V_{0.2})_xO_2 + H_2O\uparrow + N_2\uparrow + CO_2\uparrow$$

After decarburization and denitrification at 450 °C for 6 h in an air atmosphere, the black powders change its color from whitish to grayish yellow. Crystal size and dopant type or concentration significantly change the color of the samples [142]. Hence, the color is also dependent on the phase of particles. The images of the nanoparticles are shown in figure 2.3.

Figure 2.3: Images of charge compensated Ga-V (1:1) co-doped TiO_2 samples prepared at 450 °C (Top panel) and 800 °C (Bottom panel) for 6 h shows color changes with doping composition.

The nanoparticles are further heated at eight different temperatures in 50 °C steps size from 450 °C to 800 °C, stabilizing for 6 h at each temperature to observe the phase transition behavior. Processing parameters were kept invariant for all samples at all temperature as discussed in section 2.2(a). Images of samples heated at 800 °C are shown in figure 2.3.

2.2 Characterization Techniques

All characterization techniques are briefly discussed below:

2.2.1 Thermogravimetric analysis (TGA)

TGA is a unique thermal technique vastly used for the analysis of solid materials including organic, inorganic, polymer and composite materials. Generally, it is used to decide the percentage of inorganic compounds present in the synthesized samples. It can calculate (1) amount of volatile elements/moisture/liquid present in the compounds, (2) crystallization temperature, and (3) degradation rate.

Figure 2.4: TGA/DSC system used in this work.

TGA measurements are carried out in this work using METTLER TOLEDO (TGA/DSC1) system attached with the STARe software system from room temperature to 800 °C in an air atmosphere with a heating rate of 5 °C min^{-1}.

2.2.2 Nitrogen (N_2) adsorption-desorption study

Surface texture of nanomaterials like surface area, pore volume/size distribution is determined by N_2 physisorption. Samples calcined at 450°C are used in this analysis. Samples are degassed at 300 °C under vacuum for 4 h. Surface area of the materials is calculated from N_2 adsorption isotherm by Brunauer, Emmett, and Teller (BET) theory. Pore volume/size distribution is calculated from a desorption isotherm using Barret–Joyner– Halenda (BJH) method. Surface area and pore volume/size distribution related information are provided below.

When highly dispersed solid/nanoparticles in a vacuum are exposed to N_2 gas, the solid/nanoparticle starts adsorbing the N_2 gas. Adsorption process happens through monolayer adsorption. This process completes via multilayer adsorption and capillary condensation. A monolayer of N_2 molecules is absorbed on the surface of a target sample at a low pressure. Amount of N_2 adsorbed is used to determine the surface area. Specific surface area of the sample is calculated by the number of N_2 molecules required to fill the monolayer on the samples using Brunauer, Emmett, and Teller (BET) theory. BET equation is shown below.

$$\frac{P}{V\,(P_0-P)} = \frac{1}{V_m C} + \frac{P\,(C-1)}{V_m P_0 C} \qquad \text{(Eq. 2.1)}$$

where P_0 is saturated pressure and P is equilibrium pressure of adsorbates at the temperature of adsorption, V is adsorbed N2 molecules and V_m is the monolayer adsorbed N_2 molecules and C is the BET constant.

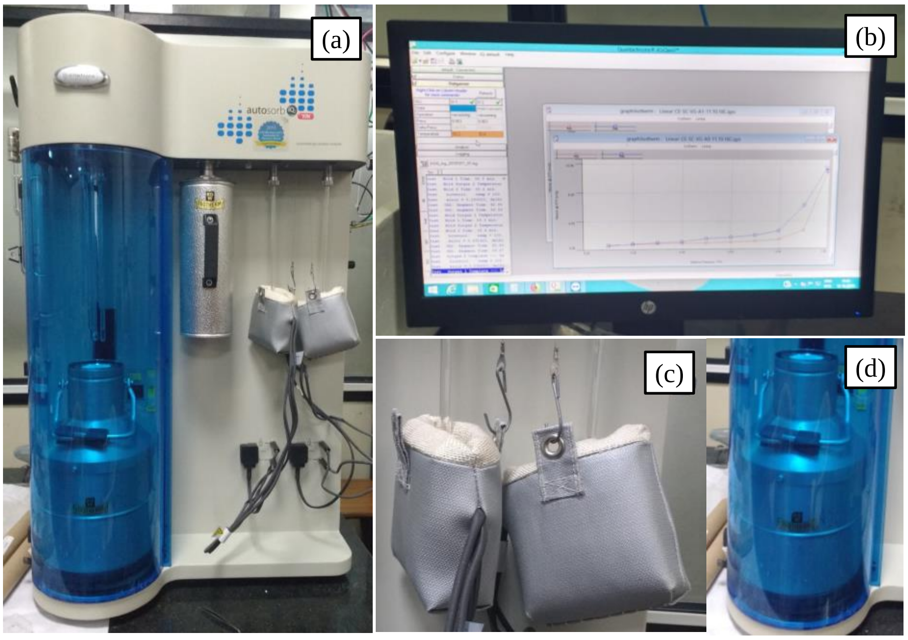

Figure 2.5: N_2 adsorption-desorption setup using an automated gas sorption analyzer Quantchrome autosorb iQ2. (a) Complete setup used in our experiment, (b) computer attached with the setup, (c) heating unit for degassing and (d) N_2 cylinder.

According to IUPAC definition, materials are classified according to their different pore diameter (D). Types are classified as microporous (≤ 2 nm), mesoporous (2 ≤ D ≤ 50 nm) and macroporous (D ≥ 50 nm) [143].

At the time of absorption, after monolayer formation, quantity of adsorbed N_2 molecules increases as a result of increased pressure. This quantity of N_2 molecules increased drastically due to capillary condensation in the mesopores. Adsorption isotherm is completed, when all the pores are filled. From the equilibrium gas pressures using Barrett, Joyner, and Halenda (BJH) computational method, one can calculate the pore sizes.

At the time of desorption, pores remove its adsorbed N_2 gas molecules at a certain relative pressure corresponds to the size of the core. Once core N_2 molecule is removed, a layer of N2 still remains on the surface.

The thickness of this layer can be determined for a certain relative pressure from a thickness equation. Pore size/ volume distribution of the samples with various pore sizes can be fixed by above equation.

Hysteresis loops are formed due to capillary condensation and evaporations as they do not happen at the same pressure. Nature of this hysteresis loops determines the pore shapes [144, 145].

Literature shows that there are mainly four types of loops observed [143]. These are H1, H2, H3, and H4. Corpuscular systems and agglomerated spherical particles show type H1 and H2 loops, whereas, H3 and H4 type of loops are due to slit-shaped pores or plate-like particles. Although N_2 adsorption-desorption process appears to be well established, it is still difficult to confirm the pore structures accurately due to the surface and structural heterogeneity of the samples.

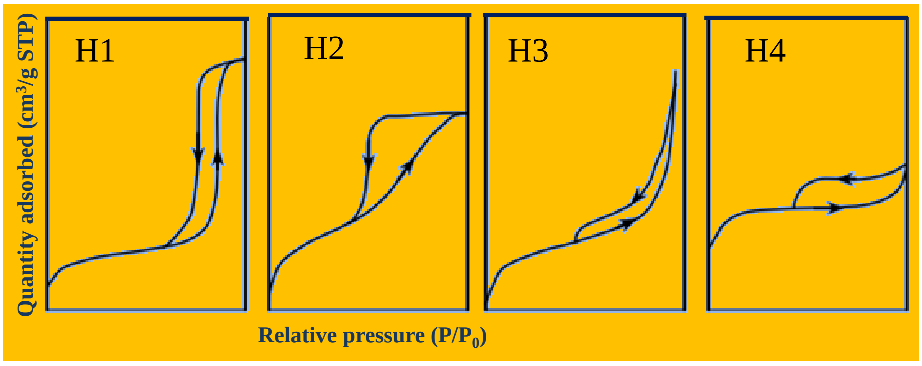

Figure 2.6: Four different types of hysteresis loops according to IUPAC report [146].

2.2.3 X-Ray Diffraction

X-ray Diffraction (XRD) is a technique for analyzing the structure and phase of a material. It works on the principle of interference of X-rays after diffraction from a regular arrangement of atoms. Interatomic distances between the atomic layers are of the order of wavelength of the X-rays. Using this technique, we can also find the *d*-spacing, stress, strain and other lattice parameters of a given material.

When X-rays fall on a set of crystalline planes at an incident angle, θ, they get diffracted. When *d* (interatomic distance) and θ satisfies the condition that the path difference, 2*d*sinθ, equals the integral multiple of the wavelength, Braggs relation 2*d*sinθ = nλ is satisfied and constructive interference takes place. A schematic diagram best explains the Braggs condition. By analyzing these sets of data we can find lattice parameters.

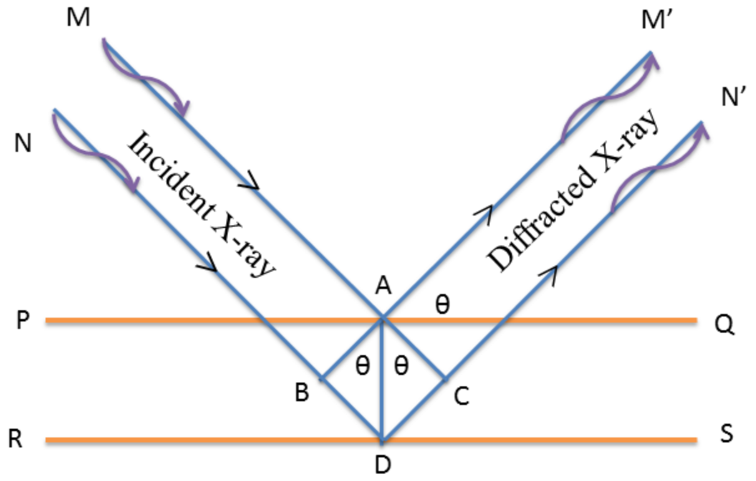

Figure 2.7: Diffraction of X-rays through lattice/atomic planes of a crystal (indicating Bragg's law).

Geometrical path difference, Δ, between two rays, MAM' and NDN',

$\Delta = BD + DC = AD\sin\theta + AD\sin\theta = 2AD\sin\theta = 2d\sin\theta$ …… (Eq. 2.1)

For constructive interference, path difference must be an integer multiple of wavelength, i.e.,

$\Delta = n\lambda$……………………………………………………… (Eq. 2.2)

Thus, from equations 2.1 and 2.2, the Bragg's condition for constructive interference of diffracted X-rays is

$2d\sin\theta = n\lambda$……………………………………………… (Eq. 2.3)

where n is an integer.

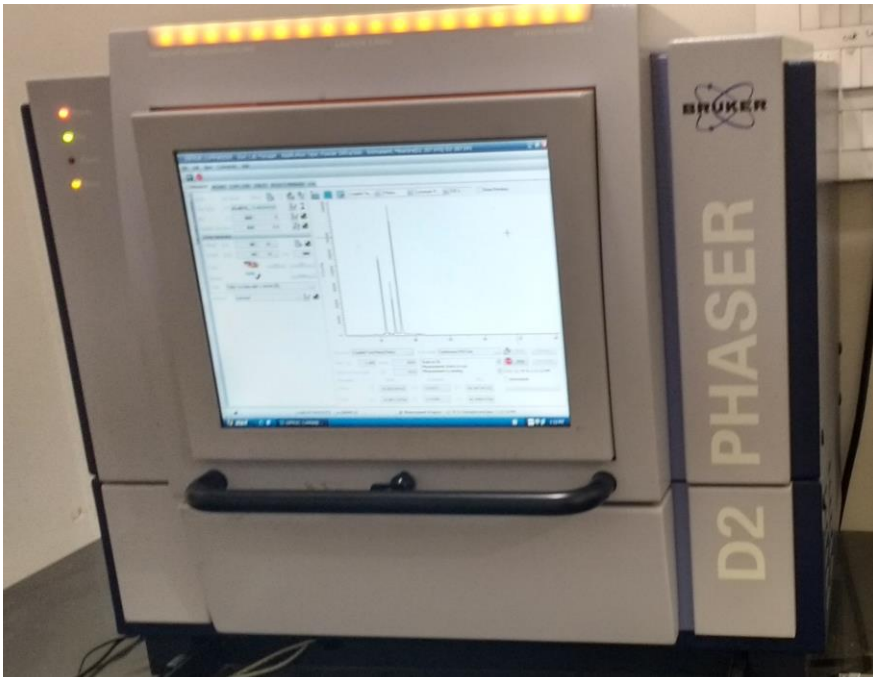

Figure 2.8: Bruker D2 phaser diffractometer (tabletop powder XRD machine) for XRD measurement.

Rietveld refinement

Rietveld refinement of XRD and neutron diffraction data provides the following information:

- Confirms the phases present in the sample
- Estimates structural parameter such as lattice constants, unit cell volume, density, atomic position, angle and bond length between the elements, microstrain etc.
- Estimates the fraction of different phases present in a mixed phase sample
- Determines the phase transition behavior of any material

Profile of powder diffraction pattern depends on characteristics of incident X-ray and neutron beam, experimental arrangement, and on size and shape of the sample.

Parameters refined at the time of refinement

- Scale factor
- Overall β factor

- Lattice parameter (*a*, *b*, and *c*)
- FWHM parameters (U, V, W, IG)
- Background

However, some parameters are not refined at the time of refinement. These are:

- Space group symmetry
- Chemical composition of the sample
- Analytical function (describing shape of diffraction profiles)
- Polynomial function describing the background
- Wavelength of X-ray or neutron beam
- Intensity ratio of the doublet ($K_{\alpha 1}$ and $K_{\alpha 2}$)

2.2.4 X-ray photoelectron spectroscopy (XPS)

Photoelectricity is the effect of electron emission from the surface of a metal due exposure to light. The frequency of the photon, υ, needs to be more than the threshold frequency (υ_0) of the metal. The threshold frequency is related to the work function, W, of the metal as $W = h\upsilon_0$, where h is the Planck's constant. The maximum kinetic energy of the emitted electrons, KE_{max}, is the difference of energies between the incident photon and the work function. Albert Einstein, in his revolutionary work, formulated a simple equation connecting these energies, using quantum theory of light as,

$$h(\upsilon-\upsilon_0) = KE_{max} \quad \text{(Eq. 2.4)}$$

However, the above equation is only applicable for metal surfaces, where the electrons are already at the Fermi level. In semiconductors and insulators, the electrons need energy to reach the Fermi level and a definite amount of energy named as binding energy, E_B, needs to be supplied before the electron can be released from the material. Hence the above equation modifies to,

$$h(\upsilon-\upsilon_0)-E_B= KE_{max} \quad \text{(Eq. 2.5)}$$

When a lattice is distorted due to some perturbation source the bond lengths between ions gets modified. In reality, these are manifestations of changes in the electronic clouds of the ions. These changes in the electronic clouds change the binding energies of the electrons responsible for the bonding. The core electrons too, cannot remain unperturbed due to these changes in the valence electrons. Hence as a whole the binding energy shifts to newer values. Hence, any modified system energies which can probe the core, as well as valence electrons, are powerful tools of understanding the electronic properties of the system.

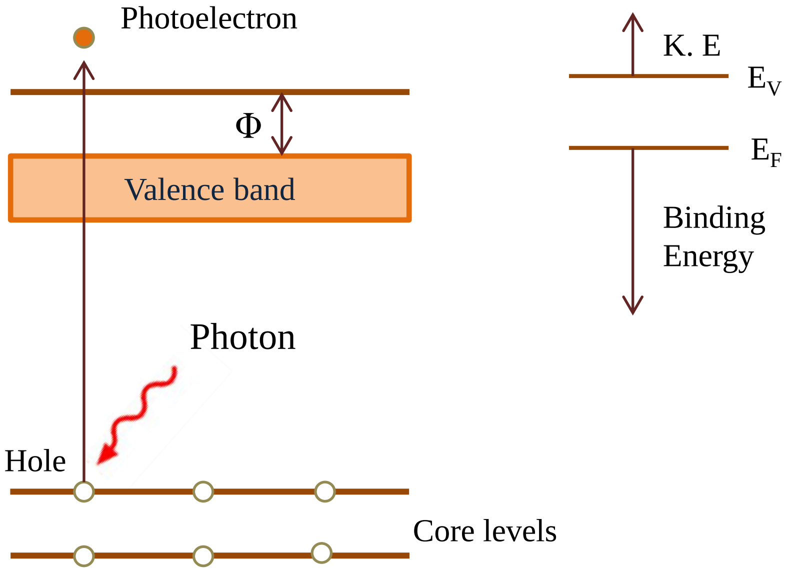

Figure 2.9: Schematic diagram showing working mechanism of X-ray photoelectron spectroscopy.

Using detecting systems like channeltron, etc. the kinetic energy of the electrons can be assessed. Binding energy is calculated using the above equation. X-ray photoelectron spectroscopy (XPS) is a powerful technique used widely by physicists and chemists all throughout the world to understand the valence state of the constituent elements and determine vacancies and other irregularities present in the sample.

2.2.5 X-ray absorption spectroscopy (XAS)

XAS is an extremely powerful technique capable of providing information about the valence states and local structure of individual component elements of a material. Any modifications in structure and ionic properties can be evaluated taking advantage of the absorption processes involved when core electrons are excited to higher energy states and thereafter analyzing the interference effect due to the scattering processes involved with the atoms in the immediate locality of a scattering atom. Highly intense synchrotron radiation with a variable X-ray beam is used for XAS measurement. Energy of the X-ray source is varied from 0.5–500 KeV. The broad range of energy enables electrons from different shells (L, M, N etc.) of an element to be excited to higher valence states. This includes even the K-shell. Absorption happens when an X-ray of an appropriate energy is incident on a core-shell electron and the entire energy is utilized by the electron to either escape or transit to a higher shell. The event can be recorded in absorption versus energy plot. Name of the edges depends on their shell number (n=1(K), 2(L), 3(M) etc.).

Bonding type (hybridization of elements), oxidation states of elements and structural distortion of a compound can be determined by X-ray absorption near edge structure (XANES) or near edge X-ray absorption fine structure (NEXAFS) near the absorption edge.

The extended range of absorption spectra (post edge) gives the information about the local arrangement of elements inside the sample. Absorption coefficient depends on probability of X-ray absorbed by the material following Beer's law

$$I = I_0 e^{-\mu t} \quad \text{……………………………………………… (Eq. 2.6)}$$

where *I* is the intensity of X-ray passing through the sample, I_0 is the intensity of incident X-ray, t is the thickness of the sample. Intensity of X-ray depends on a number of photons absorbed. Absorption coefficient (μ) is a function of atomic number (Z), density of sample (ρ), atomic mass (A) and energy of X-ray (E) which is as follows

$$\mu \approx \frac{\rho Z^4}{AE^3} \quad \text{…………………………………...…………… (Eq. 2.7)}$$

It is a basic characteristic of X-ray that μ is highly dependent on Z and E which is applied for lots of characterization technique.

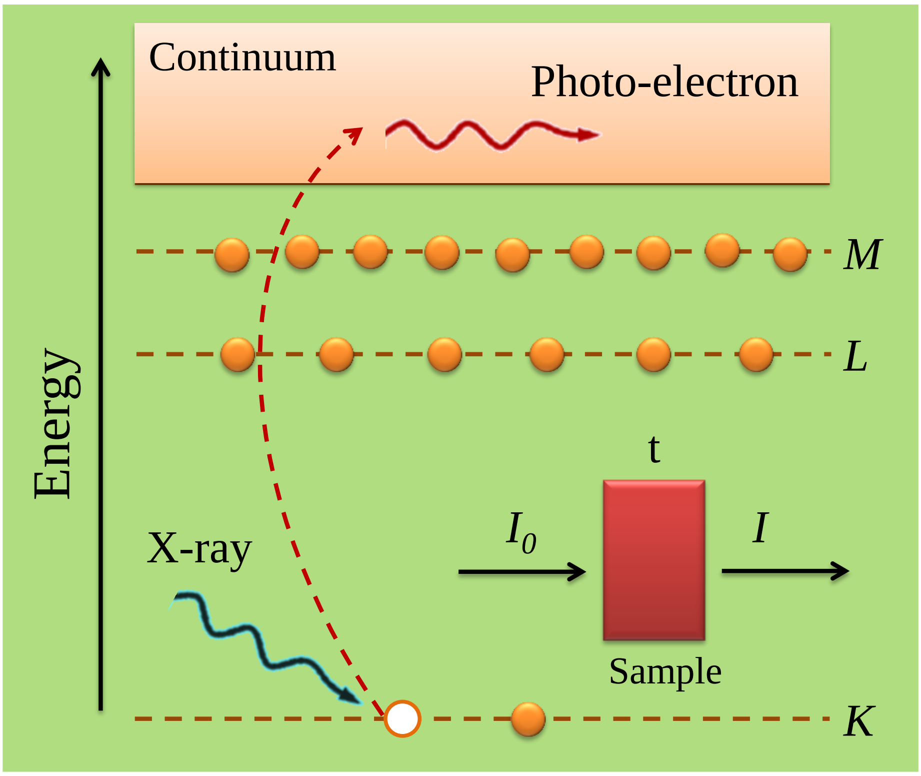

Figure 2.10: The photoelectric effect; an X-ray is absorbed and a core level electron is promoted out of the atom. Inset shows schematically for X-ray absorption measurements: An incident beam of monochromatic X-rays of intensity I_0 passes through a sample of thickness t, and the transmitted beam has intensity I.

EXAFS data contains the information about the local environment of a scattering atom. When a specific energy photon is absorbed by a scattering atom, the energy acquired is immediately released to the surrounding in all directions as a fluorescent photon. This process happens typically within a few femtoseconds of absorption. The wave property of the light allows this energy to interact with the neighboring atoms and be scattered again. The situation is replicated at every lattice site. This results in a complex interference pattern which contains the information of the scattering lengths between the atoms. Hence the bond lengths can be assessed from an EXAFS data. The data is presented as a simple energy dependence of μ at and above the binding energy of a known core level of a known atomic species. Every atom has core-level electrons with well-defined binding energies. Hence, absorption edges of a selected element can be selectively chosen. The absorption and emission can be detected by two processes: X-ray fluorescence, and a de-excitation of the core hole (Auger Effect). In the second case an electron drops from a higher electron level and a second electron is emitted into the continuum.

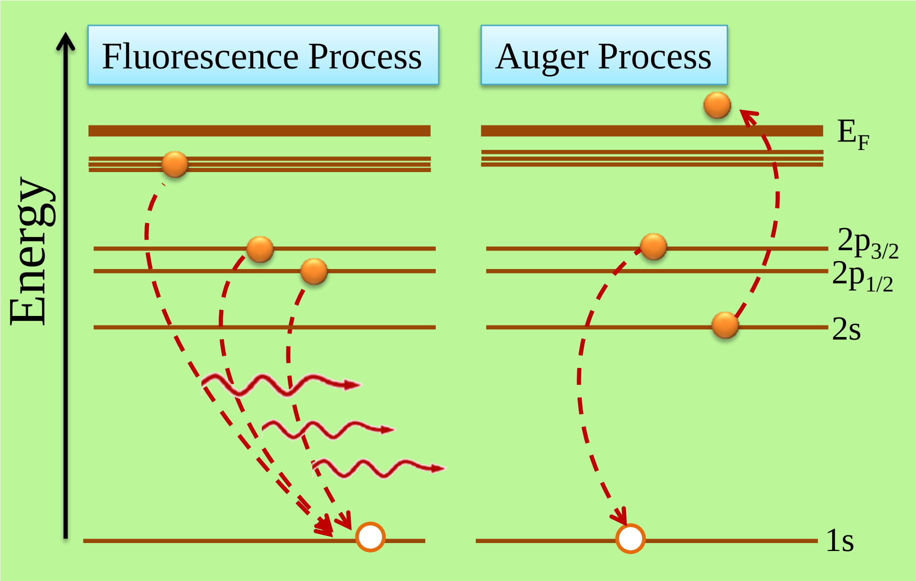

Figure 2.11: Decay of the excited state: (a) fluorescence process and (b) Auger process. In both cases, the probability of emission (X-ray or electron) is directly proportional to the absorption probability.

When hard X-ray ((> 2 KeV) energy is absorbed, fluorescence is more likely to happen, but for lower energy X-ray absorption, Auger processes predominate. Anyone of these processes can be used to determine the absorption coefficient μ. Fluorescence is commonly used for it.

In our work, XANES and EXAFS measurements were carried out on $Ti_{(1-x)}V_xO_2$ samples. Fluorescence mode is used for Ti K-edge and V K-edge measurements. To confirm the valence states of Ti and V, linear combination fitting of the data at the edge is performed using Athena software. EXAFS results of the sample are analyzed by Artemis software to investigate the local environment of the elements.

2.2.6 Raman spectroscopy

Raman spectroscopy provides fingerprint information of a material. It is a vibrational spectroscopy which detects the phonon modes of the materials and thereby identifies the possible phase of the materials. The spectroscopy is highly sensitive to changes in crystal structure, phase transition, defects, stoichiometry, strain etc. as vibrational properties are highly modified by subtle changes in bond lengths and strain.

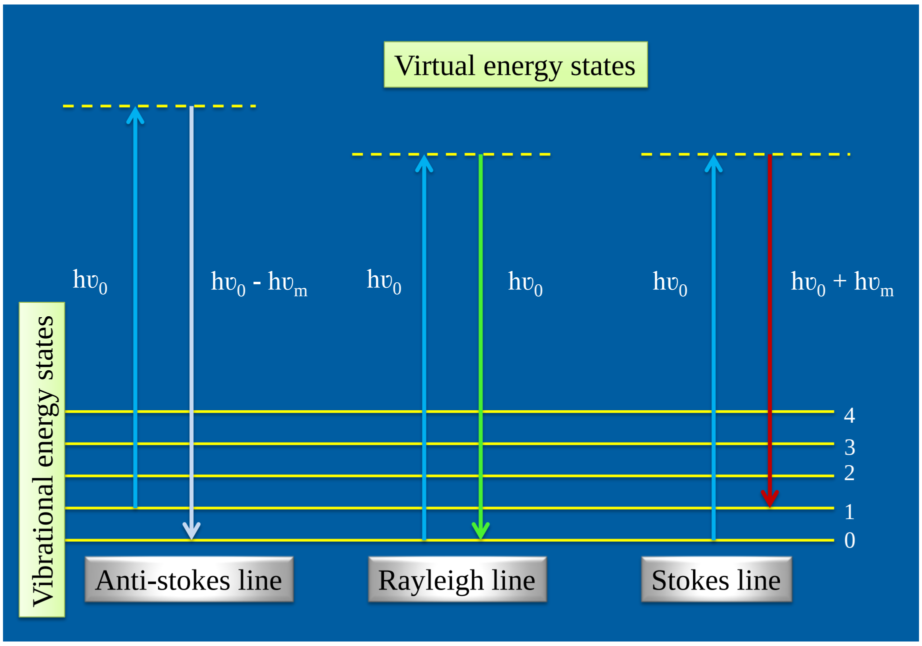

Figure 2.12: Vibrational energy level diagram of Rayleigh, Stokes and anti-stokes line of Raman spectroscopy.

The sample is excited by a monochromatic light. The molecules on which the light is incident can absorb the photon and momentarily go to virtual excited states. The excited molecules emit photons when they return to the ground state. However, if the vibrational ground state has several vibrational states then the return not is to the exact same vibrational state. Depending on whether the state reached is the same or not the photon released will be of the same energy or of a different one. Hence, elastic (Rayleigh scattering) and inelastic (Raman scattering) processes are observed. When the energy level returned is at a higher energy than the initial state, then the light emitted will have lesser energy than the light absorbed. This type of spectrum is known as Anti-Stoke's spectrum, while the reverse situation is known as the Stoke's spectrum.

At room temperature, population of ground states is higher than excited states. Hence, intensity of Stoke's line is higher than anti-Stoke's line. The ratio of the Stoke's to anti-Stoke's lines can provide information about the temperature of the sample. The Stoke's line provides the correct information about the sample's vibrational properties.

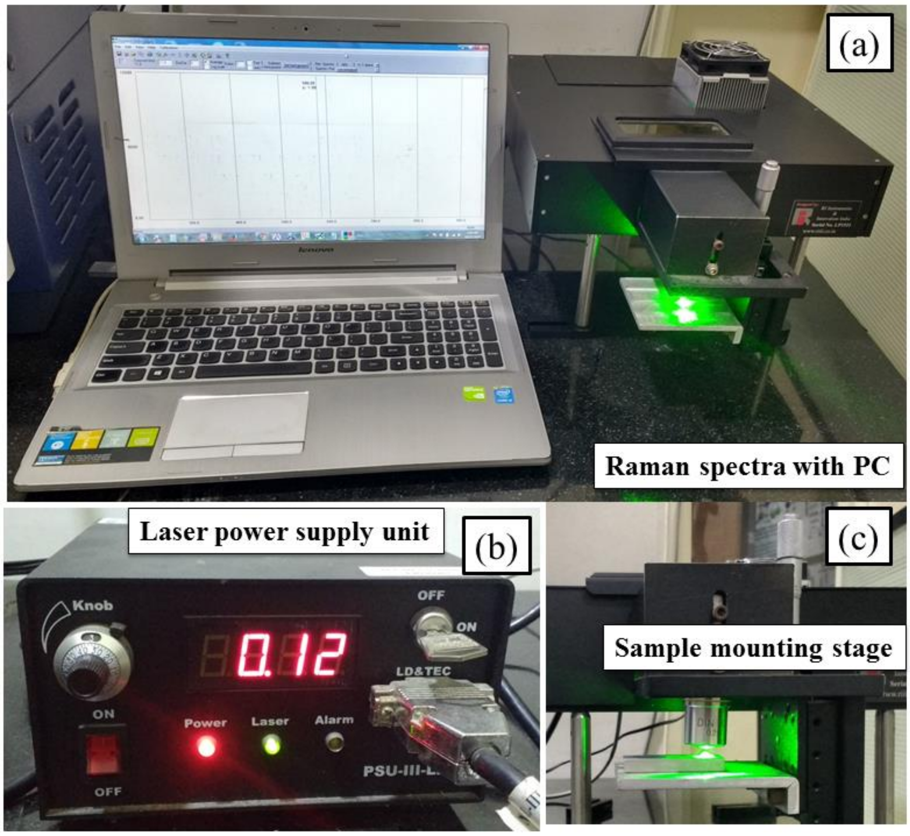

Figure 2.13: (a) Raman spectroscopy connected with PC. (b) Laser power supply unit and (c) sample mounting stage.

In our work, pure and modified TiO_2 powder has been studied using Raman spectroscopy.

Depending on incident photon energy, different vibrational modes behave differently. In case of UV laser source, the ratio of the area of the prominent modes of anatase and rutile phases is used to see phase transition behavior. On the other hand, in case of visible laser source, the area under B_{1g} mode of anatase and E_g mode of rutile is used for the same. In our case, wavelength used for Raman spectroscopic measurement is 488 nm and 532 nm which are in visible light region. Hence, the area under B_{1g} mode of anatase and E_g mode of rutile is used to see phase transition behavior.

2.2.7 Electron Microscopy

Electron microscopes are high-resolution microscopes which can investigate the detailed surface morphology or the crystalline structure of samples using electrons instead of normal visible light. Electrons being of much smaller size than normal visible light photons can resolve the surface morphology better producing high-resolution images. The electrons can either fall on a surface and detect the details of the morphology of the samples or diffract through thin layers of the sample, to produce diffraction patterns which can analyze the crystalline structure of the material. Using high energy electron beam from an electron gun and collimating the beam by a series of electromagnetic lenses, the sample can be illuminated with a spectrum of different monochromatic electron beams.

2.2.7.1 Transmission electron microscope (TEM)

In case of TEM, the beam needs to be energetic enough (high energy electrons) to penetrate the thin layer or edge of the samples and get diffracted to reach the detector, and hence provide the required crystallographic information. Hence, sample should be thin enough to allow the electron to pass through the sample. To make thin sample, powders of TiO_2 are dispersed into ethanol and ultrasonicated for few minutes, then the liquid is kept on carbon-supported copper grids dropwise. High accelerating voltage has an extremely short wavelength of electrons which provide the information in atomic scale. X-ray is generated with a transmitted electron at the time of electron-atom interaction. High-resolution TEM (HRTEM), provides information about the lattice spacing and particle orientation. On the other hand, selected area electron diffraction (SAED) provides information about the crystallinity and nature of materials (like amorphous, single crystal and polycrystalline). Instrument is composed of an electron gun, condenser, objective lens, sample stage, detector, fluorescent screen, scanner, and computer. Schematic diagram of TEM is shown below.

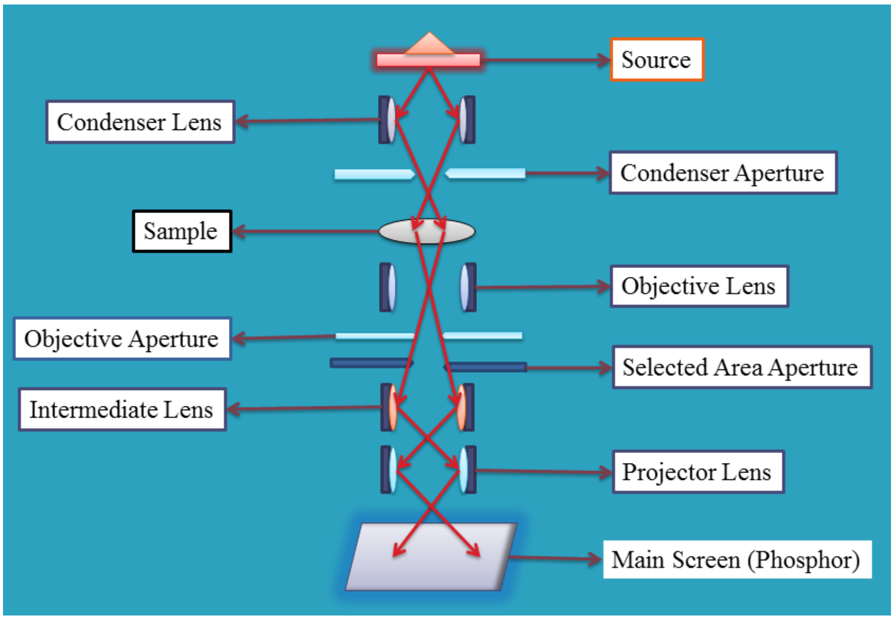

Figure 2.14: Schematic diagram of transmission electron microscopy (TEM).

In our TEM analysis, two different models of TEM machines have been used. In both the cases, the maximum accelerating voltage was 200 KeV.

2.2.7.2 Scanning electron microscope (SEM)

A normal SEM follows the same schematic as an electron microscope. The electron beam is incident on the sample surface and various processes of scattering take place, including back-Scattered, secondary, and Auger processes, etc. The normal SEM generally uses a thermionic beam gun and can resolve in the scale of a few microns to sub-micron orders. In comparison in a FESEM, the electrons are released by a field emission source. An electromagnetic beam gun is used in FESEM. The electron beam is more powerful in FESEM which enables one to attain extremely high magnification, high resolution, therefore, excellent picture quality. A resolution, as small as ~1 nm, can be achieved using

FESEM.

X-rays are also produced in the process when an electron knocks out a core electron from a surface atom and an X-ray is liberated by a higher energy electron filling up the hole created. The process helps to assess and determine the energy spectrum of the X-rays and thereby analyze the elemental composition of the material. This process known as energy dispersive X-ray spectroscopy (EDX) can reveal chemical composition of the sample. These X-ray photons have energies specific to the elements in the specimen. These X-rays are used for elemental analysis of the sample. It usually has energies between 0.1 and 20 keV. Apart from chemical composition, 2-dimensional elemental mapping can be performed by this instrument to see the distribution of elements in the sample.

Due to the high energy of the electrons, the particle size detected by it is extremely small. This can resolute much better and can thereby see the sample's surface, topography, morphology. The interaction of electron with matter results in an emission of secondary electrons (SEs), backscattered electrons (BSEs), Auger electrons, X-rays, etc.

Secondary electrons are ejected from few nm of the sample surface. These are generated by the interaction of primary electrons with the sample surface. They have energy < 50 eV and originate from the sample’s surface. Hence, they contain detailed information about the surface. The angle and velocity of these secondary electrons are highly dependent on the surface structure of an object. Secondary electrons are catch by a detector. The electronic signal produced by the absorption of these secondary electrons are amplified and transformed to a video scan-image for analysis.

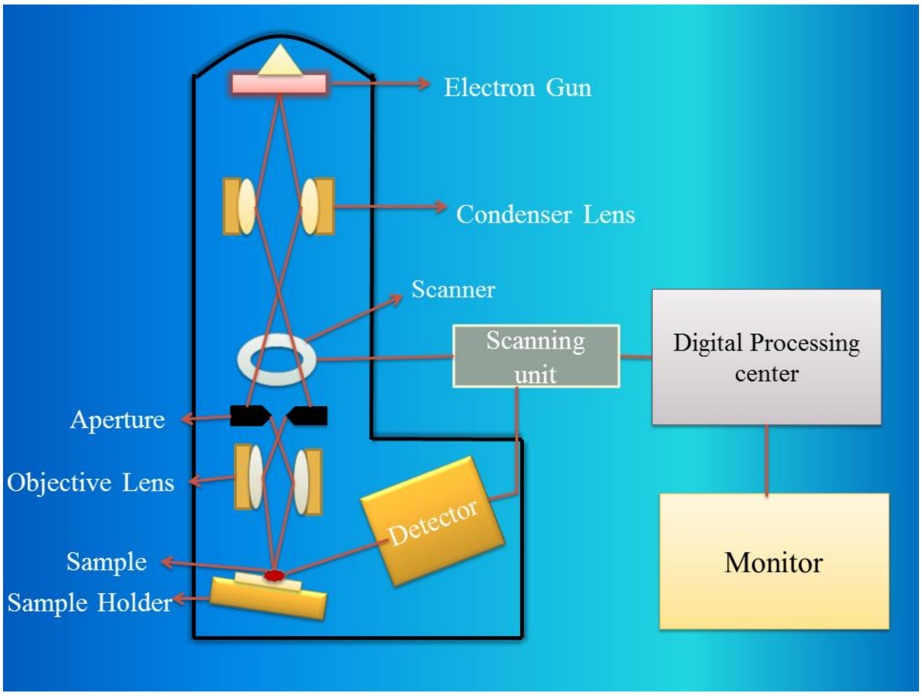

Figure 2.15: Schematic diagram of scanning electron microscopy (SEM).

Backscattered electrons are ejected from the deeper regions of the sample and they originate as a result of interaction of incident electrons and atoms in the specimen. This results in a change in the electrons' trajectory. The number of backscattered electron is proportional to their atomic number. Backscattered electrons provide information about topography, crystallography and magnetic field of the sample. These are usually high energy electrons (E >50 eV) and used for analysis of chemical composition of the specimen.

In our investigation, FESEM images from the powder sample were collected. As the samples in this investigation are nonconductive, hence gold coating was carried out on it to avoid the charging effect.

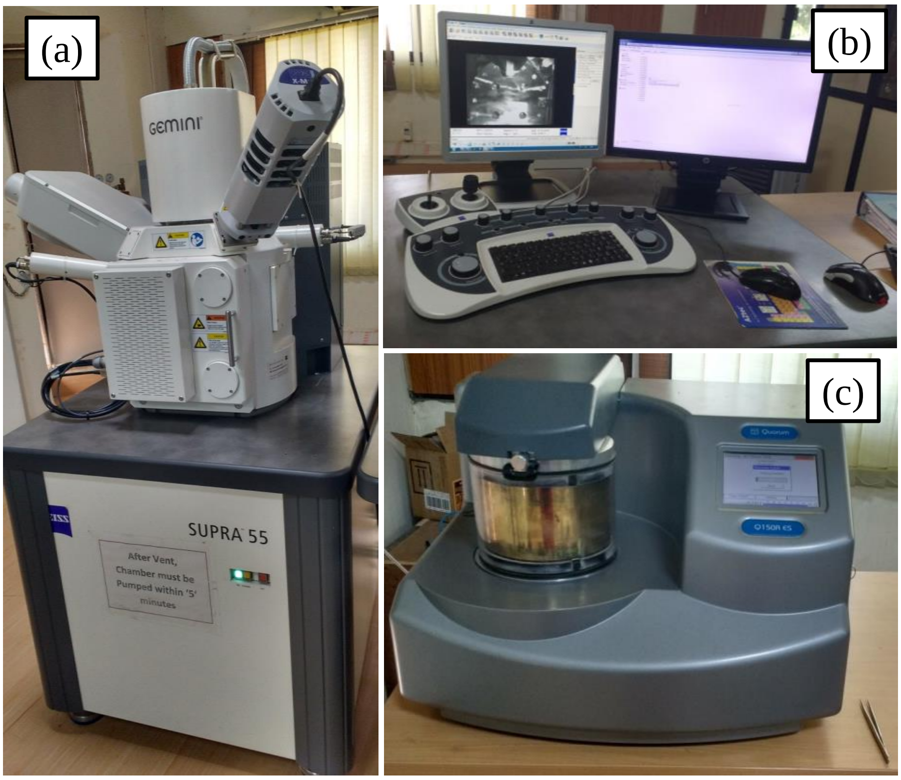

Figure 2.16: (a) Image of Supra55 Zeiss-FESEM used in our work, (b) Inca software attached within the computer for EDX and elementary mapping and (c) Gold coating set up.

2.2.8 UV-Vis Absorption Spectroscopy and Diffuse Reflectance Spectroscopy

Absorption, scattering, reflection, transmission occur simultaneously when electromagnetic (EM) radiations are incident on materials. These processes occur in our everyday life regularly without our conscious understanding. However, if it is designed properly, these processes can be utilized to understand the properties of the materials. The rotational, vibrational and electronic energies add up to account for the total potential energy of a molecule. The energy of an incident radiation is absorbed by a molecule if and only if the incident energy is equal to the energy between two energy levels of the material.

Working Principle

Amount of absorbed radiation by a molecule is dependent on the difference between the incident intensity (I_0) and reflected or transmitted intensity (I). Quantitatively absorbance of radiation is described by the equation:

$A = -\log(\frac{I}{I_0})$.. (Eq. 2.8)

where, A is absorbance, I_0 and I are the intensities of incident and transmitted radiation respectively at a given wavelength. A tungsten-halogen or deuterium lamp is used as a source of radiation in UV-VIS spectroscopy. A monochromator is used to select the wavelength of incident radiation. A detector is used to convert UV- visible light into an electrical signal as a final component of the spectrophotometer.

In the case of powder samples, light is scattered in a diffused manner. Hence, the integration of the entire light is essential. Diffuse reflectance is measured by an integrating sphere detector. This is an attachment to a UV-Vis spectrometer (Carry 60, Agilent) (figure 2.17). Bandgap is calculated using Tauc plot $(F(R))\, h\upsilon = A(h\upsilon - E_G)^n$, where, R is the reflectance, A is a constant, υ is the frequency of illumination, h is Planck's constant, E_G is the bandgap and n is a unitless parameter with value ½ or 2 for direct or indirect bandgap semiconductor respectively. From the literature[35], it was observed that anatase is an indirect (n=2) bandgap semiconductor whereas rutile is a direct (n = 1/2) bandgap semiconductor. Hence, bandgap of the samples is measured accordingly.

Figure 2.17: Experimental set up for diffuse reflectance measurement: (a) Carry 60 UV-Vis spectrometer and (b) schematic of diffuse reflectance.

Chapter 3

Effect of Ga doping on grain growth, structural phase transition and optical properties of TiO_2

3.1 Overview

The anatase to rutile phase transition (A→R) is drastically modified by doping. Hence, properties of TiO_2 can be efficiently tailored by doping. The A→R can be delayed by doping Ce, La, Nb, Nd, Si, Sm, Sr [27, 147] and promoted by doping Al, Co, Li, Na, Sb, V [27, 148]. Theoretical calculations predict that trivalent Ga doping may delay A→R [27]. There are a few reports on optical properties of Ga-doped TiO_2, but they are contradictory to each other. With Ga incorporation, some people reported a decrease in band gap [149, 150] while some of them showed an increase [151]. A few reported unsystematic changes [152] or even no change [153] at all. To the best of our knowledge, the effect of systematic Ga doping on A→R and on grain growth process of rutile phase is not available in the literature.

In this chapter, the effect of systematic Ga doping on structural phase transition, grain growth process and optical properties of TiO_2 is presented. Crystal structure and A→R transition is confirmed by XRD and Raman spectroscopy. Presence of oxygen vacancies (O_V), interstitials (Ga^{3+}) and substitutional sites due to Ga-doping are estimated using XPS. Effect of Ga-doping on grain growth in the anatase and rutile phases is estimated by HRTEM and FESEM images. Elemental composition and distribution of elements in the samples are analyzed by EDX and elemental mapping. Bandgap of the samples is calculated by DRS measurements. Results presented in this chapter are published in peer-reviewed journals[$].

[$] *N. Khatun et al. J. Appl. Phys. 123, (2018) 245702.*

3.2 Experimental

Phase confirmation and transition (A→R) were investigated by powder X-ray diffraction (XRD) using Bruker D2 Phaser diffractometer (Cu K_{α}=1.54 Å). Phase transition was also investigated and confirmed by Raman spectroscopy using a Research India Raman Spectroscopy (model number-RIRM151). Raman spectra were obtained using a green laser of wavelength 532 nm. A detailed structural analysis of TG samples was carried out by Rietveld refinement from XRD data. High-resolution transmission electron microscopy (HRTEM) (JEOL JEM-2100 LaB6) and field emission scanning electron microscopy (Supra55 Zeiss- FESEM) was used to observe the effects of Ga incorporation on grain growth process of TiO_2. Electronic structure and valence states of elements were examined by high-resolution X-ray photoelectron spectroscopy (XPS) (Thermo Kalpha+ spectrometer). Diffuse reflectance spectroscopy (DRS) measurements were carried out using Bentham TMc300 Monochromator to estimate changes in the bandgap.

3.3 Results and Discussion

3.3.1 Thermal gravimetric analysis

Sol-gel processed pure TiO_2 (T0) powders need to be heated at a specific temperature in order to remove carbon, nitrates, moisture, and other undesirable materials. The decarburization and denitrification temperature is known as calcination temperature. Different materials have different calcination temperature which varies with synthesis condition and synthesis technique. In order to optimize the calcination temperature, thermogravimetric (TGA) analysis has been done on the as-prepared powders (dry gel) as shown in figure 3.1.

TGA measurement on dry gel powder (T0) was performed from room temperature (RT-27 °C) to 800 °C. Weight loss of 1.04%, from RT to ~110 °C, was observed in pure TiO_2 (T0) (figure 3.1). This is due to elimination of physically adsorbed water [154]. In the temperature regime ~110 to 315 °C a sharper weight loss of ~2.52% was observed. This may be attributed to the rupture of polymeric chains present in the black powders and removal of ethylene glycol units [155].

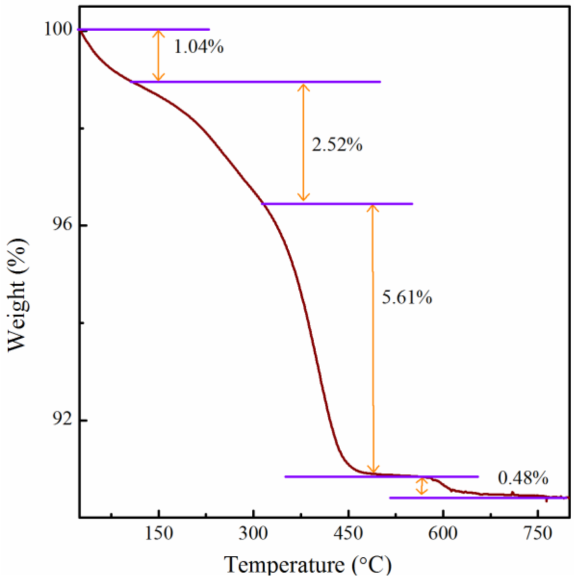

Figure 3.1: Thermogravimetric analysis of pure TiO_2 (T0) in temperature range of 27 °C to 800 °C showing loss of adsorbed water, nitrates and carbonates.

A final sharp weight loss of ~5.61% was observed in the temperature regime ~315-430 °C. This drastic loss is due to decomposition of the organic compounds into carbon dioxide and nitrogen dioxide, desorption of chemisorbed water molecules [156, 157]. This temperature was high enough to take care of the unreacted precursors and thereby form crystalline nanoparticles of the desired stoichiometry. Note that beyond ~430-450 °C, there is almost no change in weight loss. Thus, 450 °C was selected as the optimum calcination temperature which is high enough to achieve crystallization. This temperature is optimum to reduce the thermal growth of the calcined particles to maintain nano-scale features. A minor weight loss of 0.48%, in between 550 to 650 °C can be ascribed to the removal of the surface hydroxyl groups present in the samples [158].

3.3.2 Structural analysis

XRD pattern of the Ga doped TiO_2 samples (calcined at 450 °C for 6h) are of tetragonal anatase phase of TiO_2 with space group $I4_1/amd$

(COD ID- 9015929) (figure 3.2:(a)). There are no traces of the rutile phase at this temperature. Anatase phase transforms into the rutile phase with further heating at higher temperatures (figure 3.2). Compared to pure TiO_2, in Ga-doped samples phase transformation (A→R) is delayed and anatase phase is retained. This tendency increases with increasing amount of Ga content. All samples are completely converted into the rutile phase at 800 °C. XRD patterns confirm a tetragonal rutile phase with $P4_2/mnm$ space group (COD ID-1532819) (figure 3.2 (h)).

Figure 3.3 shows the zoomed view of XRD pattern in the range $2\theta = 24.5\text{-}28°$, where most intense peaks of anatase (110) and rutile (101) are situated. For pure TiO_2 (T0), phase transition (A→R) starts at ~450-500 °C due to specific reagents (ethylene glycol and citric acid) [96] used in this method. T0 transforms to entire rutile phase at 700 °C. In the intermediate temperature (450-700 °C), samples are in a mixed phase. The phase transition (A→R) shifts towards higher temperatures with increasing Ga incorporation. It is observed that complete conversion to rutile phase is also affected by Ga incorporation. Up to 550 °C, rutile phase is not observed in all Ga doped samples. TG2 starts showing small traces of the rutile phase at ~600 °C. For TG5 and TG7 samples, phase transition starts in between 600-650 °C, while for TG10 in between 650-700 °C. TG2 and TG5 samples are completely converted into rutile phase at ~750 °C, while the same happens for TG7 and TG10 at ~800 °C. Hence, Ga doping delayed both onset and A→R temperature of TiO_2.

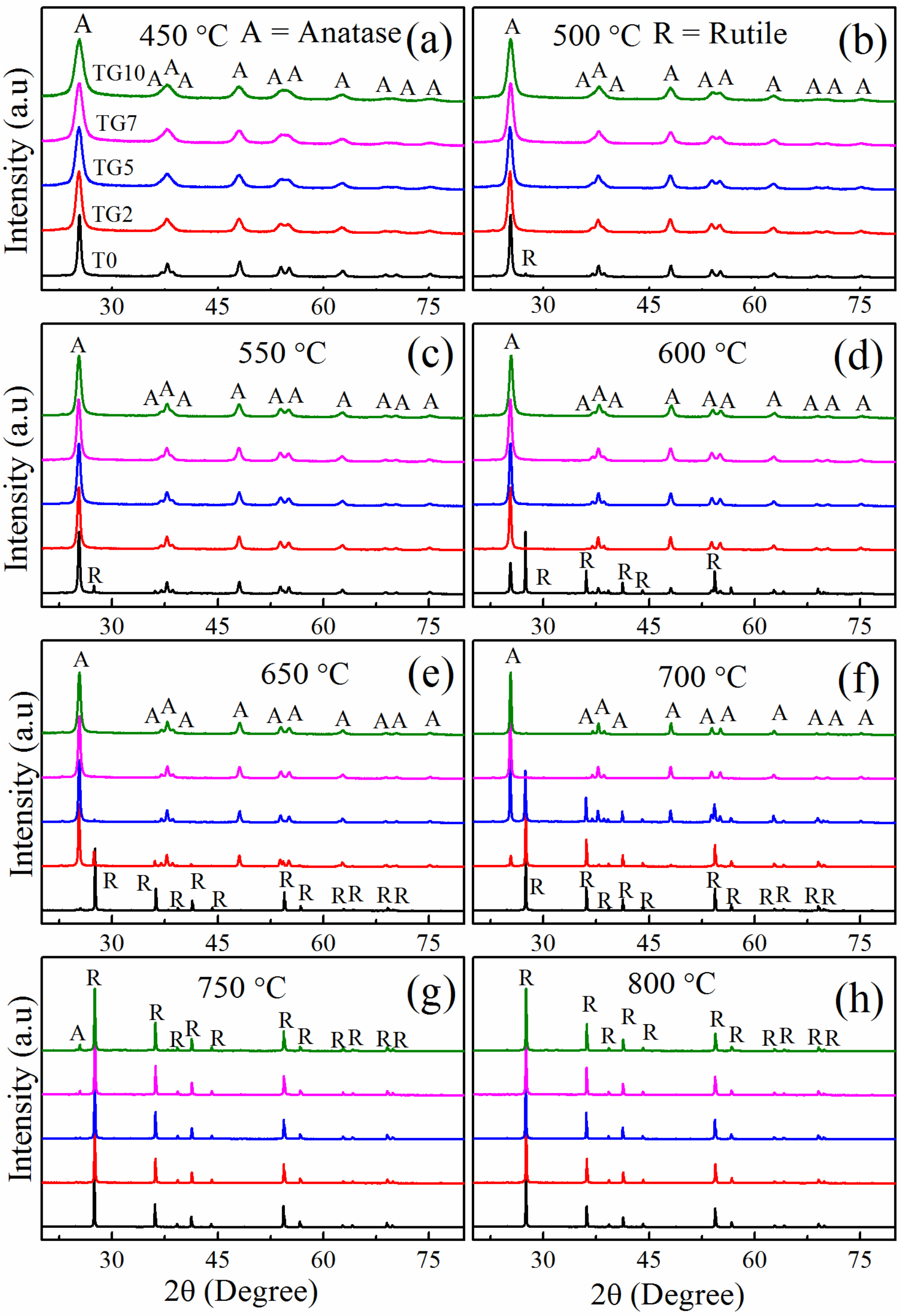

Figure 3.2: XRD pattern of all Ga doped TiO_2 samples heated at eight different temperatures ((a) 450 °C, (b) 500 °C, (c) 550 °C, (d) 600 °C, (e) 650 °C, (f) 700 °C, (g) 750 °C, and (h) 800 °C).

For quantitative analysis, rutile phase fraction (f_R), has been evaluated using Spurr and Mayers equation[159]:

$$f_R = \frac{1}{1+(\frac{1}{0.8})\frac{I_A}{I_R}} \quad \ldots\ldots\ldots\ldots\ldots\ldots\ldots\ldots\ldots\ldots\ldots\ldots\ldots\ldots \text{(Eq. 3.1)}$$

where I_A is the intensity of the most intense peak of anatase (101)

(2θ=25.34°) and I_R is the same for rutile (110) (2θ=27.40°) phases. Temperature dependence of f_R (figure 3.4 (a)) ensures an inhibition of phase transformation.

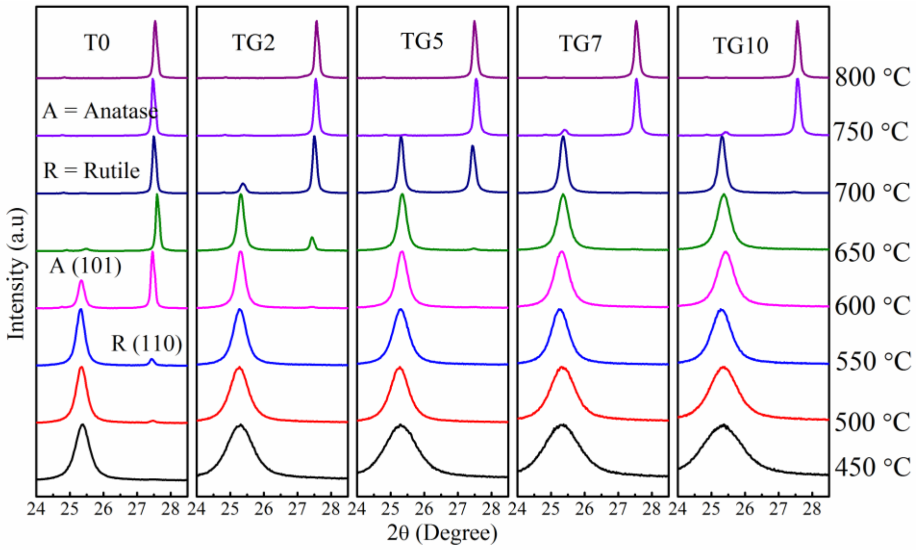

Figure 3.3: XRD pattern of all Ga doped TiO_2 samples at eight different temperatures (~450-800 °C) in the range of 2θ=24.5-28° showing a gradual shift in A→R phase transition to a higher temperature due to Ga doping in TiO_2.

All processing parameters (like heating/cooling rates, environment of calcination, etc.) are kept constant. Hence, this inhibition of phase transformation entirely depends on concentration of Ga doping.

Activation energy of phase transition is calculated by Arrhenius equation:

$$ln(f_R) = -\frac{E_A}{RT} \quad \text{……………………………………….. (Eq. 3.2)}$$

where f_R is the fraction of rutile phase present in the sample, R is the universal gas constant (8.314 J/mol. K.), T is the temperature in Kelvin and E_A is the activation energy of phase transition (A→R).

Linear fits of ln(f_R) vs 1/T are shown in figure 3.4 (b-f). It is observed that E_A increases drastically with incorporation of Ga up to TG5. However, for TG7 and TG10, the rate of increment of E_A retarded and shows a nearly saturated behavior (figure 3.4 (g)). Activation energy varies from 125 kJ/mol to 300 kJ/mol for pure TiO_2 to TG10. Note that A→R conversion is associated with lattice contraction mainly along *c* axis. Hence, a delay in such transition (A→R) and associated huge change in activation energy hints at an increase of lattice constant *c* (also unit cell volume) with Ga incorporation.

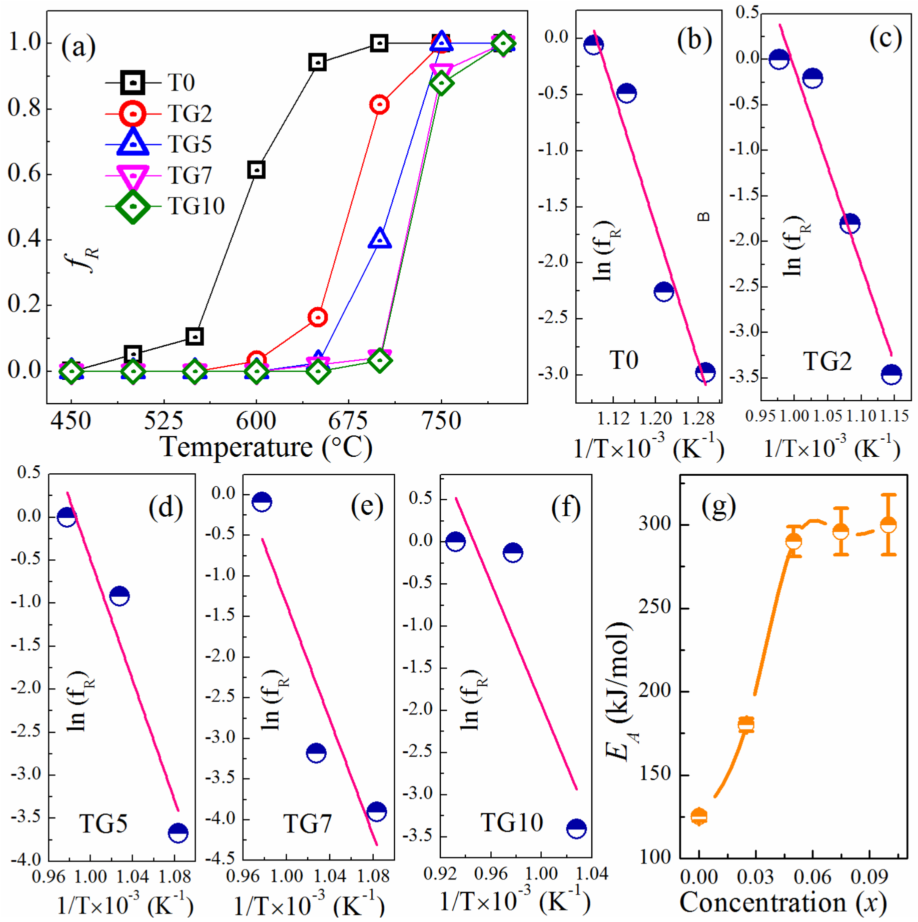

Figure 3.4: (a) Fraction of rutile phase with temperature for all Ga-doped samples showing delayed phase transition due to Ga doping. (b), (c), (d), (e), and (f) show ln(f_R) vs 1/T fits for T0, TG2, TG5, TG7, and TG10 samples, (g) shows variation of activation energy with Ga concentration.

Samples in the anatase phase, when heated to a higher temperature (≥500 °C) leads to rearrangement of Ti-O bonds, as a result, *c* axis contract [27]. Unit cell volume also contracts and phase transformation (A→R) occurs. Lattice constant *c* is smaller in rutile phase compared to anatase phase. Hence, reason behind this delay of phase transformation (A→R) can be explained in terms of change in lattice constant *c*.

Rietveld refinement of pure anatase (450 °C) and rutile (800 °C) samples are shown in figure 3.5 and 3.6.

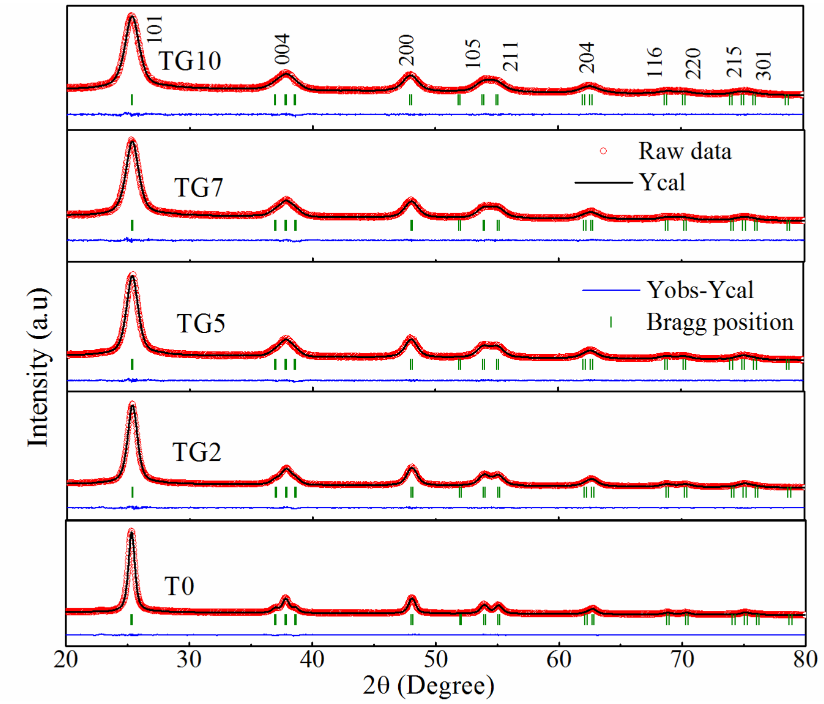

Figure 3.5: Rietveld refinement of anatase Ga doped TiO_2 samples prepared at 450 °C.

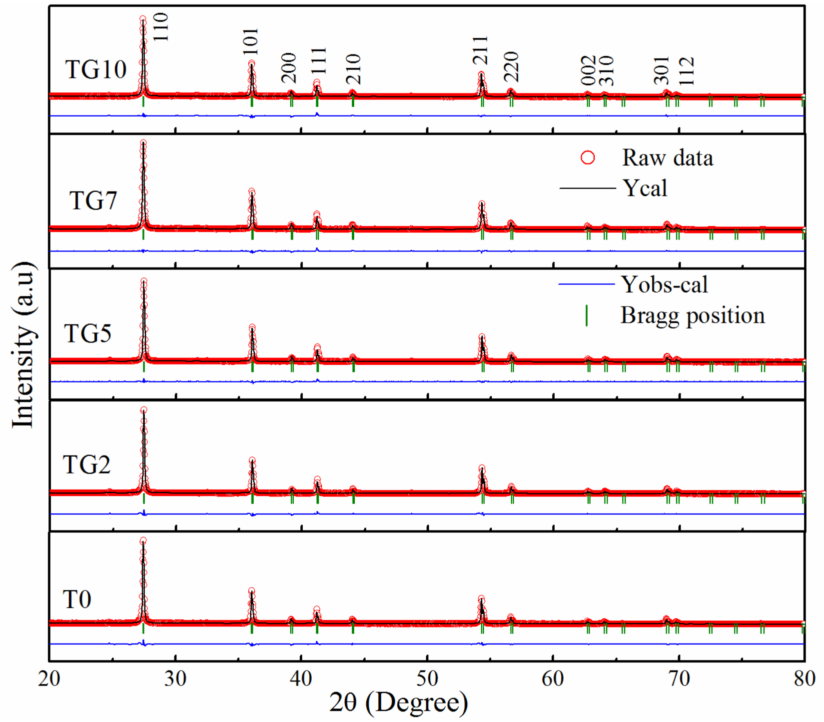

3.6: Rietveld refinement of rutile Ga doped TiO_2 samples prepared at 800 °C.

Rietveld refinement of anatase samples reveals considerable increment in all three lattice constants up to TG5 (figure 3.7: (a)). The rate of increment reduces for higher doping (TG7 and TG10). As a result, unit cell volume also shows a similar trend (inset of figure 3.7: (a)). This expansion of lattice (or especially lattice constant *c*) in anatase phase with increasing Ga content is responsible for the delay of A→R phase transition.

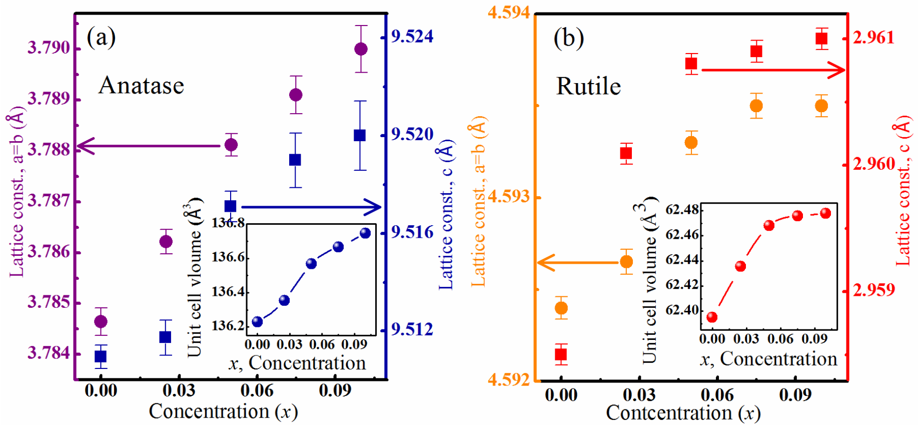

Figure 3.7: (a) Variation of lattice constants with Ga content in TiO_2 sample prepared at 450 ^{0}C (anatase) and (b) 800 ^{0}C (rutile). Insets of the corresponding figures show unit cell volume changes with Ga content for both the phases.

Rietveld refinement of XRD data for a complete rutile phase (800 °C) also shows a similar trend of increment as in anatase phase. At higher doping, a saturation-like tendency is observed for all three lattice constants. Hence, the unit cell volume follows a similar trend as lattice constants (figure 3.7: (b)).

Shannon *et al.* [33] reported that due to oxygen vacancies lattice gets contracted, which in turn accelerate A→R phase transformation. On the other hand, Ti interstitials expand the lattice which inhibits phase transformation. Ti^{4+}(VI) in TiO_2 has an ionic radius ~ 0.745Å. Ga^{3+} (VI) ion have lesser charge and slightly bigger ionic radius (~0.76 Å) compared to Ti^{4+}. When Ga^{3+} is incorporated in TiO_2, charge imbalance is introduced in the lattice which can be compensated by two ways, either by the creation of oxygen vacancies (O_V) or by introducing Ti and Ga interstitials (note that Ti^{4+} and Ga^{3+} both have comparable ionic radii). Two Ga^{3+} ions in TiO_2 matrix will give rise to one oxygen vacancy. On the other hand, three Ga^{3+} ions create one Ga^{3+}/Ti^{3+} interstitial. Okajima *et al.*[160] reported that Ga doping induces O_v in TiO_2 lattice. Malati et al.[161] reported that generation of oxygen deficient material is responsible for decrease in activation energy for A→R phase transformation. But, in these Ga-doped samples, an opposite phenomenon is observed, E_a increases with increasing Ga incorporation. Hence, it is possible that Ga doping not only creates oxygen vacancies but also forms interstitials (Ga^{3+} or Ti^{3+}). This results in lattice expansion. Inhibition of phase transition observed from XRD and Raman spectra hints at a more significant role of Ga^{3+}/Ti^{3+} interstitials along with oxygen vacancies for A→R phase transformation.

In case of Al, Cu and Mn-doped TiO_2 [128, 137, 140, 141, 162, 163], oxygen vacancies and/or interstitials also affect the phase transition. Ionic size of Al^{3+}(VI) ~0.675 Å, Cu^{2+}(VI) ~0.87 Å, Mn^{2+}(VI) ~0.81 Å and Mn^{4+}(VI) ~0.67 Å, are comparable to Ti^{4+}(VI) ~0.745 Å. In all the above cases there is a charge difference. To compensate this charge difference, oxygen vacancies and Ti^{3+} interstitials are created. Interplay of these competing mechanisms affects phase transition. In case of Al-doped TiO_2, Al^{3+} has slightly smaller ionic size than Ti^{4+}. However, it was observed that lattice constant c increases for 20% Al-doping but decreases for 30% [141]. However, all Al-doped samples have a higher value of c than un-doped TiO_2, while a remains invariant. Ti^{3+} interstitials are held responsible for inhibition of phase transition. On the other hand, slightly larger Mn doping shows interesting behavior during phase transition. At lower doping (≤ 0.2%), some Mn ions form interstitials and delay the phase transition, whereas at higher doping (≥ 0.2%) Mn ions substitute Ti ions and thereby accelerate the phase transition[140]. In the case of slightly larger Cu^{2+} doping, phase transition was accelerated due to oxygen vacancies [164].

In case of Ga-doped samples, at lower doping (≤ 0.05), considerable increment in lattice constants may happen due to interstitials (Ti^{3+} and Ga^{3+}). For higher doping (≥ 0.05), Ga^{3+} ions might occupy more substitutional sites or create oxygen vacancies. This may compensate the effect of interstitials and retard further lattice expansion.

3.3.3 Raman spectroscopic studies

Raman spectroscopy is a very sensitive tool for determining crystal phases of materials. Hence, phase confirmation of Ga doped TiO_2 samples and effect of Ga doping on phase transition ($A\rightarrow R$) are analyzed by Raman spectroscopy. Vibrational modes of T0 (heated at 450 °C), matches well with phonon modes of crystalline pure anatase TiO_2. The modes are identified at: 145 cm^{-1} (E_g), 198 cm^{-1} (E_g), 398 cm^{-1} (B_{1g}), 516 cm^{-1} (A_{1g}+ B_{1g}) and 641 cm^{-1} (E_g) [68] (figure 3.8 (a)). Ga doped samples (TG2, TG5, TG7, and TG10) heated at the same temperature also shows similar vibrational modes as pure TiO_2. However, slight blue shifting of first E_g (145 cm^{-1}) mode position is observed (inset of figure 3.8 (a)). This shift is observed for TG2 and TG5 only. For TG7 and TG10 further blue shift is not observed. Figure 3.8 (b) shows full width at half maxima (FWHM) of the first E_g mode increased with increasing Ga concentration. This blue shift and increase of FWHM may happen due to increased strain, a decrease of particle size or phonon confinement [165]. Hence, it is expected that due to Ga doping strain may increase and particle size should decrease. Any vibrational modes related to rutile TiO_2 are absent at this temperature (450 °C). Hence, all samples are in pure tetragonal anatase phase (space group: $I4_1/amd$) of TiO_2.

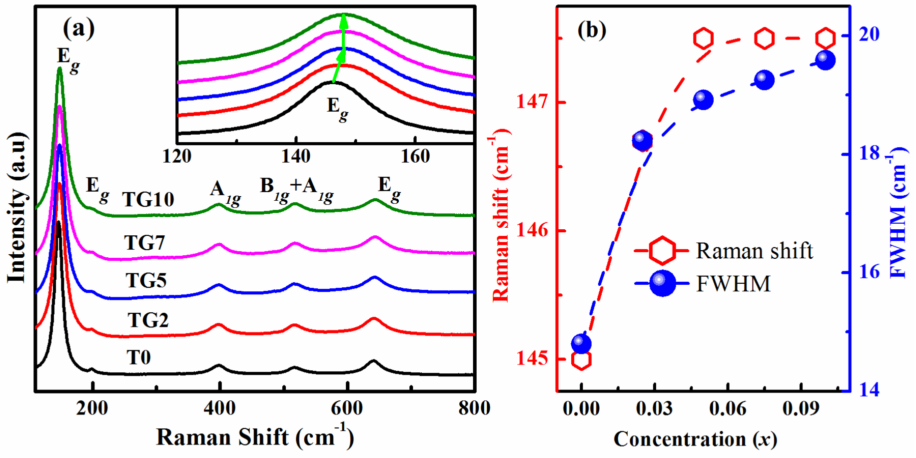

Figure 3.8: (a) Raman spectrums of Ga doped TiO_2 samples prepared at 450 °C. (a) Inset shows the blue shifting of the first E_g mode of corresponding spectrums. (b) Change in Raman shift and FWHM of the first E_g mode with Ga concentration.

When samples are further heated at a higher temperature, phase transformation (A→R) takes place and vibrational modes corresponding to rutile phase appear (figure 3.10). For T0, traces of rutile phase are observed at ~500 °C. For Ga doped samples, the appearance of the rutile phase is delayed. The transition starts at higher temperatures (or onset temperature delayed) with increasing Ga content (TG2 ~ 500-600 °C, TG5 and TG7 ~600-650 °C, and TG10 ~ 650-700 °C). Phonon modes of T0, heated at 700 °C, matches entirely with phonon modes of crystalline tetragonal rutile TiO_2 ((143 (B_{2g}), 244 (M), 441(E_g) and 609 (A_{1g}) cm^{-1})). This is consistent with the XRD results. However, traces of anatase phase remain in Ga doped samples heated at the same temperature (700 °C). Hence, all samples are further heated at higher temperatures for complete conversion into rutile phase. At 800 °C, all samples are converted into the rutile phase.

There are no considerable shifts in vibrational modes (B_{1g}, M, A_{1g}) position of Ga doped samples compared to pure TiO_2 in rutile phase, except E_g mode. E_g shows nominal blue shifting with increasing Ga content (figure 3.9). Parker *et al.* [166] showed that blue shifting of E_g mode happened when the oxygen content in TiO_2 lattice increases.

Hence, this blue shifting hint that oxygen content may increase due to Ga incorporation.

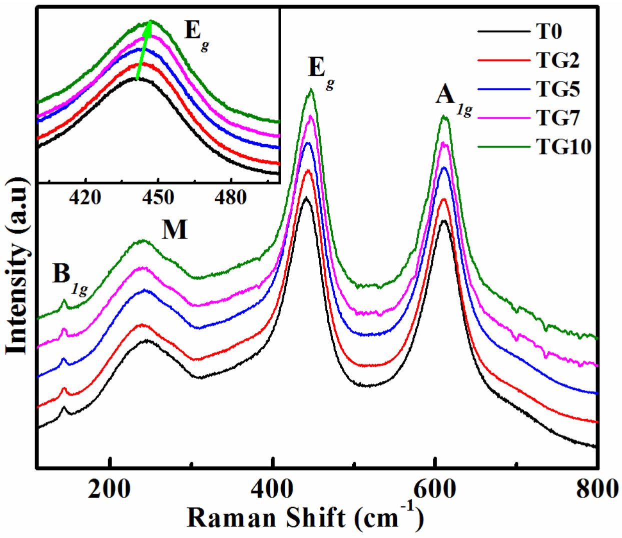

Figure 3.9: RT Raman spectrums of Ga doped TiO_2 samples prepared at 800 °C. Inset shows the blue shifting of E_g mode of corresponding spectrums.

In between 450-800 °C, samples show a mixed (A and R) phases. For 532 nm laser wavelength, B_{1g} (396 cm^{-1}) of anatase and E_{1g} (446 cm^{-1}) of rutile are very sensitive[36]. Thus, the area of B_{1g} (A_A) and E_{1g} (A_R) modes are used to calculate weight ratio of anatase and rutile phases ~ W_A/W_R [167]. The rutile phase fraction, f_R, calculated from Raman spectra is consistent with XRD results (figure 3.10. (f)).

Activation energy, E_A is calculated using the aforementioned Arrhenius equation from Raman spectra. It is observed that E_A increases with Ga incorporation and follows a similar trend as observed from XRD analysis (figure 3.11). These results also indicate that Ga doping inhibits phase transition (A→R).

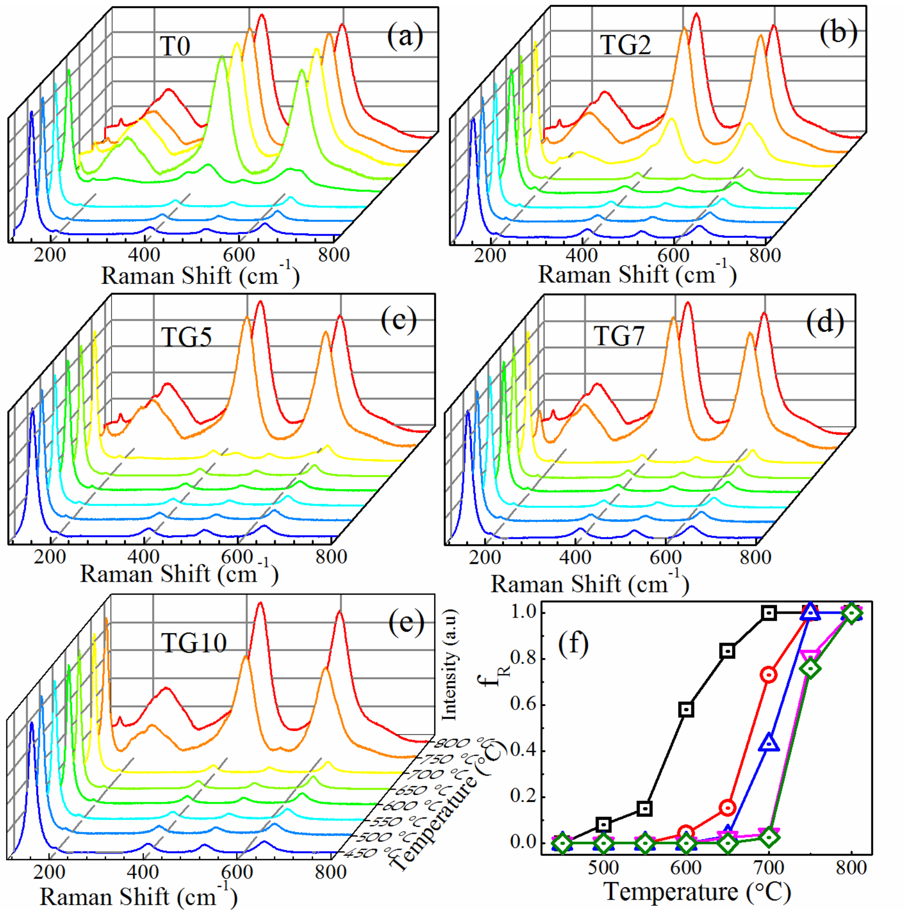

Figure 3.10: Raman spectra in the range ~100-800 cm^{-1} of all the samples at temperature range 450-800 °C showing A→R phase transition ((a) T0, (b) TG2, (c) TG5, (d) TG7 and (e) TG10). (f) Delayed rutile phase transition in Ga-doped samples is confirmed from rutile phase fraction with temperature.

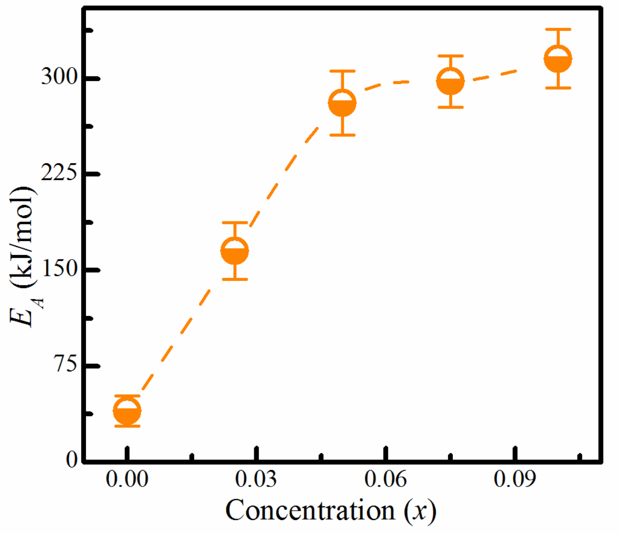

Figure 3.11: Change in activation energy with Ga concentration from the Raman spectrum.

3.3.4 XPS analysis

High-resolution XPS is used to identify chemical states, oxygen vacancies and interstitials in the samples. Figure 3.12 shows fitting of XPS spectra for Ti 2p, O 1s, and Ga 3d of T0, TG5, and TG10 samples.

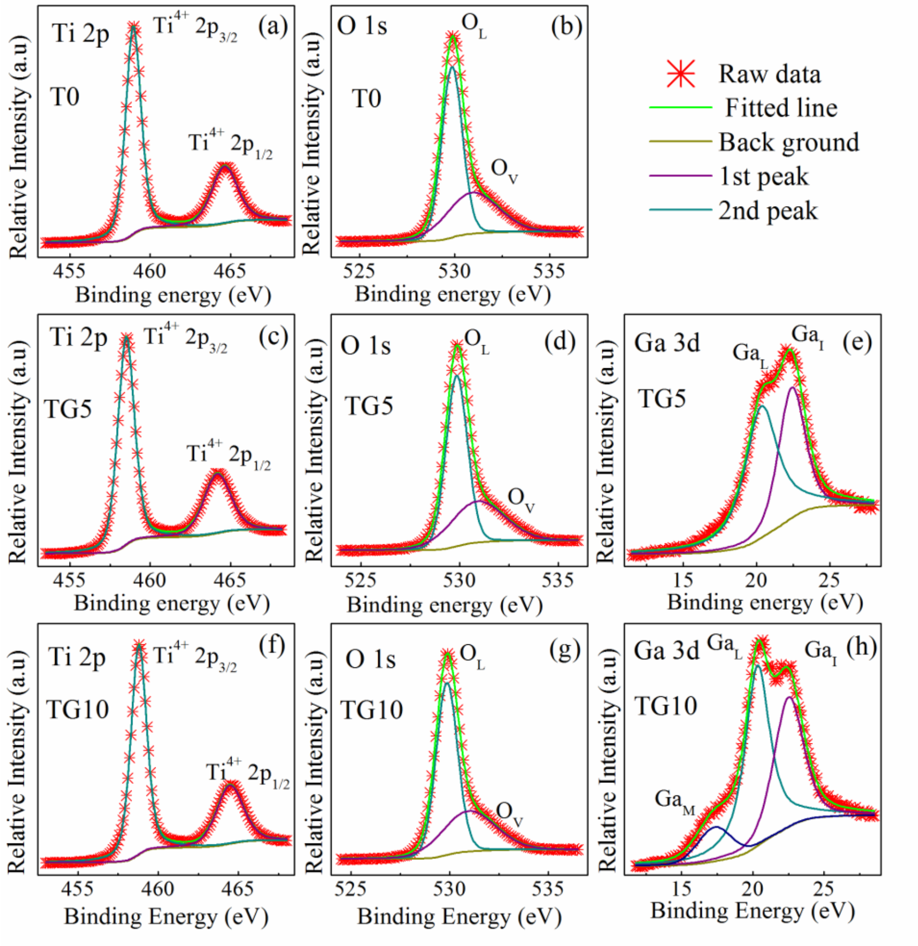

Figure 3.12: XPS spectra of anatase phase (450 °C) samples: (a-b) T0, (c-e) TG5 and (f-h) TG10.

Deconvolution of Ti 2p of T0 yields two peaks at binding energy ~458.9 eV (Ti $2p_{3/2}$) and 464.6 eV (Ti $2p_{1/2}$), with a spin-orbit splitting of 5.7 eV, where Ti is in 4+ valence state [168, 169]. It also shows that there is no evidence of any Ti^{3+} species. Similar behavior is observed in case of TG5 (i.e. deconvolution of Ti 2p yields two peaks at binding energy ~ 458.5 eV ($2p_{3/2}$) and ~ 464.2 eV ($2p_{1/2}$), with a spin-orbit splitting 5.7 eV) with a minute difference in FWHM of Ti $2p_{1/2}$ compared to that of T0. For T0, FWHM of Ti $2p_{1/2}$ is ~1.13 eV and for

TG5 it is ~1.20 eV (provided in Table 3.1). This increment in FWHM implies the presence of less-oxidized metal ions in TG5 sample (or existence of very small amount of Ti^{3+} species). For TG10, deconvolution of Ti 2p (figure 3.12 (f)) shows similar splitting (~458.8 eV (Ti $2p_{3/2}$) and 464.5 eV (Ti $2p_{1/2}$)) as observed in T0 with unchanged spin-orbital splitting of 5.7 eV. FWHM decreases from 1.20 eV (TG5) to 1.15 eV (TG10) which signifies the presence of Ti^{3+} species decreases. Note that the FWHM of TG10 though lower than TG5, but it is higher than that of T0. Hence Ti^{3+} species is lesser in TG10 than TG5.

Table. 3.1: XPS fitting results of T0, TG5, and TG10 samples.

Sample	Orbital	Bonds	Binding Energy (eV)	FWHM (eV)	Area (%)
T0	Ti $2p_{1/2}$	Ti-O	464.62	1.13	67.94
	Ti $2p_{3/2}$		458.94	1.94	32.06
	O 1s	Ti-O (O_L)	529.86	1.28	62.13
	O 1s	Ti-O (O_V)	530.93	3.24	37.87
TG5	Ti $2p_{1/2}$	Ti-O	464.18	1.20	67.79
	Ti $2p_{3/2}$		458.50	1.98	32.21
	O 1s	Ti-O (O_L)	529.86	1.28	62.16
	O 1s	Ti-O (O_V)	530.92	3.23	37.84
	Ga 3d	Ga-O (Ga_L)	20.33	2.72	59.98
	Ga 3d	Ga-Ti, Ga-O (Ga_I)	22.4	2.13	40.02
TG10	Ti $2p_{1/2}$	Ti-O	464.46	1.15	67.50
	Ti $2p_{3/2}$	Ti-O	458.79	1.98	32.05
	O 1s	Ti-O (O_L)	529.86	1.28	62.95
	O 1s	Ti-O (O_V)	530.97	3.21	37.05
	Ga 3d	Ga-O (Ga_L)	20.32	2.09	51.89
	Ga 3d	Ga-Ti, Ga-O (Ga_I)	22.51	2.45	37.75
	Ga 3d	Ga-Ga (Ga_M)	17.32	2.84	10.36

Deconvolution of Ga 3d spectrum (TG5) yields two peaks at binding energy 20.3 eV and 22.4 eV (figure 3.12 (e)). A similar lower binding energy peak at ~20.3 eV was reported by Luo et al. [170] in Ga doped TiO_2. This was discussed in terms of substitution of Ti^{4+} ions by Ga^{3+} ions (Ga_L). The higher binding energy peak at 22.4 eV was interpreted by Banerjee et al. [153] as Ga interstitial sites (Ga_I) in TiO_2 [153]. Hence, from the presence of both peaks in Ga 3d spectrum of TG5, it is confirmed that Ga occupies both substitutional and interstitial sites of TiO_2. Similar peaks corresponding to Ga_L and Ga_I are observed for TG10 at 20.3 eV and 22.5 eV (figure 3.12 (h)). However, for TG10, the relative intensities, as well as areas of Ga_L to Ga_I, changed when compared to TG5 (Table 3.1). It is clear that contribution of Ga_L is dominant in TG10 than TG5. Hence, number of interstitials sites is more compared to substitutional sites for lower doping ($x \leq 0.05$) while for higher doping ($x \geq 0.05$), number of substitutional sites is more compared to interstitials. However, in TG10 a small peak at 17.3 eV is also present. According to literature, this peak arises from metallic Ga (Ga_M) present in the samples [171]. From area calculations, it is found that this peak contributes to about 10% of the entire Ga content. Hence, it is worth mentioning that a small fraction of Ga might have gone out from lattice structure but yet the net amount of Ga in the TiO_2 lattice is more than TG5.

Deconvolutions of O 1s feature displays two types of oxygen. A lower binding energy peak at ~529.9 eV (for T0, TG5, and TG10) corresponds to regular lattice oxygen (O_L) [172]. The higher binding energy peak at ~530.9 eV (for T0, TG5, and TG10) is due to oxygen vacancies (O_V) present in the sample [173, 174]. Concentration of O_L and O_V present in the samples are calculated by the area of corresponding peaks (concentration of O_L and O_V are shown in Table 3.1). It is observed that oxygen vacancies are almost same for T0 and TG5 while TG10 shows a considerable decrease (T0:37.87%, TG5:37.84% and TG10:37.05%). This implies that oxygen vacancies decrease at higher Ga doping. From Ga 3d spectrum, it is observed that Ga^{3+} ions occupy both substitutional and interstitial sites. Hence, due to interstitial Ga^{3+} ions, a net amount of positive charge increases in the lattice. To balance this positive charge, oxygen content increases in the lattice which slightly reduce the oxygen vacancies in the lattice. Although the proportion of substitution increases for higher doping, the amount of interstitials still increases as the amount of doping concentration increases. Hence, a decrease in the number of oxygen vacancies observed from O 1s spectra is due to this interstitials.

Hence, for lower doping ($x \leq 0.05$), a considerable increment in lattice constants are due to bigger radius of substitutional Ga^{3+} ions in the lattice. However, at higher doping ($x \geq 0.05$), Ga^{3+} ions occupied more substitutional sites and some amount of Ga ions move out from the lattice structure which compensates the effect of interstitials and oxygen vacancies thereby lattice expansion retarded and phase transition showing saturated behavior.

3.3.5 Grain growth and morphological analysis

Particles size of rutile phase is larger than anatase phase samples. For anatase phase (450 °C) crystallite size is estimated from broadening of (101) peak, using Scherrer equation and verified using HRTEM images. Particles size of rutile TG samples (800 °C) is larger than 100 nm. Hence, particles size of in rutile phase is estimated from FESEM micrographs.

From TEM images (figure 3.13 (a and b)), it is observed that both the particles are irregular spherical in shape and size decreases from ~14 nm (T0) to ~7 nm (TG5) due to Ga incorporation. d-spacing of HRTEM images (figure 3.13 (c and d)) corresponds to T0 (d_{101}~0.35 nm and d_{200}~0.19 nm) and TG5 (d_{101}~0.35 nm and d_{301}~0.24 nm) show both the particle are in pure anatase phase. There is no reflection related to rutile particles. SAED patterns also reveal anatase phase of T0 and TG5 samples (figure 3.13 (e and f)). Clarity of the rings ensures good crystalline nature of the samples. Crystallites size of the nanoparticle is calculated from 101 peak broadening of XRD data using Scherrer equation:

$$D = \frac{k\lambda}{\beta cos\theta} \qquad \text{(Eq. 3.3)}$$

where D is the crystallites size, k is a dimensionless shape factor and its value is ~0.9, β is the FWHM of 101 peaks after removing instrumental broadening and θ is Bragg angle.

Crystallite sizes reduce from 16.5 nm (T0) to 6.6 nm (TG10) (figure 3.13 (f)) due to Ga incorporation which is consistent with TEM results.

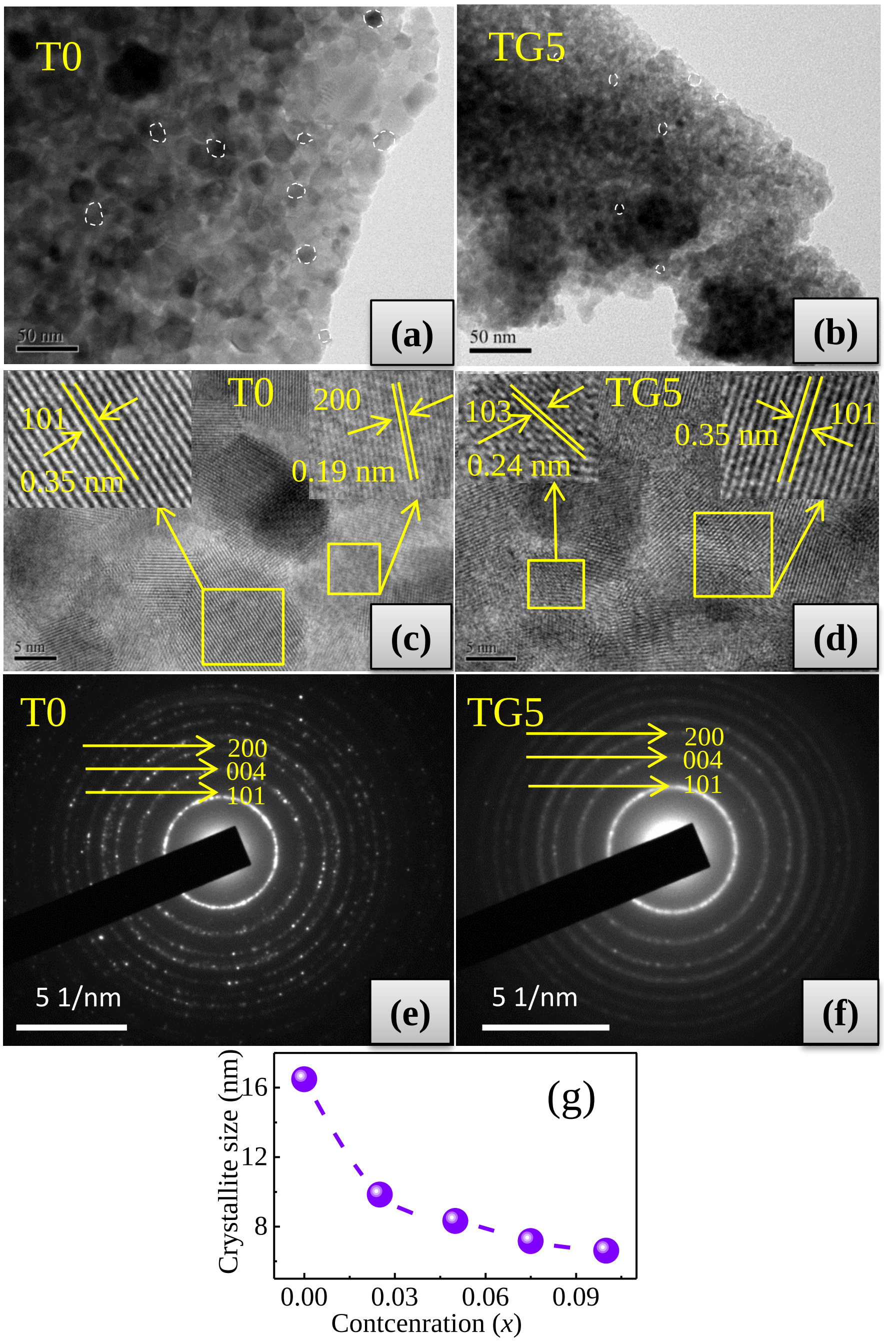

Figure 3.13: TEM images of T0 (a) and TG5 (b) nanoparticles in pure anatase phase (450 ^{o}C). (c) and (d) shows the HRTEM images of corresponding samples. (e) and (f) show SAED pattern of T0 and TG5 samples. (g) Variation of crystallite size calculated from Scherrer equation with Ga doping.

Synthesis of these nanoparticles (~13.4-6 nm) is possible due to the choice of ethylene glycol, citric acid and pre-calcination heating temperature (100 °C). The choice of such a combination ensures the formation of crystalline nanoparticles upon calcination at a low temperature ~450 °C. Doping hinders grain growth in anatase phase due to increasing strain imposed by the foreign element doping into TiO_2 lattice [68, 147, 175].

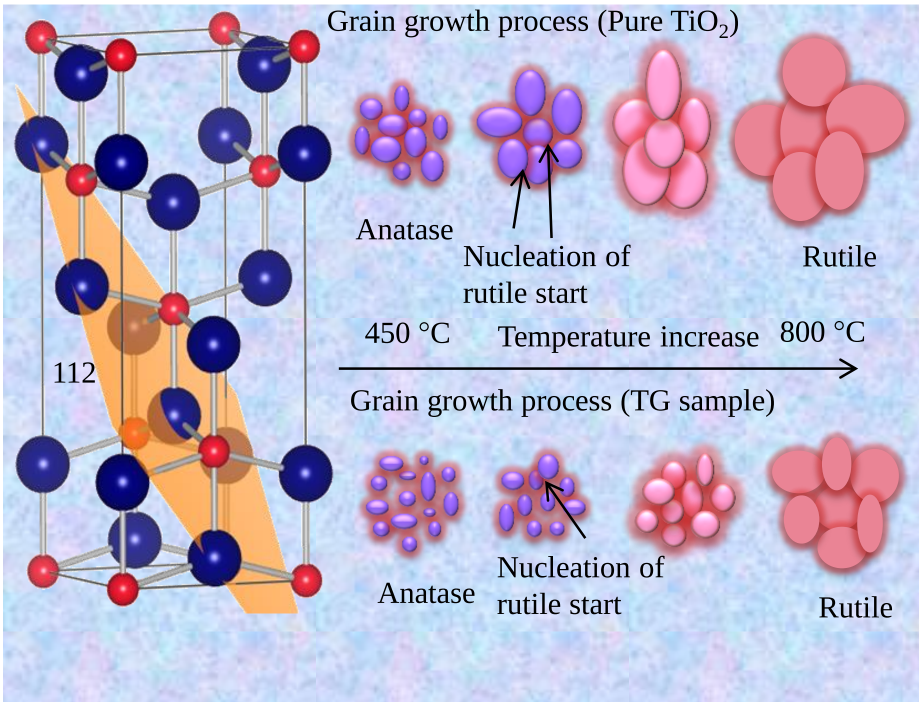

Figure 3.14: Twin boundary (112) of anatase phase where nucleation of rutile phase first starts (Left). Schematic diagram of the grain growth process of pure and Ga doped samples with temperature (Right). Grain growth process of pure TiO_2 (Top) and restrain grain growth process due to Ga doping (Bottom).

It was reported that rutile phase starts to nucleate at (112) twin boundaries of anatase phase (figure 3.14). This involves displacement of one-half of titanium ions within the twin slab [176]. Proportions of rutile phase increase during A→R phase transformation. In addition to nucleation at twin boundaries, rutile phase nucleation starts easily at interfaces of agglomerated anatase particles as compared to outer surfaces [177]. Such interfaces help to decrease activation barrier for nucleation of rutile particle [178]. Figure 3.14 shows the schematic diagram of grain growth process of pure TiO_2 and Ga doped (TG) samples.

FESEM images of T0, TG2, TG5, TG7, and TG10 in a complete rutile phase (800 °C) are presented in figure 3.15. It is observed that particle sizes reduce with Ga doping. An increment in activation energy may be responsible for slow nucleation process (restraining grain growth process) of rutile particles. Both crystallites size (in case of A) and particles size (in case of R) are restrained by incorporation of Ga. This restrained grain growth process not only affects surface properties but also optoelectronic properties.

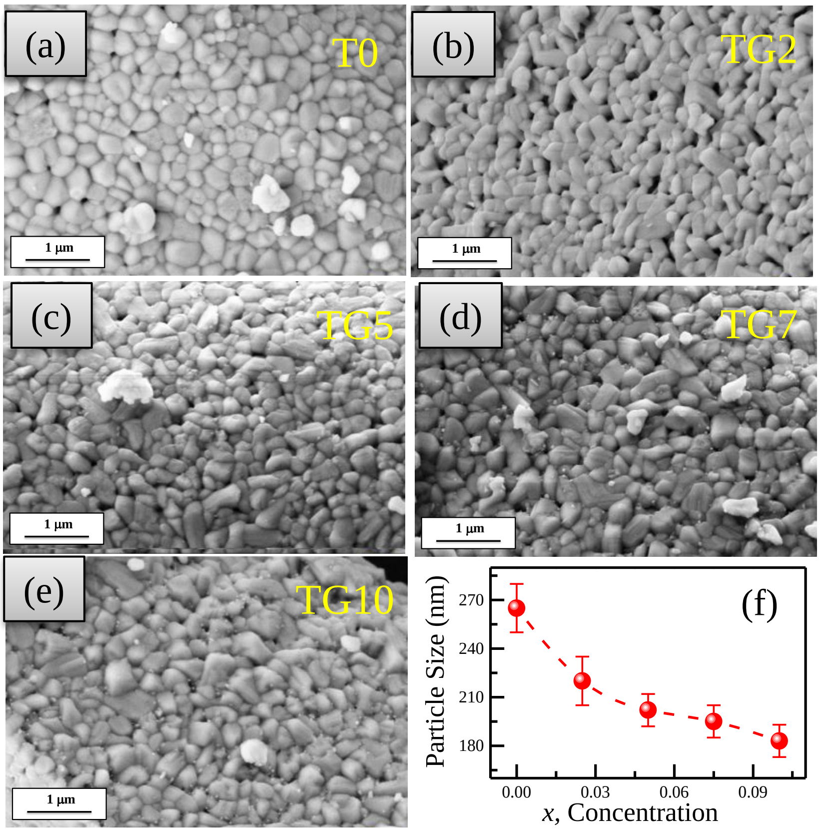

Figure 3.15: FESEM images (a-e) of the samples prepared at 800 °C and (f) variation of particles size with doping concentration.

Elemental composition (Ga, Ti, and O) of rutile TG5 sample is estimated using energy dispersive X-ray (EDX) analysis mounted on FESEM. Proportion of constituent elements is close to the intended values of compositions (listed in the table, inset of figure 3.16 (b)).

Elemental scans reveal homogeneous distribution of Ti, Ga, and O in the sample (figure 3.16 (c, d, and e)). A homogeneous distribution is a result of the synthesis route using a sol-gel process. This process enables uniform mixing of all elements (Ga, Ti, and O) at the molecular level.

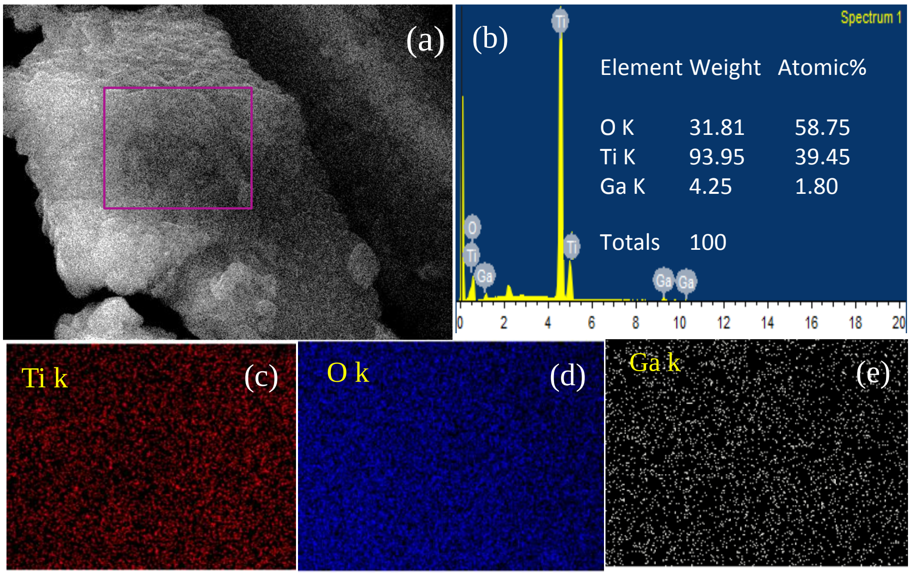

Element	Weight	Atomic%
O K	31.81	58.75
Ti K	93.95	39.45
Ga K	4.25	1.80
Totals	100	

Figure 3.16: Elemental analysis of TG5 sample prepared at 800 °C; where (a) SEM image, (b) elemental composition in weight and atomic ratio from EDX spectrum, and elemental mapping of Ti K (c), O K (d) and Ga K (e) showing a uniform distribution of elements.

3.3.6 Optical properties

Optical properties of TiO_2 are affected by Ga doping. Room temperature DRS measurements are carried out on anatase (450 °C) and rutile (800 °C) samples. The scattered light is collected excluding normally reflected light in a DRS measurement. This satisfies the applicability of Kubelka-Munk function given by:

$$F(R) = \frac{(1-R)^2}{2R} \text{ .... (Eq. 3.4)}$$

where R is reflectance.

Bandgap (E_G) is calculated using Tauc plot:

$$F(R)h\upsilon = A(h\upsilon - E_G)^n \text{ .... (Eq. 3.5)}$$

where, *h* is Planck's constant, ν is the frequency of illumination and *n* is a unitless parameter. The *n*-parameter depends on the type of bandgap: $n = 1/2$, specific for direct bandgap while $n = 2$ for an indirect bandgap.

Anatase TiO_2 is an indirect bandgap semiconductor while rutile TiO_2 is a direct bandgap semiconductor [35]. Hence, bandgap anatase and rutile samples are calculated using $n = 2$ (A) and 1/2 (R).

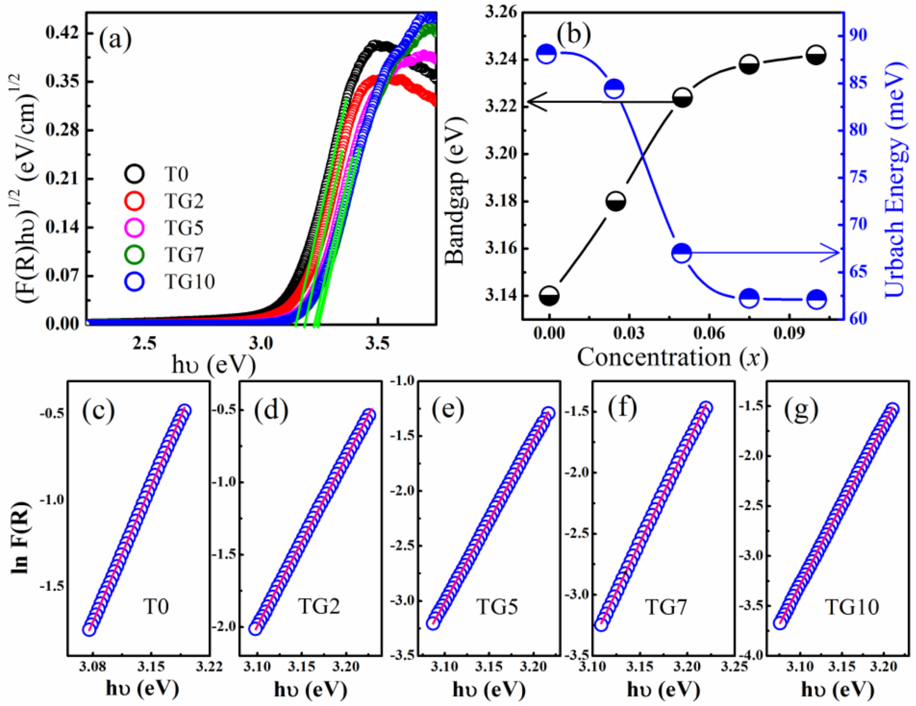

Figure 3.17: (a) DRS spectrum of samples prepared at 450 °C, (b) variation of bandgap and Urbach energy with Ga concentration. (c, d, e, f, and g) shows linear fits of lnF(R) vs *hυ* plot (blue circles are original data points and pink lines are linear fits to data points).

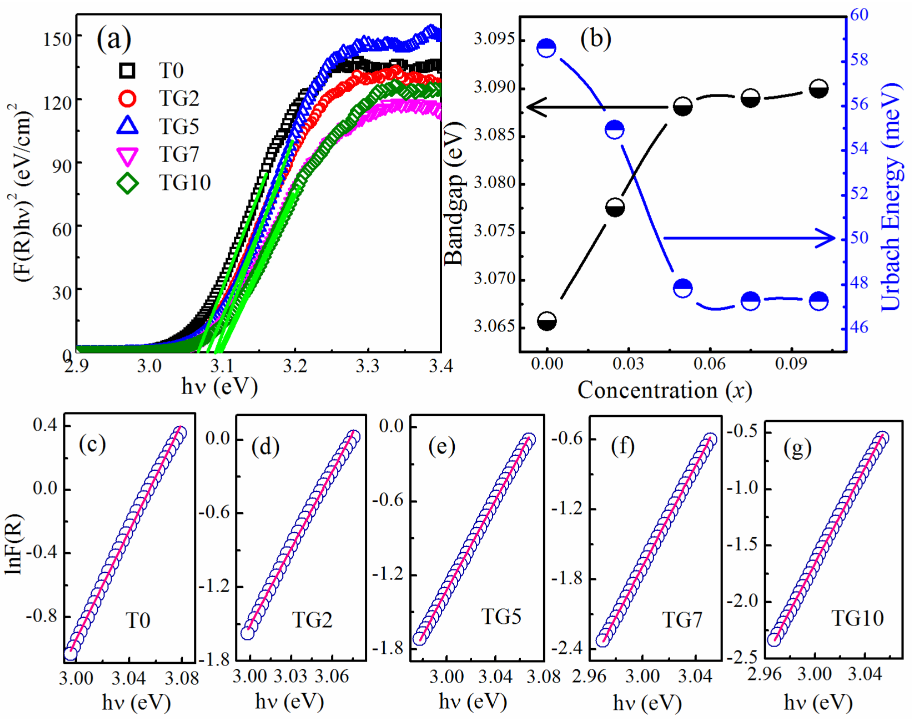

Figure 3.18: (a) DRS spectrum of all samples prepared at 800 °C, (b) variation of bandgap and Urbach energy with Ga concentration. (c, d, e, f, and g) shows linear fits of lnF(R*)* vs *hν* plot (blue circles are original data points and pink lines are linear fits to data points).

Bandgap shows a blue shift with increasing Ga content (figure 3.17 (a) and 3.18 (a)). A considerable increment in bandgap from 3.14 eV for T0 to 3.23 eV for TG5 (in case of rutile from 3.06 eV for T0 to 3.08 eV for TG5) is observed for lower Ga doping ($x \leq 0.05$). Whereas, at higher doping $x > 0.05$ (TG7 and TG10), increments in bandgap are nominal for both the phases.

In TiO_2, O 2p and Ti 3d hybridization (p-d) form strong bonding states which are responsible to form valence band (VB) [35]. On the other hand, antibonding state due to p-d hybridization between O 2p and Ti 3d forms conduction band (CB). Due to Ga doping, the hybridization between O 2p and Ga 4p gives contribution in valence band [151, 170] which results in increasing of the bandgap of TiO_2 in Ga doped samples.

Enhancement in bandgap follows similar trends of lattice expansion. This is because electronic band structure is strongly correlated with lattice structure.

In previous reports, the effect of Ga doping on the bandgap of TiO_2 was unclear and ambiguous (Table 3.2). The reason behind this unsystematic behavior of bandgap is not clear.

Table 3.2: List of reports available on Ga doped TiO_2.

Authors	Bandgap of pure TiO_2 (eV)	Ga doped TiO_2 Bandgap (eV)	Bandgap change	Reference
Deng *et al.*	2.71	2.41 (0.5 % Ga)	Decrease	[149]
Zhou et at.	3.15	3.10 (1% Ga)	Decrease	[150]
Gionco *et al.*	3.8	4.2 (3 % Ga)	Increase	[151]
Chandiran *et al.*	3.22	3.19-3.25 (0.5-2% Ga)	Unsystematic	[179]
Banerjee *et al.*	3.32	3.32 (1% Ga)	No change	[153]
Sudou *et al.*	3.29	3.35 (10% Ga) 3.31 (20% Ga) 3.36 (50% Ga)	Unsystematic	[152]
Whang *et al.*	3.1	5% Ga	Decrease	[175]

Urbach energy (E_U) is a measure of disorder present in lattice which also affects electronic band structure [180, 181]. Due to lattice distortion localized states are formed just below the absorption edge. These localized defect states affect the bandgap [182]. E_U is calculated from linear fits of "ln*F(R)* vs *hv*" plots just below the absorption edge of DRS data (figure 3.17 (c-g) for anatase and 3.18 (c-g) for rutile). Reciprocal of the slope gives E_U. It is observed that E_U decreases from

108 meV (T0) to 75 meV (TG10) with increasing Ga incorporation for anatase phase, in case of rutile it decreases from 58.59 meV (T0) to 47.25 meV (TG10)). In most semiconductors, it is observed that reduction of E_U is related to an increase in optical bandgap [183, 184]. In the present study, reduction of E_U can be attributed to regularization of lattice. Interstitials (Ga^{3+}), substitution and oxygen vacancies help for such regularization. As a result, width of localized states near band edge (band tail) decreases and bandgap increases.

3.4 Summary

In summary, following major observations are listed from this work:

1. Samples are in a pure phase of TiO_2 (from XRD).
2. Annealing in the temperature range 450-800 °C reveals Ga doping inhibits onset temperature and (A$\rightarrow$R) phase transition.
3. Raman spectra ensure the same results.
4. Activation energy of phase transition, calculated both from XRD and Raman studies, increases with increasing Ga concentration.
5. Considerable lattice expansion is observed for $x \leq 0.05$ from Rietveld refinement of XRD data of both phases. For $x > 0.05$ saturation like behavior is observed.
6. Ga^{3+} interstitials and substitution (Ti^{4+} by Ga^{3+}) and oxygen vacancies are observed from XPS spectroscopy.
7. Due to Ga^{3+} interstitials and bigger ionic radius of Ga, lattice expands and delays phase transition.
8. XRD, FESEM and HRTEM studies show Ga incorporation hinders the grain growth process for both the phases. Hence, the crystallite and particles size decreases.
9. Bandgap increases from 3.14 eV (T0) to 3.24 eV (TG10) in anatase phase. In the rutile phase, it increases from 3.06 eV (T0) to 3.09 eV (TG10)).
10. Urbach energy decreases in anatase phase from 108 meV (T0) to 75 meV (TG10). In case of rutile, it decreases from 58.59 eV

(T0) to 47.25 meV (TG10).

Hence, reduction of particle size makes this material important for photocatalytic applications due to its enhanced surface area. However, due to the large bandgap, the material is applicable for high energy light ~UV, only. As only 5% of solar spectrum is UV light, whereas 45 % is visible light, such materials need modifications. Usage of visible light is more beneficial. To overcome from this problem, our 4th chapter is planned accordingly.

Chapter 4

Effect of V doping on structural phase transition, grain growth and optical properties of TiO_2

4.1 Overview

In chapter 2, slightly bigger and less charged Ga^{3+} doping in TiO_2 was discussed. Ga-doping stabilized the anatase phase and increased the bandgap of TiO_2. Thus, Ga-doped materials can only absorb UV light. Therefore, only 5% of the solar spectrum may be absorbed by such materials. Hence, a major portion of the solar spectrum belonging to visible light ~45% cannot be used by Ga-doped TiO_2. This is a great disadvantage towards applicability of the materials.

Vanadium is an important element in tailoring bandgap of TiO_2. Effect of smaller and higher charged V^{5+} doping on structural phase transition (from XRD and Raman spectra), grain growth (from HRTEM and FESEM) and optical properties (from DRS) of TiO_2 has been investigated in this chapter. Results presented in this chapter are published in peer-reviewed journals[\$].

[\$] *N. Khatun et al. Mater. Sci. Semicon. Proc. 50, (2016) 7-13.*

[\$] *N. Khatun et al. Ceram. Int. 43(16), (2017) 14128-14134.*

4.2 **Experimental**

Structural characterization are done using Bruker D2 phaser diffractometer. XANES spectra of Ti and V K-edge are recorded at scanning EXAFS beamline (BL-9) Indus-2, RRCAT Indore, India. Raman spectroscopic measurements are carried out by HORIBA Jobin Yvon LabRAM HR using a laser of wavelength 488 nm. Morphological investigation is studied by FESEM (Carl Zeiss FESEM Supra–55) and TEM (Philips CM12 TEM). DRS measurement is carried out by Bentham TMc300 Monochromator.

4.3 Results and Discussion

4.3.1 Structural analysis

XRD patterns of pure and V doped TiO_2 samples heated at 450 °C (figure 4.1) matches well with JCPDS card #78-2486 and COD ID-1010942, which confirms tetragonal anatase phase of TiO_2 (space group $I4_1/amd$) for all the samples with no secondary phase. Also, there is no evidence of any peaks corresponding to the rutile phase.

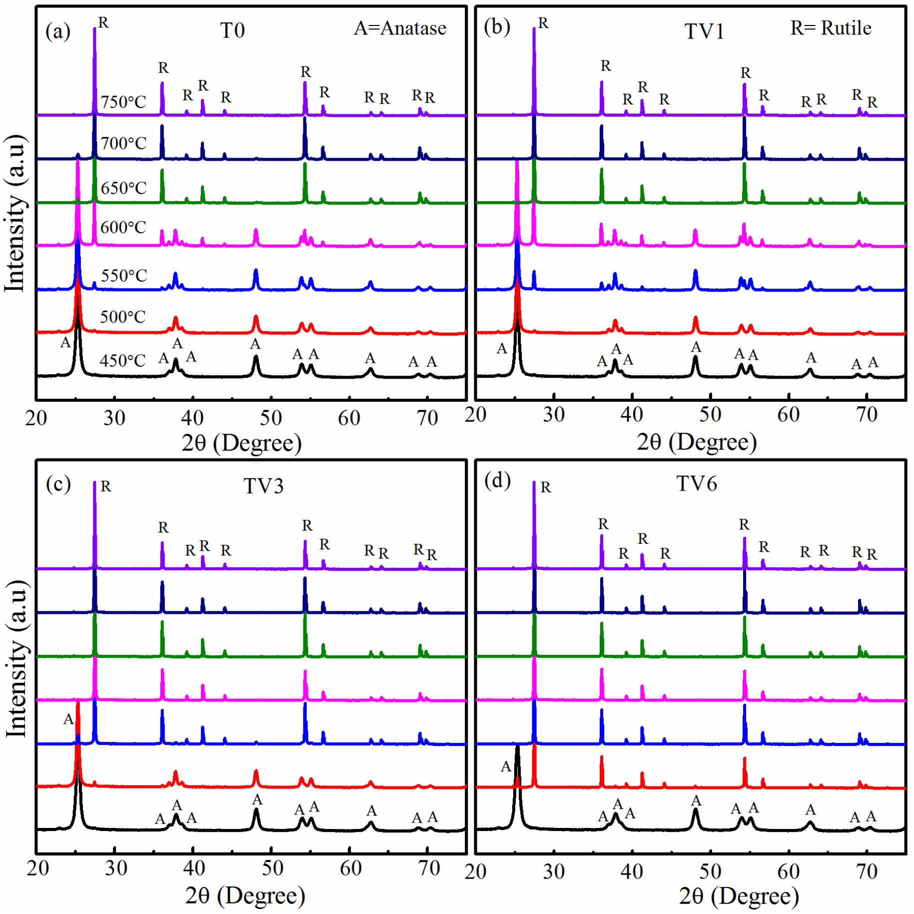

Figure 4.1: XRD patterns of V doped TiO_2 samples heated at seven different temperatures (450-750 °C).

With further heating at higher temperatures, the structure gradually changes from anatase to rutile phase. Samples prepared at 750 °C are in rutile phase and XRD pattern matches well with COD ID- 9009083 (rutile, space group - $P4_2/mnm$). There is no remnant anatase phase in the samples prepared at this temperature. At rutile phase, TV9 sample shows a small sign of impurity phase. This is because at higher temperature due to thermal instability and less space of rutile phase, some amount of V ions comes out from the lattice and forms this impurity phase. For that reason, TV9 sample is not used to see phase transition behavior. A mixed phase of anatase and rutile are observed for other samples heated at an intermediate temperature between 450-750 °C. Small rutile peaks appear after heating at 500 °C for T0 and TV1 samples. TV3 and TV6 samples heated at 500 °C introduce a clear visible rutile phase (figure 4.1). Complete conversion into rutile phase happens at 750 °C, 700 °C, 650 °C and 550 °C for T0, TV1, TV3, and TV6 samples respectively. Hence, V doping promotes the phase transition.

This can be clearly observed from the most intense peaks of anatase (101) reflection at 25.34° and rutile (110) at 27.40° (figure 4.2 (a-d)). A closer view of these two peaks is shown for all temperatures in the regime of 2θ from 24° to 28.5°.

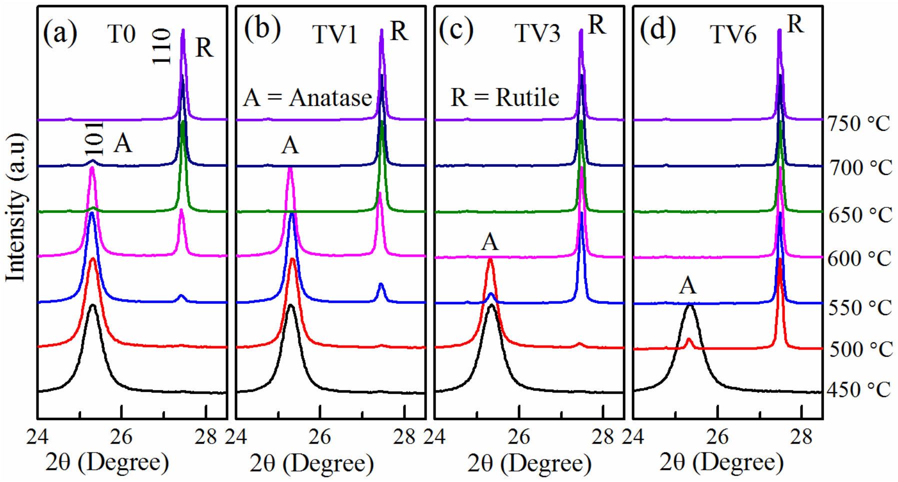

Figure 4.2: ((a-d)) Close view of XRD patterns of all samples in 2θ range from 24° to 28.5°. It shows that phase transition is promoted by V incorporation.

We have estimated the rutile phase component in the mixed phases by calculating rutile fraction % (f_R) using the same Spurr and Mayers equation [159] as discussed in chapter 3.

The gradual phase change (A→R) is observed from the phase diagram. It is a function of calcination temperature and V-content (figure 4.3 (a)). As all processing parameters are invariant, the transformation from metastable anatase to stable rutile phase entirely depends on V content.

Activation energy (E_A) of phase transition (A→R) is calculated by using the same Arrhenius equation as discussed in our previous chapter (chapter-3). It is calculated by the reciprocal of the slope of linear fits of $\ln(f_R)$ vs 1/T. It is observed that E_A decreases drastically with the incorporation of V up to TV3. However, for TV6 the rate of decrement of E_A retarded and shows a nearly saturated behavior (figure 4.3 (b)). Activation energy varies from 129 kJ/mol to 7.6 kJ/mol for pure TiO_2 to TV6. Hence, acceleration of transition (A→R) and associated huge change in activation energy hint at a decrease of lattice constants (also unit cell volume) with V incorporation.

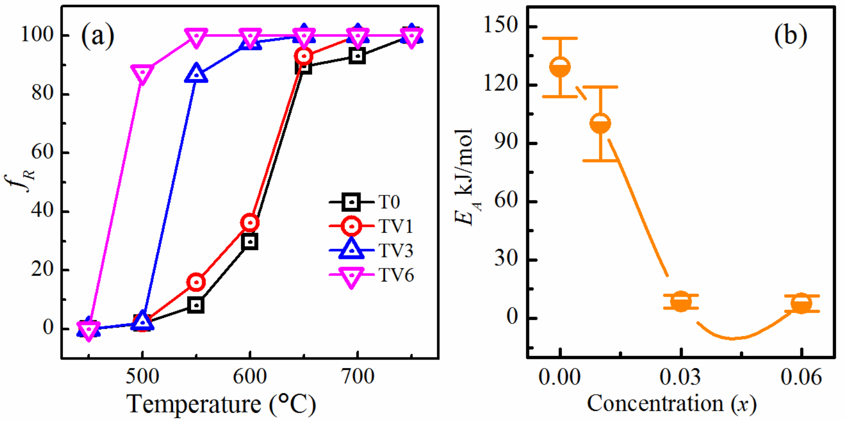

Figure 4.3: (a) Fraction of rutile phase with temperature for all V-doped samples showing promotion of phase transition due to V doping. (b) Shows variation of activation energy with V concentration.

Samples in anatase phase, when heated to a higher temperature (≥ 500 °C) leads to rearrangement of Ti-O bonds as a result unit cell volume contracts and phase transformation (A→R) occurs. In anatase phase, lattice constant $a = b$ (3.785 Å) is smaller and c (9.514 Å) is larger compared to lattice constants of rutile phase ($a = b = 4.594$ Å and $c = 2.958$ Å) [27]. Hence, unit cell volume of anatase phase is larger (136.3 Å^3) compared to rutile phase (62.4 Å^3). Therefore, (A→R) phase transition ((A→R)) can be explained in terms of change in lattice constants and unit cell volume.

From literature, it was observed that charge and ionic radius of elements are very sensitive to change the lattice constant and thereby accelerate or delay the A→R phase transition [27]. In general, if unit cell volume of anatase TiO_2 decreases, it promotes the phase transition. On the other hand, if unit cell volume of anatase TiO_2 increases, it delays the phase transition. From XRD data, it is observed that V doping promotes the phase transition. Hence it is expected that lattice constant decreases due to V incorporation in TiO_2.

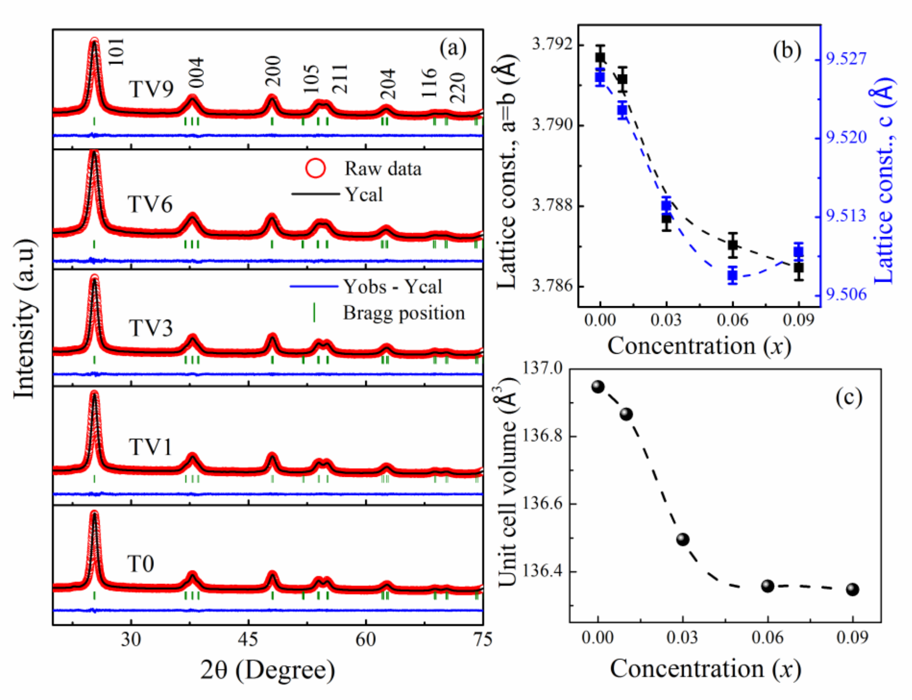

Figure 4.4: (a) Rietveld refinement of V-doped TiO_2 samples heated at 450 °C. (b) Variation of lattice constants and (c) unit cell volume with V concentration.

Rietveld refinement of XRD data in pure anatase phase (450 ^{o}C) reveals that lattice constants a, b and c decrease due to V incorporation (figure 4.4 (b)). Hence, the unit cell volume also decreases with increasing V concentration. As the ionic radius of V^{5+} (VI) (0.68Å) and V^{4+} (VI) (0.72Å) are smaller compared to Ti^{4+} (VI) (0.74Å) while V^{3+} (VI) (0.78Å) is larger, the shrinking of the unit cell volume is indicative of the presence of either V^{5+} or V^{4+} rather than V^{3+}. These decrease of lattice constants and unit cell volume is the reason to accelerate the phase transition.

The decrease of lattice constant hints that V ions occupy the lattice site (replace Ti^{4+} ions by $V^{5+/4+}$ ions) of TiO_2 lattice. It was also observed that the formation energy of anatase TiO_2 is low when V occupies the substitutional sites rather than interstitial sites [185]. Theoretically, it was proved that V occupies substitutional sites in TiO_2 [68, 186, 187] and thereby decreases all the lattice constants. This is because $V^{4+/5+}$ have smaller ionic radius compared to Ti^{4+}.

An observation of increased strain (figure 4.18 (b)) in the lattice is a consequence of lesser dopant ionic radii and therefore lattice contraction.

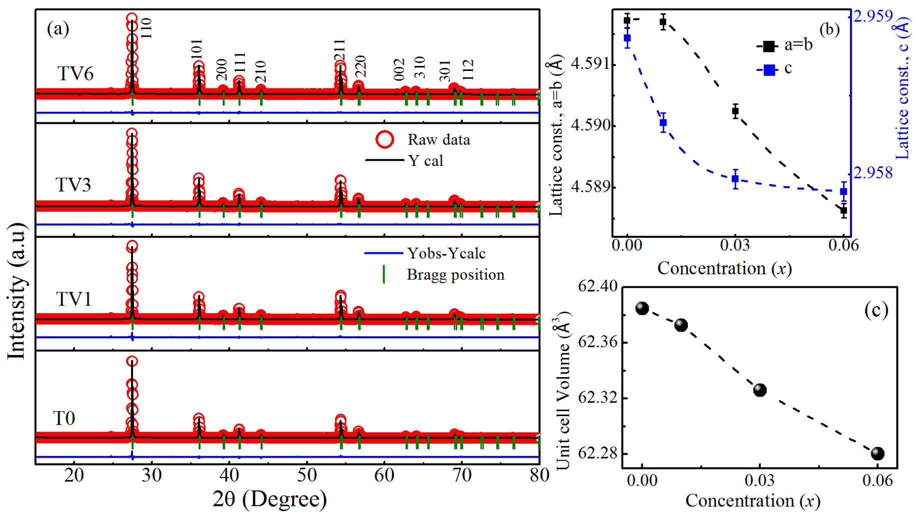

Figure 4.5: (a) Rietveld refinement of V-doped samples heated at 750 °C. (b) Variation of lattice constants with V concentration.

The incorporation of V in TiO_2 not only promotes the phase transformation to rutile phase but also its concentration has an observable effect on rutile structure. A detailed structural study is carried out on the rutile phase by Rietveld refinement on samples heated at 750 °C (figure 4.5 (a)) using Fullprof suit software. From this study, it is observed that the lattice constants decrease with increasing doping concentration (figure 4.5 (b)), as a result of which unit cell volume also decreased. As the ionic radius of V^{5+} and V^{4+} ions are smaller than Ti^{4+} ions such contraction is expected.

It has been observed that metal oxides with lower melting point lower than the melting point of TiO_2 promotes the phase transformation while higher melting point metal oxides inhibit the phase transformation [188]. The melting point of V_2O_5 is around 750 °C which is lower than the melting point of pure TiO_2 (1843 °C). Ionic radius may also have a role as a determining factor in this regard [189]. Both V^{4+}(VI) (0.68Å) and V^{5+}(VI) (0.72Å) have smaller ionic radius than Ti^{4+}(VI) (0.745Å). Both the above reasons may cause a lower onset and A→R temperature due to V incorporation, as we have observed.

4.3.2 Raman spectroscopic studies

Room temperature Raman spectra of samples in pure anatase phase are shown in figure 4.6 (a). Tetragonal anatase TiO_2 (Space group: $I4_1/amd$) have two formula units with 6 atoms per primitive unit cell [190]. According to factor group analysis, the optical phonon modes of anatase TiO_2 at Γ point of the Brillouin Zone can be represented by $\Gamma = A_{1g}\ (R') + 2\ B_{1g}\ (R') + 3\ E_g\ (R') + A_{2u}\ (IR) + B_{2u}\ (IR) + 2\ E_u\ (IR)$, whereas there are six Raman active (R′) (A_{1g}, B_{1g}, and E_g) modes and three Infrared (IR) active modes (A_{2u}, B_{2u}, and E_u) are present [190, 191]. Experimentally, these Raman active modes are found at 144 cm^{-1} (E_g), 197 cm^{-1} (E_g), 399 cm^{-1} (B_{1g}), 513 cm^{-1} (A_{1g}), 519 cm^{-1} (B_{1g}) and 639 cm^{-1} (E_g) for single crystal anatase TiO_2 observed by Ohsaka *et al.* [192].

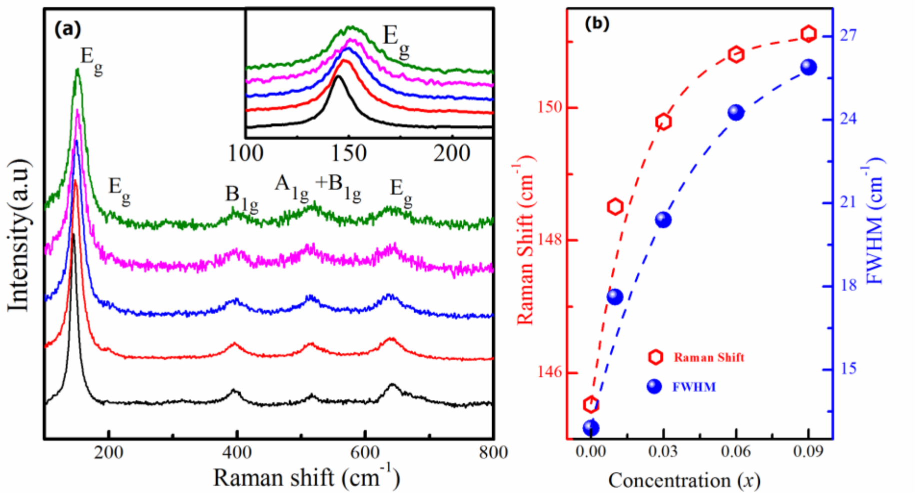

Figure 4.6: (a) Raman spectrums of samples prepared at 450 °C and (b) change in Raman shift and FWHM of first E_g mode with V concentration (dotted lines are to guide the eye).

In our investigation, it is observed that total five peaks are present (three weak peaks at 395 cm^{-1} (B_{1g}), 515 cm^{-1} (A_{1g}+ B_{1g}) and 640 cm^{-1} (E_g) and one small peak at 199 cm^{-1}(E_g) along with the most intense peak at 145 cm^{-1} (E_g)) for all of these sample. The peak positions of the Raman spectrum confirmed that it belongs to tetragonal anatase phase of TiO_2 and these spectral characteristics are similar to the previously reported studies [193, 194]. Fang *et al.* [195] showed that E_g peak comes due to O-Ti-O symmetric stretching vibration in TiO_2, B_{1g} comes due to O-Ti-O symmetric bending vibration and A_{1g} comes due to O-Ti-O anti-symmetric bending vibration.

The comparative observation on the spectrums for pure as well as V-doped TiO_2 shows FWHM of first E_g mode increases and a considerable blue shift from 145.52 cm^{-1} (T0) to 151.12 cm^{-1} (TV9) (figure 4.6 (b)) is observed with increasing Vanadium concentration.

One of the possible reasons for observation of a blue shift is due to lattice contraction (i.e. due to V-doping) can be explained with the help of force constraints and phonon confinement [196, 197]. Here, we need to remind that from XRD results that lattice constants and volume decrease with increasing V concentration. As lattice constants and volume decreases, the interatomic distance decreases leading to an increase in the force constraint which leads an impact to phonon confinement. Another reason for the blue shift can be due to increasing strain in the unit cell and decreased crystallites size [197].

Raman spectra of samples heated at 600 °C are shown in figure 4.7. For lower doped samples (T0 and TV1), vibrational modes have mixed phase of A and R. For higher doped samples (TV3 and TV6), vibrational modes are in pure rutile phase. For clear understanding, Raman spectra of T0 and TV6 are deconvoluted using Lorentzian function (figure 4.8). From these fitting, it is observed that both the samples only have vibrational modes corresponding to anatase and rutile phase, except one peak at 755 cm^{-1} which is the characteristic peak of rutile single crystal. Hence, a similar trend in phase transition with Vanadium doping is observed using Raman spectroscopy similar to XRD studies.

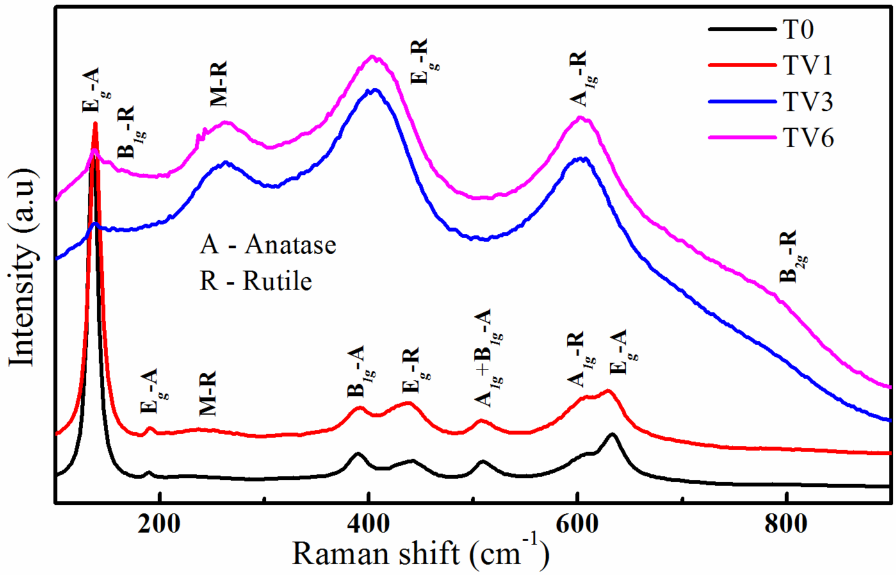

Figure 4.7: Raman spectra of samples heated at 600 °C.

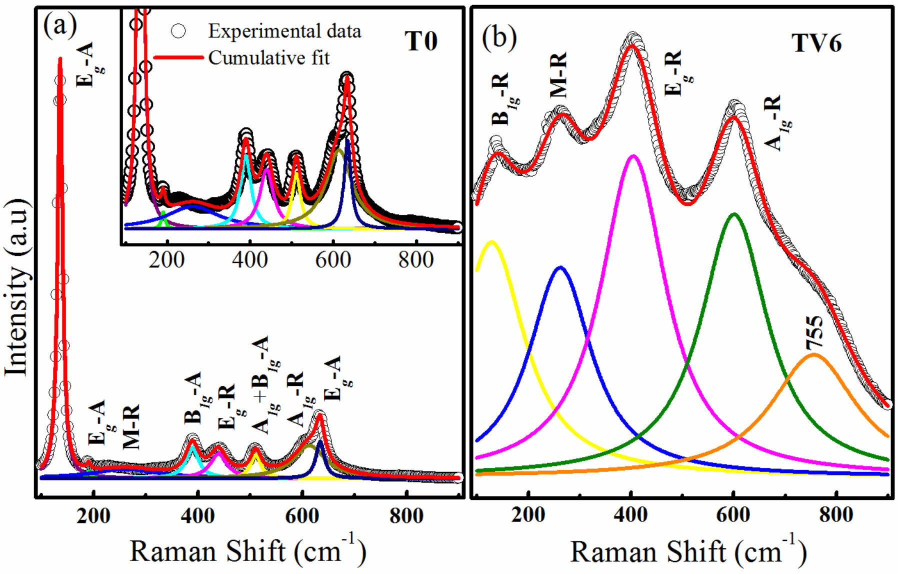

Figure 4.8: (a) and (b) Lorentzian fitting of Raman vibrational modes of samples T0 and TV6 prepared at 600 °C.

Raman spectra of samples heated at 750 °C (figure 4.9) are similar to that of rutile TiO_2 with a tetragonal structure having space groups of $P4_2/mnm$ (D_{4h}^{14}) [16, 198]. Rutile TiO_2 has two formula unit consisting of six atoms per unit cell (two Ti and four O) [26]. From factor group analysis rutile has 15 optical modes (1 A_{1g} + 1 A_{2g} + 1 A_{2u} + 1 B_{1g} + 1 B_{2g} + 2 B_{1u} + 1 E_g + 3 E_u), whereas there are four Raman active modes (A_{1g}, B_{1g}, B_{2g} and E_g) [199]. In rutile TiO_2, along with four Raman active modes one multiphonon mode (M) has been observed which is due to second order effect (SOE). Experimentally these modes are found at 143 (B_{1g}), 447 (E_g), 612 (A_{1g}), 826 (B_{2g}) and 240 (M) cm^{-1} [199, 200]. In this study, for pure TiO_2, we observe two most intense peaks at 444 (E_g) cm^{-1} and 608 (A_{1g}) cm^{-1}, two weak peaks at 145 (B_{1g}) cm^{-1} and 826 (B_{2g}) cm^{-1} along with one multiphonon mode at 23 7(M) cm^{-1}. With increasing V doping concentration these modes become broaden and a clear shifting of M and E_g modes has been observed. Deconvolution of the spectra for pure TiO_2 (figure 4.10 (a)) is performed by the Lorentzian fitting which reveals eight individual peaks: five rutile modes as discussed above and three extra peaks. These three peaks are observed at 201 cm^{-1}, 380 cm^{-1} and 692 cm^{-1}.

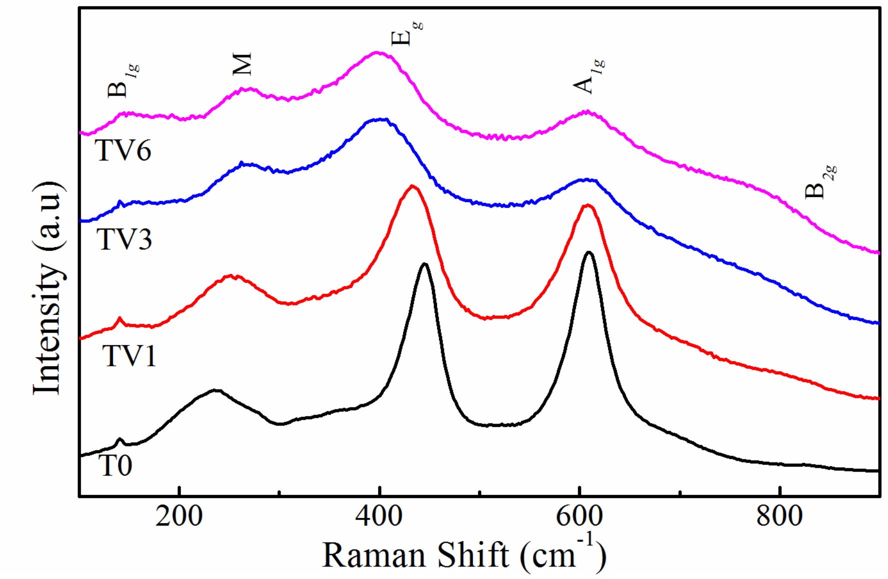

Figure 4.9: Raman spectra of samples heated at 750 °C.

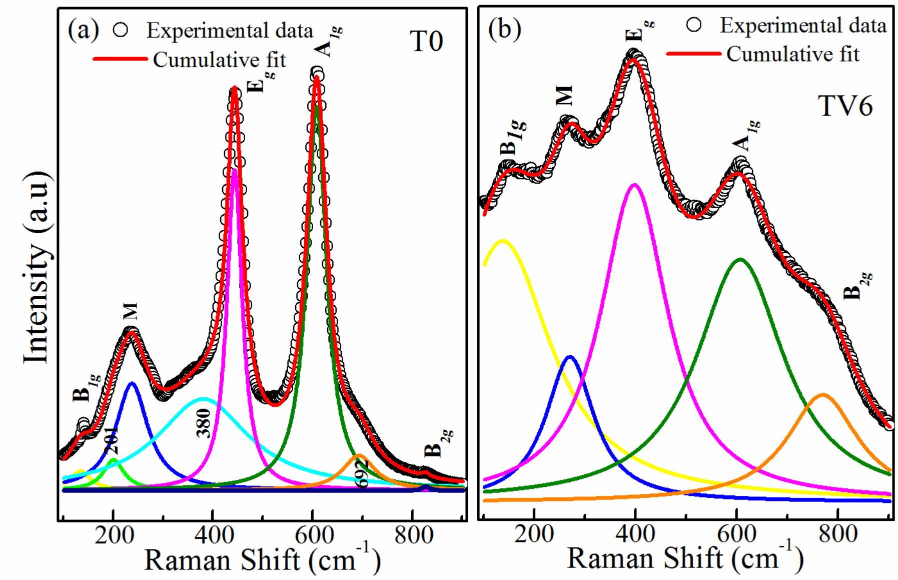

Figure 4.10: (b) and (c) Lorentzian fitting of Raman vibrational modes of T0 and TV6 samples prepared at 750 °C.

Proto *et al.* [199] reported that infrared active transverse optical modes occur at 183 (E_u) cm^{-1} and 388 cm^{-1} (E_u) for pure TiO_2 , which are close to the peaks found in our observation at 201 and 380 cm^{-1} respectively for V doped TiO_2 samples. The peak at 692 cm^{-1} can be attributed to be generated by second order process as reported by Xing-

Yuan *et al.* [201] in their observation on rutile single crystal. For TV6 samples (figure 4.10 (b)), five Lorentzian peaks are fitted to describe the data satisfactorily. All these peaks correspond to the rutile phase.

The Raman active modes consist of motion of anion (oxygen) with respect to central cation (Ti) either parallel to *c* axis (E_g) or perpendicular to *c* axis (B_{1g}, A_{1g}, and B_{2g}). B_{1g} vibrational mode is a combination of asymmetric bending of O-Ti-O bonds in the (001), (110) and (-110) planes. The E_g mode occurs due to asymmetric bending of O-Ti-O bonds in the (110) plane, caused by the anti-parallel movement of the O atoms across the O-Ti-O bond. A_{1g} mode happens due to symmetric stretching of the O-Ti-O bonds of the (110) plane caused by oscillation of the O atoms in the adjacent O-Ti-O bonds, in the direction opposite to each other [200]. The basic Raman vibrational modes of rutile TiO_2 are shown figure 4.11.

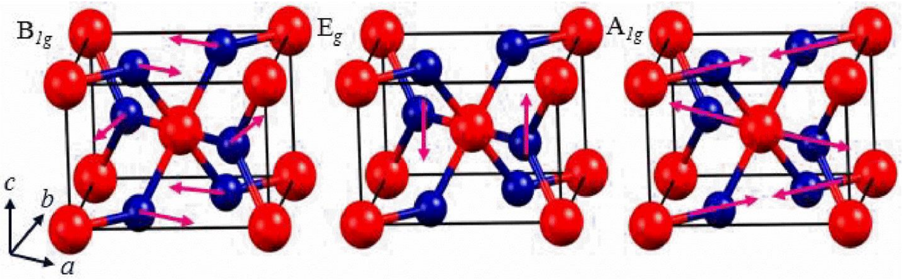

Figure 4.11: Vibration corresponding to Raman modes of rutile TiO_2 (B_{1g}, E_g and A_{1g}). The red and Navy blue balls denote Oxygen (O) and Titanium (Ti) atoms respectively and magenta arrows show the direction of vibrations.

The E_g peak exhibits a clear redshift from 444 cm^{-1} (T0) to 398 cm^{-1} (TV6) with increasing vanadium concentration (figure 4.12 (b)). The multiphonon mode (M) observed around 237 cm^{-1} shows a blueshift with increasing doping concentration from 237 to 268 cm^{-1} (figure 4.12 (a)). The multi-phonon scattering is more prominent in bulk materials than nanoparticles [202]. The particle size of the samples (750 °C) observed in SEM and TEM is more than 200 nm which is large enough to exhibit bulk-like properties; which justify the occurrence of M mode in present samples.

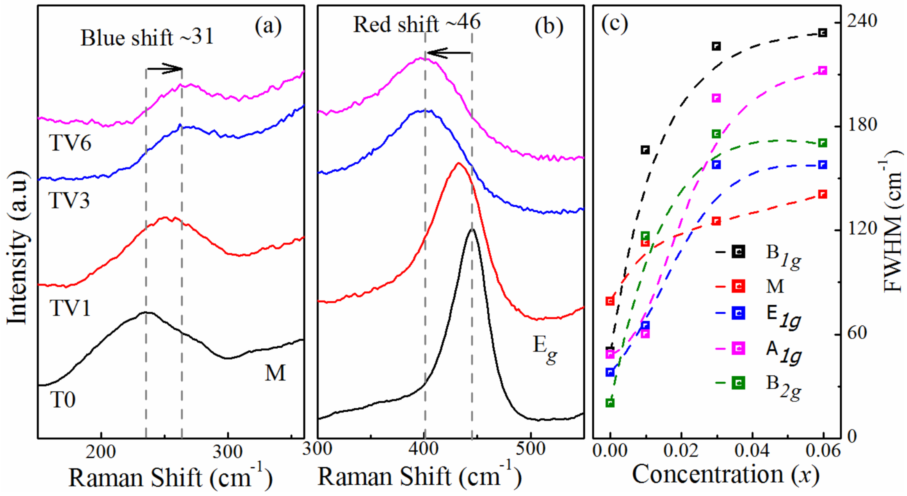

Figure 4.12: (a) Blue shift of multiphonon mode (M) and (b) redshift of E_g mode with increasing V concentration. (c) Variation of FWHM of all Raman modes with V concentration.

There are no observable changes in the peak position of B_{1g} and A_{1g} Raman modes (figure 4.9). Vanadium doping does not affect the position of B_{1g} peak. Based on a detailed analysis with simulation and experimental data, Lan *et al.* [203] explained that B_{1g} mode is contributed from quasi-harmonic and explicit anharmonic vibrations which are opposite to each other with almost equal magnitude. In quasi-anharmonic effect, vibrations are harmonic but frequency changes with volume. In our observation, with increasing vanadium concentration the unit cell volume decreases which changes the quasi-harmonic vibration. It is also to be noted that anharmonicity increases with increasing doping concentration. The cancellations of quasi-harmonic and explicit anharmonic vibrations cause no change in B_{1g} mode position. The shifting of B_{2g} mode is not clear as the intensity of this mode is very low.

From figure 4.12 (c), it is noted that phonon modes become broad for all Raman modes with increasing vanadium concentration. The FWHM is increased due to a decreased lifetime of phonon. The broadening of phonon modes is more for higher doping compared to pure TiO_2 which suggest anharmonicity systematically increased with increasing V incorporation.

4.3.3 XANES and EXAFS studies

The X-ray absorption near edge structure (XANES) analysis is a well-established technique to know the valence states of the probe elements and is strongly affected by the coordination environment of the absorbing atom [204]. The atomic environment of samples in pure anatase phase (450 °C) were studied by XANES focusing on vanadium(V) and titanium (Ti) K edges [186]. Calibration of Ti K-edge and V K-edge has been done using Ti and V foil as a reference.

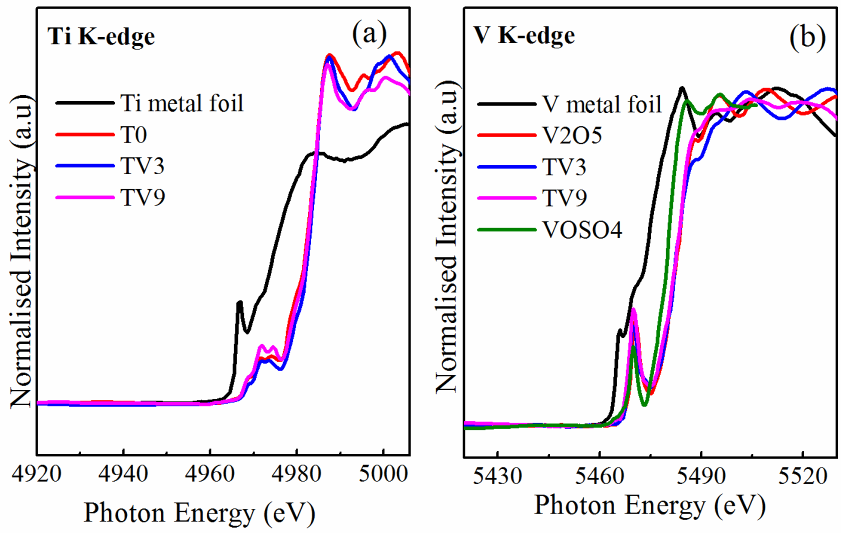

Figure 4.13: XANES spectra of T0, TV3 and TV9 samples prepared at 450 °C: (a) Ti K-edge and (b) V K-edge.

Figure (4.13 (a)) show Ti K-edge of T0, TV3, and TV9 samples. The edges of all samples coincide with each other which show Ti ions are mostly in +4 valence states. In another figure 4.13 (b), it is shown that the V K-edge of TV3 and TV9 samples are similar to that of V K-edge of V_2O_5 but not matches with $VOSO_4$. This indicates that the vanadium has a 5+ valence state in TV3 and TV9 samples.

Vittadini *et al.*[205] reported that V^{5+} is more likely the major surface species, where V^{4+} is stable inside balk. From XRD (figure 4.2), it is observed that 101 peak becomes broad which signifies that particles size decreases with increasing doping concentration. At later section (figure 4.17 and 4.18 (a)), from TEM images and Scherrer equation, it is observed that particles are in irregular spherical shape and in nano size. With increasing doping concentration, particle size decreases which result to increase of the surface area to volume ratio of the samples. Hence, at anatase phase, all the vanadium ions are mostly in 5+ Valence states [68, 188]. For charge compensation may be some Ti^{4+} convert to Ti^{3+} or V^{5+} convert to V^{4+} states.

It was aforementioned that lattice constants decreased due to V doping and is expected that V ions substituted the Ti ions and the V ions may be in 5+ or 4+ valence states. Hence, from XANES results, it is proved that V ions are mostly in 5+ states which results for a decrease of lattice constants and thereby promotes the phase transition ($A \rightarrow R$).

The normalized XANES spectra of T0, TV3 and TV6 samples in rutile phase are shown in figure 4.14 (a) and (b). It is noted that Ti K-edge positions for vanadium containing samples (TV3 and TV6) matches well with that of pure TiO_2. This confirms that most of Ti ions in doped samples are in Ti^{4+} states. XANES data of commercial V_2O_5 and $VOSO_4$ are presented as the references of V^{5+} and V^{4+} respectively. Quantification of V^{5+} and V^{4+} components in the samples is estimated from linear combination fitting (LCF) around the edge jumps of the XANES data using Athena software. The V^{5+}: V^{4+} ratio is estimated to be 67(±3):33(±3) for TV3 and 45(±3):55(±3) for TV6 samples. As Ti is in Ti^{4+} state, such a tendency for V^{4+} state is likely to avoid charge imbalance in the lattice. Theoretically, Vittadini *et al.* [205] reported that V^{5+} is more likely a major species at the surface, while internally V^{4+} is a more likely state. The surface to volume ratio decreases with increasing particle size. In later section (figure 4.20), it is observed that particle size increases with vanadium incorporation. This may be a vital reason for the change of V^{5+}: V^{4+} ratio.

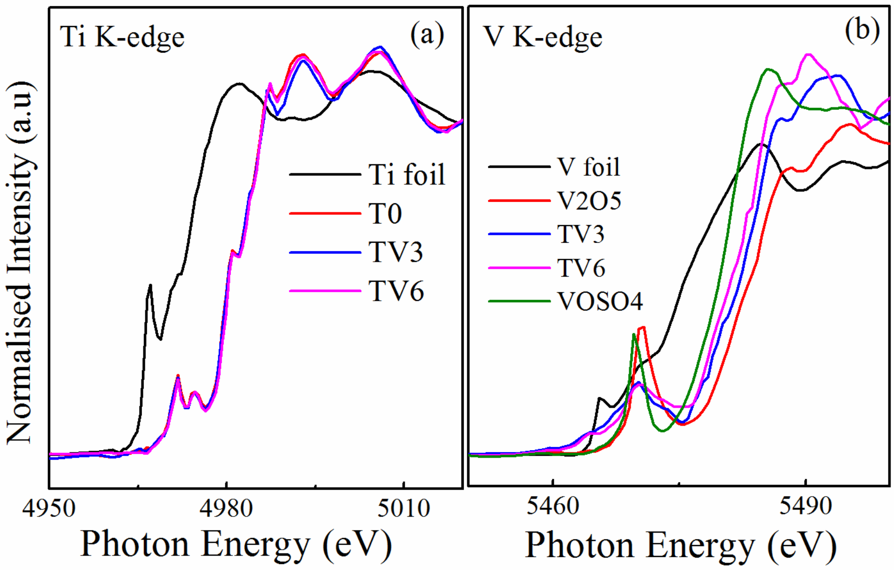

Figure 4.14: XANES spectra of T0, TV3 and TV6 samples prepared at 750 °C: (a) Ti K-edge and (b) V K-edge.

Table 4.1: Refinements structural parameters obtained from EXAFS fitting of Ti K-edge; N is the coordination number, R is the bond distance and σ^2 is the Debye-Waller factor. The numbers in parentheses indicate the uncertainty in best estimates.

		T0		TV3	
Path	N	R (Å)	σ^2 (Å^2)	R (Å)	σ^2 (Å^2)
O (1st/2nd)	6	1.968 (7)	0.0092 (5)	1.956 (9)	0.0107 (5)
Ti (3rd)	2	2.780 (4)	0.0075 (7)	2.749 (5)	0.0057 (8)
O (4th)	4	3.626 (6)	0.0085 (4)	3.783 (7)	0.0125 (9)
O (5th)	4	3.775 (7)	0.0073 (5)	3.802 (8)	0.0068 (7)
Ti (6th)	8	3.572 (9)	0.0109 (6)	3.580 (6)	0.0122 (4)

Figure 4.15 shows the EXAFS fitting of T0 and TV3 samples and the result are listed in Table 4.1. It is observed from the table that due to V incorporation bond length decreases for different paths and disorders increases for all coordination number. Such type of change in bond distance and disorders signifies that V ions properly substitute Ti ions or Ti ions are replaced by V ions in TiO_2 lattice. Hence, conclusively, V ions substitute Ti ions in TiO_2 lattice.

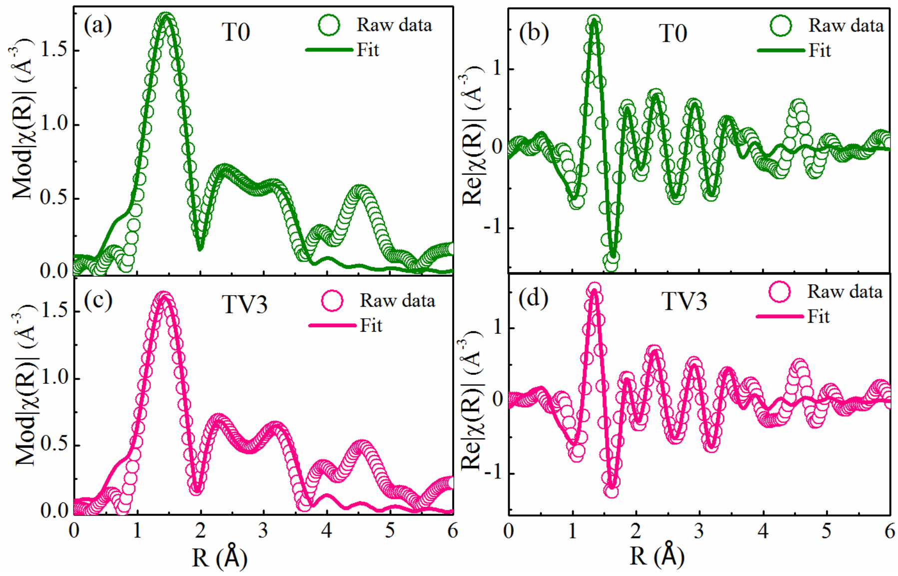

Figure 4.15: EXAFS fitting of T0 (a, b) and TV3 (c, d) samples prepared at 750 °C: R-dependent Mod$|\chi(R)|$ and Re$|\chi(R)|$.

4.3.4 Grain growth, microstructure and morphological analysis

The surface morphology, microstructure and particle size of anatase (450 ^{o}C) and rutile phase (750 ^{o}C) samples are examined using FESEM and HRTEM images. Figure 4.16 (a-c) represents SEM images of pure anatase TiO_2 nanoparticles. The shape and morphology of vanadium substituted samples do not show any drastic difference with pure one.

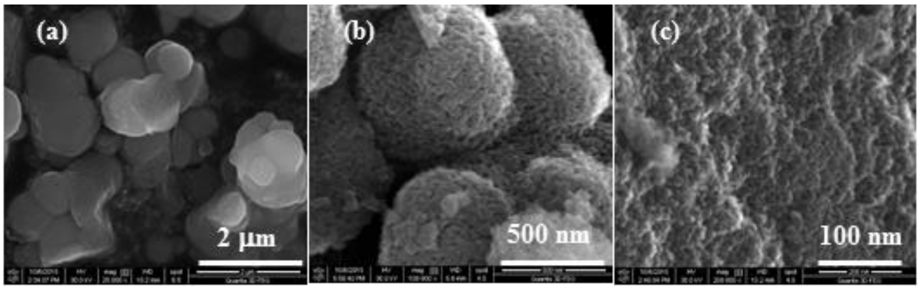

Figure 4.16: FESEM images of pure TiO_2 nanoparticle in anatase phase (450 °C) at different magnification.

The high-resolution SEM images revealed nanoparticles of size ~8-15 nm (figure 4.16 (c)). These crystallites agglomerate to round spherical particles (~50–500 nm). The agglomerated particles further fuse together to forms larger agglomerates of range ~1-5 μm (figure 4.16 (a)). As a result, irregular bigger agglomerations, as well as smaller spherical agglomerations, are observed.

The TEM images of T0 and TV9 nanoparticles are shown in figure 4.17 (a) and (d) for T0 and TV9 respectively show average size of the particles are ~11 nm and ~9 nm. Lattice fringes are observable in high-resolution images (figure 4.17 (b) for T0 and (e) for TV9). The measured *d*-space is nearly ~0.35 nm for both the samples which corresponds to 101 planes of anatase TiO_2.

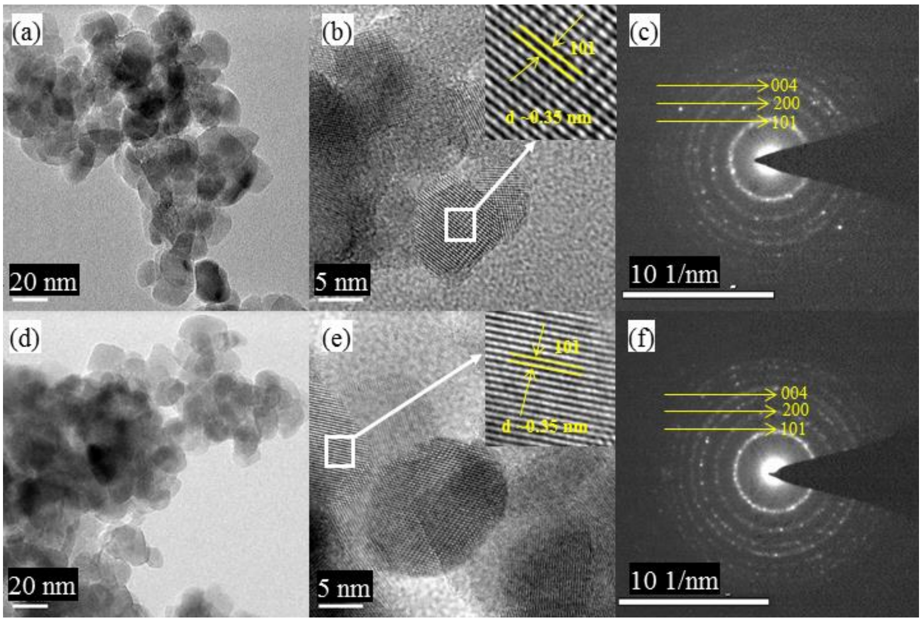

Figure 4.17: HRTEM images of T0 (a-b) and TV9 (d-e) nanoparticles prepared at 450 °C. SAED pattern of corresponding samples: (c) T0 and (f) TV9.

XRD pattern shows that the FWHM of all peaks become broader as V-concentration increases which indicate a decreasing crystallite size. From the most intense reflection peak (101), we calculated the average crystallite size using Scherrer formula (figure 4.18 (a)). The average crystallite size reduces from 11.5 nm in pure TiO_2 to 8.7 nm for TV9. The lattice strain calculated from the Williamson-Hall plot (figure 4.18 (b)) is observed that it increases with increasing V concentration.

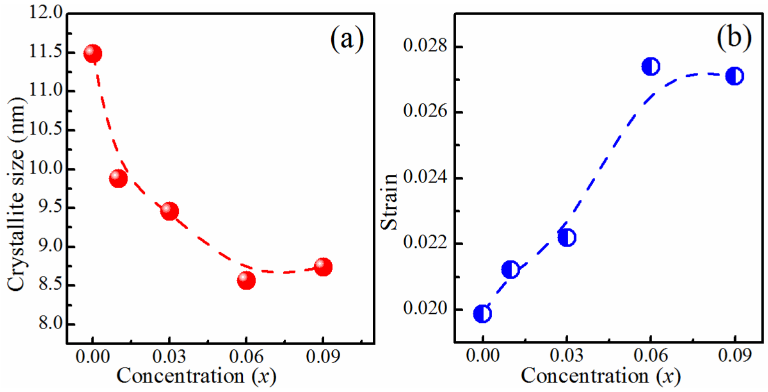

Figure 4.18: (a) Variation of crystallites size and (b) strain of V doped TiO_2 samples prepared at 450 °C with V concentration.

EDX analysis of anataseTV6 sample shows that chemical composition is close to the targeted value and elemental mapping shows, all elements are homogeneously distributed.

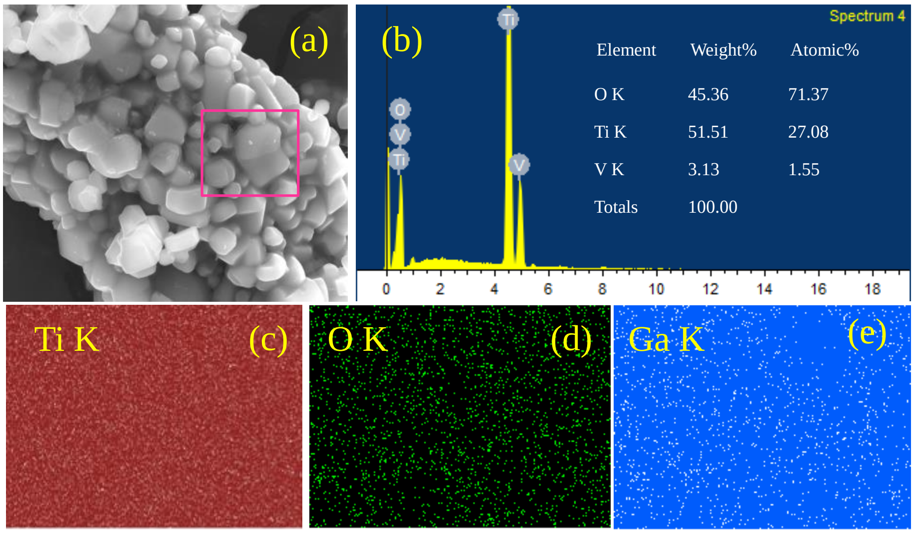

Element	Weight%	Atomic%
O K	45.36	71.37
Ti K	51.51	27.08
V K	3.13	1.55
Totals	100.00	

Figure 4.19: (a) SEM image of TV6 sample (750 °C) and (b) EDX spectrum of the same sample. Chemical compositions of the elements are shown in the inset of (b). Elemental mapping of O, Ti, and V elements are shown in (c-d).

Influence of V doping is also remarkable in rutile particles prepared at 750 °C (figure 4.20). The average particle size observed by SEM for pure TiO_2 is ~261±20 nm and increases with increasing V content.

Particles size of V doped TiO_2 samples is ~286±42 nm, ~661±101 nm and ~1205±200 nm for TV1, TV3 and TV6 respectively.

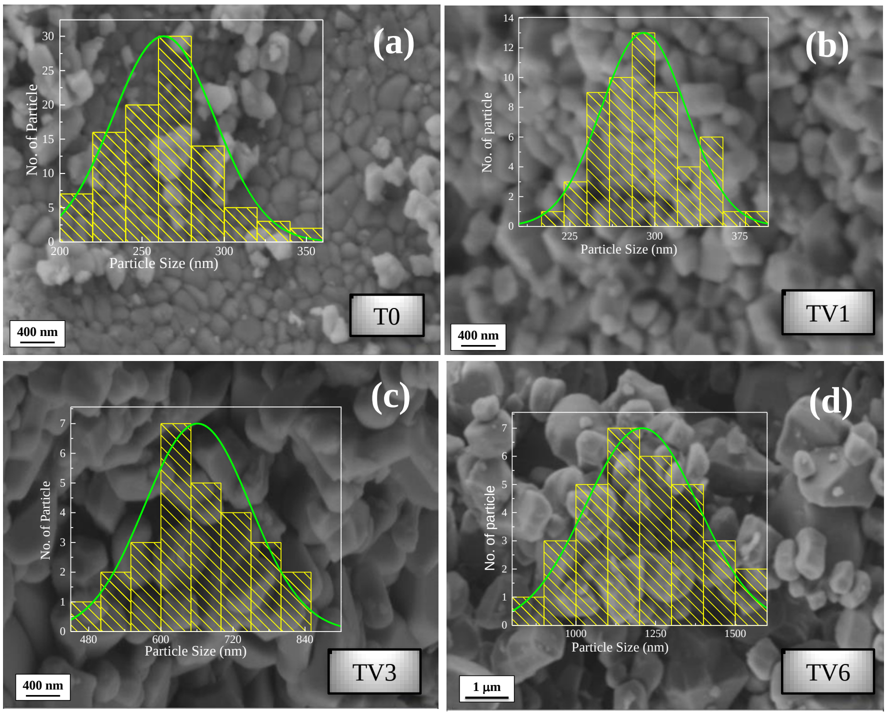

Figure 4.20: FESEM images of pure T0 (a), TV1 (b), TV3 (c) and TV6 (d)) samples prepared at 750 °C.

750 °C is sufficient temperature for rutile phase formation of pure TiO_2. But the same temperature (750 °C) becomes effectively higher for the samples with higher V concentration as their rutile phase formation completes at lower temperatures (700 °C, 650 °C and 550 °C for TV1, TV3, and TV6 respectively). The higher effective calcination temperature is an obvious reason for larger average particle size for higher doping, though the actual calcination temperature is the same for all samples. TEM images are also supportive of the particle sizes observed by SEM. For pure TiO_2, the average particle size ~249±35 nm while for TV1, TV3, and TV6, it is found to be ~287±30 nm, ~635±160 nm, and ~1167±210 nm respectively.

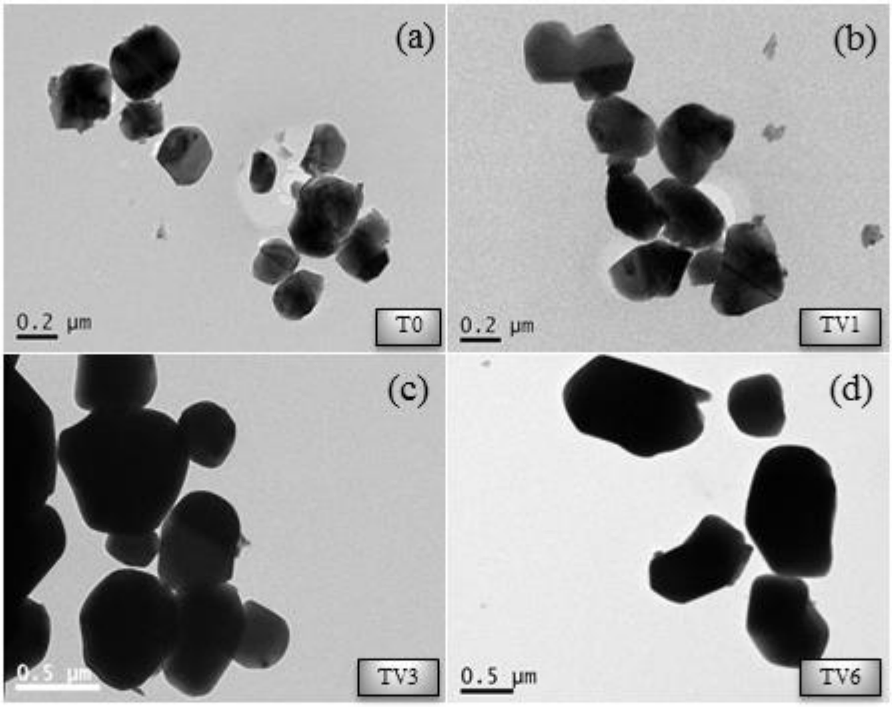

Figure 4.21: TEM images of samples prepared at 750 °C ((a) T0, (b) TV1, (c) TV3 and TV6 (d)).

4.3.5 Optical properties

Substitution of V ions in Ti lattice site not only affects phase transition and grain growth process but also modifies the optical properties of TiO_2. Room temperature DRS measurements are carried out on anatase (450 °C) and rutile (750 °C) phase samples. The scattered light is collected excluding normally reflected light in a DRS measurement. This satisfies the applicability of Kubelka-Munk function given by $F(R) = (1-R)^2/2R$, where R is reflectance. Bandgap (E_G) is calculated using Tauc plot: $F(R)h\upsilon = A(h\upsilon-E_G)^n$; where h is Planck's constant, υ is the frequency of illumination and n is a unitless parameter. The n-parameter depends on the type of bandgap: n = 1/2 specific for direct bandgap, while n = 2 for an indirect bandgap. Anatase TiO_2 is an indirect bandgap semiconductor while rutile TiO_2 is a direct bandgap semiconductor [35]. Hence, bandgap is calculated using n = 2 for anatase and1/2 for rutile samples.

In TiO_2 the valence band (VB) is composed of p-d hybridization between O 2p states and Ti 3d states which form strong bonding states in VB region. The conduction band (CB) is composed of p-d hybridization between Ti 3d states with O 2p and Ti 3p states which form antibonding states in CB [35].

From figure 4.22 (a), it is observed that bandgap of anatase samples reduced due to V incorporation. Bandgap reduces from 3.06 eV (pure TiO_2) to 2.02 eV (TV9) with increasing V concentration.

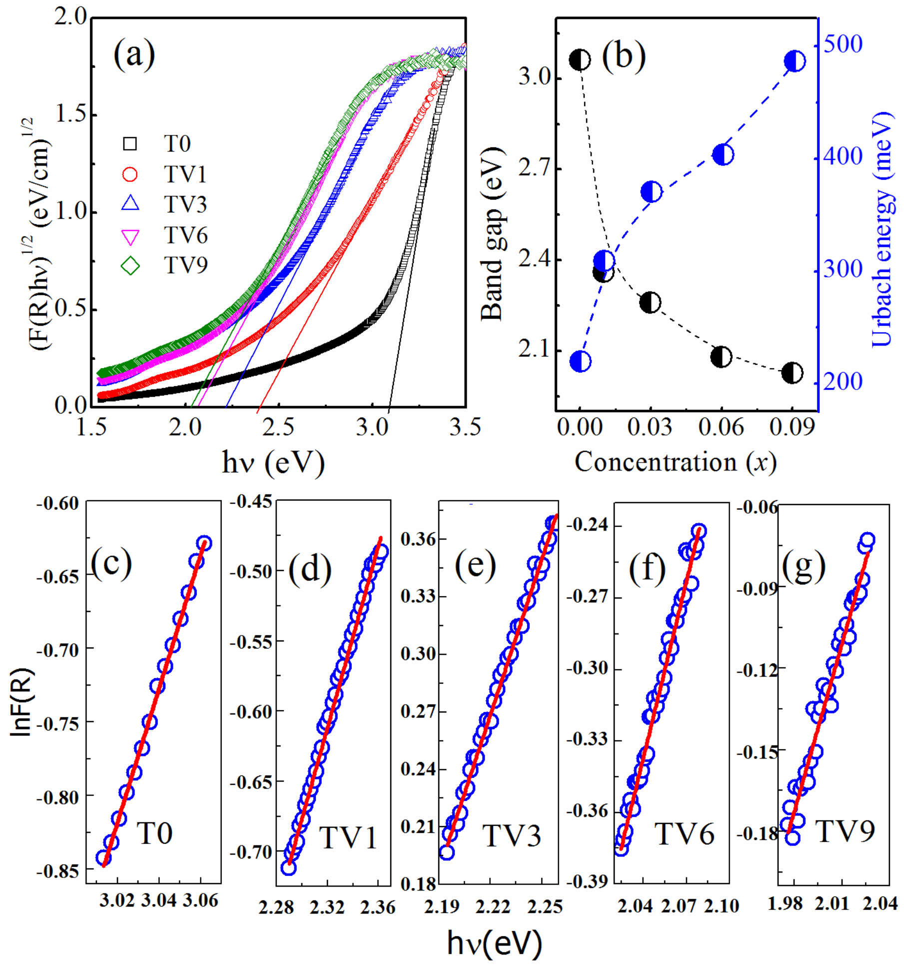

Figure 4.22: (a) DRS spectrum of samples heated at 450 °C, (b) variation of bandgap and Urbach energy with V concentration. (c, d, e, f, and g) shows linear fits of lnF(R) vs hυ plot (blue circles are original data points and red lines are linear fits to data points).

Upon vanadium doping a necessity of charge balance is essential. Some V^{5+} transformas to V^{4+} and some Ti^{4+} may also transform to Ti^{3+}, with that oxygen vacancies also changed. XANES result of anatase reveals V^{5+} ions occupy substitutional sites of TiO_2 lattice. Such substitution may create new energy levels within the bandgap. As a result of the mixing of d-shells of Ti 3d and V 3d, donor levels are formed just below the CB [142, 206, 207]. Hence, due to these donor levels close to the bottom of the CB, the effective bandgap decreases.

Structural disorder /distortions create defects in the lattice, which may cause electronic defect states inside the bandgap. Such type of defect states is responsible for tail (or Urbach tail) formation in absorption spectra. The energy associated with this tail is called Urbach energy (E_U). It is observed that with increasing V concentration Urbach tail shifted to lower energy side. E_U is calculated from linear fits of "lnF(R) vs hυ" plots just below the absorption edge of DRS data. Reciprocal of the slope gives E_U [68]. The calculation shows even in the pure TiO_2, E_U is ~219 meV which reflects the presence of defect states. With increasing V concentration, E_U increases indicating the generation of further distortion in TiO_2 lattice and for TV9, it is ~486 meV.

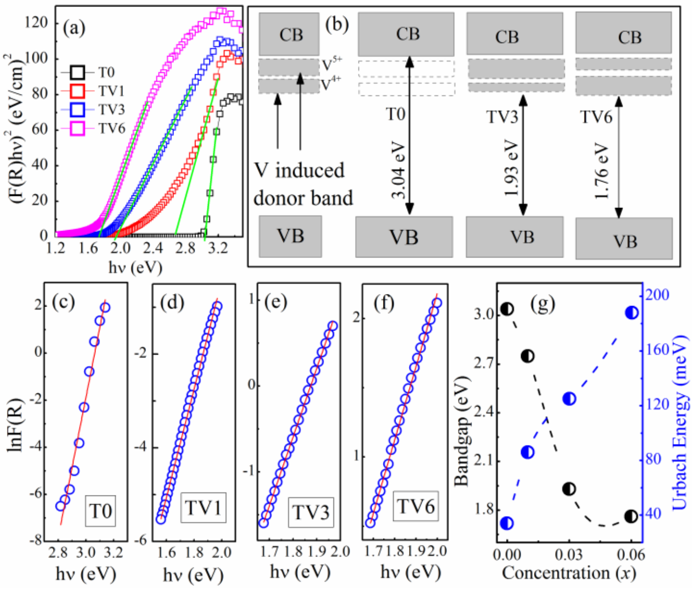

Figure 4.23: (a) DRS spectrum of samples heated at 750 °C, (b) schematic diagram of bandgap tailoring. (c, d, e, f, and g) Shows linear fits of lnF(R) vs hυ plot (blue circles are original data points and red lines are linear fits to data points). (b) Variation of bandgap and Urbach energy with V concentration.

Similar to anatase phase, absorption edge shifts to lower energy side (figure 4.23 (a)) in rutile phase. Bandgap decreases from 3.04 eV (T0) to 1.76 eV (TV6). With the help of DFT calculation using cluster model, Choi *et al.*[208] reported that bandgap of V substituted TiO_2 is narrower than the pure one and band gap changes with valence state of vanadium ($E_g(V^{5+}) > E_g(V^{4+})$). It is interestingly noticed that for V^{4+} substitution donor levels occupy a much deeper position compared to V^{5+} substitution. From XANES results, it is observed that concentration of V^{4+} species increases with increasing doping concentration: for TV3 and TV6 samples the percentage of valence states V^{5+}: V^{4+} are 67(±3):33(±3) and 45(±3):55(±3) respectively. With this analogy, a schematic diagram (figure 4.23 (b)) is drawn to explain how the vanadium ions are responsible for decrease of the effective band gap. E_U also increases in rutile phase from 34 meV for pure TiO_2 to 188 meV for TV6.

Pure TiO_2 absorbs only UV light. However, V doped samples can absorb both UV and visible light as bandgap decreases. Hence these samples can absorb a larger range of the solar spectrum. Hence, V doping makes TiO_2 useful as a photocatalyst and other optoelectronic applications under visible light.

4.4 Summary

In summary, achievements of this chapter are listed below:

1. Samples are in a pure phase of TiO_2 as observed from both XRD and Raman Spectra.
2. Acceleration of phase transition by V doping is observed from the same measurement.
3. Activation energy of phase transition decreases with increasing V concentration in the samples.
4. Rietveld refinement of the XRD data reveals lattice contraction due to V incorporation for both phases.

5. XANES and EXAFS analysis shows that V ions are properly substituted Ti ions in TiO_2 lattice.
6. V ions are in V^{5+} valence states in anatase phase whereas in rutile both V^{4+} and V^{5+} states are present. The V^{4+} proportion increases with doping concentration.
7. Grain growth is retarded in the anatase phase (observed from HRTEM and broadening of 101 peaks of XRD pattern), whereas it is accelerated in the rutile phase (observed from FESEM and TEM analysis).
8. Due to formation of donor levels associated with V incorporation, bandgap decreases from UV to Visible region for both phases.
9. Urbach energy increases due to increased lattice distortion with V incorporation in both phases.

V incorporation reduces bandgap of TiO_2 to the visible light region, but anatase phase shows transformation ($A \rightarrow R$) near temperature ~450-500 °C. In Ga doped TiO_2 samples (chapter 3), anatase phase becomes stabilized up to ~650 °C, but bandgap increases and remains in the UV region. Hence in chapter 5, Ga- V co-doping into TiO_2 are planned to achieve a material which shows stabilized anatase phase with reduced bandgap.

Chapter 5

Effect of charge compensated Ga-V (1:1) co-doping on structural phase transition, grain growth and optical properties of TiO_2

5.1 Overview

In chapter 3, it was observed that Ga ion occupy both interstitial and substitutional sites in TiO_2 lattice. Due to interstitial Ga^{3+} ions, oxygen content slightly increases which expand the lattice and thereby inhibits phase transition. Anatase phase becomes stable up to a very high temperature ~650 °C. However, bandgap of both phases increases due to Ga incorporation. In chapter 4, it was observed that V doping creates donor levels just below the CB, which effectively reduces the bandgap of TiO_2 to the visible light region. However, due to substitution of smaller V ions, lattice contracts and thereby accelerates $A\rightarrow R$ phase transition. Hence, our objective to prepare "a modified TiO_2 anatase sample, which will be stable up to a very high temperature and will absorb visible light of solar spectrum" is not yet achieved. From our experience of the previous two chapters, we have planned to prepare Ga-V co-doped sample in 1:1 ratio which is equivalent to pure TiO_2 matrix from both charge and ionic size perspective with the expectation that anatase phase will be stabilized by Ga ions and bandgap will be reduced by V ions. In this chapter effect of such expected "compensated Ga-V co-doping" on phase transition, grain growth process, surface morphology and optical properties of TiO_2 are presented.

5.2 Experimental

Structural analysis was studied by powder X-ray diffraction (XRD) patterns using Bruker D2 phaser diffractometer with Cu-Kα radiation (λ=1.5418 Å). Morphology and particle size were investigated using high-resolution transmission electron microscope (HRTEM) (JEOL JEM-2100 LaB6, accelerating voltage - 200 kV) and field emission scanning electron microscopy (Supra55 Zeiss- FESEM). Analysis of surface area and pore size distribution of the samples were done by N_2 adsorption-desorption study using an automated gas sorption analyzer Quantchrome autosorb iQ2. Diffuse reflectance spectroscopy (DRS) measurements were carried out using Agilent cary 60 UV–vis was used for DRS measurement to estimate the changes in the bandgap.

5.3 Results and discussion

5.3.1 Structural analysis

XRD pattern of Ga-V co-doped samples (T0, TGV2, TGV5, TGV7, and TGV10), heated at temperatures ~450 °C, 500 °C, 550 °C, 600 °C, 650 °C, and 700 °C, are shown in figure 5.1.

Samples heated at 450 °C for 6h matches well with COD ID-9015929 which is of tetragonal anatase phase of TiO_2 having space group $I4_1/amd$. Hence, all the samples at this temperature are in pure anatase phase. There are no traces of any rutile phase at this temperature. Also, there is no evidence of any simple or complex metal oxide phases related to Ti, Ga, and V. Anatase phase gradually starts to convert to a rutile phase with increasing temperature and forms a mixed phase (anatase and rutile). With further heating, the entire sample converts into rutile phase.

It was discussed in the previous chapter that pure TiO_2 shows small appearance of rutile phase at 500 °C. In case of co-doped samples (figure 5.2), only TGV2 and TGV5 show small appearance of rutile phase whereas TGV7 and TGV10 remain in the anatase phase. Further heating the samples at a higher temperature (~550 °C), the intensities of rutile peaks become stronger in co-doped samples than pure TiO_2.

At 700 °C, all the samples are entirely converted into rutile phase. XRD patterns of these samples match well with tetragonal rutile phase of TiO_2 having space group *P4₂/mnm* (COD ID-9009083).

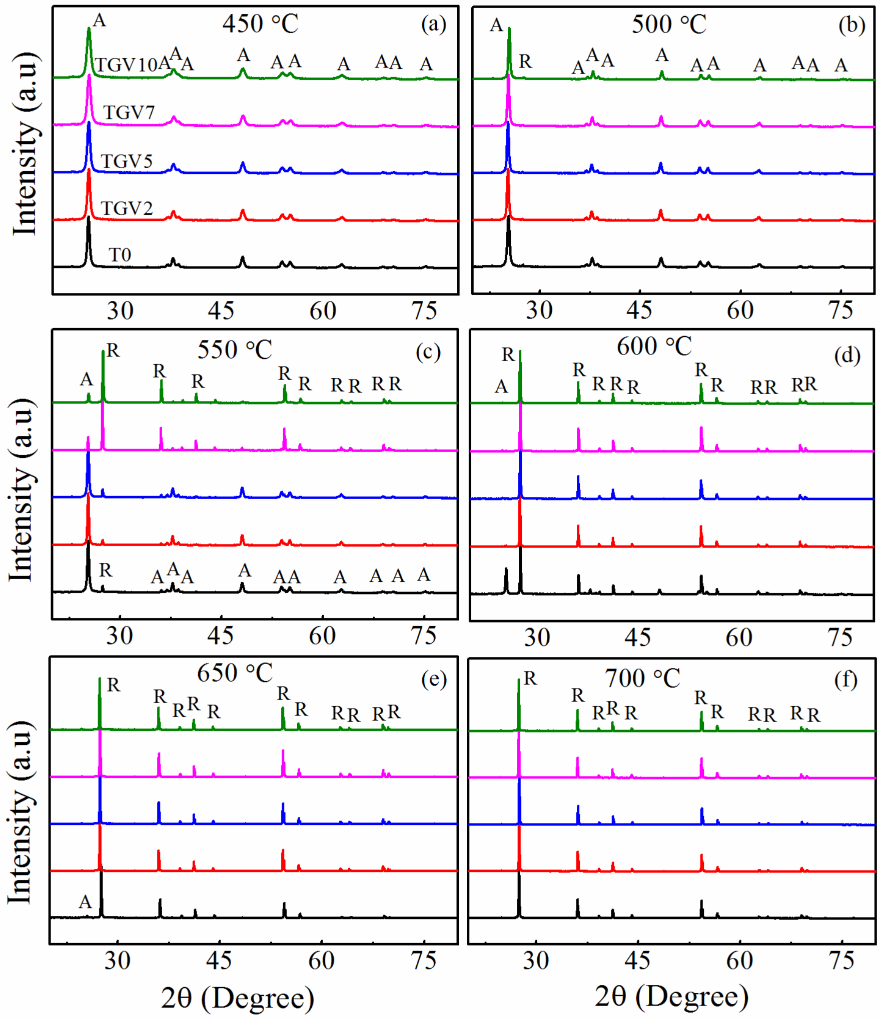

Figure 5.1: XRD patterns of all the Ga-V (1:1) co-doped samples at six different temperatures (450-700 °C) in the range of 2θ = 20-80°.

Same Spurr and Mayers equation as discussed in Chapter 3 is used to calculate the rutile phase fraction (f_R) present in the mixed phase samples (5. 3 (a)).

At 500 °C, only TGV2 and TGV5 show a small proportion of f_R while there is no presence of f_R in TGV7 and TGV10. At higher temperature

(550 °C), f_R increases with increasing doping. TGV10 completely transform into rutile phase at ~600 °C, although in TGV2, TGV5 and TGV7 samples small fraction of anatase phase still present. All the co-doped samples completely convert into rutile phase at 650 °C, while in pure TiO_2 small fraction of anatase phase is still present as observed in the previous chapter. At 700 °C, all the samples are completely converted into rutile phase.

From the analysis of XRD pattern of all samples at all temperature, it is observed that due to co-doping (Ga: V = 1:1) onset temperature shifted to a higher temperature. However, A→R (complete conversion) temperature shifted to a lower temperature. All processing parameters (like heating/cooling rates, environment of calcination, etc.) are kept invariant at all temperature; hence such type of change in onset of A→R temperature completely depends on doping concentration.

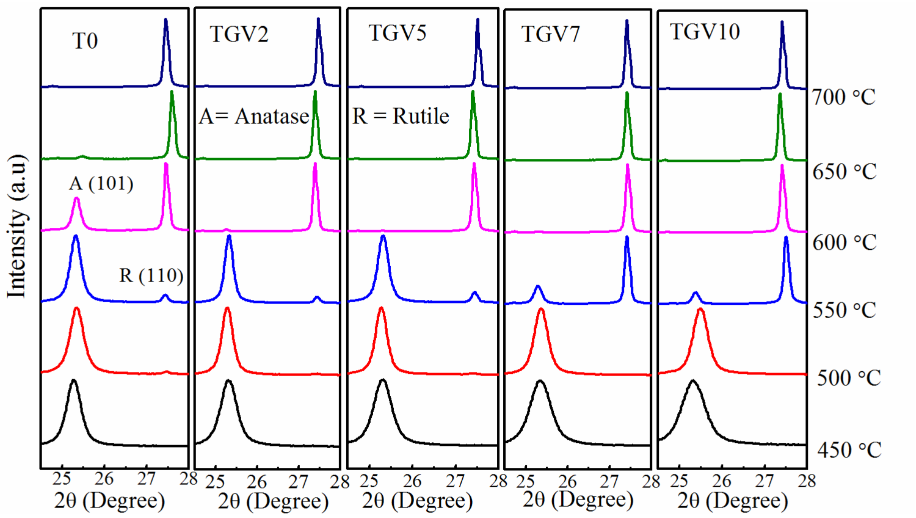

Figure 5.2: Zoomed view of XRD patterns of all the samples at six different temperatures (450-700 °C) in the range of $2\theta = 24\text{-}28.5°$.

Activation energy (E_A) of phase transition is calculated from 'f_R' value using the same (similar to Chapter 3) Arrhenius equation. E_A increases for lower doped sample but decreases for higher doped samples (figure 5.3 (b)). Such type of changes in E_A is due to change in onset and A→R temperature.

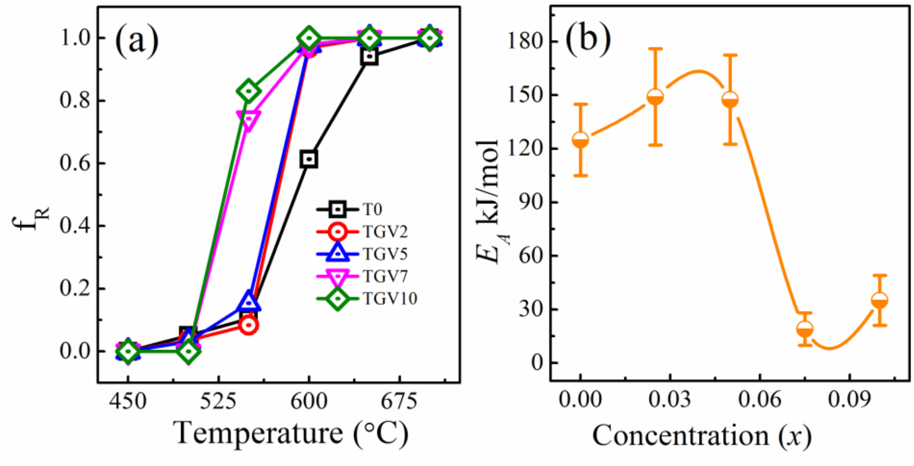

Figure 5.3: (a) Change in f_R with temperature for all the samples and (b) change in activation energy with concentration.

Figure (5.4 (a)) shows Rietveld refinement of XRD data of anatase phase samples heated at 450 °C. Lattice constants and unit cell volume both increases nominally with increasing doping concentration. This expansion of lattice is responsible for delaying onset temperature in co-doped sample. In case of only Ga doped sample (Chapter 3), some Ga^{3+} ions occupy interstitial sites in the lattice and thereby increases oxygen content. This extra oxygen expands the lattice and inhibits phase transition. On the other hand, in case of only V doped sample, V^{5+} (VI~0.68 Å) ions are smaller than Ti^{4+} (~0.745 Å) and occupy lattice sites. This results in lattice contraction, thereby promoting A→R transition.

In co-doped (Ga: V = 1:1) sample, it is expected that Ga ions occupy both substitutional and interstitial sites and V ions occupy lattice site. Thus our initial expectation that a charge compensated system may not have any difference than the parent TiO_2 seems not to be achieved as oxygen content should change. We have observed lattice expansion which hints at interstitial Ga incorporation. This may be responsible for deviation from our expectations.

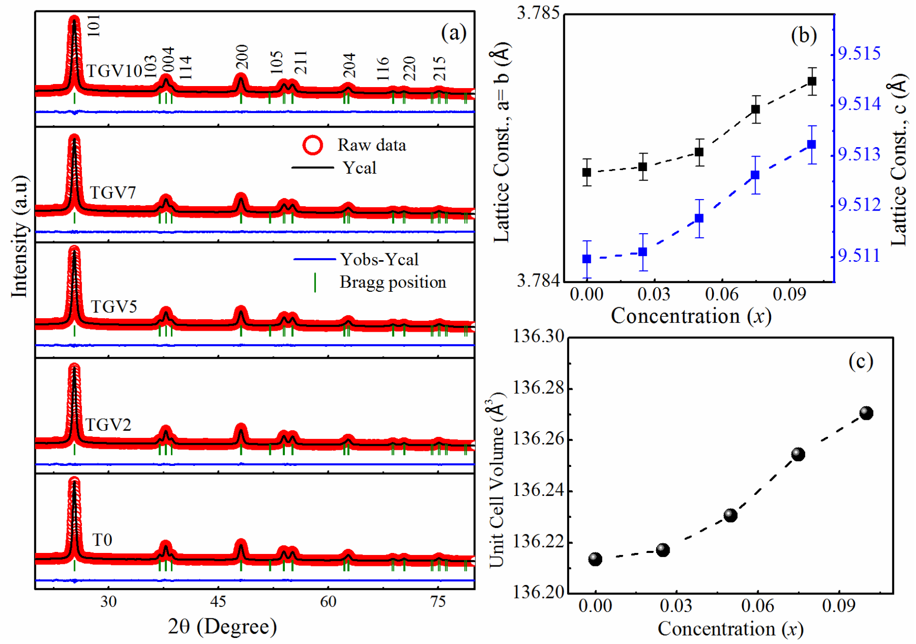

Figure 5.4: (a) Rietveld refinement of Ga-V (1:1) co-doped samples prepared at 450 °C and (b-c) change in lattice constants and unit cell volume with doping concentration.

Rietveld refinement of samples in rutile phase (figure 5.5 (a)) shows decrements of lattice constants as well as unit cell volume with increasing doping concentration. In Chapter 3, it was observed that lattice nominally expands due to Ga^{3+} ions occupy more interstitials sites than substitutional sites. On the other hand, in Chapter 4, unit cell volume decreases considerably with increasing V doping concentration. V has variable valence states (5+, 4+, 3+ and 2+). When V compound is heated at an elevated temperature in an air atmosphere, the valence state of V changed, thereby changing the ionic radius. In Chapter 4, V ions were found to be in both in V^{5+} and V^{4+} valence states in the rutile phase. Hence, in the case of co-doping, one may expect similar results. As rutile TiO_2 is formed at a higher temperature, hence, oxygen vacancies are more in rutile phase than in anatase phase. In pure rutile TiO_2, some Ti^{4+} is converted into Ti^{3+} [209], whereas in anatase phase all the Ti ions are in Ti^{4+} valence state [210]. At higher temperatures, $V^{5+}\rightarrow V^{4+}$ and $Ti^{4+}\rightarrow Ti^{3+}$ conversions take place [148, 209]. Ti^{3+} and Ga^{3+} are slightly bigger than Ti^{4+} while V^{4+} and V^{5+} are smaller. Hence, oxygen content must change accordingly to maintain charge neutrality. All the Lattice constants decrease with increasing doping concentration which hints an effect of V modifications and an increase of oxygen vacancies in the lattice.

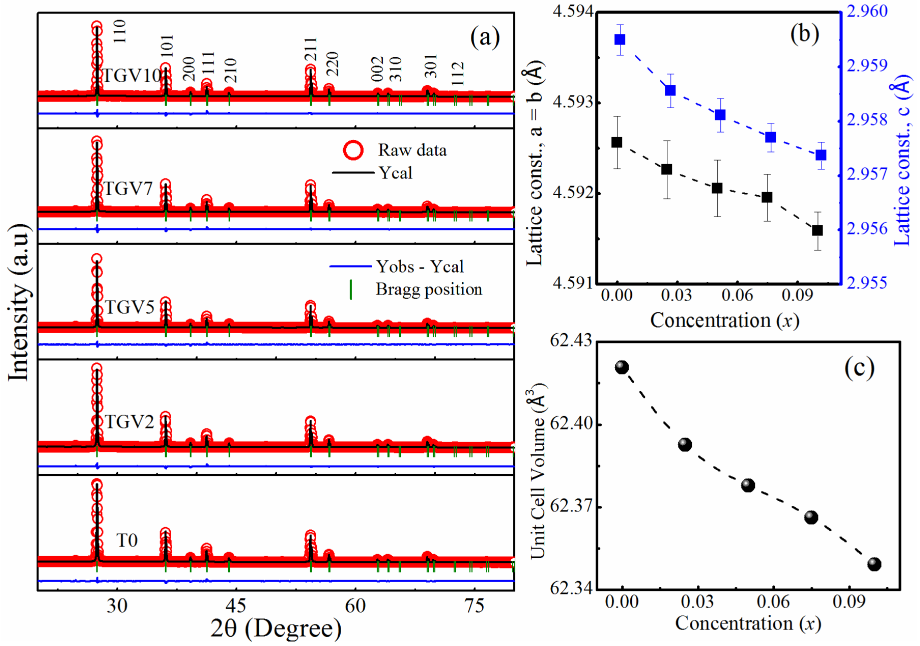

Figure 5.5: (a) Rietveld refinement of Ga-V co-doped samples prepared at 700 °C and (b-c) change in lattice constants and unit cell volume with doping concentration.

5.3.2 XPS analysis

Rietveld refinement of the XRD data reveals that Ga-V co-doping modifies the anatase lattice and nominally expands it. XPS is an excellent technique to understand the valence state of elements, its nature in the lattice and oxygen content in these samples. Hence, to understand the mechanism of lattice expansion of TGV samples, XPS measurements have been carried out. XPS spectrums are analyzed using XPS peak analyzer 4.1 software. The observed spectra include the Ti 2p, Ga 3d, and O 1s feature. The fitted spectra of TGV5 and TGV10 samples are displayed in figure 5.6.

De-convolution of Ti 2p spectra yields four peaks for both the samples (figure 5.6 (a-b)), in these four peaks, two for Ti^{3+} and two for Ti^{4+}

states. Hence, the samples have a mixed valence state of Ti^{4+} and Ti^{3+} in both the samples. The peaks of each category are separated due to spin-orbit splitting. For the Ti^{4+} valence state, the binding energies are at 459.16 eV and 464.68 eV for TGV5 with spin-orbit splitting of 5.69 eV, while for TGV10 at 459.35 eV and 465.05 eV with spin-orbit splitting of 5.7 eV. Note that the same features for a Ti^{3+} valence state are observed at 457.43 eV and 463.08 eV with spin-orbit splitting 5.65 eV for TGV5, while at 457.50 eV and 463.1 eV with spin-orbit splitting 5.6 eV for TGV10. The ratio of the areas of these peaks is used to calculate the ratio of Ti^{4+}: Ti^{3+} ions (similar to Chapter 3). For TG5, Ti^{4+}: Ti^{3+} = 74.30: 25.70, whereas in TGV10 this ratio is 55.34: 44.66. Hence, the proportion of Ti^{3+} ions present in TGV10 is more than TGV5. However, note that the entire Ti ions are in Ti^{4+} valence state in pure TiO_2. Hence, with doping, the presence of Ti^{3+} indicates the following: (1) oxygen deficiency, and (2) lattice expansion. The first is due to the lesser charge while the second is due to the larger size of Ti^{3+} (VI~0.81 Å) than Ti^{4+} (VI~0.745 Å).

Similar to chapter 3, deconvolution of Ga 3d spectrum of the samples yield two peaks both belonging to Ga^{3+} valence state (figure 5.6 (c-d)). For TGV5, peaks are obtained at 20.26 eV and 22.64 eV, while for TGV10 at 20.3 eV and 22.62 eV. The peak at lower binding energy corresponds to lattice Ga ion (Ga_L), i.e. Ga substituting Ti at a lattice site. The peak at higher binding energy corresponds to interstitials Ga (Ga_I). The ratio of G_L: Ga_I (calculated from peak areas) in TGV5 and TGV10 samples are 24.50: 75.50 and 25.40: 74.60 respectively. Hence, majority of the Ga ions are interstitial in both samples. Although percentage of Ga_I ions are almost same in TGV5 and TGV10, the total amount of Ga_I ions are more in TGV10 than TGV5 due to higher doping concentration in TGV10. These interstitials increase the oxygen content in the lattice. Therefore, a competition of the increasing and decreasing O_V is observed due to increased Ti^{3+} and Ga_I. Yet, interestingly, both are responsible for lattice expansion.

De-convolution of O 1s spectrum also displays two types of peaks for both the samples (figure 5.6 (e-f)). The lower binding energy peak is observed at 530.73 eV for TGV5 and at 530.75 eV for TGV10 corresponding to lattice oxygen (O_L) (similar to chapter 3). The higher binding energy peak is observed as 532.43 eV for TGV5 and at 531.75eV for TGV10 corresponding to oxygen vacancies (O_V). The ratio of O_L: O_V is found to be 87.50: 12.50 for TGV5 and 87.41: 12.59 for TGV10. Hence, numbers of O_V are almost same in both the samples.

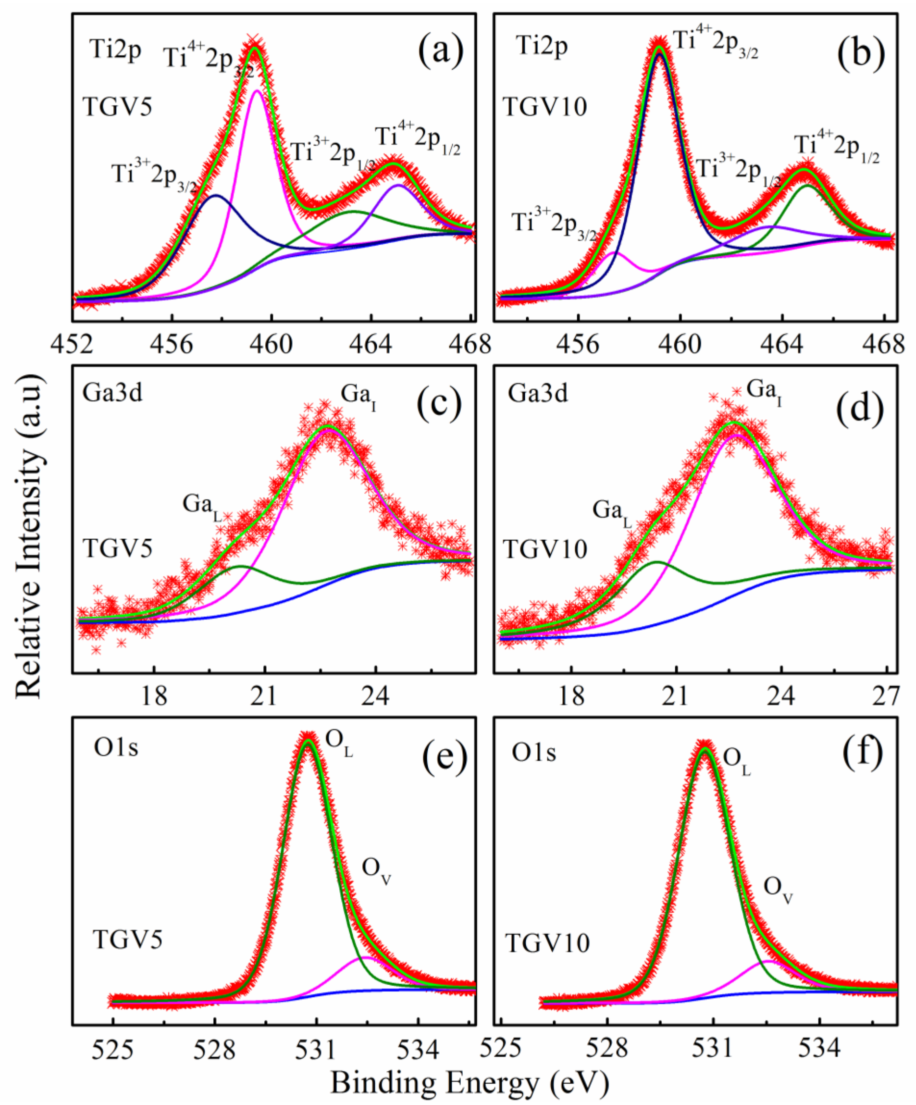

Figure 5.6: Fitting of XPS spectra of Ti 2p, Ga 3d and O 1s of TGV5 and TGV10 samples prepared at 450 °C.

Unfortunately, the XPS data of the V-Kedge is weak enough to be reported. In a pure V-doped sample (chapter 4), it is found that all the V ions are mostly in V^{5+} state. However, in a co-doped sample, V may exist in mixed V^{4+}/V^{5+} states. In either case V cannot introduce O_V due to its charge being either equal or higher than Ti^{4+}. The sizes of V^{4+}/V^{5+} (0.72/0.68 Å) are a little lesser than Ti^{4+}. Hence, the competing factors of volume reduction by V ions or O_V and volume expansion by Ga_I, $Ga_{L,}$ and Ti^{3+} ultimately leads to nominal volume expansion in the modified lattice.

5.3.3 Grain growth and surface morphological analysis

Crystallite sizes of the samples heated at 450°C are calculated from XRD peak broadening using Scherrer formula (figure 5.7 (a)). For pure TiO_2, particles size is ~17.9 nm whereas with increasing doping concentration crystallite size reduces to ~12.5 nm for TGV10. Williamson hall equation is used to calculate strain present in the samples (figure 5.7 (b)). Note that strain increases with increasing doping concentration. This increasing strain hinders grain growth process in anatase phase.

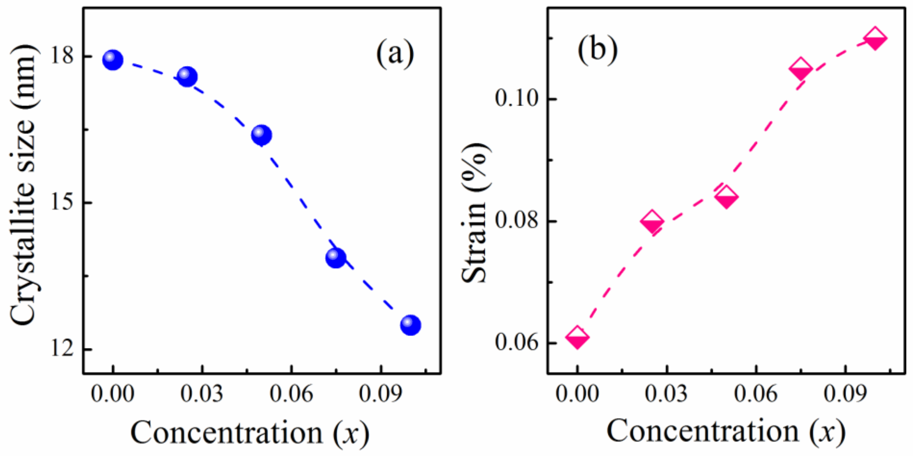

Figure 5.7: (a) Variation of crystallites size and (b) strain with doping concentration of samples prepared at 450 °C.

HRTEM images reveal irregular spherical shaped particles for T0 and TGV5 samples (figure 5.8). Particle size reduces from ~15 nm for pure TiO_2 to ~9 nm for TGV5. This result is consistent with crystallite size calculated from Scherrer equation. *d*-spacing of lattice fringes (d_{101}~0.35Å for T0 and TGV5) also confirmed that both the samples are in anatase phase. The SAED patterns reveal defined clear rings which correspond to polycrystalline anatase nanoparticles. Clarity of the rings reflects proper crystalline nature.

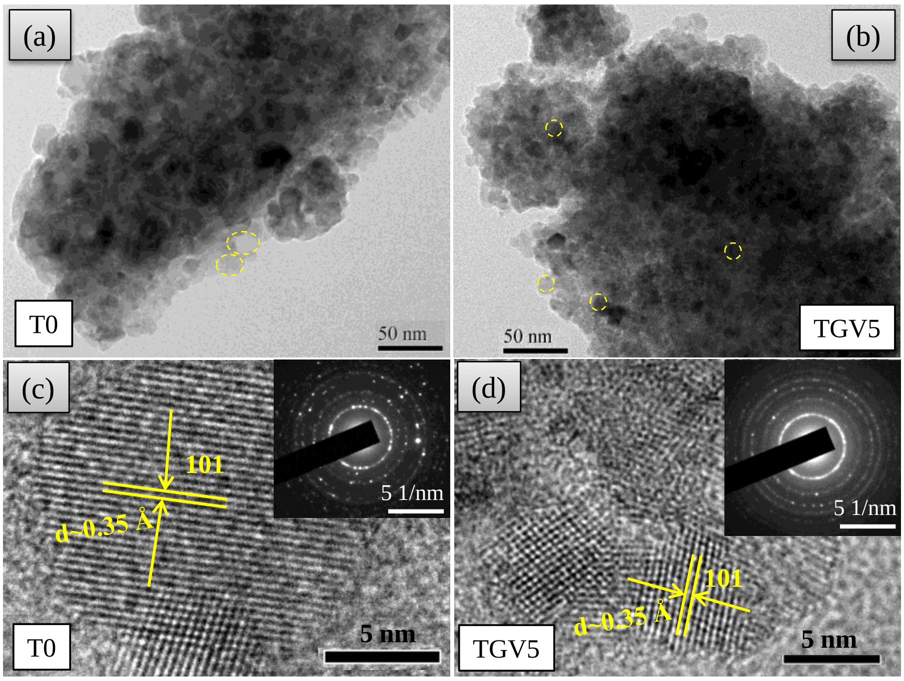

Figure 5.8: HRTEM images of T0 ((a) and (c)) and TGV5 ((b) and (d)) samples. Inset shows the SEAD pattern of the corresponding sample.

Particle shape changes from irregularly spherical to rod-like structures in rutile phase samples. Particle sizes of the samples are calculated from Image J software. For pure TiO_2, particles size is ~ 210 nm. For Ga-V co-doped samples, length and width of the rod are calculated. These are provided in Table 5.2.

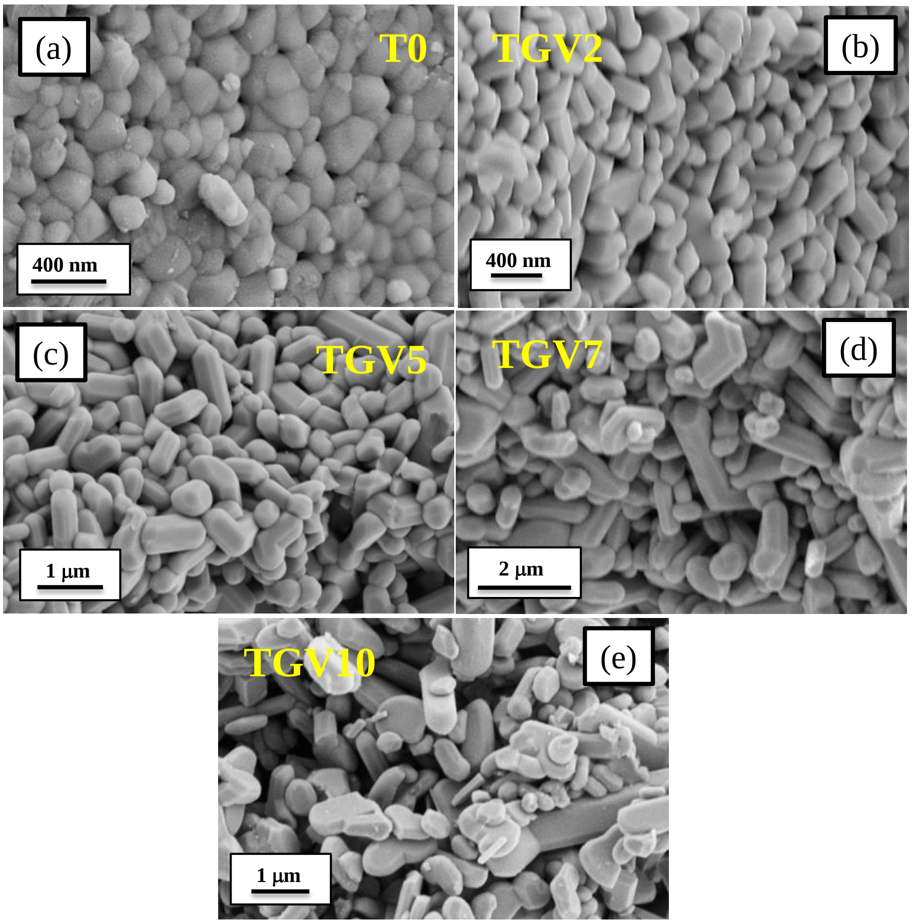

Figure 5.9: FESEM images of the samples prepared at 700 °C: (a) T0, (b) TGV2, (c) TGV5, (d) TGV7, and (e) TGV10.

Table 5.1: Particles size of the samples prepared at 700 °C.

Samples	Diameter	Length
T0	210 nm	---
TGV2	180-220 nm	350-600 nm
TGV5	200-400 nm	600 nm -1.5 μm
TGV7	300-600 nm	1-2.5 μm
TGV10	500 nm -1 μm	1.5-6 μm

Length and diameter of the samples increase with increasing doping concentration. Ga doping retards grain growth process (Chapter 3), while V doping promotes (Chapter 4). Hence, V incorporation may be responsible for grain growth in co-doped samples.

EDX analysis ensures that the chemical composition of TGV10 sample is close to targeted value. Elemental mapping confirms the homogeneous distribution of Ga, Ti, and V in the samples.

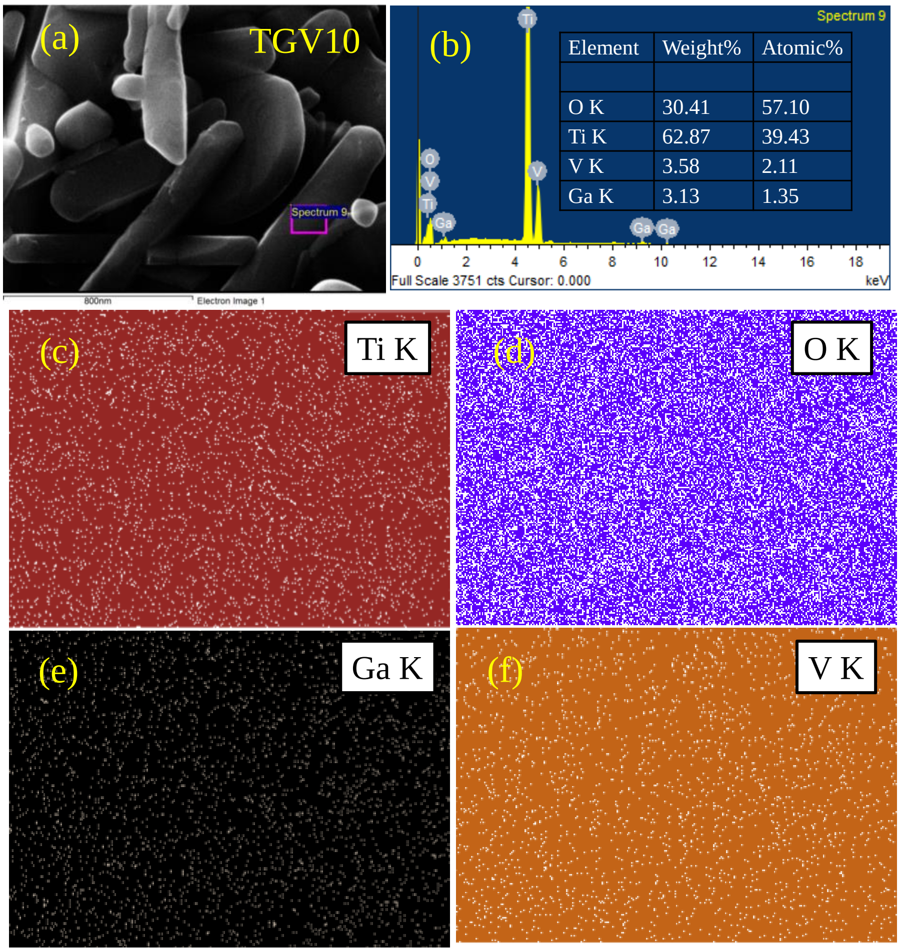

Element	Weight%	Atomic%
O K	30.41	57.10
Ti K	62.87	39.43
V K	3.58	2.11
Ga K	3.13	1.35

Figure 5.10: EDX and elemental mapping of TGV10 sample prepared at 700 °C.

5.3.4 Surface area and pore size studies

To calculate the surface area of the anatase nanoparticles, Brunauer–Emmett–Teller (BET) measurements are carried out on the 450 °C heated anatase samples. Nitrogen adsorption/desorption isotherms of the samples are shown in figure 5.11 (a-e).

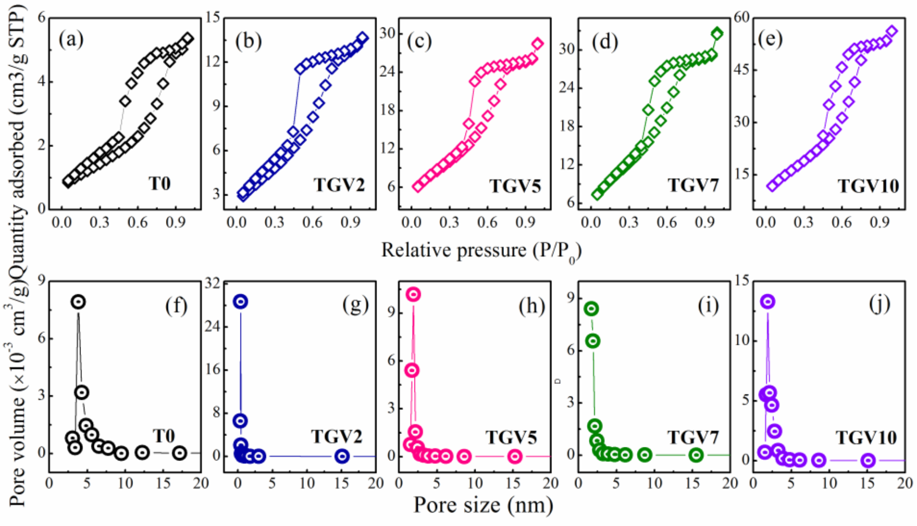

Figure 5.11: (a-e) Nitrogen adsorption/desorption isotherms of the samples prepared at 450 °C and (f-j) pore size distribution curve on desorption isotherm (using BJH method) of the samples.

According to IUPAC classification, isotherms are of type IV. The hysteresis loops are of typical H2(a) type [143]. BET surface area increases with increasing doping concentration (from 4.55 m^2/g (T0) to 59.62 m^2/g (TGV10)). Size and morphology of nanoparticle determine the surface area of the nanoparticle. From TEM analysis, it is observed that particles size decreases with increasing Ga-V incorporation. Smaller the size, larger is the surface area. Hence, the increase of surface area with increasing doping concentration is in good agreement with particles size obtained from TEM. Figure 5.11 (f-j) shown the pore size distribution of the nanoparticles. Pore size distribution of the samples is calculated from Barrett-Joyner Halenda (BJH) method on desorption isotherm. Analysis of pore size distribution shows that pore size of all the samples is less than 4 nm. From the value of pore size, it can be concluded that all the samples are mesoporous type [143]. The mesoporous nature and high surface area may provide a large number of active sites for photocatalytic activity (PCA) of co-doped samples.

5.3.5 Optical properties

Charge compensated Ga-V co-doping not only affects phase transition and grain growth process but also influences the optical properties of TiO_2. Absorption edges and bandgap of the samples are investigated by using DRS measurements. Bandgap of anatase samples (heated at 450 °C) is calculated from $(F(R)h\upsilon)^{1/2}$ vs hυ plot at $(F(R)h\upsilon)^{1/2} = 0$. In case of rutile samples, bandgap is calculated from $(F(R)h\upsilon)^2$ vs hυ plot at $(F(R)h\upsilon)^2=0$.

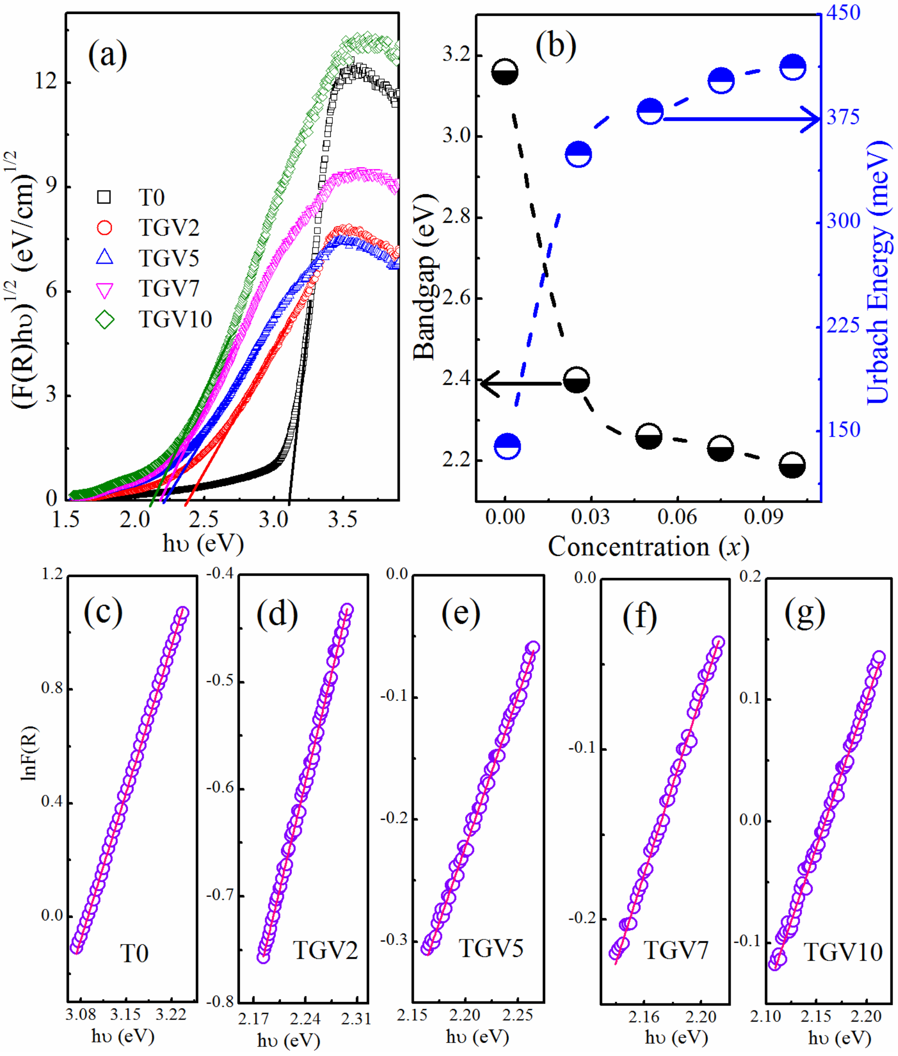

Figure 5.12: (a) DRS spectrum of all the samples prepared at 450 °C, (b) variation of bandgap and Urbach energy with Ga-V doping concentration. (c, d, e, f, and g) shows linear fits of lnF(R) vs hυ plot (violet circles are original data points and pink lines are linear fits to data points).

It is observed that bandgap decreases from 3.16 eV (T0) to 2.19 eV (TGV10) in anatase phase (figure 5.12 (b)), whereas in rutile (figure 5.13 (b)) phase bandgap decreases from 3.08 eV (T0) to 2.19 eV (TGV10).

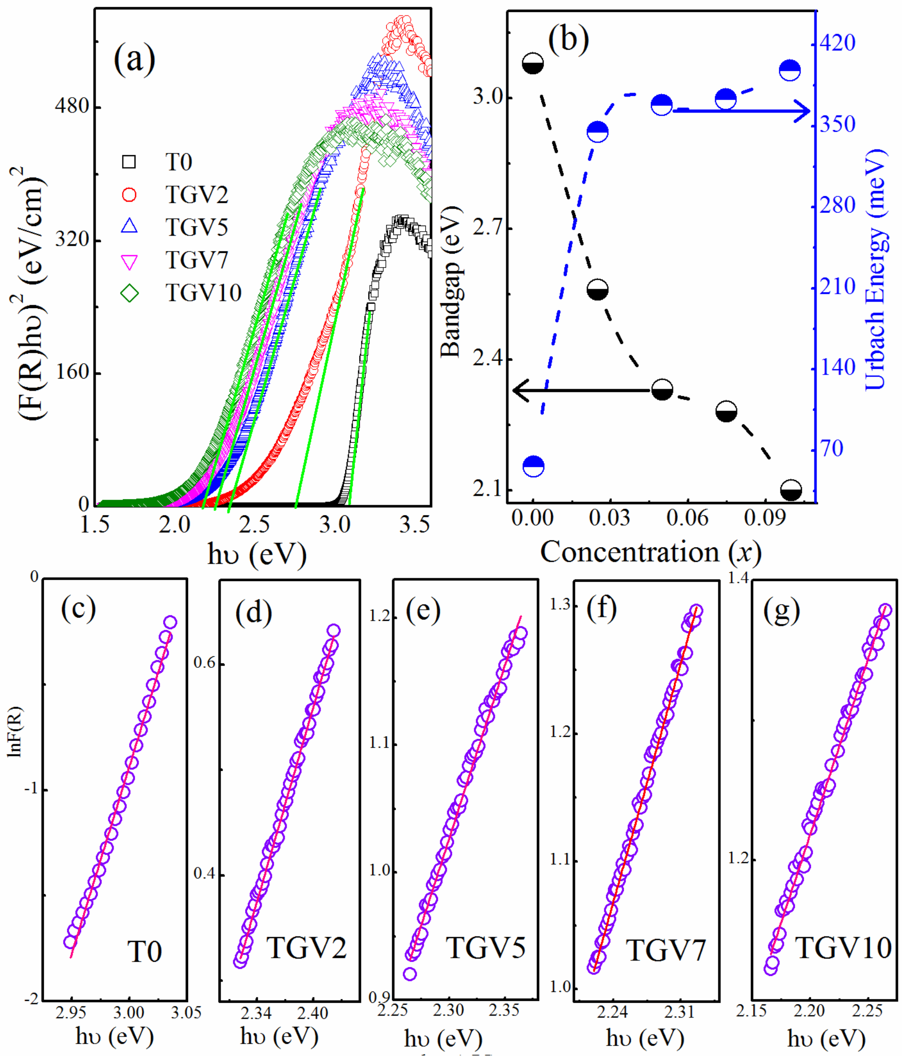

Figure 5.13: (a) DRS spectrum of all the samples prepared at 700 °C, (b) variation of bandgap and Urbach energy with Ga-V doping concentration. (c, d, e, f, and g) shows linear fits of lnF(R) vs hυ plot (violet circles are original data points and pink lines are linear fits to data points).

From XPS, it is observed that due to such type of co-doping (Ga:V=1:1), some Ti^{4+} ions transform to Ti^{3+}. Ga ions occupy both interstitial and lattice sites with majority as interstitials. Oxygen content also changed in the system. These changes result in structural modifications of the lattice. Changes in bandgap and band edges may follow due to the fact that electronic band properties are strongly co-related with crystal structure. Hence, a drastic reduction of bandgap is observed with minimal addition of Ga-V followed by further reduction with higher doping.

Due to Ga incorporation, a nominal increase of bandgap of TiO_2 is observed in Chapter 3. On the other hand, V doping creates donor levels just below the conduction band which thereby drastically reduces the effective bandgap of TiO_2 to the visible light region (Chapter 4).

Here, in Ga-V (1:1) co-doped TiO_2 sample, it is found that bandgap decreases with increase of co-doping concentration in both phases. As the effect of Ga is nominal compared to V, this reduction of bandgap is mainly due to V doping in TiO_2.

Due to structural distortion in the lattice, localized energy states are formed within the forbidden bandgap. These localized states also affect the bandgap of TiO_2. Urbach energy (E_U) is a measure of energy due to structural distortion in the lattice. E_U is calculated from linear fits of "lnF(R)-hυ" plots just below the absorption edge of DRS data. Reciprocal of the slope gives E_U [68]. In anatase phase, E_U increases from 139 meV (T0) to 412 meV (TGV10) (figure 5.12 (b)). For rutile phase; E_U increases from 56 meV (T0) to 398 meV (TGV10) (figure 5.13 (b)). This increase of E_U is also responsible to reduce the bandgap of TiO_2.

5.4 Summary

Summaries of this chapter are mentioned below

1. XRD patterns show that all the samples are in a pure phase of TiO_2.
2. Due to Ga-V (1:1) co-doping, onset temperature shifted to a higher temperature region, whereas complete conversion

(A→R) temperature shifted to lower temperature region as compared to pure TiO_2.

3. Activation energy increases first and then decreases with increasing doping concentration.
4. Rietveld refinement reveals that lattice expands nominally in anatase phase whereas contract in rutile phase.
5. Ti ions have both Ti^{4+} and Ti^{3+} valence states in co-doped sample. All the Ga ions are in 3+ valence state and occupy both lattice and interstitial sites in the lattice.
6. Grain growth process hinders in anatase phase whereas enhanced in rutile phase with increasing doping concentration.
7. Surface area increases with increasing doping concentration.
8. Bandgap decreases to the visible light region in both the phases and Urbach energy increases with increasing doping concentration.

Above results indicate that the co-doped samples can be used as a good candidate for photocatalytic application in presence of visible light, but anatase phase is not stable up to a very high temperature. Hence, chapter 6 is planned, to keep in mind to prepare samples which will absorb visible light and anatase phase become stable to up to a very high temperature.

Chapter 6

Effect of charge uncompensated Ga-V (4:1) co-doping on grain growth, structural phase transition and optical properties of TiO_2

6.1 Overview

In chapter 3, it was observed that Ga ion occupy both interstitial and substitutional sites in TiO_2 lattice. Due to interstitial Ga^{3+} ions, oxygen content increases which expand the lattice and thereby inhibits phase transition. Anatase phase becomes stable up to a very high temperature ~650 °C. However, bandgap of both phases increases due to Ga incorporation. In chapter 4, it was observed that V doping creates donor levels just below the CB, which effectively reduces the bandgap of TiO_2 to visible light region. However, due to substitution of smaller V ions, lattice contracts and thereby accelerates A→R phase transition. Our attempt to achieve "a modified TiO_2 anatase sample, which will be stable up to a very high temperature and will absorb visible light of solar spectrum" was tried with a charge compensated Ga-V (1:1) co-doping in Chapter 5. It was observed that bandgap reduces to visible light region but phase transition happens at a lower temperature (~ 450-500 °C). Hence, in this work uncompensated Ga-V (4:1) co-doping has been chosen to fulfill both the criteria (reduced bandgap anatase phase sample which can sustain its phase up to very high temperature). Effect of uncompensated Ga-V co-doping on structural phase transition, grain growth process and optical properties of TiO_2 has been discussed. Results presented in this chapter are published in peer-reviewed journals[$].

[$] *N. Khatun et al. Cream. Inter. 44 (18) (2018) 22445-22455.*

6.2 Experimental

Structural analysis was studied by powder X-ray diffraction (XRD) patterns using Bruker D2 phaser diffractometer with Cu-Kα radiation (λ=1.5418 Å). Morphology and particle size were investigated using high-resolution transmission electron microscope (HRTEM) (JEOL JEM-2100 LaB6, accelerating voltage - 200 kV) and field emission scanning electron microscopy (Supra55 Zeiss- FESEM). Analysis of surface area and pore size distribution of the samples were done by N_2 adsorption-desorption study using an automated gas sorption analyzer Quantchrome autosorb iQ2. Diffuse reflectance spectroscopy (DRS) measurements were carried out using Bentham TMc300 Monochromator to estimate the changes in the bandgap.

6.3 Results and Discussion

6.3.1 Structural Analysis

XRD pattern for all samples (T0, TGV1, TGV3, and TGV4), heated at temperatures ~450 °C, 500 °C, 550 °C, 600 °C, 650 °C, 700 °C, 750 °C, and 800 °C, are shown in figure 6.1. XRD pattern for all samples heated at 450 °C for 6h (figure 6.1 (a)) matches well with COD ID-9015929 which is of tetragonal anatase phase of TiO_2 having space group $I4_1/amd$. Hence, all the samples are in pure anatase phase. There are no traces of any rutile phase at this temperature. Also, there is no evidence of any simple or complex metal oxide phases related to Ti, Ga, and V. With increasing temperature the anatase phase of the samples gradually starts to convert to a rutile phase and forms a mixed phase. Further heating at a higher temperature (~800 °C), all the TGV samples are converted into an entire rutile phase. XRD patterns of Ga-V co-doped samples (800 °C), matches well with COD ID-9009083 which is of tetragonal rutile phase of TiO_2 having space group $P4_2/mnm$. The samples heat treated between 450-800 °C shows mixed phase of anatase and rutile.

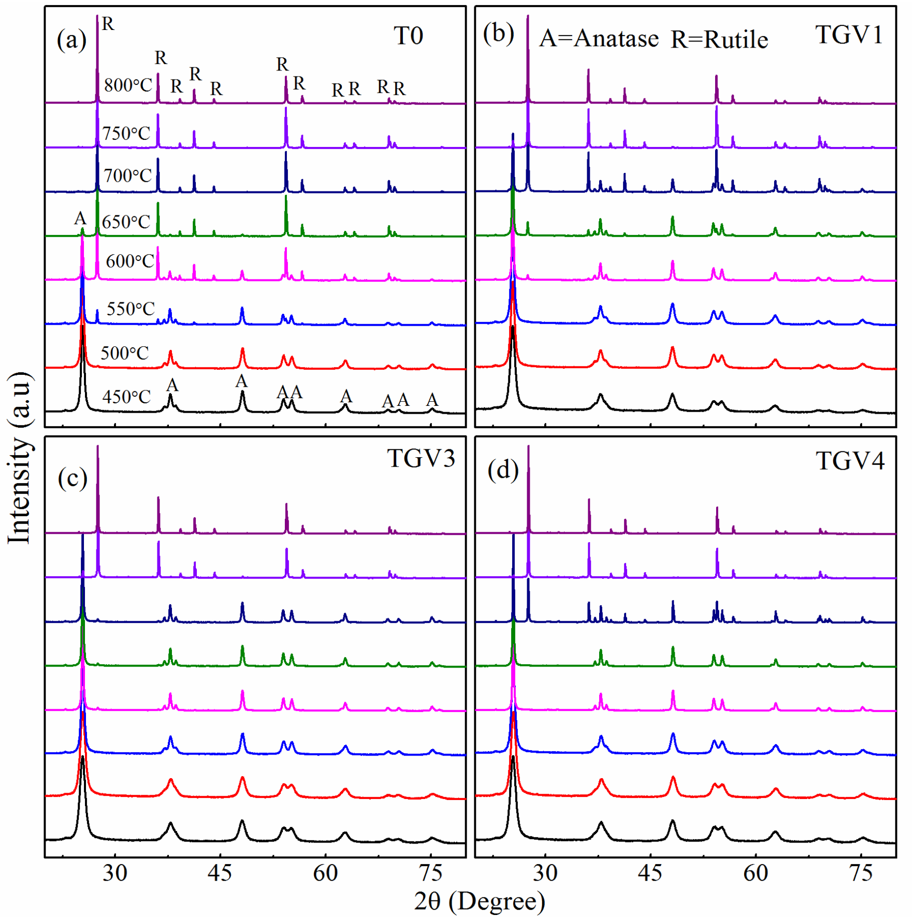

Figure 6.1: XRD patterns of all the samples prepared at eight different temperatures (450-800 °C) in the range of 2θ = 20-80°.

For pure TiO_2 (T0), A→R phase transformation starts in between ~450-500 °C. Phase transition at this particular temperature happens due to the choice of specific reagents (ethylene glycol and citric acid) [96] used in this method. Complete transformation into the rutile phase is observed at ~750 °C. In case of co-doped (Ga-V) samples, no trace of the rutile phase has been detected below ~550 °C. For TGV1 and TGV3, A→R phase transition starts ~550-600 °C. For TGV4, A→R phase transition starts at ~650-700 °C. A complete conversion into the rutile phase happens at ~800 °C. It is observed from the XRD patterns that the appearance of the rutile phase and complete conversion into the rutile phase both are shifted to higher temperature with increasing doping concentration. Hence, Ga and V co-doping into TiO_2 inhibits the phase transition or stabilize the anatase phase to a higher temperature (for TGV1 and TGV3 up to ~550 °C while for TGV4 up to ~650 °C).

Vigilant investigation on XRD patterns of the samples at rutile phase (800 °C) shows small appearance of β-Ga_2O_3 phase for TGV3 and TGV4 samples (figure 6.2) which matches with COD ID-2004987 (β-Ga_2O_3). However, in the anatase phase, such type of impurity has not been detected. Anatase phase has some inherent empty space inside crystal structure [30]. Therefore Ga and V easily incorporated into TiO_2 lattice and occupy the position of interstitials and substitutional sites. Density (ρ) of rutile phase (4.25 gm/cm^3) is higher than anatase (3.89 gm/cm^3) [27]. Hence, rutile phase has less empty space compared to anatase phase. As Ga^{3+} (0.76Å) ion has slightly bigger ionic radius compared to both Ti^{4+} (0.745Å) and $V^{5+/4+}$ (0.68Å/0.72Å), therefore at higher temperature due to thermal instability and less space, Ga^{3+} ions move out from TiO_2 lattice and segregate on the surface of the particles. These Ga ions at higher temperature react with environment oxygen and form β-Ga_2O_3 which are highly dispersed on the surface of particles. β-Ga_2O_3 is a stable crystalline form of gallium oxide at a higher temperature (≥650 °C)[170].

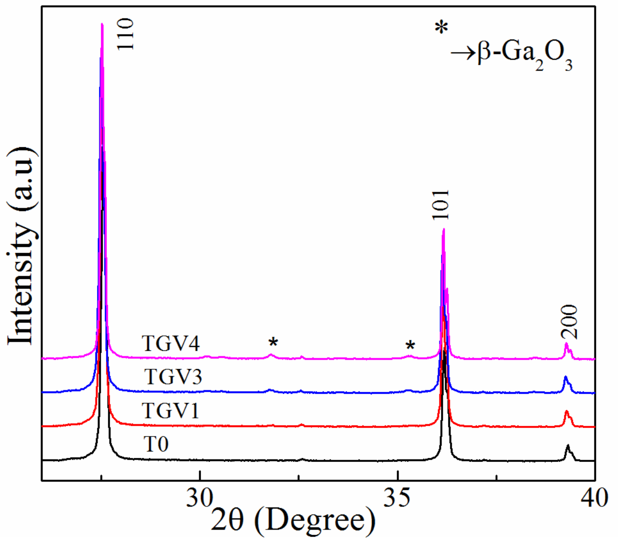

Figure 6.2: XRD pattern of samples heated at 800 °C in the range 2θ = 26-40°.

Rutile phase fraction (f_R) in the mixed phases is estimated at different temperatures using Spurr and Mayers equation [159]. Temperature dependence of f_R (figure 6.3) for co-doped samples ensures an inhibition of phase transformation with increasing doping concentration. All processing parameters (like heating/cooling rates, environment of calcination, etc.) are kept constant. Hence, this inhibition of phase transformation entirely depends on concentration of Ga and V co-doping.

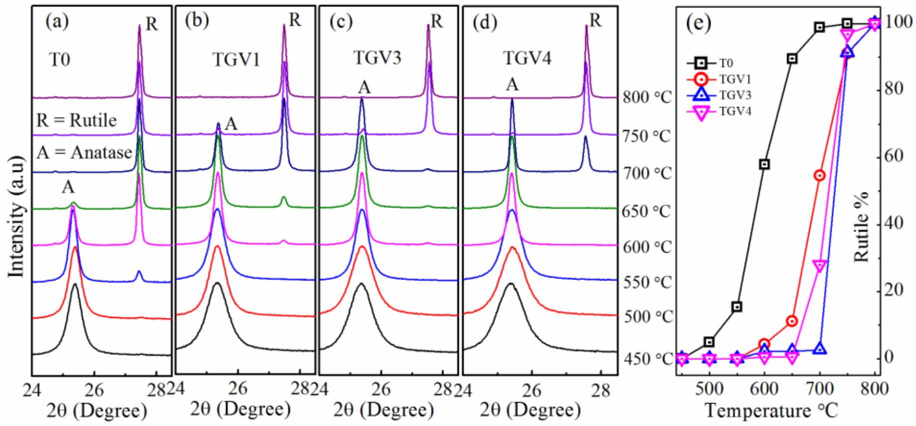

Figure 6.3: XRD patterns of all the samples prepared at eight different temperatures (~450-800 °C) in the range of 2θ = 24.5-28°. (e) Fraction of rutile phase (f_R) at a different temperature.

In general, oxygen vacancy results in lattice contraction and promotes A→R phase transition. On the other hand, interstitials expand the lattice and thereby inhibits the phase transition [33]. Ga ion has slightly bigger ionic (VI-0.76 Å) radius and lesser charge +3 compared to Ti^{4+} (VI-0.745 Å), while V has variable charge states (3+,4+,5+) with ionic radius (V^{3+} (VI-0.78 Å), V^{4+} (VI-0.72 Å), and V^{5+} (VI-0.68 Å)). From literature, it was observed that charge states and ionic radius are very sensitive to accelerate and delay the A→R phase transition [27]. Ga and V ions have different charge states. Total charge compensation can only happen if amount of Ga and V are equal and the entire V-population is in V^{5+} state. Ga: V ratio in all the samples is 4:1. Hence, for charge compensation, it either creates oxygen vacancies or form interstitials. As discussed above, interstitials are responsible for inhibition of phase transitions and XRD results show inhibition of phase transition due to co-doping. This hints that the effect of interstitials is more prominent compared to oxygen vacancies.

Activation energy (E_A) is the minimum energy required to overcome the energy barrier for A→R phase transition between the two phases. It was also observed from literature[161] that E_A decreases due to oxygen vacancies whereas interstitials are responsible for the increase of E_A. E_A is calculated using Arrhenius equation: $ln(f_R) = -\frac{E_A}{RT}$; where, f_R is the fraction of rutile phase present in a sample, R is universal gas constant and T is the temperature in Kelvin. Linear fits of ln(f_R) vs 1/T gives E_A (figure 6.4 (a, b, c, and d)). It is observed that there is a drastic increase in E_A from pure TiO_2 (120 kJ/mol) to TGV3 (243 kJ/mol). For TGV4, E_A decreases slightly (240 kJ/mol) from TGV3 but remains higher compared to T0 and TGV1. This increasing trend of E_A (figure 6.4 (e)) support that the effect of interstitials is more prominent than oxygen vacancies which expands the lattice in Ga-V co-doped samples. This expansion of lattice results in inhibition of phase transition and is consistent with XRD results.

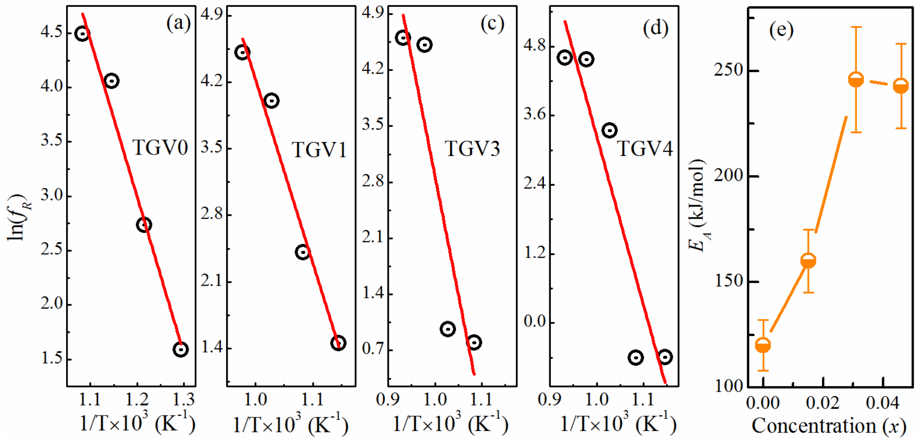

Figure 6.4: Fits of ln(f_R) vs 1/T ((a): T0; (b): TGV1; (c): TGV3 and (d): TGV4). (e) Variation of activation energy with doping concentration (solid line is just a guide to the eye).

Samples in anatase phase, when heated to a higher temperature (≥ 500 °C) leads to rearrangement of Ti-O bonds as a result unit cell volume contracts and phase transformation (A→R) occurs. In anatase phase, lattice constant $a = b$ (3.785 Å) is smaller and c (9.514 Å) is larger compared to lattice constants of rutile phase ($a = b = 4.594$ Å and $c = 2.958$ Å) [27]. Hence, unit cell volume of anatase phase is larger (136.3 Å^3) compared to rutile phase (62.4 Å^3). For phase transition, lattice constant a always increase and c decrease. Hence, this delay of phase transition can be explained in terms of change in lattice constants.

Figure 6.5 (a) shows the Rietveld refinement of TGV samples in pure anatase phase (450 °C). It is observed that all the three lattice constants increase with increasing doping concentration (figure 6.5 (b)). Unit cell volume also follows a similar trend as observed in lattice constants (figure 6.5 (c)).

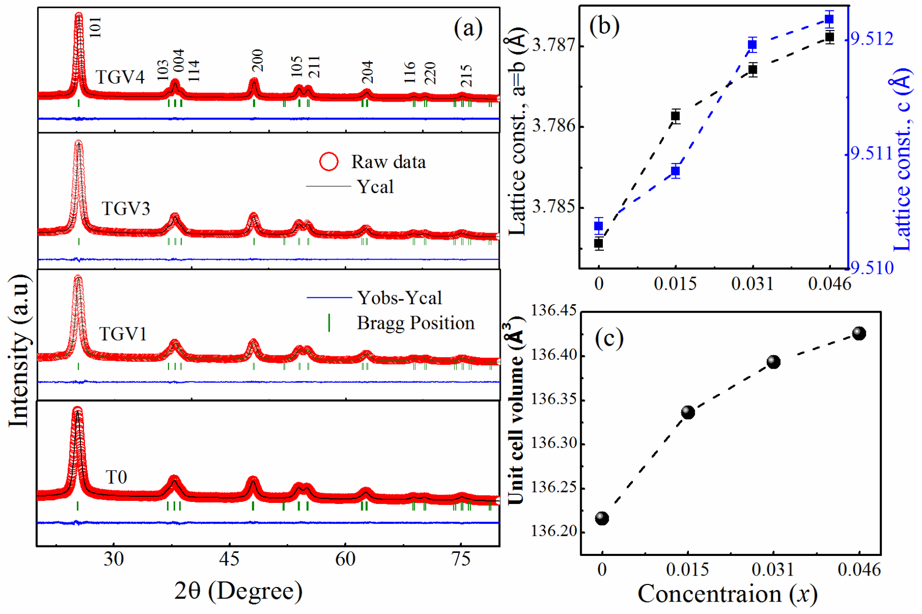

Figure 6.5: (a) Rietveld refinement of Ga-V (4:1) co-doped samples prepared at 450 °C. (b) Change of lattice constants, and (c) unit cell volume with Ga-V doping concentration.

Cr^{3+} has a comparable ionic radius (0.755 Å) as Ga^{3+} and has same charge state. Zhu *et al.* [211] from their DFT calculation showed that anatase phase formation energy is low when Cr^{3+} occupies interstitials sites than substitutional sites. With increasing doping concentration,

Cr^{3+} going from interstitial to substitutional sites was observed to vary. Hence, Ga^{3+} ions too may have the same tendency to go more into interstitial sites than substitutional sites. Banerjee et al.[153] experimentally showed that Ga^{3+} ions occupy more interstitial sites than substitutional sites in TiO_2. These interstitial sites are responsible for the expansion of lattice and inhibit the phase transition. Depero *et al.*[212] experimentally proved that Ga doping inhibits phase transition. It was also observed that formation energy of anatase TiO_2 is low when V occupies the substitutional sites rather than interstitial sites [185]. Hence, theoretically and experimentally it was proved that V occupies substitutional sites in TiO_2 [68, 186, 187] and thereby decrease all the three lattice constants. This is because $V^{4+/5+}$ have smaller ionic radius compared to Ti^{4+}. Vittadini et al.[205] reported that V^{5+} is more likely the major surface species where V^{4+} is stable inside balk. From TEM results, it was observed that particles are in spherical shape and in nano size (discussed later). With increasing doping concentration, particles size decreases which results to increase the surface area to volume ratio of the samples. BET measurement shows surface area increases with increasing doping concentration (table 6.1). Hence, at anatase phase, all the vanadium ions are mostly in 5+ oxidation states [68, 188]. Hence, contraction of lattice constants and thereby unit cell volume by V incorporation promoted the A→R phase transition [148]. In chapter 5, it was observed that Ga ions occupy both interstitial and substitutional sites. Hence, in all the co-doped samples as Ga content is more compared to V (Ga:V=4:1), the effect of Ga interstitials play a significant role over V substitution and oxygen vacancies which expands the lattice. Rietveld refinement on anatase phase shows this expansion of lattice and results in inhibition of phase transition.

From Rietveld refinement on rutile phase (800 °C), it is observed that lattice constants *a* and *b* increase with increasing doping concentration. However, lattice constant *c* nominally increases for TGV1 and thereafter decreases rapidly for TGV3 and TGV4 (6.7 (a)). Unit cell volume also increases for TGV1 and thereafter decreases (for TGV3 and TGV4) (6.7 (b)). As mentioned above that for TGV3 and TGV4, due to thermal instability and less space, few Ga ions move out from lattice structure. Hence, relative percentage of $V^{4+/5+}$ ions compared to Ga^{3+} ions increases from targeted values (4:1). In rutile phase, due to higher temperature (800 °C), particles size increases for all TGV samples and with increasing doping content and grain growth process enhanced (discussed later at figure 6.12). Hence, surface area to volume ratio decreases which results to increase in V^{4+} species in the samples as discussed above that V^{4+} is more likely stable into the bulk.

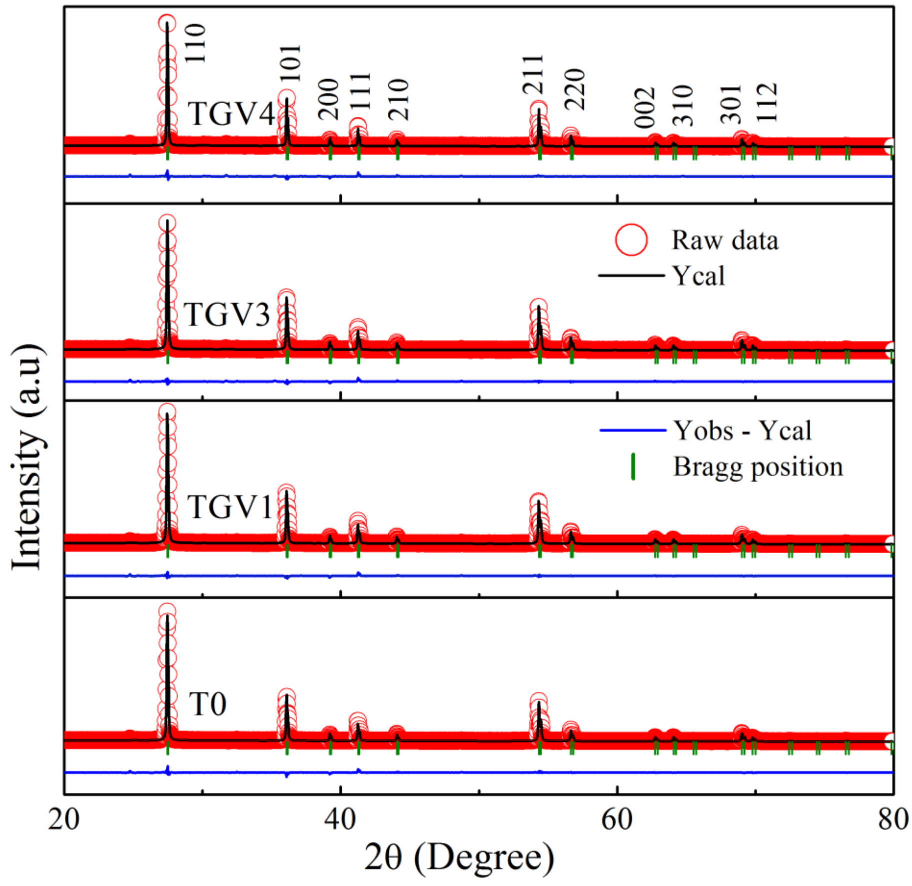

Figure 6.6: Rietveld refinement of Ga-V (4:1) co-doped samples prepared at 800 °C.

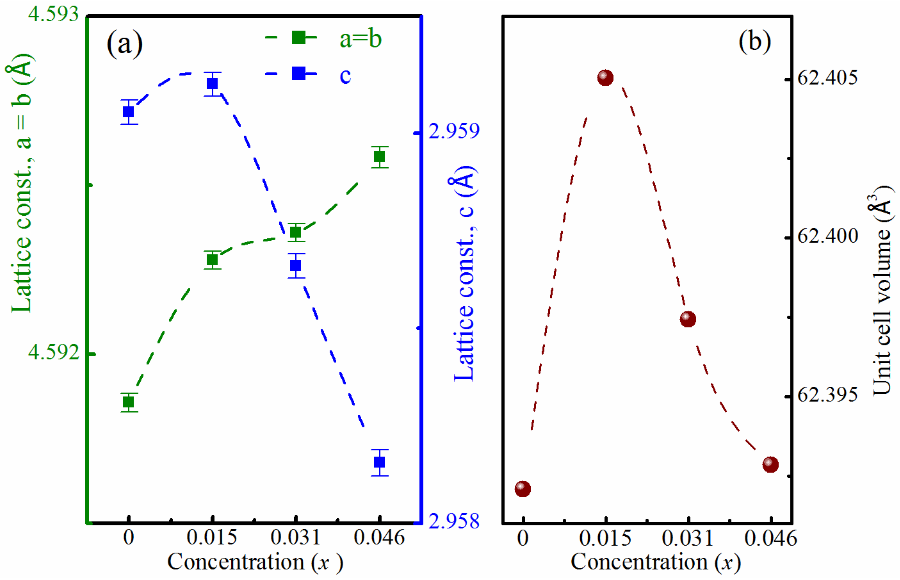

Figure 6.7: (a) Change of lattice constants and (b) unit cell volume with Ga-V (4:1) doping concentration.

In chapter 4, it was observed that V ions are in mixed valence states of V^{5+}/V^{4+} and with increasing doping concentration presence of V^{4+} ions increases. In rutile phase, both the V^{5+} and V^{4+} ions occupy the substitutional sites in TiO_2 lattice. $V^{5+/4+}$ ions have smaller ionic radius compared to Ti^{4+} and Ga^{3+} which results in a decrease of lattice constants *c* as well as unit cell volume. Ga^{3+} ions occupy more interstitials sites than substitutional sites in TiO_2 discussed above. At lower doping (TGV1), as all the Ga ions are inside the crystal structure and due to significant role of this Ga^{3+} interstitials unit cell volume increased. However at higher doping (TGV3 and TGV4), due to substitutional $V^{4+/5+}$ ions and oxygen vacancies unit cell volume decreased.

6.3.2 Particle size, microstructure, and morphological analysis

HRTEM is a very powerful tool to investigate a particle in a very small range (~1-2 nm). It gives crystallographic information and clear morphology of the nanoparticles. Figure 6.8 (a and c) shows the TEM images of T0 and TGV3 samples. Almost spherical shape particles are observed for both the samples. Particles size of both the sample has been calculated using Image J software. Histogram of T0 and TGV3 sample (inset of figure 6.8 (a) and (c)) shows average particles size are in the range of ~12-15 nm and ~8-10 nm respectively. It is observed that particle size reduces due to co-doping. In V doped TiO_2, it was observed that crystallite size reduced with doping [186, 188]. Ga doping also reduces crystallites size [170, 179]. Hence, a combination of V and Ga co-doping is supposed to reduce crystallite size. TEM results confirm the same. In most cases, strain increases upon doping of foreign elements into TiO_2 and this strain hinders the grain growth process of nanoparticles.

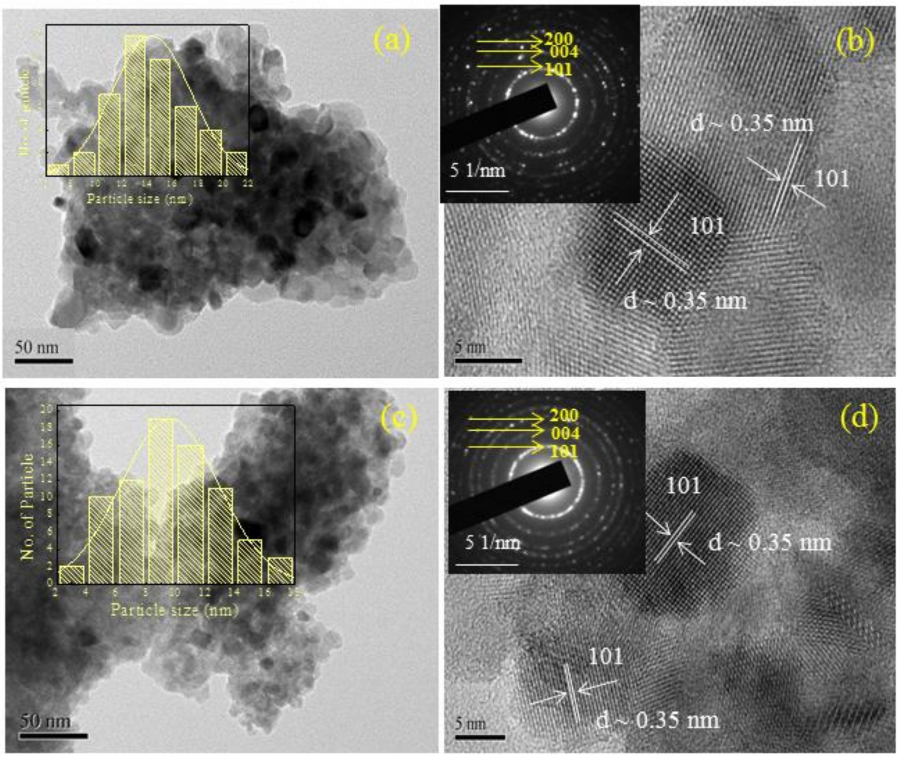

Figure 6.8: (a) TEM images of T0 and (c) TGV3 samples prepared at 450 °C. Inset shows the histogram of particles size distribution of corresponding samples. (b and d) HRTEM images of T0 and TGV3 and insets show SAED pattern of corresponding samples.

From HRTEM images, it is observed that *d*-spacing of lattice fringes of both the samples are ~0.35 nm which corresponds to 101 planes of anatase TiO_2 (figure 6.8 (b: T0 and d:TGV3). Clarity of the fringes signifies that both the samples are well crystalline. Such a good crystallinity at a low temperature ~450 °C, is possible due to proper choice of specific reagents (ethylene glycol and citric acid) [94, 96] used in this synthesis methods. The ring-like SAED patterns (inset of figure 6.8 (b: T0 and d: TGV3) reveals the polycrystalline nature and confirms anatase phase of TiO_2 of both the samples.

To investigate the effect of Ga and V co-doping on grain growth process, crystallite sizes (at 450 °C) is calculated using the Scherrer equation. It is observed that crystallites size decreases from 18.1 (pure TiO_2) nm to 8.8 nm (TGV4) by Ga-V incorporation (figure 6.9 (e)). Hence, co-doping restrains the grain growth process of anatase nanoparticles which is consistent with TEM results. In most metal oxides this restrains grain growth is due to increasing strain in the nanoparticles.

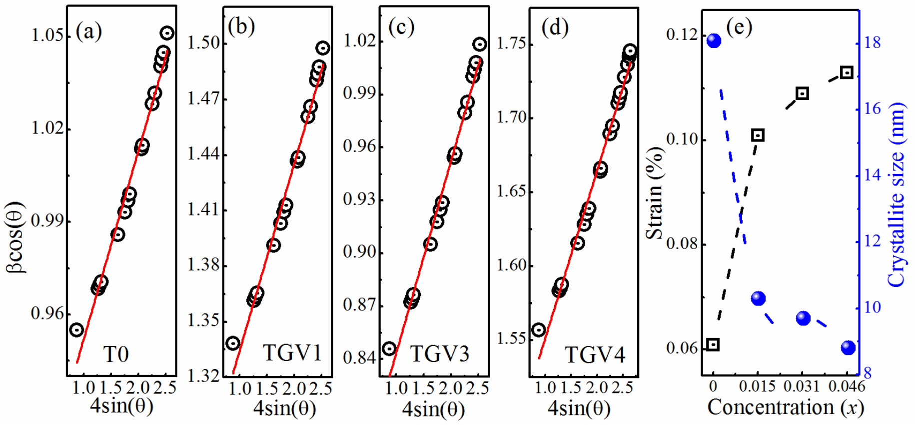

Figure 6.9: Linear fits of βcos(θ) vs 4sin(θ) of Ga-V (4:1) co-doped samples prepared at 450 °C. (e) Change of strain and crystallites size with doping concentration.

Such increase of strain in lattice due to Ga-V co-doping has been verified by the shape and peak positions of the pure samples (450 °C). Usually, crystallites in polycrystalline aggregates are in a state of compression or tension by its neighboring crystallites which produce uniform or non-uniform strain in the lattice.

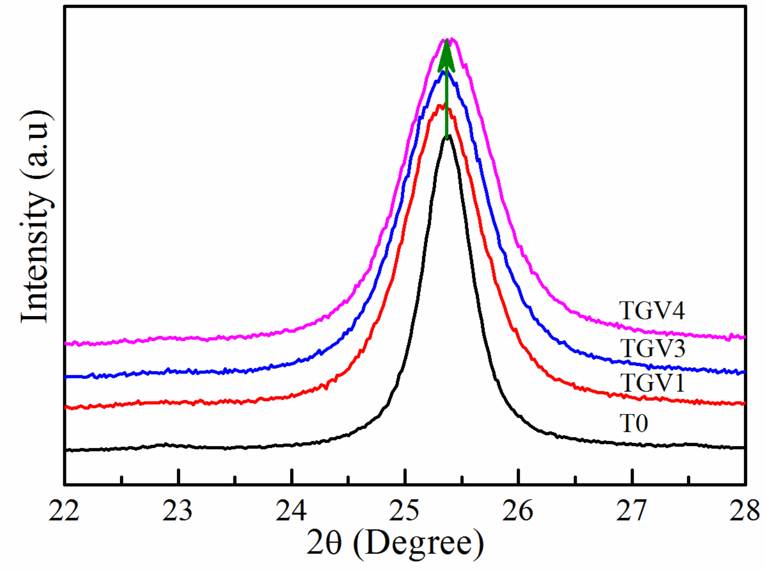

Figure 6.10: XRD patterns of samples prepared at 450 °C in the range 2θ = 22-28°.

From the literature, it was observed that shifting of diffraction peak creates uniform strain whereas peak broadening without changing peak position creates non-uniform strain [153]. Careful inspection reveals that the 101 peaks become broad but the position remains almost the same of the samples (figure 6.10). Hence, incorporation of Ga and V at lattice sites as well as in interstitial sites may be responsible for such nonuniform stain. Williamson Hall plot is used to calculate quantitative changes in strain due to Ga-V co-doping. Slope of linear fits of $\beta\cos(\theta)$ vs $4\sin(\theta)$ gives strain; where β is the FWHM of corresponding peaks. It is observed that strain increases with doping concentration (figure 6.9 (e)). This increasing strain due to Ga-V incorporation retards the grain growth process of anatase nanoparticle.

Figure 6.11 shows the FESEM images of the rutile phase samples (800 °C). Oliver et al. [213], from their DFT calculations on rutile phase, reported that (110) surface has the lowest surface energy (1.78 J/m^2), whereas (100) surface perpendicular to (110) surface has highest surface energy (2.08 J/m^2). During crystal growth, the low energy surface (110) grows fastest and high energy surface (100) tend to decrease its surface area to minimize the total energy per crystal [214]. As mentioned above, particles are almost in spherical shape of anatase samples (450 °C). With increasing temperature anatase phase is converted into mixed phase and with further heating transform into an entire rutile phase. Similarly, particle shape and size also changed with temperature. With increasing temperature spherical anatase crystals enlarge its size and become elongate spherical to rod-like structure.

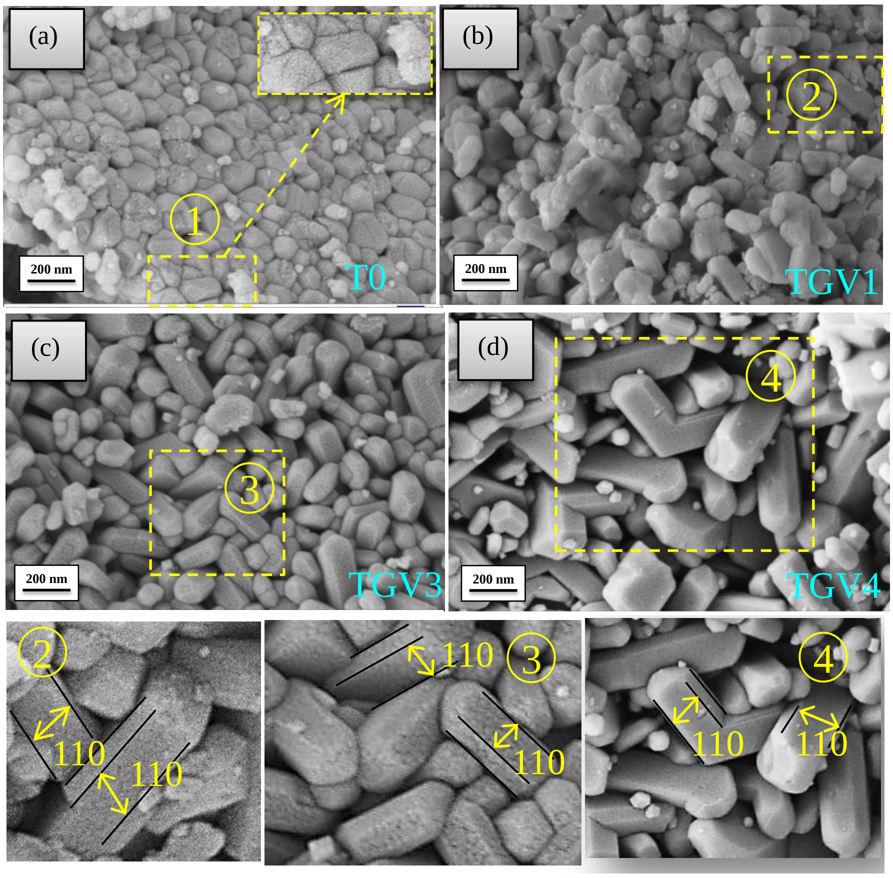

Figure 6.11: FESEM images of the samples prepared at 800 °C: (a) T0, (b) TGV1, (c) TGV3, and (d) TGV4.

For pure TiO_2 (T0), particles are in irregular spherical shape or distorted rod-like structure and average particles size is ~200 nm (calculated using Image J software). From these images (all the images are in the same magnification), it clearly observed that particles have prominent rod-like structure and grain growth process enhanced with increasing doping concentration. It was observed that Ga doping restrains the rutile grain growth process [212]. Whereas in chapter 4, it was observed that V enhanced the grain growth process. Effect of vanadium is more sensitive for grain growth process of rutile particle than gallium. Hence, the faster grain growth process in co-doped samples is mainly due to the effect of vanadium. According to the nature of surface edges and area at par with reported literature, 110 surfaces are the most prominent surfaces of rutile particles [213, 215, 216]. Some portions of FESEM images of TGV samples have been zoomed to show these surfaces. For T0 samples, the zoomed view is shown in the inset of figure 6.11 (a). The zoomed views of the co-doped samples are shown as ② (TGV1), ③ (TGV3), and ④ (TGV4).

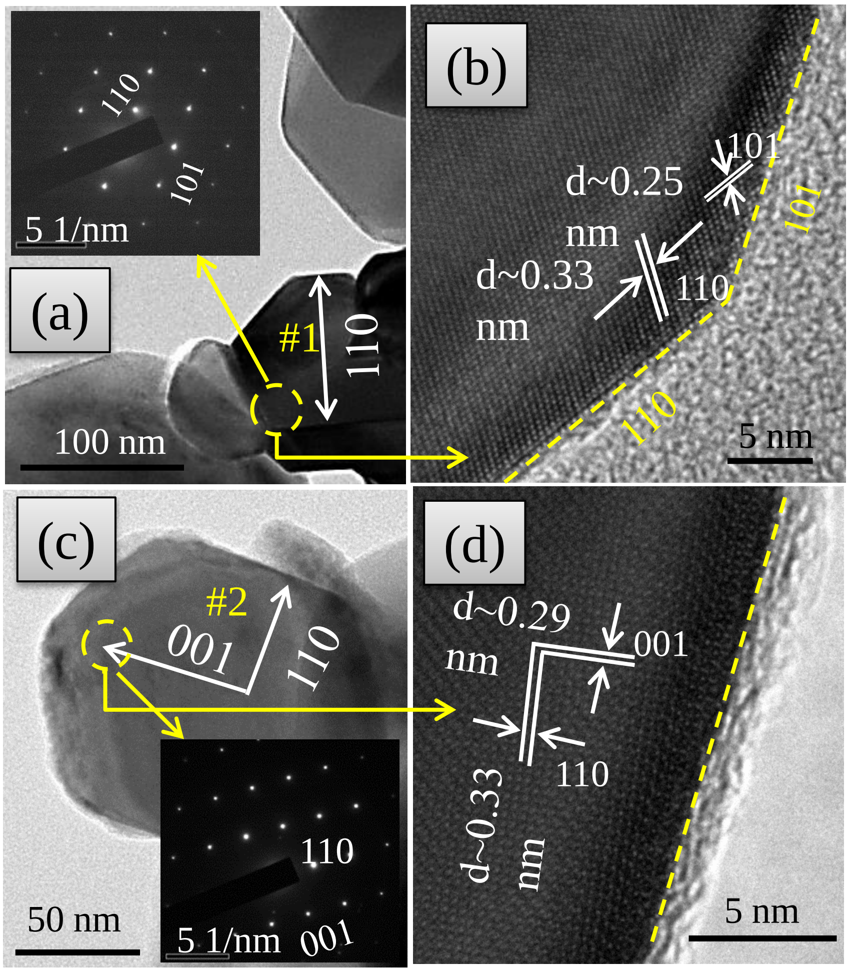

Figure 6.12: (a) and (c) Show TEM images of TGV1 sample prepared at 800 °C and inset show the corresponding SAED patterns. HRTEM images (b) and (d) show lattice fringes of the particles.

TEM images of TGV1 sample heated at 800 °C are shown in figure 6.12 ((a) and (c)). SAED patterns of the particle are shown as insets of corresponding images and it belongs to the rutile phase of TiO_2. The *d*-spacing of HRTEM images are also belonging to the same crystallographic planes (particle #1, d_{110}~0.33 nm and d_{101}~0.25nm (figure 6.12 (b)) while in particle #2, d_{110}~0.33 nm and d_{001}~0.29 nm (figure 6.12 (d))). From these images, it is observed that 110 facets are the major surface of the particles. The size of the particles seems to be in the range of ~100 nm and beyond. This is smaller than the average size obtained from FESEM studies. A possible reason may be the sample preparation process for TEM measurements. Disperse solution of samples are prepared in ethyl alcohol and a droplet is dropped on TEM grids and dried. In most cases, only the lighter and smaller particles get selected in this process.

6.3.3 Surface area and pore size studies

Nitrogen adsorption/desorption isotherms (figure 6.13) of all the samples display type IV isotherms according to IUPAC classification. Hysteresis loop of the isotherms is of typical H2(a) type [143]. BET surface area increases from 4.55 m^2/g (T0) to 96.53 m^2/g (TGV4). Surface area depends on the size and morphology of nanoparticles. Smaller the size, larger is the surface area of nanoparticles. This increase of surface area is the result of reduced crystallites size by Ga-V incorporation as mentioned above. Pore size distribution is calculated from BJH method on the desorption isotherms (figure 6.13 (e-h)). Pores sizes for all samples are <4 nm. Mesoporous materials have pore diameters ranging from 2 nm to 50 nm [143]. Hence, these samples can be classified as mesoporous materials based on the pore diameter and nature of the hysteresis loop. A larger surface area due to Ga-V incorporation provides a large number of active sites which makes the materials better for PCA.

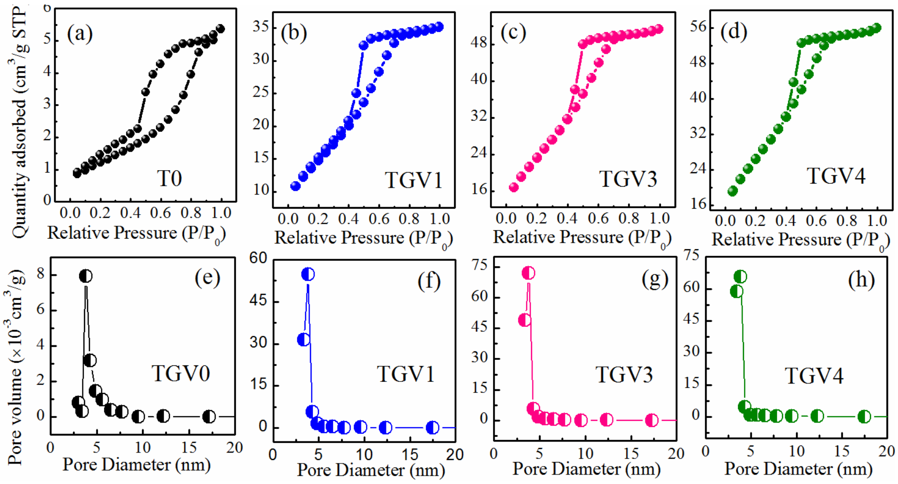

Figure 6.13: (a-d) Nitrogen adsorption/desorption isotherms of the samples prepared at 450 °C and (e-h) Barrett-Joyner Halenda (BJH) pore size distribution curve of the samples.

Table 6.1: BET surface area, pore diameter, pore volume of Ga-V (4:1) co-doped TiO_2 samples prepared at 450 °C.

Sample name	BET surface area (m^2/g)	Pore diameter (nm)	Pore volume (cm^3/g)
T0	4.55	3.819	0.009
TGV1	53.95	3.823	0.044
TGV3	85.25	3.826	0.060
TGV4	96.53	3.829	0.061

6.3.4 Optical properties

Ga-V (4:1) co-doping also affects the optical properties of TiO_2. Room temperature DRS measurement has been carried out to investigate the bandgap of the samples (figure 6.14 (a) and (b)). Bandgap is calculated using the same Tauc plot as used in our previous chapters. It is observed that bandgap decreases due to co-doping for both the phases. At anatase phase, bandgap decreases from 3.14 eV (T0) to 2.86 eV (TGV4) (figure 6.14 (c)) and at rutile phase, bandgap decreases from 3.06 (T0) to 2.84 eV (TGV4) (figure 6.14 (d)). O 2p and Ti3d hybridization (p-d) form strong bonding states which is responsible to form valence band (VB) in TiO_2. On the other hand antibonding states due to p-d hybridization between O 2p, Ti 3d and Ti 2p form conduction band (CB) [35]. Due to Ga doping, the hybridization between O 2p and Ga 4p gives defects states in valence band which therefore widen the bandgap of TiO_2 [151, 170]. From literature, it was also observed that the effect of Ga for enhancement of bandgap is not much pronounced [152, 153, 170, 179]. In case of V doped TiO_2, p-d hybridization of O 2p, Ti 3d, and V 3d form impurity energy levels (or donor levels) inside the bandgap. Due to these energy levels bandgap decreases [188]. It was also observed that the effect of V is more sensitive compared to Ga for bandgap change. Hence, due to combined effect of both V and Ga, bandgap decreases in co-doped samples.

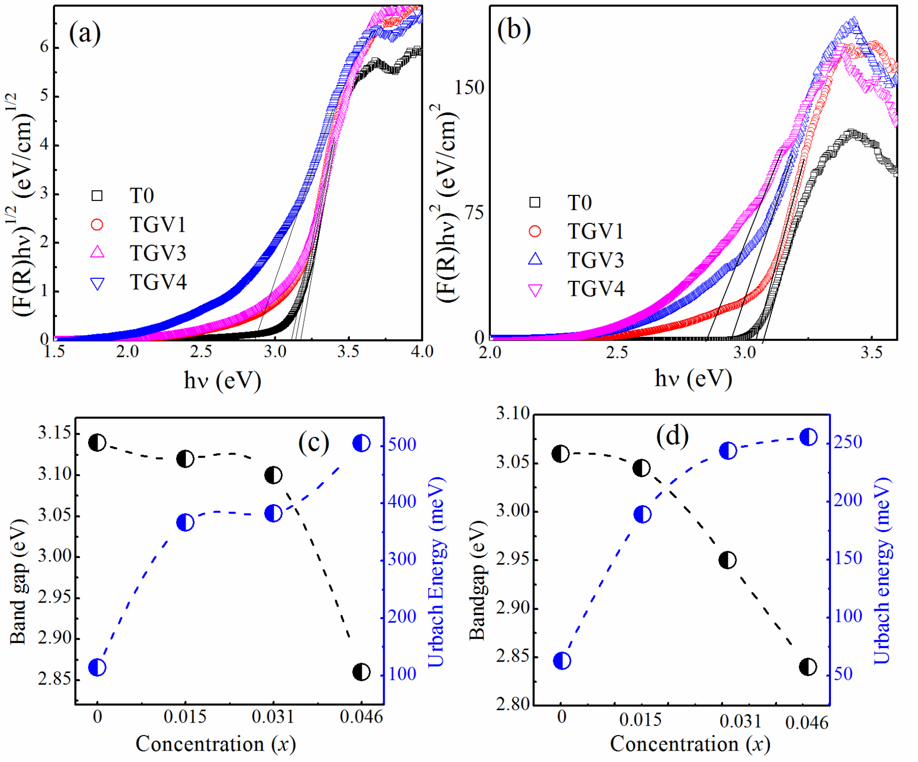

Figure 6.14: Room temperature DRS data of Ga-V (4:1) co-doped samples prepared at 450 °C (a) and 800 °C (b). (c) and (d) shows the change of bandgap and Urbach energy with doping concentration.

In case of rutile phase, bandgap gradually shifted to lower values from 3.06 eV (T0) to 2.84 eV (TGV4) with increasing doping concentration. For TGV1, bandgap shows slight red shift because V concentration is very low in the samples (Ga: V ~4:1). For TGV3 and TGV4, it is observed from XRD data that some amount of Ga^{3+} ions move out of the lattice and forms β-Ga_2O_3 phase. Hence, relative amount of $V^{4+/5+}$ to Ga^{3+} is increased (Ga:V=4:1; ratio decreased) compared to intended values. It was discussed that V^{4+} ion is more effective than V^{5+} ion in reducing the bandgap [208] of TiO_2: ($E_g(V^{4+})<E_g(V^{5+})$). This may also be a reason, for a gradual shift of bandgap at rutile phase.

Structural modifications are inevitable when foreign elements are incorporated into any lattice. It is known that electronic band structure is strongly correlated with lattice structure. Urbach energy (E_U) is a measure of lattice distortion in the samples which affects electronic band structure [180, 181]. In most semiconductors, it was observed that bandgap decreases if E_U increases [183, 184]. E_U is calculated from linear fits of "lnF(R)-hυ" plots just below the absorption edge of DRS data. Reciprocal of the slope gives E_U [68]. In anatase phase, E_U increases from 145 meV for T0 to 506 meV for TGV4 (figure 6.14 (c)). Whereas for rutile phase; E_U increases from 63 meV for T0 to 256 meV for TGV4 (figure 6.14 (d)). This increase in E_U signifies a more distorted lattice due to co-doping and a band tailing (Urbach tail) just below absorption edge.

6.4 Summary

Major outcomes of this chapter are listed below

1. XRD pattern shows that both onset/A→R temperature shifts to higher temperature region. Anatase phase becomes stable up to ~650 °C.
2. Activation energy of phase transition increases with increasing Ga-V incorporation.
3. Lattice expands with increasing doping concentration in

anatase phase.

4. Grain growth process hinders in anatase phase but enhanced in rutile phase. HRTEM analysis shows that (110) surface play a major contribution to the total surface area in rutile particle.
5. Strain increases with increasing doping concentration in anatase phase.
6. BET analysis shows that surface area increases from 4.55 m^2/g (x=0) to 96.53 m^2/g (x=0.046) by Ga-V incorporation.
7. Bandgap decreases in both phases and reduces to the visible light region.

Hence, co-doped anatase nanoparticles can be used as a good photocatalyst using visible light up to a higher temperature ~650 °C. It can also be used in other optoelectronic devices.

Chapter 7

Conclusions and future scope

There are different parameters which control stabilization of anatase phase and reduce bandgap. In this work, lesser charged but larger Ga^{3+} and more charged but smaller V^{5+} ions are used in different combination to see its effect on the above properties. The series studied are as follows (a) $Ti_{(1-x)}Ga_xO_2$, (b) $Ti_{(1-x)}V_xO_2$, (c) $Ti_{(1-x)}(Ga_{0.5}V_{0.5})_xO_2$ and (d) $Ti_{(1-x)}(Ga_{0.8}V_{0.2})_xO_2$.

7.1 Major findings and achievements

7.1.1 Synthesis and solubility

- Solubility limit of sol-gel prepared $Ti_{(1-x)}Ga_xO_2$, (modified with lesser charged Ga^{3+} in place of Ti^{4+}) is ~10% for both anatase and rutile phases. Secondary phases are observed above 10% doping.
- In case of $Ti_{(1-x)}V_xO_2$, (higher charged V^{5+} doping) the solubility limit is ~9% in anatase phase but ~6% in rutile phase.
- For $Ti_{(1-x)}(Ga_{0.5}V_{0.5})_xO_2$, solubility limit remains same ~10% for both phases similar to $Ti_{(1-x)}Ga_xO_2$.
- However, for $Ti_{(1-x)}(Ga_{0.8}V_{0.2})_xO_2$ the solubility limit reduces to ~4.6 % for anatase phase, and ~1.5% for rutile phase.

7.1.2 Phase transition and activation energy

Analysis of XRD pattern and Raman spectra shows that all the samples heated at 450 °C are in anatase phase. Anatase phase gradually starts to convert into rutile phase at an onset temperature ~450-500 °C (pure TiO_2). With further heating, the entire anatase phase transforms into rutile phase at A→R temperature. The minimum energy required for this phase transition is called activation energy (E_A). Due to doping (Ga, V, Ga-V), onset and A→R temperature changes (figure 7.1).

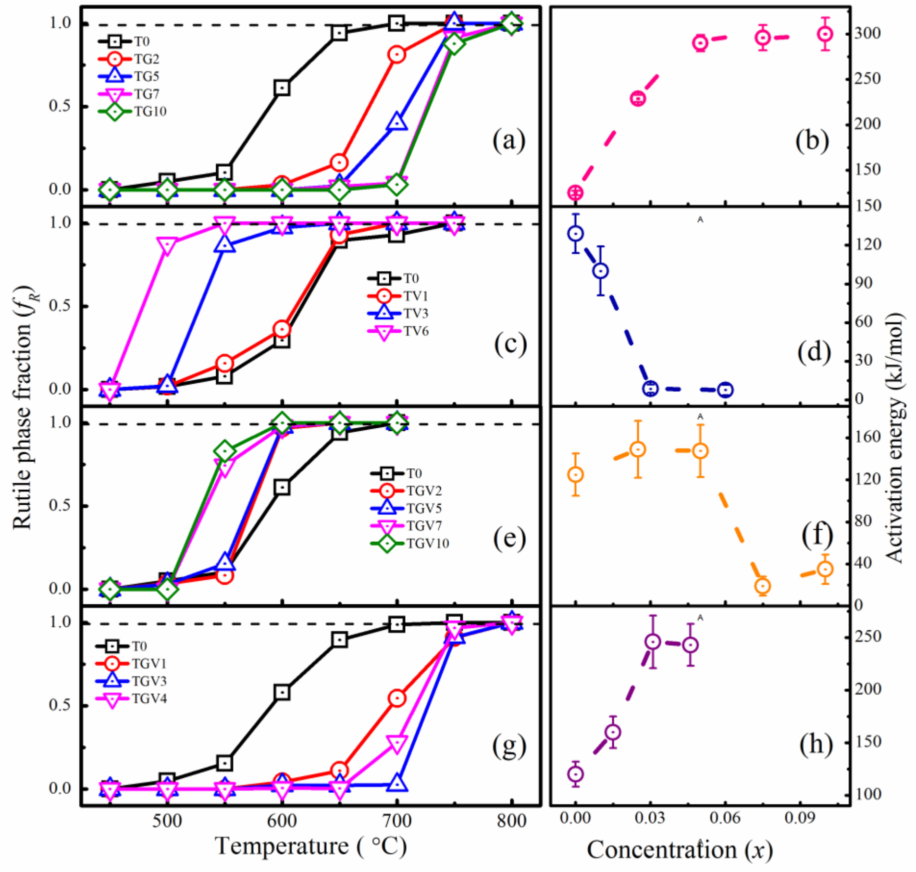

Figure 7.1: Rutile phase fraction (f_R) at different temperature (450-800 °C) and change in activation energy of Ga (a-b), V (c-d), Ga-V (1:1) (e-f) and Ga-V (4:1) (g-h) doped samples.

- **Ga doped**

Onset and A→R temperature are both delayed by incorporation of lesser charged but bigger size Ga^{3+} ions. XPS study of these samples shows that at lower doping (≤0.05), Ga^{3+} ions prefer to occupy more interstitial sites (Ga_I) than substitutional (properly replace Ti^{4+} ions) sites (Ga_L) while reverse happens at higher doping (>0.05). These Ga_I are responsible to increase oxygen content in the lattice. This leads to lattice expansion which results in delaying both the temperature.

Literature reveals that E_A increases due to interstitials and decreases due to oxygen vacancies. In this case, E_A increases in agreement with literature. At lower doping, E_A increases drastically and then saturates at higher doping as Ga_I is higher at lower doping which then decreases at higher doping.

- **(b) V^{5+} doped**

Onset and A→R temperature, shifts to lower value by doping of higher charged but smaller V^{5+} ions. XANES analysis of anatase phase samples confirms that the entire V ions are mostly in V^{5+} states. Also, some Ti^{4+} ions convert into Ti^{3+} ions. V^{5+} ions properly substitute Ti^{4+} in TiO_2 lattice. Size of V^{5+} is smaller than Ti^{4+} and Ti^{3+}. This results in contraction of lattice and promotes phase transition. This lattice contraction is also responsible for decrease of E_A with increasing V concentration.

- **(c) Ga-V (1:1) Co-doped**

Onset temperature is delayed whereas A→R temperature is promoted by Ga-V (1:1) co-doping. From both charge and size perspective the Ga-V modified TiO_2 system is equivalent to pure TiO_2. However, the crystal structure is modified in spite of the charge/size invariance. XPS measurements of these samples show that Ti has two type of valence states Ti^{4+} and Ti^{3+}. Ga ions are in Ga^{3+} states and occupy both interstitial and substitutional sites. This is similar to $Ti_{1-x}Ga_xO_2$. Oxygen vacancies are increased in co-doped samples than pure TiO_2. It is an expectation that most of the V ion are in V^{5+} states. Hence, expansion of lattice due to bigger size of Ti^{3+} and Ga_I are compensated by both oxygen vacancies and smaller size V^{5+} ions. But the combined effect of all these factors nominally expands the lattice and thereby slightly delayed the onset temperature. At higher temperature, V shows mixed valence states of V^{5+}/V^{4+} (Chapter 4). Due to high temperature, oxygen vacancies may increase in rutile phase. Hence, lattice contracts and thereby promoted A→R temperature.

Onset temperature delays with increasing doping concentration. An opposite behavior is observed for A→R temperature. Therefore, E_A increases at first and then decreases.

(d) Ga-V (4:1) co-doped

Similar to chapter 3, onset and A→R temperature both are delayed. Here, Ga^{3+} : V^{5+} = 4:1. Ga has a tendency to occupy more interstitial sites than substitutional sites. Thus, Ga_I is responsible for above-delayed behavior. E_A follows a similar trend as observed in Ga doped sample.

7.1.3 Structural properties

Crystal structures of Ga / V modified TiO_2, in both anatase and rutile phases, are studied by Rietveld refinement (using Fullprof suit software) of RT XRD data (figure 7.2). Difference in charge and ionic radius of Ga and V than Ti are responsible for it.

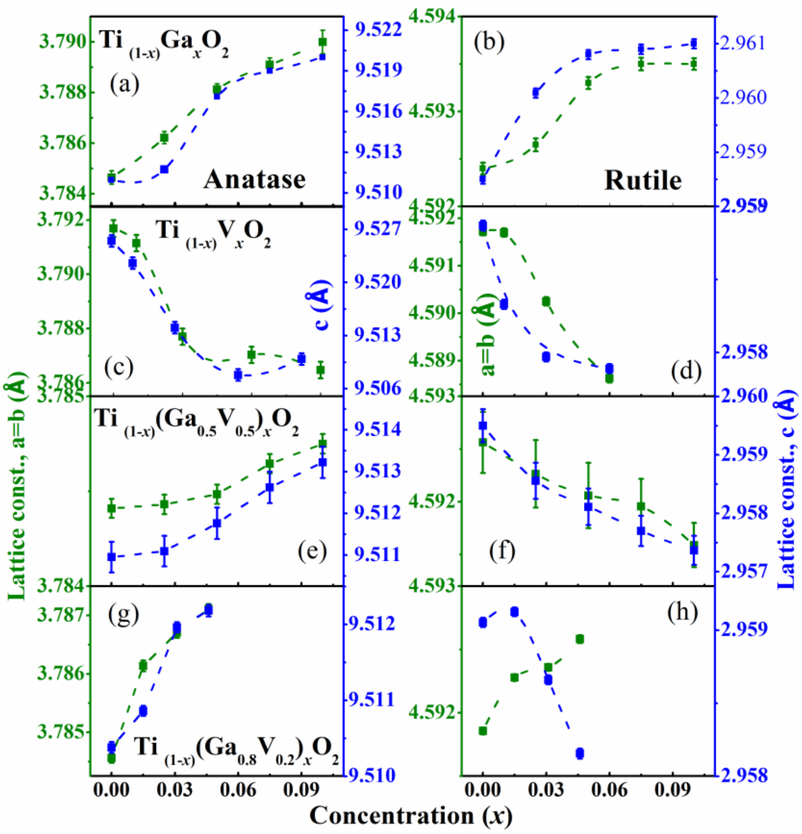

Figure 7.2: Variation of lattice constants of anatase and rutile phase of TiO_2 by Ga (a-b), V (c-d), Ga-V (1:1) (e-f) and Ga-V (4:1) (g-h) doping into TiO_2.

- **Ga doped**

Larger Ga^{3+} ions tend to occupy more interstitial sites. This is responsible for increase in lattice constants (*a, b, c*) with increasing doping concentration in both the phases.

- **(b) V doped**

Lattice constants (*a, b, c*) of V doped TiO_2 samples decreases with increasing V incorporation. V ions are mostly in V^{5+} states in the anatase phase and in a mixed valence state (V^{5+} and V^{4+}) in rutile phase (chapter 4). Smaller V^{5+}/V^{4+} ions compared to a larger Ti^{4+} are responsible for lattice contraction in both the phases.

- **(c) Ga-V (1:1) co-doped**

Ti^{3+} and Ga_I (discussed in chapter 5) are responsible for nominal increases in lattice constants in anatase phase. Rutile phase formed at higher temperature, shows contracted lattice parameters due to increase of oxygen vacancies in modified TiO_2.

- **(d) Ga-V (4:1) co-doped**

Due to similar reasons as discussed in Ga doped TiO_2 samples, lattice constants increases in the anatase phase. In the rutile phase, all three lattice constants *a*, *b*, and *c* first increases up to TGV1. Thereafter *a*, *b* continue to increase in both the phases but *c* increase in anatase phase and decreases in rutile phase. In rutile phase, some Ga ions move out of the lattice. This effectively increases the V concentration and thereby a lattice contraction is observed at higher doping.

7.1.4 Grain growth, particles size, and lattice strain

Variation of crystallites size and strain with doping concentration are shown in figure 7.3. Crystallite size decreases while strain increases with increasing doping concentration in samples of anatase phase. The presence of a dopant in the TiO_2 lattice generates strain due to difference in charge and size. The increased strain retards grain growth in anatase phase, therefore particle size reduces.

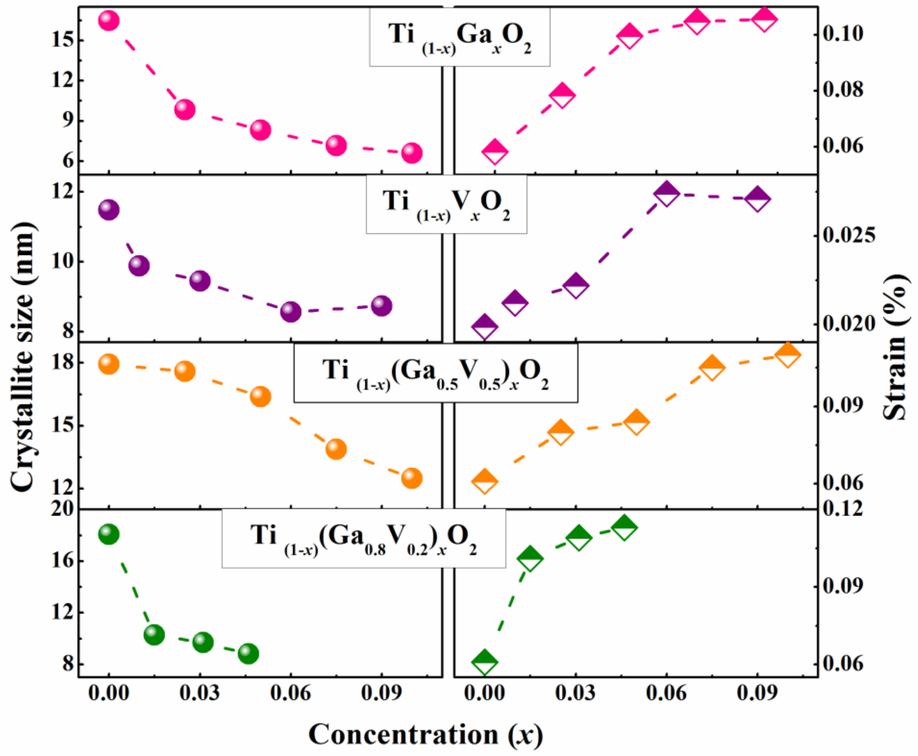

Figure 7.3: Change in crystallites size and strain of Ga (a-b), V (c-d), Ga-V (1:1) (e-f) and Ga-V (4:1) (g-h) doped samples prepared at 450 °C.

Inconsistency in grain growth process is observed in rutile phase. Ga doping inhibits A→R transition, therefore retards grain growth and reduces particles size. On the other hand, V doping promotes A→R transition and thus accelerates grain growth which results in increase in particles size in V doped samples. It is also noticed that the effect of V doping on grain growth is predominant than Ga doping. Hence, grain growth accelerates and particle size increases in $Ti_{(1-x)}(Ga_{0.5}V_{0.5})_xO_2$ and $Ti_{(1-x)}(Ga_{0.8}V_{0.2})_xO_2$ samples, mainly due to vanadium.

7.1.5 Bandgap and Urbach energy

Electronic band structure of TiO_2 is strongly correlated with the crystal structure and crystal structure is modified by doping and co-doping. Hence, bandgap of TiO_2 is also modified. Lattice disorder creates localized defect states near the absorption edge which affects the bandgap. The variation of bandgap (E_G) and Urbach energy (E_U) are shown in figure 7.4 for both the phases.

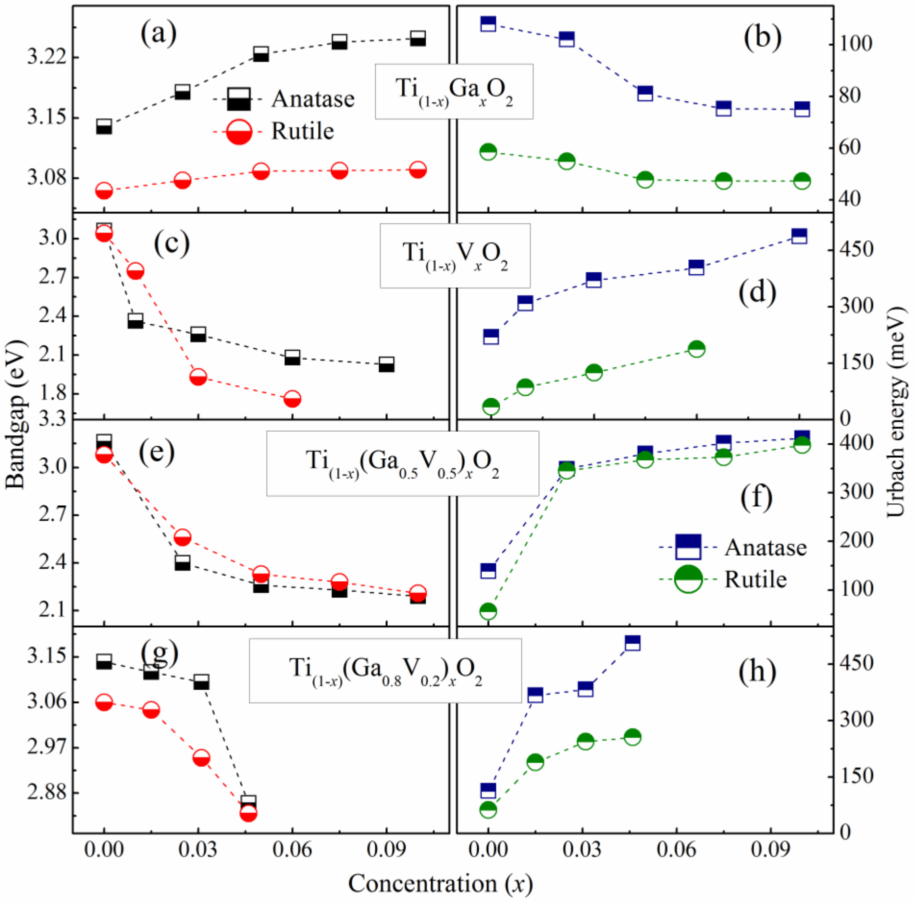

Figure 7.4: Variation of bandgap and Urbach energy by incorporation of Ga (a-b), V (c-d), Ga-V (1:1) (e-f) and Ga-V (4:1) (g-h).

Due to Ga doping, hybridization between O 2p and Ga 4p gives contribution in valence band which thereby increases the bandgap of TiO_2 phases. On the other hand, E_U decreases in both the phases. The small distortion and strain present in the crystal structure of anatase and rutile phase TiO_2 along with the empty space of the TiO_6 octahedra enable the Ga ions to easily occupy the interstitial sites without exerting any extra strain on the lattice. On the contrary, it helps the lattice to become more ordered. This ordered lattice effectively reduces the localized states near the absorption edge and thus effectively increases the bandgap.

V^{5+}/V^{4+} doping creates donor levels just below the CB. These donor levels reduce E_G in the visible light region for both the phases. In the rutile phase, V^{4+} proportion increases at higher doping. Donor levels due to these V^{4+} ions are located at deeper positions below the CB than V^{5+}. Hence, bandgap reduces more at higher doping in rutile phase.

Due to smaller size of V^{5+}/V^{4+} ions lattice contracts. However, lattice disorder increases due to this lattice contraction. This distorted lattice thus increases the localized states near the absorption edge and thereby E_U increases. This increase of E_U also reduces E_G of TiO_2.

In chapter 3 and chapter 4, it is discussed that Ga doping has a nominal effect on E_G whereas V has a strong effect on it. Hence, in Ga-V co-doped samples (1:1 and 4:1), bandgap decreases with increasing doping concentration mainly due to V.

E_U increases in both the co-doped samples. In general increase of E_U results in a reduction of E_G. Hence, this increase of E_U is also responsible to decrease the E_G of TiO_2 to the visible light region in both the co-doped samples.

For a quick overview of our achievements, results of all the four series are listed below:

Table 7.1: Effect of Ga, V, Ga-V (1:1) and Ga-V (4:1) doping on different parameters of TiO_2

Samples		Ga	V	Ga: V = 1:1	Ga: V = 4: 1
Onset temperature (°C)		*l*	*p*	*l*	*l*
Complete conversion temperature (°C)		*l*	*p*	*p*	*l*
Activation energy (KJ/mol)		*i*	*d*	first *i* then *d*	*i*
Lattice constant (A)	a=b (Å)	*i*	*d*	*i*	*i*
	c (Å)	*i*	*d*	*i*	*i*
Lattice constant (R)	a=b (Å)	*i*	*d*	*d*	*i*
	c (Å)	*i*	*d*	*d*	first *i* then *d*
Crystallite size (nm)		*d*	*d*	*d*	*d*
Strain (%)		*d*	*d*	*d*	*d*
Bandgap (eV)	A	*i*	*d*	*d*	*d*
	R	*i*	*d*	*d*	*d*
Urbach energy (meV)	A	*d*	*i*	*i*	*i*
	R	*d*	*i*	*i*	*i*

**l*→delayed, *p*→promoted, *i*→increased, *d*→decreased

Anatase phase becomes stabilized up to a very high (~650-700 °C) temperature in air atmosphere by the effect of Ga doping. On the other hand, V doping reduces its bandgap to visible light reason. In Ga-V (4:1) co-doped samples, we obtain both the phenomena together. Our critical analysis on phase transition, grain growth and optical properties of TiO_2, may widen a path for its applications in multifunctional fields.

7.2 Future Scope

- Most of the semiconducting nanoparticle applications of TiO_2 are in anatase phase. Absorbing visible light is also good for applications. Our results suggest that Ga-V (4:1) samples can serve as a good photocatalyst in presence of visible light up to a very high temperature.
- Bandgap of Ga doped TiO_2 samples increases and from literature, it is observed that electrical conductivity increases by Ga incorporation. This type of materials may be used for conductive oxide (TCO) materials.
- These modified TiO_2 samples can also be used for different type of gas sensing applications.
- From the year 2013, it was observed that co-doping of trivalent and pentavalent dopants in TiO_2 has been given colossal permittivity which is stable in a broad temperature and frequency range. Hence, temperature and frequency dependent dielectric measurement of these Ga-V co-doped samples can also be tired to check colossal permittivity of these materials. This property can be used for capacitor applications.
- Change of calcination environment of these materials may also widen its functionality.

[1] B. Buchholcz, H. Haspel, Á. Kukovecz, Z. Kónya. (2014), Low-temperature conversion of titanate nanotubes into nitrogen-doped TiO_2 nanoparticles, CrystEngComm, 16, 7486. (doi: 10.1039/c4ce00801d)

[2] B.E. Hardin, E.T. Hoke, P.B. Armstrong, J.-H. Yum, P. Comte, T. Torres, J.M.J. Fréchet, M.K. Nazeeruddin, M. Grätzel, M.D. McGehee. (2009), Increased light harvesting in dye-sensitized solar cells with energy relay dyes, Nat. Photonics, 3, 406-411. (doi: 10.1038/nphoton.2009.96)

[3] R. Boppella, A. Mohammadpour, S. Illa, S. Farsinezhad, P. Basak, K. Shankar, S.V. Manorama. (2016), Hierarchical rutile TiO_2 aggregates: A high photonic strength material for optical and optoelectronic devices, Acta Materialia, 119, 92-103. (doi: 10.1016/j.actamat.2016.08.004)

[4] F. Wang, G. Zhang, Z. Zhao, H. Tan, W. Yu, X. Zhang, Z. Sun. (2015), TiO_2 nanosheet array thin film for self-cleaning coating, RSC Adv., 5, 9861-9864. (doi: 10.1039/c4ra13705a)

[5] N. Mufti, I.K.R. Laila, Hartatiek, A. Fuad. (2017), The effect of TiO_2 thin film thickness on self-cleaning glass properties, J. Phys. Conf. Ser., 853, 012035. (doi: 10.1088/1742-6596/853/1/012035)

[6] J. Yu, P. Zhou, Q. Li. (2013), New insight into the enhanced visible-light photocatalytic activities of B-, C- and B/C-doped anatase TiO_2 by first-principles, Phys. Chem. Chem. Phys., 15, 12040-12047. (doi: 10.1039/c3cp44651d)

[7] V.J. Babu, A.S. Nair, Z. Peining, S. Ramakrishna. (2011), Synthesis and characterization of rice grains like Nitrogen-doped TiO_2 nanostructures by electrospinning–photocatalysis, Mater. Lett., 65, 3064-3068. (doi: 10.1016/j.matlet.2011.06.035)

[8] B. Park, E.J. Cairns. (2011), Electrochemical performance of TiO_2 and NiO as fuel cell electrode additives, Electrochem. Commun., 13, 75-77. (doi: 10.1016/j.elecom.2010.11.017)

[9] T.K. Das, P. Ilaiyaraja, P.S.V. Mocherla, G.M. Bhalerao, C. Sudakar. (2016), Influence of surface disorder, oxygen defects

and bandgap in TiO_2 nanostructures on the photovoltaic properties of dye sensitized solar cells, Sol. Energy Mater. Sol. Cells, 144, 194-209. (doi: 10.1016/j.solmat.2015.08.036)

[10] M. Zukalova, A. Zukal, L. Kavan, M.K. Nazeeruddin, P. Liska, M. Gratzel. (2005), Organized mesoporous TiO_2 films exhibiting greatly enhanced performance in dye-sensitized solar cells, Nano Lett., 5, 1789-1792. (doi: 10.1021/nl051401l)

[11] J. Bai, B. Zhou. (2014), Titanium dioxide nanomaterials for sensor applications, Chemical reviews, 114, 10131-10176. (doi: 10.1021/cr400625j)

[12] H. Tokudome, Y. Yamada, S. Sonezaki, H. Ishikawa, M. Bekki, K. Kanehira, M. Miyauchi. (2005), Photoelectrochemical deoxyribonucleic acid sensing on a nanostructured TiO_2 electrode, Appl. Phys. Lett., 87, 213901. (doi: 10.1063/1.2135392)

[13] M.J.A. Ruszala, N.A. Rowson, L.M. Grover, R.A. Choudhery. (2015), Low larbon gootprint TiO_2 substitutes in paint: A review, Int. J. Chem. Eng. Appl., 6, 331-340. (doi: 10.7763/ijcea.2015.v6.505)

[14] Y. Wang, J. Li, L. Wang, T. Qi, D. Chen, W. Wang. (2011), Preparation of rutile titanium dioxide white pigment by a novel NaOH molten-salt process: Influence of doping and calcination, Chem. Eng. Technol., 34, 905-913. (doi: 10.1002/ceat.201100006)

[15] B.K. B. GRZMIL, and M. RABE. (2004), Inhibition of the anatase—rutile phase transformation with addition of K_2O, P_2O_5, and Li_2O, Chem. Pap., 58, 410-414. (doi: 10.9790/4861-0904043239)

[16] M. Landmann, T. Köhler, S. Köppen, E. Rauls, T. Frauenheim, W.G. Schmidt. (2012), Fingerprints of order and disorder in the electronic and optical properties of crystalline and amorphous TiO_2, Phys. Rev. B, 86. (doi: 10.1103/PhysRevB.86.064201)

[17] J. Muscat, V. Swamy, N.M. Harrison. (2002), First-principles calculations of the phase stability ofTiO_2, Phys. Rev. B, 65. (doi:

10.1103/PhysRevB.65.224112)

[18] R. Marchand, L. Brohan, M. Tournoux. (1980), TiO_2 (B) a new form of titanium dioxide and the potassium octatitanate $K_2Ti_8O_{17}$, Mater. Res. Bull., 15, 1129-1133. (doi: 10.1016/0025-5408(80)90076-8)

[19] S.K. Filatov, N.A. Bendeliani, B. Albert, J. Kopf, T.I. Dyuzheva, L.M. Lityagina. (2007), Crystalline structure of the TiO_2 II high-pressure phase at 293, 223, and 133 K according to single-crystal x-ray diffraction data, Dokl. Phys., 52, 195-199. (doi: 10.1134/s1028335807040064)

[20] J. Haines, J.M. Léger. (1993), X-ray diffraction study of TiO_2 up to 49 GPa, Phys. B: Condensed Matter, 192, 233-237. (doi: 10.1016/0921-4526(93)90025-2)

[21] K. Lagarec, S. Desgreniers. (1995), Raman study of single crystal anatase TiO_2 up to 70 GPa, Solid State Commun., 94, 519-524. (doi: 10.1016/0038-1098(95)00129-8)

[22] J.S. Olsen, L. Gerward, J.Z. Jiang. (1999), On the rutile/α-PbO_2-type phase boundary of TiO_2, J. Phys. Chem. Solids, 60, 229-233. (doi: 10.1016/s0022-3697(98)00274-1)

[23] N.A. Dubrovinskaia, L.S. Dubrovinsky, R. Ahuja, V.B. Prokopenko, V. Dmitriev, H.P. Weber, J.M. Osorio-Guillen, B. Johansson. (2001), Experimental and theoretical identification of a new high-pressure TiO_2 polymorph, Phys. Rev. Lett., 87, 275501. (doi: 10.1103/PhysRevLett.87.275501)

[24] M. Latroche, L. Brohan, R. Marchand, M. Tournoux. (1989), New hollandite oxides: TiO_2(H) and $K_{0.06}TiO_2$, J. Solid State Chem., 81, 78-82. (doi: 10.1016/0022-4596(89)90204-1)

[25] H. Sato, S. Endo, M. Sugiyama, T. Kikegawa, O. Shimomura, K. Kusaba. (1991), Baddeleyite-type high-pressure phase of TiO_2, Sci., 251, 786-788. (doi: 10.1126/science.251.4995.786)

[26] J. Muscat, V. Swamy, N.M. Harrison. (2002), First-principles calculations of the phase stability of TiO_2, Phys. Rev. B, 65. (doi: 10.1103/PhysRevB.65.224112)

[27] D.A.H. Hanaor, C.C. Sorrell. (2010), Review of the anatase to

rutile phase transformation, J. Mater. Sci., 46, 855-874. (doi: 10.1007/s10853-010-5113-0)

[28] T. Luttrell, S. Halpegamage, J. Tao, A. Kramer, E. Sutter, M. Batzill. (2014), Why is anatase a better photocatalyst than rutile?--Model studies on epitaxial TiO_2 films, Sci. Rep., 4, 4043. (doi: 10.1038/srep04043)

[29] L.S. Dubrovinsky, N.A. Dubrovinskaia, V. Swamy, J. Muscat, N.M. Harrison, R. Ahuja, B. Holm, B. Johansson. (2001), Materials science. The hardest known oxide, Nat., 410, 653-654. (doi: 10.1038/35070650)

[30] W.-J. Yin, S. Chen, J.-H. Yang, X.-G. Gong, Y. Yan, S.-H. Wei. (2010), Effective band gap narrowing of anatase TiO_2 by strain along a soft crystal direction, Appl. Phys. Lett., 96, 221901. (doi: 10.1063/1.3430005)

[31] T. Mitsuhashi, O.J. Kleppa. (1979), Transformation enthalpies of the TiO_2 polymorphs, J. Am. Ceram. Soc., 62, 356-357. (doi: 10.1111/j.1151-2916.1979.tb19077.x)

[32] A. Sclafani, J.M. Herrmann. (1996), Comparison of the photoelectronic and photocatalytic activities of various anatase and rutile forms of titania in pure liquid organic phases and in aqueous solutions, J. Phys. Chem., 100, 13655-13661. (doi: 10.1021/jp9533584)

[33] R.D. Shannon, J.A. Pask. (1965), Kinetics of the anatase-rutile transformation, J. Am. Ceram. Soc., 48, 391-398. (doi: 10.1111/j.1151-2916.1965.tb14774.x)

[34] E.P. Meagher. (1979), Polyhedral thermal expansion in the TiO_2 polymorphs: Refinement of the crystal structures of rutile and brookite at high temperature, Can. Mineral., 17, 77-85. (doi:

[35] J. Zhang, P. Zhou, J. Liu, J. Yu. (2014), New understanding of the difference of photocatalytic activity among anatase, rutile and brookite TiO_2, Phys. Chem. Chem. Phys., 16, 20382-20386. (doi: 10.1039/c4cp02201g)

[36] R. Plugaru, A. Cremades, J. Piqueras. (2004), The effect of annealing in different atmospheres on the luminescence of

polycrystalline TiO_2, J. Phys.: Condens. Matter, 16, S261-S268. (doi: 10.1088/0953-8984/16/2/031)

[37] B. Choudhury, M. Dey, A. Choudhury. (2013), Shallow and deep trap emission and luminescence quenching of TiO_2 nanoparticles on Cu doping, Appl. Nanosci., 4, 499-506. (doi: 10.1007/s13204-013-0226-9)

[38] C. Huang, X. Liu, L. Kong, W. Lan, Q. Su, Y. Wang. (2007), The structural and magnetic properties of Co-doped titanate nanotubes synthesized under hydrothermal conditions, Appl. Phys. A, 87, 781-786. (doi: 10.1007/s00339-007-3902-3)

[39] C. Stella, D. Prabhakar, M. Prabhu, N. Soundararajan, K. Ramachandran. (2015), Oxygen vacancies induced room temperature ferromagnetism and gas sensing properties of Co-doped TiO_2 nanoparticles, J. Mater. Sci. - Mater. Electron., 27, 1636-1644. (doi: 10.1007/s10854-015-3935-x)

[40] F.J. Knorr, J.L. McHale. (2013), Spectroelectrochemical photoluminescence of trap states of nanocrystalline TiO_2 in aqueous media, J. Phys. Chem. C, 117, 13654-13662. (doi: 10.1021/jp402264p)

[41] D.K. Pallotti, E. Orabona, S. Amoruso, C. Aruta, R. Bruzzese, F. Chiarella, S. Tuzi, P. Maddalena, S. Lettieri. (2013), Multi-band photoluminescence in TiO_2 nanoparticles-assembled films produced by femtosecond pulsed laser deposition, J. Appl. Phys., 114, 043503. (doi: 10.1063/1.4816251)

[42] B. Santara, P.K. Giri, K. Imakita, M. Fujii. (2014), Microscopic origin of lattice contraction and expansion in undoped rutile TiO_2 nanostructures, J. Phys. D: Appl. Phys., 47, 215302. (doi: 10.1088/0022-3727/47/21/215302)

[43] D.K. Pallotti, L. Passoni, P. Maddalena, F. Di Fonzo, S. Lettieri. (2017), Photoluminescence mechanisms in anatase and rutile TiO_2, J. Phys. Chem. C, 121, 9011-9021. (doi: 10.1021/acs.jpcc.7b00321)

[44] J.J.M. Vequizo, S. Kamimura, T. Ohno, A. Yamakata. (2018), Oxygen induced enhancement of NIR emission in brookite TiO_2

powders: comparison with rutile and anatase TiO_2 powders, Phys. Chem. Chem. Phys., 20, 3241-3248. (doi: 10.1039/c7cp06975h)

[45] S. Marinel, D.H. Choi, R. Heuguet, D. Agrawal, M. Lanagan. (2013), Broadband dielectric characterization of TiO_2 ceramics sintered through microwave and conventional processes, Ceram. Int., 39, 299-306. (doi: 10.1016/j.ceramint.2012.06.025)

[46] S. Chao, F. Dogan. (2011), Effects of manganese doping on the dielectric properties of titanium dioxide ceramics, J. Am. Ceram. Soc., 94, 179-186. (doi: 10.1111/j.1551-2916.2010.04039.x)

[47] R. Asahi, Y. Taga, W. Mannstadt, A.J. Freeman. (2000), Electronic and optical properties of anataseTiO_2, Phys. Rev. B, 61, 7459-7465. (doi: 10.1103/PhysRevB.61.7459)

[48] W. Dong, W. Hu, A. Berlie, K. Lau, H. Chen, R.L. Withers, Y. Liu. (2015), Colossal dielectric behavior of Ga+Nb co-doped rutile TiO_2, ACS Appl. Mater. Interfaces, 7, 25321-25325. (doi: 10.1021/acsami.5b07467)

[49] W. Hu, Y. Liu, R.L. Withers, T.J. Frankcombe, L. Noren, A. Snashall, M. Kitchin, P. Smith, B. Gong, H. Chen, J. Schiemer, F. Brink, J. Wong-Leung. (2013), Electron-pinned defect-dipoles for high-performance colossal permittivity materials, Nat Mater, 12, 821-826. (doi: 10.1038/nmat3691)

[50] B. Choudhury, R. Verma, A. Choudhury. (2014), Oxygen defect assisted paramagnetic to ferromagnetic conversion in Fe doped TiO_2 nanoparticles, RSC Adv., 4, 29314. (doi: 10.1039/c3ra45286g)

[51] N.N. Hai, N.T. Khoi, P.V. Vinh. (2009), Preparation and magnetic properties of TiO_2 doped with V, Mn, Co, La, J. Phys. Conf. Ser., 187, 012071. (doi: 10.1088/1742-6596/187/1/012071)

[52] B. Choudhury, A. Choudhury, D. Borah. (2015), Interplay of dopants and defects in making Cu doped TiO_2 nanoparticle a ferromagnetic semiconductor, J. Alloys Compd., 646, 692-698. (doi: 10.1016/j.jallcom.2015.06.199)

[53] N.N. Bao, J.B. Yi, H.M. Fan, X.B. Qin, P. Zhang, B.Y. Wang, J. Ding, S. Li. (2012), Vacancy-induced room-temperature

ferromagnetism in Ga–TiO_2, Scr. Mater., 66, 821-824. (doi: 10.1016/j.scriptamat.2012.02.031)

[54] B. Choudhury, A. Choudhury. (2013), Room temperature ferromagnetism in defective TiO_2 nanoparticles: Role of surface and grain boundary oxygen vacancies, J. Appl. Phys., 114, 203906. (doi: 10.1063/1.4833562)

[55] H. Wang, Z. Zong, Y. Yan. (2014), Mechanism of multi-defect induced ferromagnetism in undoped rutile TiO_2, J. Appl. Phys., 115, 233909. (doi: 10.1063/1.4884223)

[56] B. Santara, P.K. Giri, S. Dhara, K. Imakita, M. Fujii. (2014), Oxygen vacancy-mediated enhanced ferromagnetism in undoped and Fe-doped TiO_2 nanoribbons, J. Phys. D: Appl. Phys., 47, 235304. (doi: 10.1088/0022-3727/47/23/235304)

[57] A. Fujishima, K. Honda. (1972), Electrochemical photolysis of water at a semiconductor electrode, Nat., 238, 37. (doi: 10.1038/238037a0)

[58] T. Verdier, M. Coutand, A. Bertron, C. Roques. (2014), Antibacterial activity of TiO_2 photocatalyst alone or in coatings on E. coli: The influence of methodological aspects, Coat., 4, 670-686. (doi: 10.3390/coatings4030670)

[59] A. Kubacka, M.S. Diez, D. Rojo, R. Bargiela, S. Ciordia, I. Zapico, J.P. Albar, C. Barbas, V.A. Martins dos Santos, M. Fernandez-Garcia, M. Ferrer. (2014), Understanding the antimicrobial mechanism of TiO(2)-based nanocomposite films in a pathogenic bacterium, Sci. Rep., 4, 4134. (doi: 10.1038/srep04134)

[60] L. Chu, Z. Qin, J. Yang, X. Li. (2015), Anatase TiO_2 nanoparticles with exposed {001} facets for efficient dye-sensitized solar cells, Sci. Rep., 5, 12143. (doi: 10.1038/srep12143)

[61] J. Li, D. Xu. (2010), Tetragonal faceted-nanorods of anatase TiO_2 single crystals with a large percentage of active {100} facets, Chem. Commun. (Camb), 46, 2301-2303. (doi: 10.1039/b923755k)

[62] T. Ohno, K. Sarukawa, K. Tokieda, M. Matsumura. (2001), Morphology of a TiO_2 photocatalyst (Degussa, P-25) consisting of anatase and rutile crystalline phases, J. Catal., 203, 82-86. (doi: 10.1006/jcat.2001.3316)

[63] B. Ohtani, O.O. Prieto-Mahaney, D. Li, R. Abe. (2010), What is Degussa (Evonik) P25? Crystalline composition analysis, reconstruction from isolated pure particles and photocatalytic activity test, J. Photochem. Photobiol. A: chem., 216, 179-182. (doi: 10.1016/j.jphotochem.2010.07.024)

[64] R.M. Brand, J. Pike, R.M. Wilson, A.R. Charron. (2003), Sunscreens containing physical UV blockers can increase transdermal absorption of pesticides, Toxicol. Ind. Health, 19, 9-16. (doi: 10.1191/0748233703th169oa)

[65] T.G. Smijs, S. Pavel. (2011), Titanium dioxide and zinc oxide nanoparticles in sunscreens: focus on their safety and effectiveness, Nanotechnol. Sci. Appl., 4, 95-112. (doi: 10.2147/NSA.S19419)

[66] T. Mazza, E. Barborini, P. Piseri, P. Milani, D. Cattaneo, A. Li Bassi, C.E. Bottani, C. Ducati. (2007), Raman spectroscopy characterization of TiO_2 rutile nanocrystals, Phys. Rev. B, 75. (doi: 10.1103/PhysRevB.75.045416)

[67] K. Ding, Z. Miao, B. Hu, G. An, Z. Sun, B. Han, Z. Liu. (2010), Study on the anatase to rutile phase transformation and controlled synthesis of rutile nanocrystals with the assistance of ionic liquid, Langmuir, 26, 10294-10302. (doi: 10.1021/la100468e)

[68] N. Khatun, E.G. Rini, P. Shirage, P. Rajput, S.N. Jha, S. Sen. (2016), Effect of lattice distortion on bandgap decrement due to vanadium substitution in TiO_2 nanoparticles, Mater. Sci. Semicon. Proc., 50, 7-13. (doi: 10.1016/j.mssp.2016.04.002)

[69] B. Bharati, N.C. Mishra, D. Kanjilal, C. Rath. (2018), 500 keV Ar^{2+} ion irradiation induced anatase to brookite phase transformation and ferromagnetism at room temperature in TiO_2 thin films, Appl. Surf. Sci., 428, 723-729. (doi: 10.1016/j.apsusc.2017.09.070)

[70] X. Ye, J. Sha, Z. Jiao, L. Zhang. (1997), Thermoanalytical characteristic of nanocrystalline brookite-based titanium dioxide, Nanostruct. Mater., 8, 919-927. (doi: 10.1016/s0965-9773(98)00013-0)

[71] G.T. D.A.H. Hanao , and C.C. Sorrell (2011), Morphology and photocatalytic activity of highly oriented mixed phase titanium dioxide thin films, Surf. Coat. Technol., 205, 3658 - 3664. (doi: 10.1016/j.surfcoat.2011.01.007)

[72] M. Umadevi, R. Parimaladevi, M. Sangari. (2014), Synthesis, characterization and photocatalytic activity of fluorine doped TiO_2 nanoflakes synthesized using solid state reaction method, Spectrochim. Acta A: Mol. Biomol. Spectrosc., 120, 365-369. (doi: 10.1016/j.saa.2013.10.046)

[73] J. Hu, Y. Cao, K. Wang, D. Jia. (2017), Green solid-state synthesis and photocatalytic hydrogen production activity of anatase TiO_2 nanoplates with super heat-stability, RSC Adv., 7, 11827-11833. (doi: 10.1039/c6ra27160j)

[74] C. Wang, N. Zhang, Q. Li, Y. Yu, J. Zhang, Y. Li, H. Wang, N. Alford. (2015), Dielectric relaxations in rutile TiO_2, J. Am. Ceram. Soc., 98, 148-153. (doi: 10.1111/jace.13250)

[75] M.Y. Tse, X. Wei, J. Hao. (2016), High-performance colossal permittivity materials of (Nb + Er) co-doped TiO_2 for large capacitors and high-energy-density storage devices, Phys. Chem. Chem. Phys., 18, 24270-24277. (doi: 10.1039/c6cp02236g)

[76] J. Li, F. Li, C. Li, G. Yang, Z. Xu, S. Zhang. (2015), Evidences of grain boundary capacitance effect on the colossal dielectric permittivity in (Nb + In) co-doped TiO_2 ceramics, Sci. Rep., 5, 8295. (doi: 10.1038/srep08295)

[77] X. Wang, B. Zhang, G. Shen, L. Sun, Y. Hu, L. Shi, X. Wang, C. Jie, L. Zhang. (2017), Colossal permittivity and impedance analysis of tantalum and samarium co-doped TiO_2 ceramics, Ceram. Int., 43, 13349-13355. (doi: 10.1016/j.ceramint.2017.07.034)

[78] N. Liu, X. Chen, J. Zhang, J.W. Schwank. (2014), A review on

TiO_2-based nanotubes synthesized via hydrothermal method: Formation mechanism, structure modification, and photocatalytic applications, Catal. Today, 225, 34-51. (doi: 10.1016/j.cattod.2013.10.090)

[79] T. Kasuga, M. Hiramatsu, A. Hoson, T. Sekino, K. Niihara. (1998), Formation of titanium oxide nanotube, Langmuir, 14, 3160-3163. (doi: 10.1021/la9713816)

[80] Y. Wu, L. Song, Y. Hu. (2011), Fabrication and characterization of TiO_2 nanotube–epoxy nanocomposites, Ind. Eng. Chem. Res., 50, 11988-11995. (doi: 10.1021/ie2016587)

[81] Z.R. Tang, Y. Zhang, Y.J. Xu. (2012), Tuning the optical property and photocatalytic performance of titanate nanotube toward selective oxidation of alcohols under ambient conditions, ACS Appl. Mater. Interfaces, 4, 1512-1520. (doi: 10.1021/am3001852)

[82] D. Ariyanti, S. Mo’ungatonga, Y. Li, W. Gao. (2018), Formation of TiO_2 based nanoribbons and the effect of post-annealing on its photocatalytic activity, IOP Conf. Ser.: Mater. Sci. Eng., 348, 012002. (doi: 10.1088/1757-899x/348/1/012002)

[83] Y. Li, X. Han, J. Liang, X. Leng, K. Ye, C. Hou, K. Yu. (2015), Preparation of TiO_2 nanoflakes and their influence on lithium ion battery storage performance, Chem. Res. Chin. Univ., 31, 332-336. (doi: 10.1007/s40242-015-4421-y)

[84] Z. Song, H. Zhou, P. Tao, B. Wang, J. Mei, H. Wang, S. Wen, Z. Song, G. Fang. (2016), The synthesis of TiO_2 nanoflowers and their application in electron field emission and self-powered ultraviolet photodetector, Mater. Lett., 180, 179-183. (doi: 10.1016/j.matlet.2016.05.178)

[85] X. Feng, J. Zhai, L. Jiang. (2005), The fabrication and switchable superhydrophobicity of TiO_2 nanorod films, Angew. Chem. Int. Ed. Engl., 44, 5115-5118. (doi: 10.1002/anie.200501337)

[86] S. Xie, X. Han, Q. Kuang, J. Fu, L. Zhang, Z. Xie, L. Zheng. (2011), Solid state precursor strategy for synthesizing hollow TiO_2 boxes with a high percentage of reactive {001} facets exposed, Chem. Commun. (Camb), 47, 6722-6724. (doi:

10.1039/c1cc11542a)

[87] Y. Dai, C.M. Cobley, J. Zeng, Y. Sun, Y. Xia. (2009), Synthesis of anatase TiO_2 nanocrystals with exposed {001} facets, Nano Lett., 9, 2455-2459. (doi: 10.1021/nl901181n)

[88] J. Yu, J. Fan, K. Lv. (2010), Anatase TiO_2 nanosheets with exposed (001) facets: improved photoelectric conversion efficiency in dye-sensitized solar cells, Nanoscale, 2, 2144-2149. (doi: 10.1039/c0nr00427h)

[89] N. Wu, J. Wang, N. Tafen de, H. Wang, J.G. Zheng, J.P. Lewis, X. Liu, S.S. Leonard, A. Manivannan. (2010), Shape-enhanced photocatalytic activity of single-crystalline anatase TiO_2 (101) nanobelts, J. Am. Chem. Soc., 132, 6679-6685. (doi: 10.1021/ja909456f)

[90] X. Yang, C. Wang, Y. Yang, Y. Zhang, X. Jia, J. Chen, X. Ji. (2015), Anatase TiO_2 nanocubes for fast and durable sodium ion battery anodes, J. Mater. Chem. A, 3, 8800-8807. (doi: 10.1039/c5ta00614g)

[91] K. Sabyrov, N.D. Burrows, R.L. Penn. (2012), Size-dependent anatase to rutile phase transformation and particle growth, Chem. Mater., 25, 1408-1415. (doi: 10.1021/cm302129a)

[92] N. Smirnova, I. Petrik, V. Vorobets, G. Kolbasov, A. Eremenko. (2017), Sol-gel Synthesis, Photo- and Electrocatalytic Properties of Mesoporous TiO2 Modified with Transition Metal Ions, Nanoscale Res. Lett., 12, 239. (doi: 10.1186/s11671-017-2002-3)

[93] P. Wang, T. Xie, L. Peng, H. Li, T. Wu, S. Pang, D. Wang. (2008), Water-assisted synthesis of anatase TiO_2 nanocrystals: Mechanism and sensing properties to oxygen at room temperature, J. Phys. Chem. C, 112, 6648-6652. (doi: 10.1021/jp800409f)

[94] A.B.-N. A. Shalaby, R. Iordanova, Y. Dimitriev. (2013), A study of the effect of citric acid on the crystallinity of ZnO/TiO_2 nanopowders, J. Chem. Technol. Metall., 48, 585-590. (doi:

[95] A.C.F.d.M.d.C. Pollyana Caetano Ribeiroa, Ruth Herta Goldschmidt Aliaga Kiminamib, José Marcos Sasaki, Hélio

Lucena Lira. (.2013), Synthesis of TiO_2 by the pechini method and photocatalytic degradation of methyl red, Mater. Res., 16, 468-472. (doi: 10.1590/S1516-14392012005000176)

[96] K. Farhadian Azizi, M.M. Bagheri-Mohagheghi. (2012), Transition from anatase to rutile phase in titanium dioxide (TiO_2) nanoparticles synthesized by complexing sol–gel process: effect of kind of complexing agent and calcinating temperature, J. Sol-Gel Sci. Technol., 65, 329-335. (doi: 10.1007/s10971-012-2940-2)

[97] P.P. Ahonen, E.I. Kauppinen, J.C. Joubert, J.L. Deschanvres, G.V. Tendeloo. (2011), Preparation of nanocrystalline titania powder via aerosol pyrolysis of titanium tetrabutoxide, J. Mater. Res., 14, 3938-3948. (doi: 10.1557/jmr.1999.0533)

[98] D.Q. Ho, S. Kim. (2018), Role of aluminum doping in anatase-to-rutile transformation from thermodynamic view point, phys. status solidi (RRL) - Rapid Res. Lett., 1800234. (doi: 10.1002/pssr.201800234)

[99] M. Wang, J. Wen, Y. Sawada, Y. Hoshi, Z. Hou. (2014), Effect of oxygen and WO_3 additive on anatase-to-rutile phase transformation in TiO_2 nanoparticles, J. Therm. Anal. Calorim., 119, 435-439. (doi: 10.1007/s10973-014-4204-6)

[100] Y. Iida, S. Ozaki. (1961), Grain growth and phase transformation of titanium oxide during calcination, J. Am. Ceram. Soc., 44, 120-127. (doi: 10.1111/j.1151-2916.1961.tb13725.x)

[101] K.-N.P. Kumar. (1995), Growth of rutile crystallites during the initial stage of anatase-to-rutile transformation in pure titania and in titania-alumina nanocomposites, Scr. Metall. Mater., 32, 873-877. (doi: 10.1016/0956-716x(95)93217-r)

[102] L. Gerward, J. Staun Olsen. (1997), Post-rutile high-pressure phases in TiO_2, J. Appl. Crystallogr., 30, 259-264. (doi: 10.1107/s0021889896011454)

[103] V. Swamy, B.C. Muddle. (2007), Ultrastiff cubic TiO_2 identified via first-principles calculations, Phys. Rev. Lett., 98, 035502. (doi: 10.1103/PhysRevLett.98.035502)

[104] H.M. Albetran, B.H. O'Connor, I.M. Low. (2017), Effect of pressure on TiO_2 crystallization kinetics using in-situ high-temperature synchrotron radiation diffraction, J. Am. Ceram. Soc., 100, 3199-3207. (doi: 10.1111/jace.14798)

[105] M.P. Finnegan, H. Zhang, J.F. Banfield. (2007), Phase stability and transformation in titania nanoparticles in aqueous solutions dominated by surface energy, J. Phys. Chem. C, 111, 1962-1968. (doi: 10.1021/jp063822c)

[106] T. Sugimoto, X. Zhou, A. Muramatsu. (2002), Synthesis of uniform anatase TiO_2 nanoparticles by gel-sol method. 1. Solution chemistry of $Ti(OH)^{(4-n)+(n)}$ complexes, J. Colloid. Interface Sci., 252, 339-346. (doi: 10.1006/jcis.2002.8454)

[107] A. Liberti, V. Chiantella, F. Corigliano. (1963), Mononuclear hydrolysis of titanium (IV) from partition equilibria, J. Inorg. Nucl. Chem., 25, 415-427. (doi: 10.1016/0022-1902(63)80192-x)

[108] C. Rath, P. Mohanty, A.C. Pandey, N.C. Mishra. (2009), Oxygen vacancy induced structural phase transformation in TiO_2 nanoparticles, J. Phys. D: Appl. Phys., 42, 205101. (doi: 10.1088/0022-3727/42/20/205101)

[109] M. Tsega, F.B. Dejene. (2017), Influence of acidic pH on the formulation of TiO_2 nanocrystalline powders with enhanced photoluminescence property, Heliyon, 3, e00246. (doi: 10.1016/j.heliyon.2017.e00246)

[110] Y. Hu, H.L. Tsai, C.L. Huang. (2003), Phase transformation of precipitated TiO_2 nanoparticles, Mater. Sci. Eng.: A, 344, 209-214. (doi: 10.1016/s0921-5093(02)00408-2)

[111] G.-h. Li, Y.-f. Zheng, C.-a. Ma, W. Tian. (2008), Preparation of nanoanatase and its in situ XRD study, Trans. Nonferrous Met. Soc. China, 18, 469-473. (doi: 10.1016/s1003-6326(08)60083-7)

[112] G. Rajender, P.K. Giri. (2016), Strain induced phase formation, microstructural evolution and bandgap narrowing in strained TiO_2 nanocrystals grown by ball milling, J. Alloys Compd., 676, 591-600. (doi: 10.1016/j.jallcom.2016.03.154)

[113] B. Choudhury, A. Choudhury. (2013), Local structure

modification and phase transformation of TiO_2 nanoparticles initiated by oxygen defects, grain size, and annealing temperature, Int. Nano Lett., 3, 55. (doi: 10.1186/2228-5326-3-55)

[114] H.M. Moghaddam, S. Nasirian. (2012), Dependence of activation energy and lattice strain on TiO_2 nanoparticles?, Nanosci. Methods, 1, 201-212. (doi: 10.1080/17458080.2011.620023)

[115] M.R. Ranade, A. Navrotsky, H.Z. Zhang, J.F. Banfield, S.H. Elder, A. Zaban, P.H. Borse, S.K. Kulkarni, G.S. Doran, H.J. Whitfield. (2002), Energetics of nanocrystalline TiO_2, Proc Natl Acad Sci U S A, 99 Suppl 2, 6476-6481. (doi: 10.1073/pnas.251534898)

[116] H. Zhang, J.F. Banfield. (2000), Understanding polymorphic phase transformation behavior during growth of nanocrystalline aggregates: Insights from TiO_2, J. Phys. Chem. B, 104, 3481-3487. (doi: 10.1021/jp000499j)

[117] H. Zhang, J.F. Banfield. (1998), Thermodynamic analysis of phase stability of nanocrystalline titania, J. Mater. Chem., 8, 2073-2076. (doi: 10.1039/a802619j)

[118] P.K. Naicker, P.T. Cummings, H. Zhang, J.F. Banfield. (2005), Characterization of titanium dioxide nanoparticles using molecular dynamics simulations, J. Phys. Chem. B, 109, 15243-15249. (doi: 10.1021/jp050963q)

[119] A.A. Gribb, J.F. Banfield. (1997), Particle size effects on transformation kinetics and phase stability in nanocrystalline TiO_2, Am. Mineral., 82, 717-728. (doi: 10.2138/am-1997-7-809)

[120] H.-I. Hsiang, S.-C. Lin. (2008), Effects of aging on nanocrystalline anatase-to-rutile phase transformation kinetics, Ceram. Int., 34, 557-561. (doi: 10.1016/j.ceramint.2006.12.004)

[121] W. Dong, Y. Sun, C.W. Lee, W. Hua, X. Lu, Y. Shi, S. Zhang, J. Chen, D. Zhao. (2007), Controllable and repeatable synthesis of thermally stable anatase nanocrystal-silica composites with highly ordered hexagonal mesostructures, J. Am. Chem. Soc., 129,

13894-13904. (doi: 10.1021/ja073804o)

[122] S.C. Zhu, S.H. Xie, Z.P. Liu. (2015), Nature of rutile nuclei in anatase-to-rutile phase transition, J. Am. Chem. Soc., 137, 11532-11539. (doi: 10.1021/jacs.5b07734)

[123] K. Okada, N. Yamamoto, Y. Kameshima, A. Yasumori, K.J.D. MacKenzie. (2004), Effect of silica additive on the anatase-to-rutile phase transition, J. Am. Ceram. Soc., 84, 1591-1596. (doi: 10.1111/j.1151-2916.2001.tb00882.x)

[124] Z. Zhenfeng, H. Xuanmeng, Z. Yi, R. Qiang. (2010), Influence of WO_3 additive on crystallite structural transformation of TiO_2 powders, Rare Met. Mater. Eng., 39, 771-774. (doi: 10.1016/s1875-5372(10)60099-9)

[125] X.-F. Yu, N.-Z. Wu, H.-Z. Huang, Y.-C. Xie, Y.-Q. Tang. (2001), A study on the monolayer dispersion of tungsten oxide on anatase, J. Mater. Chem., 11, 3337-3342. (doi: 10.1039/b100971k)

[126] S. Riyas, G. Krishnan, P.N.M. Das. (2013), Anatase–rutile transformation in doped titania under argon and hydrogen atmospheres, Adv. Appl. Ceram., 106, 255-264. (doi: 10.1179/174367607x202645)

[127] S. Hishita, I. Mutoh, K. Koumoto, H. Yanagida. (1983), Inhibition mechanism of the anatase-rutile phase transformation by rare earth oxides, Ceram. Int., 9, 61-67. (doi: 10.1016/0272-8842(83)90025-1)

[128] M.S.P. Francisco, V.R. Mastelaro. (2002), Inhibition of the anatase−rutile phase transformation with addition of CeO_2 to $CuO-TiO_2$ system: Raman spectroscopy, X-ray diffraction, and textural studies, Chem. Mater., 14, 2514-2518. (doi: 10.1021/cm011520b)

[129] H. Zhang, J.F. Banfield. (2011), Phase transformation of nanocrystalline anatase-to-rutile via combined interface and surface nucleation, J. Mater. Res., 15, 437-448. (doi: 10.1557/jmr.2000.0067)

[130] J. Criado, C. Real. (1983), Mechanism of the inhibiting effect of

phosphate on the anatase → rutile transformation induced by thermal and mechanical treatment of TiO_2, J. Chem. Soc., Faraday Trans. 1: Phys. Chem. Condens. Phases, 79, 2765. (doi: 10.1039/f19837902765)

[131] S. Vargas, R. Arroyo, E. Haro, R. Rodríguez. (2011), Effects of cationic dopants on the phase transition temperature of titania prepared by the sol-gel method, J. Mater. Res., 14, 3932-3937. (doi: 10.1557/jmr.1999.0532)

[132] T. Ihara. (2003), Visible-light-active titanium oxide photocatalyst realized by an oxygen-deficient structure and by nitrogen doping, Appl. Catal. B: Environ., 42, 403-409. (doi: 10.1016/s0926-3373(02)00269-2)

[133] M. Batzill, E.H. Morales, U. Diebold. (2006), Influence of nitrogen doping on the defect formation and surface properties of TiO_2 rutile and anatase, Phys. Rev. Lett., 96, 026103. (doi: 10.1103/PhysRevLett.96.026103)

[134] M.I. Franch, J. Peral, X. Domenech, J.A. Ayllon. (2005), Aluminium(III) adsorption: a soft and simple method to prevent TiO_2 deactivation during salicylic acid photodegradation, Chem. Commun. (Camb), 1851-1853. (doi: 10.1039/b416598e)

[135] Y. Yang, X.-j. Li, J.-t. Chen, L.-y. Wang. (2004), Effect of doping mode on the photocatalytic activities of Mo/TiO_2, J. Photochem. Photobiol. A: chem., 163, 517-522. (doi: 10.1016/j.jphotochem.2004.02.008)

[136] R.D. Shannon. (1976), Revised effective ionic radii and systematic studies of interatomic distances in halides and chalcogenides, Acta Crystallogr. Sect. A, 32, 751-767. (doi: 10.1107/s0567739476001551)

[137] J. Yang, Y.X. Huang, J.M.F. Ferreira. (1997), Inhibitory effect of alumina additive on the titania phase transformation of a sol-gel-derived powder, J. Mater. Sci. Lett., 16, 1933-1935. (doi: 10.1023/a:1018590701831)

[138] C.H. Chen, E.M. Kelder, J. Schoonman. (1999), Electrostatic sol-spray deposition (ESSD) and characterisation of

nanostructured TiO_2 thin films, Thin Solid Films, 342, 35-41. (doi: 10.1016/s0040-6090(98)01160-2)

[139] J. Yang, J.M.F. Ferreira. (1998), Inhibitory effect of the Al_2O3–SiO_2 mixed additives on the anatase–rutile phase transformation, Mater. Lett., 36, 320-324. (doi: 10.1016/s0167-577x(98)00042-1)

[140] R. Arroyo, G. Córdoba, J. Padilla, V.H. Lara. (2002), Influence of manganese ions on the anatase–rutile phase transition of TiO_2 prepared by the sol–gel process, Mater. Lett., 54, 397-402. (doi: 10.1016/s0167-577x(01)00600-0)

[141] G.C. Vásquez, M.A. Peche-Herrero, D. Maestre, B. Alemán, J. Ramírez-Castellanos, A. Cremades, J.M. González-Calbet, J. Piqueras. (2014), Influence of Fe and Al doping on the stabilization of the anatase phase in TiO_2 nanoparticles, J. Mater. Chem. C, 2, 10377-10385. (doi: 10.1039/c4tc02099e)

[142] G. Rossi, M. Calizzi, V. Di Cintio, S. Magkos, L. Amidani, L. Pasquini, F. Boscherini. (2016), Local structure of V dopants in TiO_2 nanoparticles: X-ray absorption spectroscopy, including Ab-initio and full potential simulations, J. Phys. Chem. C, 120, 7457-7466. (doi: 10.1021/acs.jpcc.5b12045)

[143] M. Thommes, K. Kaneko, A.V. Neimark, J.P. Olivier, F. Rodriguez-Reinoso, J. Rouquerol, K.S.W. Sing. (2015), Physisorption of gases, with special reference to the evaluation of surface area and pore size distribution (IUPAC Technical Report), Pure Appl. Chem., 87. (doi: 10.1515/pac-2014-1117)

[144] M. Thommes, K.A. Cychosz. (2014), Physical adsorption characterization of nanoporous materials: progress and challenges, Adsorption, 20, 233-250. (doi: 10.1007/s10450-014-9606-z)

[145] J. Landers, G.Y. Gor, A.V. Neimark. (2013), Density functional theory methods for characterization of porous materials, Colloids and Surfaces A: Physicochemical and Engineering Aspects, 437, 3-32. (doi: 10.1016/j.colsurfa.2013.01.007)

[146] W. Wang, P. Liu, M. Zhang, J. Hu, F. Xing. (2012), The Pore Structure of Phosphoaluminate Cement, Open Journal of

Composite Materials, 02, 104-112. (doi: 10.4236/ojcm.2012.23012)

[147] Anita, A.K. Yadav, N. Khatun, S. Kumar, C.M. Tseng, S. Biring, S. Sen. (2017), Size and strain dependent anatase to rutile phase transition in TiO_2 due to Si incorporation, J Mater Sci-Mater El, 28, 19017-19024. (doi: 10.1007/s10854-017-7856-8)

[148] N. Khatun, Anita, P. Rajput, D. Bhattacharya, S.N. Jha, S. Biring, S. Sen. (2017), Anatase to rutile phase transition promoted by vanadium substitution in TiO_2: A structural, vibrational and optoelectronic study, Ceram. Int., 43, 14128-14134. (doi: 10.1016/j.ceramint.2017.07.153)

[149] Q. Deng, X. Han, Y. Gao, G. Shao. (2012), Remarkable optical red shift and extremely high optical absorption coefficient of V-Ga co-doped TiO2, J. Appl. Phys., 112, 013523. (doi: 10.1063/1.4733971)

[150] J. Zhou, Y. Zhang, X.S. Zhao, A.K. Ray. (2006), Photodegradation of benzoic acid over metal-doped TiO_2, Ind. Eng. Chem. Res., 45, 3503-3511. (doi: 10.1021/ie051098z)

[151] C. Gionco, S. Livraghi, S. Maurelli, E. Giamello, S. Tosoni, C. Di Valentin, G. Pacchioni. (2015), Al- and Ga-Doped TiO_2, ZrO_2, and HfO_2: The nature of O 2p trapped holes from a combined electron paramagnetic resonance (EPR) and density functional theory (DFT) study, Chem. Mater., 27, 3936-3945. (doi: 10.1021/acs.chemmater.5b00800)

[152] S. Sudou, K. Kado, K. Nakamura. (2010), Optical properties of Ga-doped TiO_2 films prepared by spin-coating method, Trans. Mater. Res. Soc. Japan, 35, 171-174. (doi: 10.14723/tmrsj.35.171)

[153] A.N. Banerjee, S.W. Joo, B.-K. Min. (2012), Photocatalytic degradation of organic dye by sol-gel-derived gallium-doped anatase titanium oxide nanoparticles for environmental remediation, J. Nanomater., 2012, 1-14. (doi: 10.1155/2012/201492)

[154] S. Shang, X. Jiao, D. Chen. (2012), Template-free fabrication of

TiO_2 hollow spheres and their photocatalytic properties, ACS Appl. Mater. Interfaces, 4, 860-865. (doi: 10.1021/am201535u)

[155] X. Jiang, T. Herricks, Y. Xia. (2003), Monodispersed spherical colloids of titania: Synthesis, characterization, and crystallization, Adv. Mater., 15, 1205-1209. (doi: 10.1002/adma.200305105)

[156] H. Yaghoubi, N. Taghavinia, E.K. Alamdari, A.A. Volinsky. (2010), Nanomechanical properties of TiO_2 granular thin films, ACS Appl. Mater. Interfaces, 2, 2629-2636. (doi: 10.1021/am100455q)

[157] M.V. Swapna, K.R. Haridas. (2015), An easier method of preparation of mesoporous anatase TiO_2 nanoparticles via ultrasonic irradiation, J. Exp. Nanosci., 11, 540-549. (doi: 10.1080/17458080.2015.1094189)

[158] V. Caratto, L. Setti, S. Campodonico, M.M. Carnasciali, R. Botter, M. Ferretti. (2012), Synthesis and characterization of nitrogen-doped TiO_2 nanoparticles prepared by sol–gel method, J. Sol-Gel Sci. Technol., 63, 16-22. (doi: 10.1007/s10971-012-2756-0)

[159] R.A. Spurr, H. Myers. (1957), Quantitative analysis of anatase-rutile mixtures with an X-Ray diffractometer, Anal. Chem., 29, 760-762. (doi: 10.1021/ac60125a006)

[160] T. Okajima, T. Yamamoto, M. Kunisu, S. Yoshioka, I. Tanaka, N. Umesaki. (2006), Dilute Ga dopant in TiO_2 by X-ray absorption near-edge structure, Japanese Journal of Applied Physics, 45, 7028-7031. (doi: 10.1143/jjap.45.7028)

[161] M.A. Malati, W.K. Wong. (1984), Doping TiO_2 for solar energy applications, Surf. Technol., 22, 305-322. (doi: 10.1016/0376-4583(84)90094-3)

[162] G.B. Song, J.K. Liang, F.S. Liu, T.J. Peng, G.H. Rao. (2005), Preparation and phase transformation of anatase–rutile crystals in metal doped TiO_2/muscovite nanocomposites, Thin Solid Films, 491, 110-116. (doi: 10.1016/j.tsf.2005.05.035)

[163] M. Sahu, P. Biswas. (2011), Single-step processing of copper-doped titania nanomaterials in a flame aerosol reactor, Nanoscale

Res. Lett., 6, 441. (doi: 10.1186/1556-276X-6-441)

[164] O. Ola, M. Mercedes Maroto-Valer. (2014), Copper based TiO_2 honeycomb monoliths for CO_2 photoreduction, Catal. Sci. Technol., 4, 1631-1637. (doi: 10.1039/c3cy00991b)

[165] M. Šćepanović, M. Grujić-Brojčin, Z. Dohčević-Mitrović, Z.V. Popović. (2006), Effects of confinement, strain and nonstoichiometry on Raman spectra of anatase TiO_2 nanopowders, Materials Science Forum, 518, 101-106. (doi: 10.4028/www.scientific.net/MSF.518.101)

[166] J.C. Parker, R.W. Siegel. (1990), Calibration of the Raman spectrum to the oxygen stoichiometry of nanophase TiO_2, Appl. Phys. Lett., 57, 943-945. (doi: 10.1063/1.104274)

[167] M. Anpo, P.V. Kamat, Environmentally benign photocatalysts: applications of titanium oxide-based materials, Springer Science &

Business Media2010.

[168] M. Tahir, N.S. Amin. (2015), Indium-doped TiO_2 nanoparticles for photocatalytic CO_2 reduction with H_2O vapors to CH_4, Appl. Catal. B: Environ., 162, 98-109. (doi: 10.1016/j.apcatb.2014.06.037)

[169] P. Georgios, S.M. Wolfgang. (2010), X-Ray photoelectron spectroscopy of anatase-TiO_2 coated carbon nanotubes, Solid State Phenomena, 162, 163-177. (doi: 10.4028/www.scientific.net/SSP.162.163)

[170] S. Luo, T.D. Nguyen-Phan, D. Vovchok, I. Waluyo, R.M. Palomino, A.D. Gamalski, L. Barrio, W. Xu, D.E. Polyansky, J.A. Rodriguez, S.D. Senanayake. (2018), Enhanced, robust light-driven H_2 generation by gallium-doped titania nanoparticles, Phys. Chem. Chem. Phys., 20, 2104-2112. (doi: 10.1039/c7cp04155a)

[171] C. Ozgit-Akgun, E. Goldenberg, A.K. Okyay, N. Biyikli. (2014), Hollow cathode plasma-assisted atomic layer deposition of crystalline AlN, GaN and AlxGa1−xN thin films at low

temperatures, J. Mater. Chem. C, 2, 2123-2136. (doi: 10.1039/c3tc32418d)

[172] B. Bharti, S. Kumar, H.N. Lee, R. Kumar. (2016), Formation of oxygen vacancies and Ti(3+) state in TiO_2 thin film and enhanced optical properties by air plasma treatment, Sci. Rep., 6, 32355. (doi: 10.1038/srep32355)

[173] D. Chu, A. Younis, S. Li. (2012), Direct growth of TiO_2 nanotubes on transparent substrates and their resistive switching characteristics, J. Phys. D: Appl. Phys., 45, 355306. (doi: 10.1088/0022-3727/45/35/355306)

[174] J. Liu, R. Han, Y. Zhao, H. Wang, W. Lu, T. Yu, Y. Zhang. (2011), Enhanced photoactivity of V−N co-doped TiO_2 derived from a two-step hydrothermal procedure for the degradation of PCP−Na under visible light irradiation, J. Phys. Chem. C, 115, 4507-4515. (doi: 10.1021/jp110814b)

[175] J.G.K. C. M. Whang, E. Y. Kim, Y. H. Kim and W. I. Lee. (2005), Effect of Co, Ga, and Nd additions on the photocatalytic properties of TiO_2 nanopowders, Glass Phys. Chem., 31, 6. (doi:

[176] A. Zaleska. (2008), Doped-TiO_2: A review, Recent Patents on Engineering, 2, 157-164. (doi: 10.2174/187221208786306289)

[177] V. Kiisk, M. Šavel, V. Reedo, A. Lukner, I. Sildos. (2009), Anatase-to-rutile phase transition of samarium-doped TiO_2 powder detected via the luminescence of Sm^{3+}, Physics Procedia, 2, 527-538. (doi: 10.1016/j.phpro.2009.07.038)

[178] R.L. Penn, J.F. Banfield. (1999), Formation of rutile nuclei at anatase (112) twin interfaces and the phase transformation mechanism in nanocrystalline titania, Am. Mineral., 84, 871-876. (doi: 10.2138/am-1999-5-621)

[179] A.K. Chandiran, F.d.r. Sauvage, L. Etgar, M. Graetzel. (2011), $Ga^{3+}$and Y^{3+} cationic substitution in mesoporous TiO_2 photoanodes for photovoltaic applications, J. Phys. Chem. C, 115, 9232-9240. (doi: 10.1021/jp1121068)

[180] S.J. Ikhmayies, R.N. Ahmad-Bitar. (2013), A study of the optical bandgap energy and Urbach tail of spray-deposited CdS:In thin

films, J. Mater. Res.Technol., 2, 221-227. (doi: 10.1016/j.jmrt.2013.02.012)

[181] A. Paleari, F. Meinardi, A. Lauria, R. Lorenzi, N. Chiodini, S. Brovelli. (2007), High-energy shift of the Urbach ultraviolet absorption from attenuated dynamical disorder in fluorine modified sol-gel silica, Appl. Phys. Lett., 91, 141913. (doi: 10.1063/1.2794429)

[182] K. Zheng, K. Žídek, M. Abdellah, P. Chábera, M.S. Abd El-sadek, T. Pullerits. (2013), Effect of metal oxide morphology on electron injection from CdSe quantum dots to ZnO, Appl. Phys. Lett., 102, 163119. (doi: 10.1063/1.4803173)

[183] A.S. Hassanien, A.A. Akl. (2015), Influence of composition on optical and dispersion parameters of thermally evaporated non-crystalline $Cd_{50}S_{50}{-}xSe_x$ thin films, J. Alloys Compd., 648, 280-290. (doi: 10.1016/j.jallcom.2015.06.231)

[184] S. Benramache, B. Benhaoua, F. Chabane. (2012), Effect of substrate temperature on the stability of transparent conducting cobalt doped ZnO thin films, J. Semicon., 33, 093001. (doi: 10.1088/1674-4926/33/9/093001)

[185] R. Long, N.J. English. (2010), First-principles calculation of electronic structure of V-doped anatase TiO_2, Chem. phys. chem, 11, 2606-2611. (doi: 10.1002/cphc.201000329)

[186] W. Avansi, R. Arenal, V.R. de Mendonça, C. Ribeiro, E. Longo. (2014), Vanadium-doped TiO_2 anatase nanostructures: the role of V in solid solution formation and its effect on the optical properties, CrystEngComm, 16, 5021. (doi: 10.1039/c3ce42356e)

[187] M. Amini, H. Naslhajian, S.M.F. Farnia. (2014), V-doped titanium mixed oxides as efficient catalysts for oxidation of alcohols and olefins, New J. Chem., 38, 1581. (doi: 10.1039/c4nj00066h)

[188] W. Zhou, Q. Liu, Z. Zhu, J. Zhang. (2010), Preparation and properties of vanadium-doped TiO_2 photocatalysts, J. Phys. D: Appl. Phys., 43, 035301. (doi: 10.1088/0022-3727/43/3/035301)

[189] C. Ciomaga, M. Viviani, M.T. Buscaglia, V. Buscaglia, L.

Mitoseriu, A. Stancu, P. Nanni. (2007), Preparation and characterisation of the Ba(Zr,Ti)O_3 ceramics with relaxor properties, J. Eur. Ceram. Soc., 27, 4061-4064. (doi: 10.1016/j.jeurceramsoc.2007.02.095)

[190] M. Grujić-Brojčin, M.J. Šćepanović, Z.D. Dohčević-Mitrovi, I. Hinić, B. Matović, G. Stanišić, Z.V. Popović. (2005), Infrared study of laser synthesized anatase TiO_2 nanopowders, J. Phys. D: Appl. Phys., 38, 1415-1420. (doi: 10.1088/0022-3727/38/9/014)

[191] G. Zeng, K.-K. Li, H.-G. Yang, Y.-H. Zhang. (2013), Micro-Raman mapping on an anatase TiO_2 single crystal with a large percentage of reactive (001) facets, Vib. Spectrosc., 68, 279-284. (doi: 10.1016/j.vibspec.2013.08.012)

[192] T. Ohsaka. (1980), Temperature dependence of the Raman spectrum in anatase TiO_2, J. Phys. Soc. Jpn., 48, 1661-1668. (doi: 10.1143/jpsj.48.1661)

[193] S. Kelly, F.H. Pollak, M. Tomkiewicz. (1997), Raman spectroscopy as a morphological probe for TiO_2 aerogels, J. Phys. Chem. B, 101, 2730-2734. (doi: 10.1021/jp962747a)

[194] W.F. Zhang, Y.L. He, M.S. Zhang, Z. Yin, Q. Chen. (2000), Raman scattering study on anatase TiO_2 nanocrystals, J. Phys. D: Appl. Phys., 33, 912-916. (doi: 10.1088/0022-3727/33/8/305)

[195] F. Tian, Y. Zhang, J. Zhang, C. Pan. (2012), Raman spectroscopy: A new approach to measure the percentage of aanatase TiO_2 exposed (001) facets, J. Phys. Chem. C, 116, 7515-7519. (doi: 10.1021/jp301256h)

[196] H.C. Choi, Y.M. Jung, S.B. Kim. (2004), Characterization of Raman spectra of size-selected TiO_2 nanoparticles by two-dimensional correlation spectroscopy, Bull. Korean Chem. Soc., 25, 426-428. (doi: 10.5012/bkcs.2004.25.3.426)

[197] M.J. Šćepanović, M. Grujić-Brojčin, Z.D. Dohčević-Mitrović, Z.V. Popović. (2007), Temperature dependence of the lowest frequency E*g* Raman mode in laser-synthesized anatase TiO_2 nanopowder, Appl. Phys. A, 86, 365-371. (doi: 10.1007/s00339-006-3775-x)

[198] M. Mikami, S. Nakamura, O. Kitao, H. Arakawa. (2002), Lattice dynamics and dielectric properties of TiO_2 anatase: A first-principles study, Phys. Rev. B, 66. (doi: 10.1103/PhysRevB.66.155213)

[199] S.P.S. Porto, P.A. Fleury, T.C. Damen. (1967), Raman spectra of TiO_2, MgF_2, ZnF_2, FeF_2, and MnF_2, Phys. Rev., 154, 522-526. (doi: 10.1103/PhysRev.154.522)

[200] Y. Zhang, C.X. Harris, P. Wallenmeyer, J. Murowchick, X. Chen. (2013), Asymmetric lattice vibrational characteristics of rutile TiO_2 as revealed by laser power dependent Raman spectroscopy, J. Phys. Chem. C, 117, 24015-24022. (doi: 10.1021/jp406948e)

[201] G. Xing-Yuan, X. Da-Peng, D. Zhan-Hui, S. Wen-Hui. (2006), Preparation and Raman spectrum of rutile single crystals using floating zone method, Chin. Phys. Lett., 23, 1645-1647. (doi: 10.1088/0256-307x/23/6/080)

[202] F. Wang, W. Liu, Y. Wu, M.Y. Sfeir, L. Huang, J. Hone, S. O'Brien, L.E. Brus, T.F. Heinz, Y.R. Shen. (2007), Multiphonon Raman scattering from individual single-walled carbon nanotubes, Phys. Rev. Lett., 98, 047402. (doi: 10.1103/PhysRevLett.98.047402)

[203] T. Lan, X. Tang, B. Fultz. (2012), Phonon anharmonicity of rutile TiO_2 studied by Raman spectrometry and molecular dynamics simulations, Phys. Rev. B, 85. (doi: 10.1103/PhysRevB.85.094305)

[204] A. Sakunthala, M.V. Reddy, S. Selvasekarapandian, B.V.R. Chowdari, P.C. Selvin. (2011), Energy storage studies of bare and doped vanadium pentoxide, (V1.95M0.05)O5, M = Nb, Ta, for lithium ion batteries, Energy Environ. Sci., 4, 1712. (doi: 10.1039/c0ee00513d)

[205] A. Vittadini, M. Casarin, A. Selloni. (2005), First principles studies of vanadia-titania monolayer catalysts: mechanisms of NO selective reduction, J. Phys. Chem. B, 109, 1652-1655. (doi: 10.1021/jp044752h)

[206] T. Umebayashi, T. Yamaki, H. Itoh, K. Asai. (2002), Analysis of electronic structures of 3d transition metal-doped TiO_2 based on band calculations, J. Phys. Chem. Solids, 63, 1909-1920. (doi: 10.1016/s0022-3697(02)00177-4)

[207] A. Kubacka, A. Fuerte, A. Martínez-Arias, M. Fernández-García. (2007), Nanosized Ti–V mixed oxides: Effect of doping level in the photo-catalytic degradation of toluene using sunlight-type excitation, Appl. Catal. B: Environ., 74, 26-33. (doi: 10.1016/j.apcatb.2007.01.011)

[208] A.Y. Choi, C.-H. Han. (2014), A study on the band gap and the doping level of V-doped TiO_2 with respect to the Visible-light photocatalytic activity, J. Nanosci.Nanotechnol., 14, 8070-8073. (doi: 10.1166/jnn.2014.9469)

[209] Z. Li, J. Wu, D. Xiao, J. Zhu, W. Wu. (2016), Colossal permittivity in titanium dioxide ceramics modified by tantalum and trivalent elements, Acta Materialia, 103, 243-251. (doi: 10.1016/j.actamat.2015.09.046)

[210] N. Khatun, S. Tiwari, C.P. Vinod, C.-M. Tseng, S. Wei Liu, S. Biring, S. Sen. (2018), Role of oxygen vacancies and interstitials on structural phase transition, grain growth, and optical properties of Ga doped TiO_2, J. Appl. Phys., 123, 245702. (doi: 10.1063/1.5027672)

[211] W. Zhu, X. Qiu, V. Iancu, X.Q. Chen, H. Pan, W. Wang, N.M. Dimitrijevic, T. Rajh, H.M. Meyer, 3rd, M.P. Paranthaman, G.M. Stocks, H.H. Weitering, B. Gu, G. Eres, Z. Zhang. (2009), Band gap narrowing of titanium oxide semiconductors by noncompensated anion-cation codoping for enhanced visible-light photoactivity, Phys. Rev. Lett., 103, 226401. (doi: 10.1103/PhysRevLett.103.226401)

[212] L.E. Depero, A. Marino, B. Allieri, E. Bontempi, L. Sangaletti, C. Casale, M. Notaro. (2011), Morphology and microstructural properties of TiO_2 nanopowders doped with trivalent Al and Ga cations, J. Mater. Res., 15, 2080-2086. (doi: 10.1557/jmr.2000.0299)

[213] P.M. Oliver, G.W. Watson, E.T. Kelsey, S.C. Parker. (1997), Atomistic simulation of the surface structure of the TiO_2 polymorphs rutileand anatase, J. Mater. Chem., 7, 563-568. (doi: 10.1039/a606353e)

[214] A.S. Barnard, P. Zapol. (2004), Effects of particle morphology and surface hydrogenation on the phase stability of TiO_2, Phys. Rev. B, 70. (doi: 10.1103/PhysRevB.70.235403)

[215] Z. Lai, F. Peng, H. Wang, H. Yu, S. Zhang, H. Zhao. (2013), A new insight into regulating high energy facets of rutile TiO_2, J. Mater. Chem. A, 1, 4182. (doi: 10.1039/c3ta00188a)

[216] T. Ohno, K. Sarukawa, M. Matsumura. (2002), Crystal faces of rutile and anatase TiO_2 particles and their roles in photocatalytic reactions, New J. Chem., 26, 1167-1170. (doi: 10.1039/b202140d)